This book was bound by
Badminton Press
18 Half Croft, Syston, Leicester, LE7 8LD
Telephone: Leicester (0533) 602918.

THE DETECTION OF LASER INDUCED DAMAGE IN OPTICAL MATERIALS

by

Lutphy Ali Mahmood, B.Sc., M.Sc.

A Doctoral Thesis submitted in partial fulfilment of the requirement for the award of Doctor of Philosophy of the Loughborough University of Technology.

December 1985.

Supervisor: Dr. D.C. Emmony.

To:

Nahla and Farah

Contents

Acknowledgements

It is a pleasure to acknowledge the encouragement and guidance of my supervisor, Dr. D.C. Emmony.

I would also like to thank the technical staff of the Physics Department for their skilful help.

I am indebted for the diligence of Mrs. B. Wright who worked long and carefully to transform hand written pages into neat typescript.

Thanks also to the University of Salah-Al-Deen (IRAQ) for providing the financial support.

Above all, I especially wish to thank my colleagues with whom I have had many valuable discussions.

Summary

Laser induced damage caused by the interaction of intense optical radiation with matter is one of the most serious problems encountered in the operation and design of high energy laser systems. The most widely used technique to detect damage is to simply irradiate and visually inspect the sample for signs of damage. This method although valuable does not provide real-time damage monitoring and has limited quantitative capabilities.

In this project three sensitive real-time monitoring techniques of the early stages of laser induced damage have been investigated. In the first the damage was monitored using the photoacoustic effect, in which the damage is related to the acoustic signal generated in the optical component and detected by a piezo-electric transducer attached to the sample. In the second technique "the mirage effect", a He-Ne laser beam was used to probe the refractive index gradient in the air above the sample surface generated by the absorption of the pump laser radiation, in this case the laser light absorption and the onset of damage was related to the deflection of the He-Ne beam. In this mirage method, both parallel probing and glancing reflection have been used. Finally laser induced scattering was used to detect the onset of damage. In this technique a He-Ne laser is reflected off the sample surface. The specular

reflection is blocked by a stop and only the scattered light is collected by the detector. Damage is correlated to the increase in the scatter of the He-Ne laser beam. Damage experiments have been carried out in the infra-red (CO_2 - 10.6μm) and U.V. (KrF - 248nm).

It has been shown that it is possible to detect the earliest stages of the onset of damage giving information about parameters such as the spot-size dependence on highly reflecting laser mirrors and thin film coated components.

CHAPTER ONE

Review of Laser Induced Damage in Optical Materials

1.1 INTRODUCTION.

The development and application of high-energy lasers during the past decade has generated profound interest in the behaviour of optical materials under intense illumination. These optical materials, have been in performance and power density limiting elements in high power and high energy laser systems since the early days of laser physics. The demands imposed on optical materials when they are incorporated into laser systems operating at high power levels, represent a new class of problems for the manufacturers of optical materials.

Properties that are wholly negligible at low power levels, like weak absorption and the presence of minute inhomogeneities can lead to catastrophic material failure in the hostile environment of a laser operating with high pulsed energies. By the late sixties, it was clear that the advance of high-power laser systems was being impeded by the limitations imposed by material failure, Marker et. al[1] (early in 1963) was the first one to report damage to transparent dielectrics and the production of a spark in air by focussing a pulsed ruby laser.

For many years the subject of laser induced damage in optical materials remained largely an empirical or engineering science. Although a vast amount of theoretical and experimental effort was expended in study of damage processes, quantitative reproducible breakdown thresholds

with unambiguous theoretical interpretations have been obtained only during the last few years. The situation was similar to the progress made in understanding DC breakdown in electrical insulators. There too, the field developed largely by engineering trial and error and basic quantitative understanding was not achieved until reproducible experimental results on well prepared materials were obtained[2]. The difficulties in DC breakdown experiments were manifold; the influence of electrodes, space charges, the risetime of the voltage pulse and the origin of the first few electrons to start the avalanche. The experimental data in DC electrical breakdown was fully explained by the theories of electron-avalanche and Seitz[3] estimated that the electron density should build up to 10^8 - $10^{10} cm^{-3}$ for the breakdown to start. It will be shown later in this review that the same theory "the electron-avalanche" is capable of explaining laser induced damage in optical materials.

In the beginning of laser damage studies, an experiment might begin and end with only one single firing of a ruby laser, it was not surprising therefore that there were many difficulties in laser induced damage which often prevented the establishment of reproducible results, among these difficulties were:

1. Irreproducibility in the spatial and temporal behaviour of the laser.

2. The presence of absorbing defects.

3. In transparent materials the phenomena of self-focussing often determines the damage threshold.

The damage itself begins with an overpopulation of loosely bonded electrons, this population may be quite undetectable by the conventional techniques of spectroscopy. By way of linear and non-linear optical processes, these electrons are freed and energised by the large optical field in the laser pulse, the electrons will then rise from the valance band (the bound state) to the conduction band (free state) and produce more electrons by collision. This process leads to a large charge build up. The resulting phasma is highly absorbing and channels even more energy from the laser pulse into the material in the form of heat, then, if the temperature is raised to the point of melting, damage occurs to the optical material.

Damage to optical materials can be divided into the following:

1. Single pulse damage.

2. Continuous wave damage.

3. Multipulse laser induced damage.

Continuous wave (cw) damage mechanisms differ from those of single pulse damage in that the time constants of operation are substantially different. In the case

of pulsed operation, the time constant is short and the electric field effects predominate. While in the operation of a (cw) laser, the time constant is so long that the damage phenomena are controlled by thermal effects. More correctly, for pulse time constants in the picosecond and nanosecond regimes, the electric field predominates. However, when the pulse regime is in the microsecond level, thermal effects begin to become ascendant. With the advent of highly repetitive pulsed systems both single and (cw) damage mechanisms become important. Since single pulse damage is the subject of the experimental work reported in this thesis and is considered to be the most important one, both continuous and repetitive damage will not be considered any further in this review.

The description of single pulse laser induced damage throughout materials which it has been studied, divides into three material classes; these are dielectrics, metals and thin film coatings. The following section will outline the experimental methods used to perform laser induced damage before the physical processes involved in laser induced damage in the three materials classes are dealt with.

1.2 METHODS OF PERFORMING DAMAGE STUDIES.

It is generally appreciated by many workers in the damage field that in order to get reproducible results,

careful mode control of the laser must be backed by careful measurements of both the temporal and spatial profile of the damaging pulse. The typical arrangement for the measurement of a damage threshold is shown in Figure 1.1.

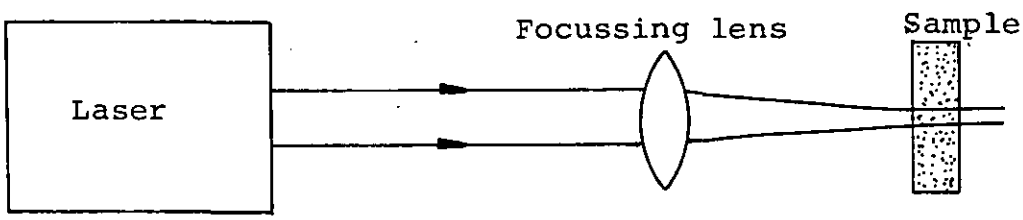

Figure 1.1: Geometry for laser induced damage measurement.

Damage tests may be performed at the focus or away from it depending on whether the laser energy is large enough. A laser pulse is focussed by a lens, the sample is positioned so that the first surface lies in the focal plane of the lens if the surface damage threshold is to be measured. For bulk damage the focal plane is positioned inside the material of the sample. In order to calculate the damage threshold of the sample, the sample is irradiated by a series of pulses of different energies. The intensity of each pulse must be measured. In order to determine the laser intensity present in the interaction region, three parameters of the laser pulse must be measured, these are; the energy in the pulse E, the interaction area A, and the

pulse duration τ. The intensity I (sometimes called the fluence), the rms optical electrical fields E, the energy density F and the power p are given by:

$$I = n\varepsilon_o c E^2 = \frac{F}{\tau} = \frac{p}{A} = \frac{E}{\tau A} \qquad (1.1)$$

where n, ε_o, c are the refractive index of the medium, the permitivity of free space and the velocity of light in the medium respectively. The measurement of the total energy of the laser pulse can be carried out using calibrated photodiodes and calorimeters; these can offer accuracy of up to 99% but must be pre-calibrated against standards[4]. The pulse duration measurement is a more difficult task where short pulses are concerned. Generally a combination of a photodiode and an oscilloscope are used to measure the pulse duration. The third parameter to be measured is the spatial profile of the laser pulse; many methods are available to do this, for example, it can be measured by scanning a pinhole across the beam where the profile is required. The signal is recorded at each point and the intensity is plotted as a function of position. The profile can also be measured by reflecting a weak replica of the main pulse by a beam splitter. The replica is then allowed to travel to an optical path equivalent to that of the damaging pulse and ending at a recording medium, e.g. photographic film, or a T.V. camera. Two dimensional data then can be obtained from the processed

film or some form of video store. A third method for spatial profile measurement is to use a photodiodes array, this technique is in fact the basis of some commercial instruments[5].

1.3 LASER INDUCED DAMAGE MECHANISMS.

In this section the physical mechanisms which are responsible for laser damage in dielectric materials will be presented first. Breakdown mechanisms in metals and thin film coatings will be considered later.

In dielectric materials the following mechanisms are operative.

I. Electron-avalanche.

In the electron-avalanche model of laser induced damage of dielectric materials, a small number of initiating electrons drift upward in energy in the conduction band through the interaction with the laser electric field but are retarded by energy loss to phonons. Each electron undergoes a random walk of progressively increasing kinetic energy until it attains some threshold energy E_I, where E_I is the energy at which the electron generates a second conduction electron. The electron then falls to the bottom of the conduction band. If an exciton has been created, its rapid photoionization injects a second electron into the bottom of the conduction band. The process is repeated until a sufficient electron

density of around $10^{18}cm^{-3}$ has been created to damage the sample. This damage is associated with Joule heating.

The rate of energy gain from the laser field is given by the following relation[6].

$$\left(\frac{dE}{dt}\right)_E = \frac{e^2\tau_k\vec{E}^2}{m^*(1 + \omega^2\tau_k^2)} \tag{1.2}$$

where ω is the frequency of the electric field, τ_k is the electron relaxation time, m* is the effective mass of the electron, e is the electronic charge and $\vec{E}$ is the electric field in the laser beam. The rate of energy loss to the lattice phonons is given by:

$$\left(\frac{dE}{dt}\right)_L = \frac{h\omega_p}{\tau_\ell} \tag{1.3}$$

where ω_p is the average phonon frequency, τ_ℓ is the relaxation time for large and small angle scattering.

Damage occurs when the gain exceeds the loss, i.e. when

$$\left(\frac{dE}{dt}\right)_E > \left(\frac{dE}{dt}\right)_L \tag{1.4}$$

The electrons which initiate the avalanche are called the starting electrons. Most theories of electron-avalanche breakdown in solids at laser frequencies usually assume the presence of an electron density of $10^{10}cm^{-3}$

when the laser is turned on. In addition to this assumption, the temperature dependence of the lattice constant and phonon frequencies have not been considered. For these reasons the avalanche theory gives over-estimated results, for example, the calculated breakdown field for sodium chloride is 9.0MV/cm[6] at 10.6μm which is a factor of 4.3 times larger than the experimental value[7] of 2.1MV/cm.

In order to overcome this difficulty Vaidyanathan et. al[8] has suggested that breakdown may also arise from multiphoton absorption in which many photons (depending on the magnitude of the energy gap) are required to raise the electrons from the valance band to the conduction band. Vaidyanthan noted however, that neither the electron-avalanche nor the multiphoton ionization models can satisfactorily explain the experimentally observed damage threshold when considered alone. He suggested that it is more appropriate to combine the two mechanisms together. In spite of that, the combined mechanism failed to explain all the experimentally observed features of laser induced damage to dielectric materials. The combined model gave 5.0MV/cm for the breakdown field in sodium chloride at 10.6μm which is still a factor of 2.5 larger than the experimentally determined value.

Sparks has shown that the experimental data contradicts the assumed presence of initial electrons since the

calculated conductivity for an electron density of 10^8 - $10^{10}cm^{-3}$ will lie in the semiconductor range rather than the insulator range. Moreover, the conductivity for most insulators lies between 10^{-14} to 10^{-22}ohm.cm[9] and if we take the value of 10^{-14} as a lower limit and substitute in the conductivity equation taking the value of $2 \times 10^{-15}sec^{-1}$ for τ_k we get for the electron density

$$N_c = \frac{m^*\sigma}{e^2\tau_k} = 2 \times 10^4 cm^{-3} .$$

The probability of finding an electron in the focal volume will be proportional to N_cV, where V is the interaction volume. For good focussing V is about $10^{-10}cm^3$, therefore

$$N_cV \cong 2 \times 10^{-6} .$$

This negligibly small probability of finding an electron in the interaction volume indicates that there is not a sufficient electron density to initiate the electron-avalanche. In order to overcome these difficulties, Sparks et. al[10] introduced modifications to the theory of electron-avalanche, these are

1. The phonons with which the electrons interact are not restricted to those in the first Brillouin zone as in the previous theories.

2. Both acoustic and optical phonons are included in the interaction with electrons.

3. The electron-phonon scattering rate depends on the energy of the electron.

4. The starting electrons are not initially present and they must be generated by the laser pulse.

5. The lattice constant and the phonon frequencies are both temperature dependent.

With these modifications, the agreement between the experimental value of the breakdown threshold with those calculated was quite satisfactory. A comparison between the experimental values and the theoretical values are shown in Figure 1.2. The calculated breakdown thresholds are in good agreement with the experimental values for $\lambda > 1\mu m$. The new theory, however, failed for wavelengths less than $1\mu m$ unless multiphoton absorption is considered as an additional mechanism causing the breakdown. Since the electron-avalanche theory is now accepted as a fundamental mechanism for laser induced damage and with the foregoing discussion in mind, we are now in a position to explain in some detail the electron-avalanche theory. The evolution of the avalanche breakdown is composed of three stages.

A. The Liberation of the Initial Electrons.

There are several sources for the initial electrons,

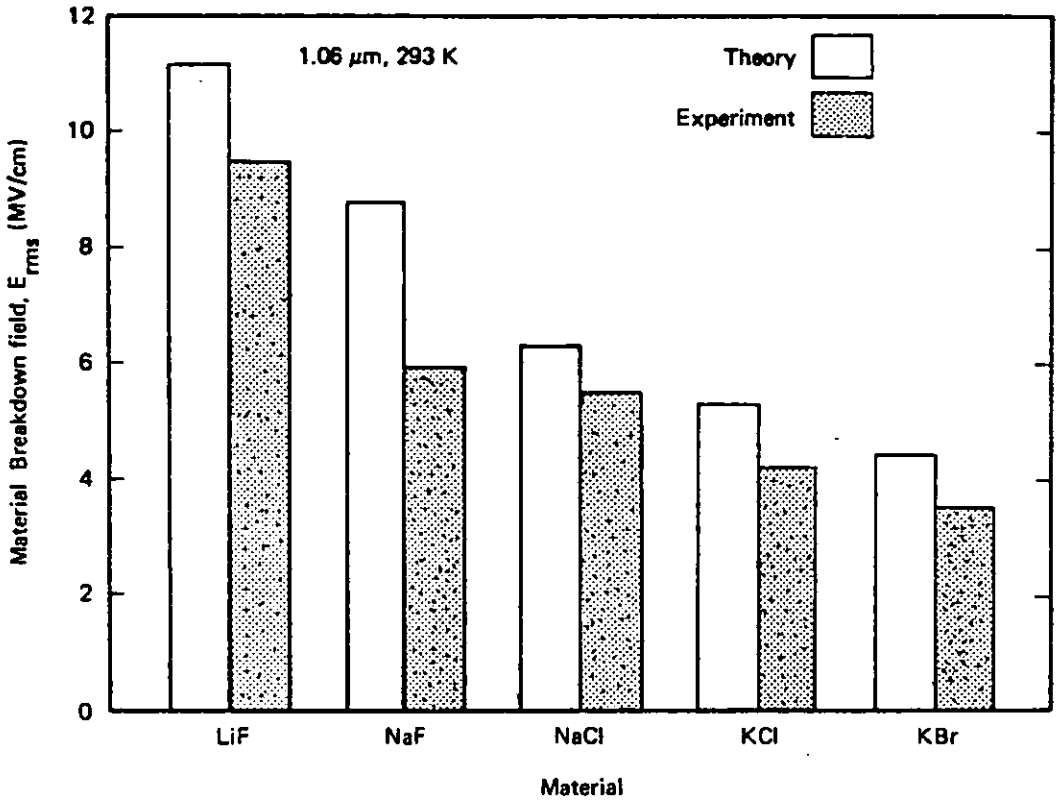

Figure 1.2: Comparison of the experimental[11] breakdown thresholds in some dielectric materials at 1.06μm compared with the theoretical values (solid line bars). (after ref.6).

one could be a shallow traps which result in chemical imperfections, oxides, colour centre etc., for example, the F-centre which is comprised of an electron localised at a cation vacancy is located within 1 - 3 eV of the conduction band of the host lattice. In sodium chloride, the F-centre lies about 2 - 4 eV below the conduction band. Hence two photons from Nd lasers (2.33 eV) can generate an electron in sodium chloride by two photon absorption. But, at 10.6μm (0.112 eV), the 2.4 eV transition would require 21 photons. It is likely that less exotic channels provide the initial electrons at 10.6μm, such as thermal emission from submicroscopic metal collids or inclusions. In general then, the supply of the initial electrons is of a varied origin and the exact quantities of the initial electrons made available will depend on several factors: the damage threshold, the pulse duration, the photon energy of the laser pulse and the energy gap of the impurity. Finally, as further evidence that the initial electrons causing the avalanche have to be generated, Yoshiyoki et. al[12] measured laser induced breakdown in KC1, KI and LiF. He applied a DC bias to the sample in order to collect the charge induced by the laser pulse. The results showed that the collected charge increased in proportion to I^n (where I is the laser intensity and n is a constant) at power levels below the breakdown threshold. In the pre-breakdown region, however, the

collected charge increased exponentially with increasing laser intensity leading to final breakdown. From these results, the mechanism of laser induced breakdown in alkali-halide crystals was concluded as follows: free electrons from shallow donar levels such as colour centres are accelerated by the laser electric field and cause electron-avalanche, which is analogous to the case of D.C. breakdown.

B. Electron Multiplication and Plasma Production.

The second stage in the breakdown process is the multiplication of the initial electrons in the strong optical light wave. Energy is supplied to the generated electrons which, at the same time, undergo inelastic collisions with the lattice at a rate of τ_k^{-1} producing more electrons and so the avalanche proceeds. The exponential growth of the electron density can be described by the following equation[7].

$$N(t) = N_o \exp\left[\eta \int_{\infty}^{\tau} (E(t`)\, dt`\right] \qquad (1.5)$$

where N_o is the number of starting electrons per unit volume, $E(t)$ is the laser pulse electric field and η is the probability per unit time for an electron to undergo an ionizing collision, this is equivalent to the probability for an electron to reach the ionization energy. Breakdown occurs when N exceeds $10^{18} cm^{-3}$.

At this density the energy deposition rate by absorption of laser light becomes so high that the temperature rise of the lattice is significant and consequently a plasma is formed. Experimental evidence showed that the plasma build-up time is indeed very short. For example, Anthens and Bass[13] used a streak camera with 6-psec resolution to observe plasma build-up in the breakdown of silica by 25psec, 5.32nm laser pulses, they measured a build-up time of < 10psec (this time may even be limited by the resolution of the camera itself).

C. Transfer of Heat from the Plasma to the Lattice.

The final stage of the breakdown process follows the production of the plasma. The plasma absorbs energy from the laser pulse and the rate of absorption W(t) at time t is given by the following expression[6]:

$$W(t) = \frac{e^2 \tau_k}{m^*} \frac{|E(t)|^2 N(t)}{1 + \omega^2 \tau_k^2} \quad . \tag{1.6}$$

The temperature of the lattice can then be calculated by simply integrating equation (1.6) to give

$$T(r, z, t) = \frac{1}{C} \int_{-\infty}^{\tau} W(r, z, t)\, dt \tag{1.7}$$

where C is the heat capacity of the dielectric. In this stage the major heating of the lattice will begin,

the plasma channels energy from the laser to the lattice. It is evident that the thermal properties of the sample are important in this stage. Associated effects such as thermally induced stress and crack production may be important in some other materials as well, such as thin film coatings.

II. Superposition of stress waves[14].

This mechanism for damage in transparent solids essentially involves cumulative compression of the elastic field with a large growth of the stress amplitude. The mechanism assumes that there is a small absorption even in transparent materials and when a very large amount of energy is transmitted through the material some will be absorbed. Even though the absorbed energy is very small compared to the total energy transmitted, it is absorbed in a short time compared to the elastic relaxation time of the material. The absorbed energy and consequently thermal expansion raises the pressure in the absorbing region. As the pressure relaxes, rarefraction waves move through the material and under some conditions may be superimposed to give very large stress even though the original ampitude was very small. The solution of the wave equation for an assumed cylindrical region of absorption indicated that a rarefraction wave of increasing amplitude would move inward from the boundary of the cylinder. Bullough

and Gilman[14] estimated that for a 1GW.cm^{-2} laser pulse the pressure could reach 10 newtons.cm^{-2} for an absorption coefficient of only 1cm^{-1}.

III. Absorption of defects.

Some workers[15] have explained their results in terms of defects in the host material as a primary source of laser induced damage. The principle assumption in this mechanism is that the presence of defects will lead to an increased absorption of the incident light, accompanied perhaps by a hypersonic pulse, so that pressure and thermal stresses result in expansion of the material around the defect and possibly heating to the point of thermal destruction.

IV. Interband absorption.

Another possible damage mechanism is the interband optical absorption which would have the same effect of producing electrons in the conduction band with subsequent electron-avalanche and breakdown. This mechanism is not readily distinguished from that of multiphoton absorption but, the effect is quantitatively the same.

1.4 SURFACE DAMAGE.

It is a generally observed phenomena that the damage threshold at the surface of transparent material is lower than that of bulk material. It was widely

believed that the mechanism of damage at the surface of transparent material would be a distinctly different process from that in the bulk[7]. However, recent evidence[7] suggests that the damage mechanism at the surface is the same one causing damage in the bulk. In the majority of cases the apparently lower surface damage thresholds were due to the chemical contamination of the surface[7]. Surfaces can be cleaned by, for example, argon ion bombardment and the damage threshold can be raised significantly, approaching the damage threshold of that of the bulk[17]. The lower damage threshold is also due to the presence of surface imperfections resulting from the polishing process in the form of grooves, cracks or pores[18]. Typical dimensions of these imperfections are smaller than a wavelength, since the surfaces of the component have been prepared and selected for optical quality. For such small dimensions the electric field configuration in the neighbourhood of these physical imperfections shown in Figure 1.3 can be calculated by means of electrostatics. Bloembergen[18] has indicated that the interaction of the incident laser electric field with the imperfect surface results in the enhancement of the electric field at these defect sites, the magnitude of the enhancement is given by the following equation:

$$E_{enh} = \frac{1}{1 + \frac{1 - n^2}{n^2} L} E_o \qquad (1.8)$$

where L is the depolarisation factor which depends on the geometrical shape of the defect. Thus for a sphere $L = \frac{1}{3}$, for crack $L = 1 - \frac{\pi}{2}.\frac{c}{a}$ (where c is the width of the crack and a is its depth) and for a cylinder $L = \frac{1}{2}$. The electric field enhancement therefore would be

$$E_{enh} = \frac{3n^2}{2n^2 + 1} E_o \quad \text{for sphere}$$

$$E_{enh} = \frac{2n^2}{n^2 + 1} E_o \quad \text{for cylinder}$$

$$E_{enh} = n^2 E_o \quad \text{for a crack}$$

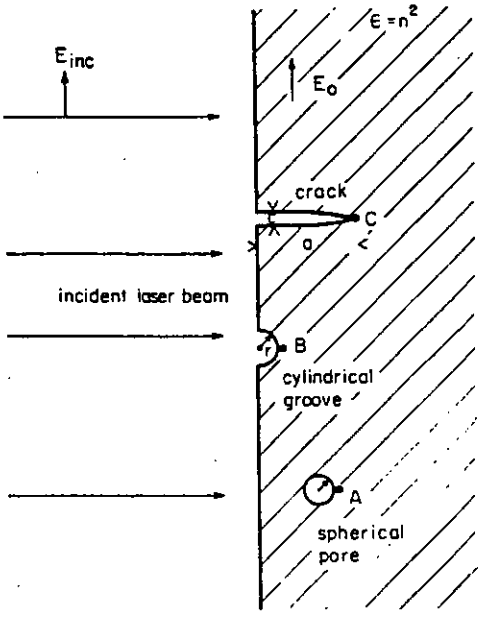

Figure 1.3: Representative geometries for electric field enhancement near pores, scratches or cracks. Typical dimensions are r = 0.1μm, c = 0.1μm and a = 1μm (after ref.18).

The magnitude of enhancement at the sites A, B, C in Figure 1.3 for a CO_2 laser wavelength substrate materials are listed in Table 1.1.

TABLE 1.1 : Electric field enhancement factors for CO_2 laser substrates.

Material	Refractive Index	Sphere	Cylinder	Crack
NaC1	1.50	1.23	1.38	2.25
Ge	4.00	1.45	1.88	16.00
CdTe	2.69	1.40	1.76	7.76
ZnSe	2.40	1.38	1.70	5.76
KC1	2.45	1.38	1.71	6.0025

It is obvious that a crack will cause the greatest enhancement especially for a large index material. Since it is the interaction of the electric field which causes the damage to the surface via absorption and the subsequent avalanche, the defect sites are susceptible to early damage. In terms of the incident laser intensity the damage threshold is reduced by the square of the enhancement factor and thus for a crack in germanium for example, the damage threshold could be reduced by a factor of 256.

As mentioned earlier the damage threshold at the surface could be increased and made equal to the bulk damage threshold by extremely fine polishing and one would not need to eliminate cracks and scratches with dimensions less than 10^{-6}m. However even with this small dimension there would still be enhancement in the electric field, but the region of enhancement is so limited that the avalanche cannot fully develop, if the diffusion time of the carriers out of the edge region is shorter than the duration of the laser pulse the damage threshold will be increased, compensating for the decrease in damage threshold due to field concentration.

The implications for coated surfaces are serious. From microscopic examination it is known that most coatings faithfully replicate the contour of the substrate, so the coating will experience an enhanced electric field also. Either the coating itself will damage at a lower intensity or the substrate will be damaged. Experimentally[19] the damage threshold of three AR-coated germanium deposited in the same run showed that the sample with visible polishing scratches failed at 70% of the damage threshold of the other two which did not have any visible scratches.

Another peculiar aspect of laser induced to transparent materials is that when a transparent dielectric material is exposed to a collimated beam of

laser light, the exit surface will damage at a threshold level less than the front surface. Crisp et. al[20] and co-workers have showed that this is due to the effect of Fresnal reflection. At normal incidence to the dielectric surface, part of the incident laser beam is reflected and part is transmitted. At the front surface the reflected wave is 180° out of phase with the incident wave and the transmitted laser intensity is related to the incident intensity by:

$$I_{ent} = \frac{4}{(n + 1)^2} I_o \qquad (1.9)$$

where n is the refractive index of the dielectric material. At the exit surface, the reflected wave suffers no phase shift and so the intensity at the exit surface is related to the intensity of the incident wave at the entrance surface by:

$$I_{exit} = \left(\frac{4n}{(n + 1)^2}\right)^2 I_o \quad . \qquad (1.10)$$

Thus the ratio of intensity inside the dielectric medium at the exit surface to the intensity inside the medium at the entrance surface is:

$$\frac{I_{exit}}{I_{ent}} = \frac{4n^2}{(n + 1)^2} \qquad (1.11)$$

Experiments[21] carried out on ED-2 laser glass ($n = 1.55$) yielded an average ratio of about 1.5. Furthermore, experiments carried out with an intense laser beam incident at Brewsters' angle where no reflection is expected to occur, the damage level for both the entrance and the exit surfaces was the same.

1.5 THEORY OF LASER INDUCED DAMAGE IN METALS.

When an intense beam of laser light interacts with a metal surface at normal incident, a fraction of the incoming beam is absorbed, this fraction is given by[22]:

$$\alpha = 1 - R \tag{1.12}$$

where α is the absorption coefficient and R is the reflectivity of the metal. The absorption coefficient can be calculated from the measurement of the optical constants or the complex refractive index, $\hat{n}$;

$$\hat{n} = n - ik \; ; \qquad i = \sqrt{-1} \; . \tag{1.13}$$

The reflectivity at normal incidence is therefore given by:

$$R = \frac{(n - 1)^2 + k^2}{(n + 1)^2 + k^2} \tag{1.14}$$

and the absorption coefficient is given by:

$$\alpha = \frac{4n}{(n + 1)^2 + k^2} . \qquad (1.15)$$

In general n and k for metallic surfaces are functions of wavelength and temperature. For $0.4 < \lambda < 1$ μm; n and k are relatively slowly varying functions of λ. At longer wavelengths, n and k both increase rapidly with λ and α decreases. Thus the absorption of laser light by metal surfaces at normal temperature is almost an order of magnitude larger at visible wavelengths than at infra-red wavelengths. In practice this assumption cannot be relied on because of the formation of oxides or the presence of surface contamination. When this is the case the value of absorption coefficient in the infra-red can be increased substantially by cleaning and polishing.

With this brief introduction in mind we can now proceed for further discussion of laser induced damage to metals.

Generally, understanding the interaction of laser radiation with metals is very difficult because of the variety of damage mechanisms and the involvement of many parameters in the interaction region. A simple flow chart shown in Figure 1.4 indicates the power balance at any instance in time during the interaction of intense laser light with metals. The absorbed energy will be converted to heat, thus, the temperature of the

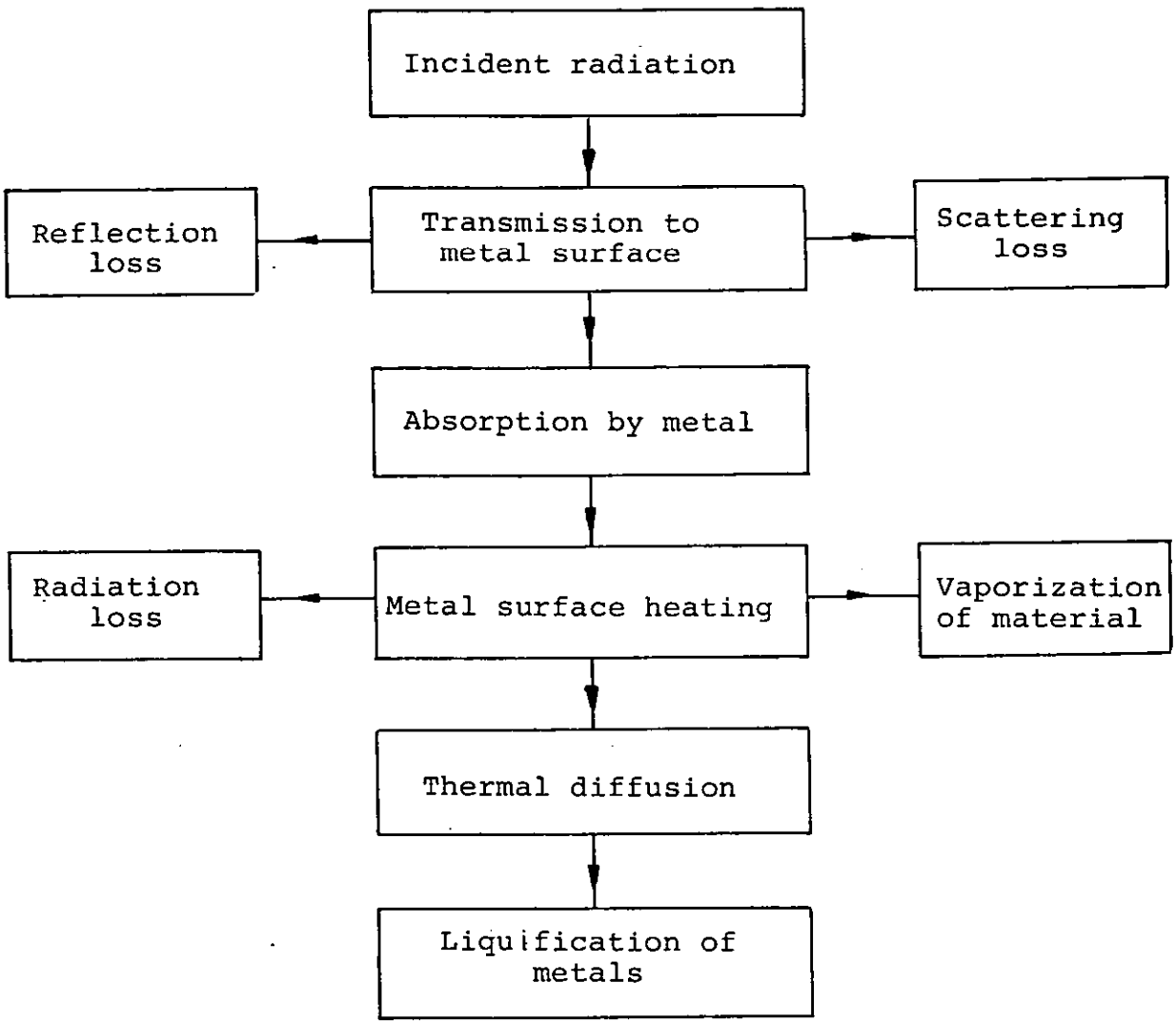

Figure 1.4: Power balance at any time during the interaction of intense laser light with a metal surface.

interaction spot will be raised substantially. The energy absorbed by the metal is equivalent to a flow of heat into the metal surface. The response of the metal to this heat flux can be calculated by solving the three-dimensional heat transfer equation[23]:

$$\rho C \frac{\partial T}{\partial t} = \frac{\partial}{\partial x}\left[\frac{K\partial T}{\partial x}\right] + \frac{\partial}{\partial y}\left[\frac{K\partial T}{\partial y}\right] + \frac{\partial}{\partial z}\left[\frac{K\partial T}{\partial z}\right] + A(x,y,z,t) \qquad (1.16)$$

where K is the thermal conductivity, ρ is the density, C is the specific heat and A is the heat flux. Most solutions to the heat transfer equation have ignored the temperature dependence of the thermal parameters presumably because inclusion of the temperature dependence makes the equation non-linear and therefore solutions would be very difficult to obtain, although numerical solutions are possible in a limited number of cases when the temperature dependence of K, ρ and C are known. Ignoring the temperature dependence of the thermal parameters especially the absorption coefficient has resulted in large errors in the theoretical value of the damage threshold in metals. In addition, most theories have neglected the contribution to the absorption coefficient from the interband transitions. Sparks et. al[24] pointed out that for a pure metal the absorptance increases by a factor of

5 - 6 typically as the temperature is increased from room temperature to the melting point. Sparks calculated the increase in the absorptance using Drude theory and the experimental value of the DC electrical conductivity as follows:-

The electron relaxation frequency is given by:

$$\tau_k = \frac{n^2 e^2 \rho_o}{m} \qquad (1.17)$$

where m and e are the electron mass and charge respectively, n is the electron density and ρ_o is the resistivity, the Drude expression for the absorption for frequencies in the range $\tau_k \lesssim \omega \lesssim \omega_p$ (where ω_p is the plasma frequency of the metal) is given by:

$$A \approx \frac{2\tau_k}{\omega_p} \quad . \qquad (1.18)$$

Since τ_k is strongly dependent on temperature[10] in the positive direction, therefore, the absorptance of metal increases in the same ratio as the temperature rise from room temperature to melting point. Sparks has obtained the exact solution for the heat-flow equation assuming the following temperature dependence for the absorptance.

$$\alpha = \alpha_o + \alpha_1 T_s \qquad (1.19)$$

where T_s is the surface temperature, α_o is the room temperature absorptance and α_1 is the contribution to

the absorptance due to the temperature increase. Sparks calculated the laser intensity in a pulse of duration τ required to raise the surface temperature of a metal to the melting point T_m to be of the following form:

$$(I\tau) = \frac{u}{\alpha_o \alpha_1} \sqrt{\tau KC} \qquad (1.20)$$

where u is a solution of the transcendental equation

$$e^{u^2} \left[i + \mathrm{erf}(u) \right] = \frac{T_m + 1/\alpha_1}{T_o + 1/\alpha_1} \quad . \qquad (1.21)$$

If we compare equation (1.21) with the clasical equation in which the absorption is independent of the temperature, i.e.

$$(I\tau) = \frac{T_m - T_o}{2\alpha_o} \sqrt{\pi KC\tau} \qquad (1.22)$$

we see that the dependence of the $(I\tau)$ melt threshold on the material parameters K, C and τ is identical except for the multiplication factor. The major difference is, $\frac{u}{\alpha_1 \alpha_o}$, this factor represents the temperature average from T_o to T_m of the quantity $T_m - T_o/2\alpha_o$ in equation (1.22). Using equation (1.21) Sparks found agreement between +16% and -17% for copper and between +14% and -12% for aluminium for 100ns long pulse at 10.6μm.

1.6 DAMAGE TO THIN FILM COATINGS.

Today, thin films are extensively used in optical devices from the extreme UV to the far IR. They play an important role in a variety of applications, for example, highly reflective mirrors, protective layers for front surface mirrors to increase their durability and effeciency single and multilayer coating, both antireflecting and high reflecting for optical components in laser systems especially those employed in the inertial confinement fusion experiments, besides many other applications. Laser induced damage in thin film coatings is a very complicated process, this is due to the fact that many parameters are involved, furthermore optical thin films are often the most damage sensitive components of high power laser systems since the absorption coefficient of most films range from 10 to 100 cm^{-1} while for the same material in the bulk form the absorption is several orders of magnitude smaller. The high absorptivity of thin films is generally attributed to impurities which are included during the deposition process or infiltrated during exposure to the environment. Experimental work[25] has indicated that the laser induced damage in thin films can be more than an order of magnitude lower than that for the same material in the bulk form.

There is a wealth of literature dealing with laser induced damage in thin films from a variety of stand points. This information had led to improved coating

and an empirical understanding of the damage mechanism in thin films.

Three mechanisms are generally used to describe damage in thin films, these are: electron-avalanche, multiphoton ionization and impurity induced damage. Unfortunately, each of these mechanisms is subject to uncertainties which make accurate calculations of absolute damage thresholds impractical. Both avalanche and multiphoton ionization calculations require complicated parameters such as material band structure and electron effective mass which are often not available for many dielectric films. On the other hand, the impurity model requires a detailed knowledge of type, size and distribution of impurities in the host material. These are essentially unknown at the present time. However the impurity model is considered to be the most accepted theory to explain many of the observations associated with laser induced damage to thin films. The model most frequently used for impurity damage is that of spherical absorbing particles embedded in the host material. The impurity absorbs the incident radiation and its temperature rises, which ultimately produces melting, vaporization or stress fracture of the film material around the impurity. If the impurities are metallic, then, an approximate solution can be obtained for the thermal equation. The solution had been obtained by Hopper et. al[26] and the temperature in the host film material is given by the following equation.

$$T = \frac{3QI}{2\pi C_p D_h mr}\left\{\frac{1}{q-m}\,\mathrm{erfc}\,\frac{r-a}{2\sqrt{D_h\tau}} - \frac{1}{q+m}\,\mathrm{erfc}\,\frac{r-a}{2\sqrt{D_h\tau}}\right.$$

$$- \frac{1}{q-m}\exp\left(\frac{(q-m)(r-a)}{2a} + \frac{(q-m)^2 D_h\tau}{4a^2}\right)$$

$$\cdot\ \mathrm{erfc}\left(\frac{r-a}{2\sqrt{D_h\tau}} + \frac{(q-m)\sqrt{D_h\tau}p}{2a}\right) + \frac{1}{q+m}$$

$$\cdot\ \exp\left(\frac{(q+m)(r-a)}{2a} + \frac{(q+m)^2 D_h\tau}{4a^2}\right)$$

$$\left.\cdot\ \mathrm{erfc}\left(\frac{r-a}{2\sqrt{D_h\tau}} + \frac{(q+m)\sqrt{D_h\tau}}{2a}\right)\right\} \qquad (1.23)$$

where C_p is the specific heat of the impurity of radius a, K_h is the thermal conductivity of the host material, D_h is the diffusivity of the host material, Q is the absorption cross section, I is the laser intensity, C_h is the specific of the host material, τ is the laser pulse duration, $q = \frac{3C_h}{C_p}$, $m = q((q-4))^{\frac{1}{2}}$ and r is the radial distance from the impurity boundary. Equation (1.23) which is known as the Hopper equation, has been used to describe laser damage in films containing metallic impurities.

Recent research[27] has shown the impurities in fluoride thin films can also be oxides. For example,

thorium fluoride (ThF_4) contains ThO_2 or $ThOF_2$. Oxides and other dielectric materials typically have a very small coefficient of thermal diffusivity in which case the use of the Hopper equation is not valid. The exact solution to the thermal equation has been obtained by Goldenberg and Trantor[28], their result for the temperature in the host film material is given by:

$$T = \frac{3QI}{4\pi K_p a}\left\{\frac{1}{3}\frac{K_p}{K_h} + \frac{1}{6}\left(1 - \frac{r^2}{a^2}\right) - \frac{2ab}{r}\int_o^\infty \exp\left(\frac{-y^2\tau}{\gamma}\right)\frac{(\sin y - y\cos y)(\sin ry/a)}{y^2\left[(c\sin y - y\cos y)^2 + b^2y^2\sin^2 y\right]}dy\right\} . \quad (1.24)$$

In this equation $\gamma = \frac{a^2}{D_p}$, $c = 1 - \frac{K_h}{K_p}$,

$$b = \frac{K_h}{K_p}\sqrt{\frac{D_h}{D_p}} .$$

It is interesting to compare the exact solution of Goldenberg with the approximate solution of Hopper, to do this, the temperature of the impurity-host boundary is set at some temperature and then the required energy density is plotted as a function of the impurity radius, Figure 1.5 shows the results for metallic impurity while Figure 1.6 shows them for dielectric impurity. As expected the agreement is good for a metallic impurity but the Hopper solution fails for dielectric impurities. It is obvious from

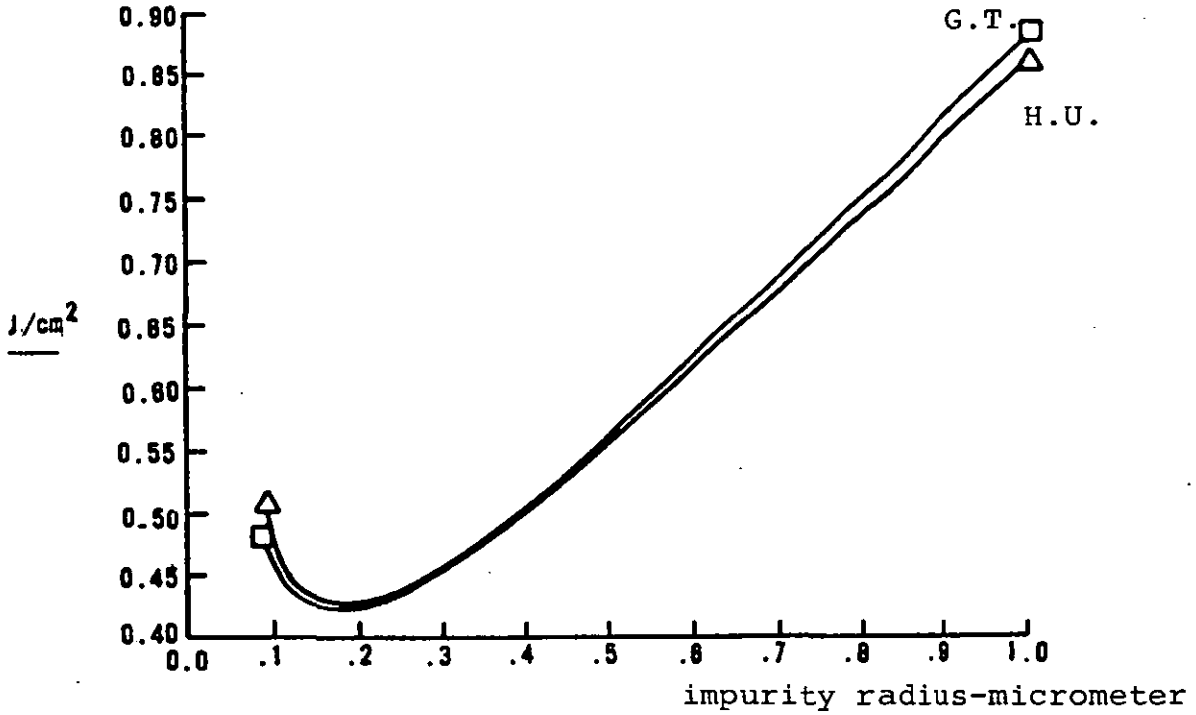

Figure 1.5: Comparison of Goldenberg and Trantor's (G.T.) solution of the thermal equations for metallic spheres in dielectric medium to the soluiton of Hopper and Ulhmann (H.U.) (after ref.16).

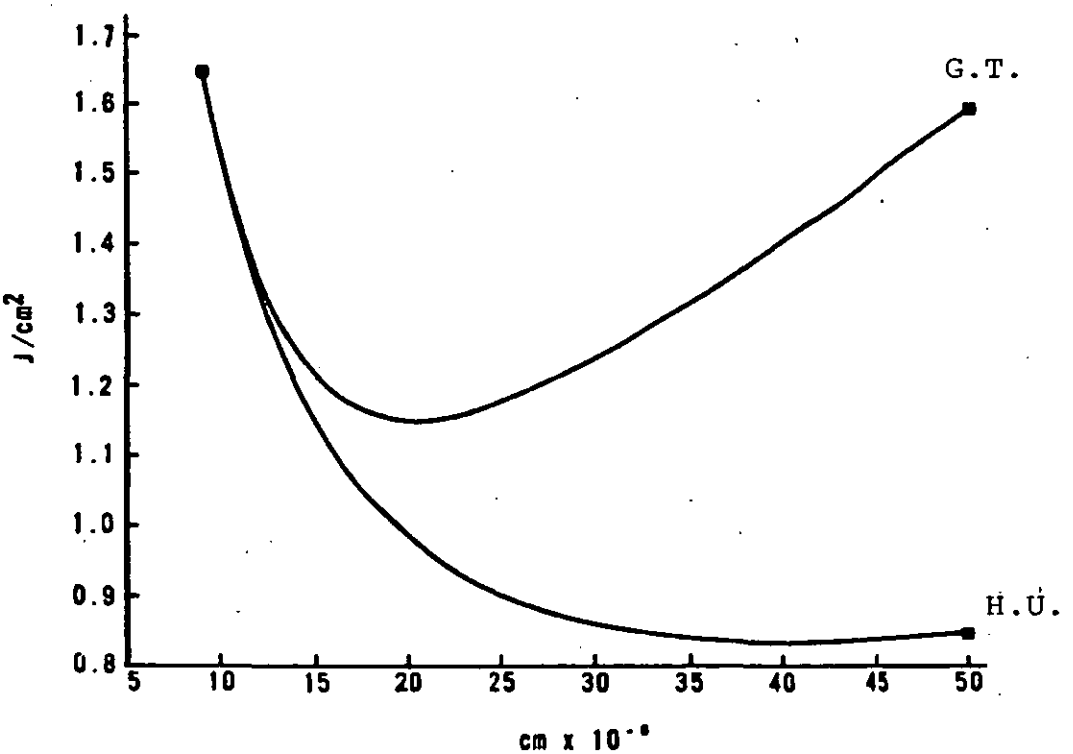

Figure 1.6: Comparison of Goldenberg and Trantor's (G.T.) solution of the thermal equation for dielectric impurities in dielectric medium to the solution of Hopper and Ulhmann (H.U.) (after ref.16).

the figures that the damage threshold is quite sensitive to the size of the impurity; a small change in the radius of the impurity can have an appreciable influence on the damage threshold. If, on the other hand, the film contains a continuous distribution of particle sizes (which is most probable) with the maximum diameter equal to the film thickness then the damage threshold is determined by the size of the impurity which has the lowest damage threshold. It should be noted that equation (1.24) was derived assuming that the absorption cross section is constant, this is only valid if the size of the impurity is much greater than the wavelength of the incident radiation. However, in the case of thin films the impurity size is limited by the thickness of the film, therefore, the impurities sizes are of the same order of the wavelength of light or smaller. For these sized impurities the absorption cross section can be derived from Mie scattering theory[29]. In this case the absorption cross section which depends on the complex index of refraction $\hat{n}$, the radius of the impurity and the size parameter q which is given by:

$$q = \frac{2\pi a}{\lambda_h} \tag{1.25}$$

where $\lambda_h = \frac{\lambda_o}{n_h}$ is the wavelength of radiation in the host, n_h is the real part of index of refraction of the host material and λ_o is the wavelength of radiation in

free space. It is clear that the optical properties of the host influence the absorption of radiation through the wavelength dependence, this influence will be seen by the imputity through the size parameter.

An exact solution to the integral in equation (1.24) does not exit. However, when $\frac{D_p \tau}{a^2} > 1$, the integral is dominated by the exponential quantity[30] and to a good approximation the remainder of the integral can be replaced by a power series in y^2; defining $I\tau$ as the damage threshold then equation (1.24) can be reduced to the following form:

$$I = 16 T_m \sqrt{\frac{\rho_h C_h K_h \tau}{\pi}} \qquad (1.26)$$

where T_m is the melting point of the film. The scaling in equation (1.26) agrees remarkably well with the experimental data[30,31]. Furthermore, equation (1.26) is interesting because it not only verifies the $(\tau)^{\frac{1}{2}}$ dependence previously suggested[31] but also predicts that the damage threshold scales linearly with the temperature and with the square root of the product of specific heat and thermal conductivity of the host material. A comparison of equation (1.26) with the numerical integration of equation (1.24) is shown in Figure 1.7.

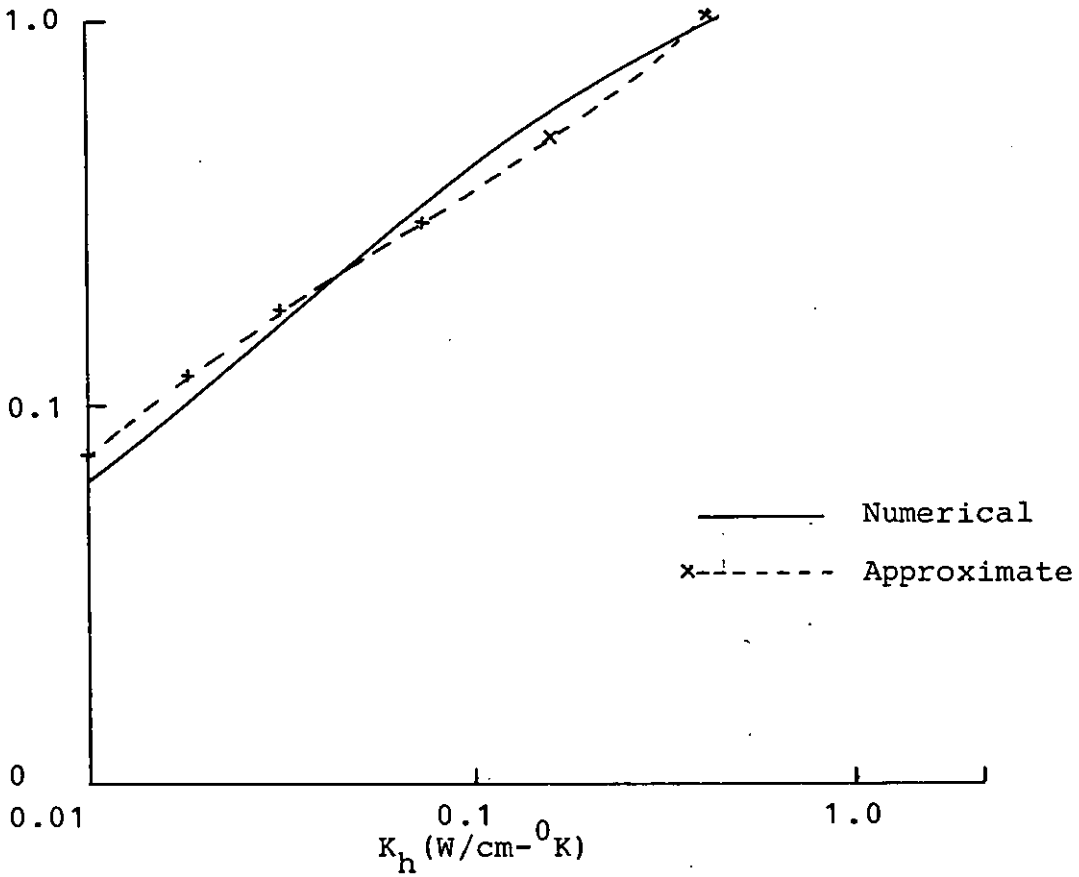

Figure 1.7: Damage Threshold as a Function of Host Conductivity: THO_2 - Impurity (after ref.30).

In conclusion the following points can be drawn from the impurity model.

1. The size of the impurity and its optical properties govern the absorption of radiation whereas the thermal properties of the host are most important in establishing the damage threshold.

2. The damage threshold is proportional to the square root of the product of the thermal conductivity and the laser pulse length.

3. The damage threshold increases with thinner films because of the exclusion of larger, easier to damage impurities.

4. The damage threshold decreases with decreasing wavelength, this behaviour is expected since Mie absorption increases as the wavelength is reduced.

5. The damage threshold is relatively insensitive to the thermal properties of the impurity but, varies with the thermal properties of the host material.

6. Other damage mechanisms like electron-avalanche and multiphoton cannot explain some aspects of the damage in thin films, for example, the increase in the damage threshold for thinner films.

7. The damage threshold of thick film decreases more slowly with decreasing wavelength than in thinner films, this is because at long wavelengths the larger, easy to damage impurities are excluded in thinner films (the largest allowable impurity size consistent with the physical geometry governed by the smallest dimension of the film, i.e. the thickness) giving a much higher damage threshold. At shorter wavelengths the smallest impurities present are damaged.

However, the impurity model has some failings which can be summarised as follows:

1. The impurity model assumes that the impurities are embedded in the host material to the extent that they never see the boundaries of the film. Obviously, this cannot be true if the sizes of the impurities are comparable to the film thickness.

2. The model assumes the impurities are perfect spheres. In fact, the impurities could be of various shapes and randomly orientated. In this case, the incident radiation would see a distribution of particle shapes. On the other hand, when the impurities are columnar structures, they are no longer randomly orientated, in which case the absorption may be sensitive to the angle of incidence of the laser pulse.

1.7 LASER INDUCED DAMAGE DEPENDENCE ON LASER AND MATERIAL PARAMETERS.

One of the most interesting and certainly one of the most frustrating aspects of measuring laser damage thresholds is that the result of such measurements are dependent on enormous range of parameters. Variables are introduced throughout the life cycle of an optical element; during fabrication such as impurities, polishing, cleaning during testing wavelength, pulse duration, spot size, statistical variation and in-between storage, handling and cleaning.

In the following sections some of the most important parameters on which laser damage depends will be explained, this explanation will apply to all optical components unless otherwise specified.

1. Pulse Duration.

I - Dielectric materials: Applying the theory of electron-avalanche which assumes that the initial electrons present are in order of $10^{10}cm^{-3}$ Fradin[33] found that the breakdown threshold in dielectric materials scales inversely with the pulse duration. Thus by taking the logarithm of equation (1.5) we get:

$$\ell n \frac{N}{N_o} \cong \int \eta(E)\,dt \simeq 18 \cong \eta\tau$$

$$\therefore \eta \sim 18\tau^{-1} \qquad (1.27)$$

In support of this relation Al-yassini and Park[39] have verified experimentally that for 10 ns pulse an electron density of 10^{18} to $10^{19}cm^{-3}$ is produced in BSC-2 glass. Figure 1.8 shows the breakdown threshold in NaC1 by laser pulses of durations between 15 ps and 10 ns.

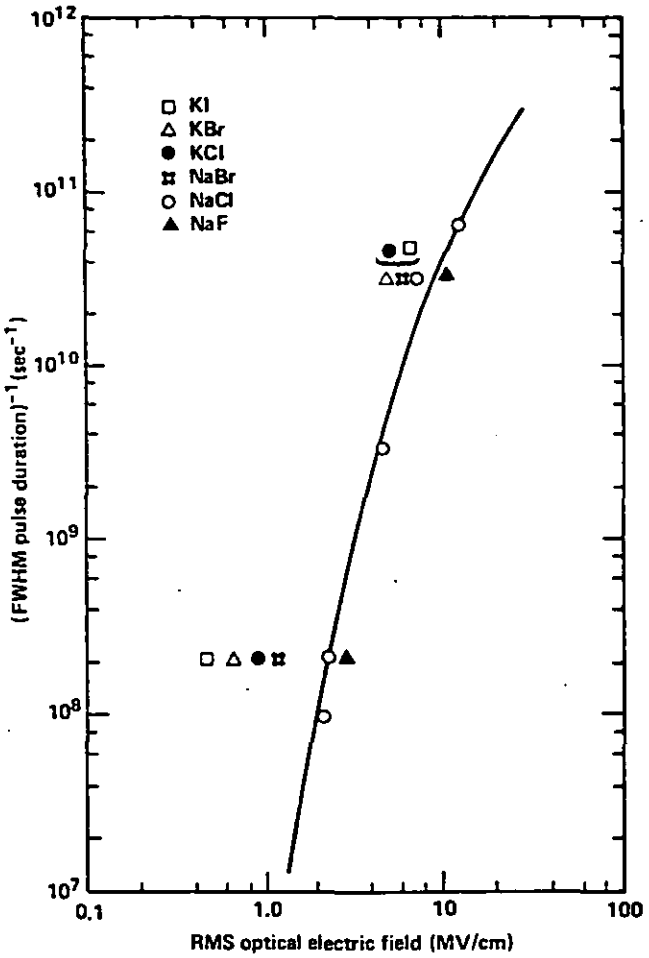

Figure 1.8: Experimental relationship between the breakdown threshold electric field strength and the laser pulse duration for alkali-halides (after ref.35).

Many workers have attempted to derive general relations for the pulse duration dependence of the breakdown threshold in dielectric materials. The work of Bettis[36], for example, predicts that the breakdown threshold will scale with $\tau^{-\frac{1}{2}}$, this scaling agrees with the notion of diffusion propagation in the breakdown

event. Radial growth of diffusion phenomena has a functional form of $(D\tau)^{\frac{1}{2}}$, where D is the diffusion coefficient. Nesterov et. al[37] showed the same relationship, i.e. $\tau^{-\frac{1}{2}}$ apply for pulses between 15ns and 1.8μs for damage on the surface of sapphire. However, Sparks et. al[10] has predicted that the breakdown threshold is weakly dependent on the pulse duration and the threshold scales with $\tau^{-1/6}$ rather than $\tau^{-\frac{1}{2}}$.

II. Thin film coatings: The pulse duration dependence for thin film coatings according to the different theories can be summarised in Table 1.2.

TABLE 1.2 : Pulse length dependence in thin film coatings.

Model	Pulse Length Dependence	Ref
Avalanche	$\frac{\tau}{\ell n \tau}$	38, 39
Multiphoton	$\tau^{0.88}$ at = 1.06μm	40
	$\tau^{0.5}$ at 0.26μm	40
Impurity	$\tau^{0.5}$	30

It can be seen that the avalanche ionization predicts an almost linear laser-pulse length dependence. In the case of multiphoton ionization, a strong pulse-length

dependence is predicted at longer wavelengths. Lastly, the predicted pulse length dependence from the impurity model fits closely to a $\tau^{\frac{1}{2}}$ curve.

III - Metals: The $\tau^{\frac{1}{2}}$ scaling predicted by elementary heat flow considerations, neglecting the temperature dependence of the optical components, is well known[41]. It has demonstrated theoretically[24] that the $\tau^{\frac{1}{2}}$ law also applies when the temperature variation of the absorption coefficient is taken into account.

2. Spot-size.

The first reported observations of the spot-size effects, the apparent increase in the surface damage threshold with decreasing spot-size, was reported nearly twelve years ago by DeShazer[42] and his co-workers. They studied the damage threshold of a coated surface of glass as a function of the irradiated spot-size. They found a general decrease in the damage threshold as the spot-size is increased, up to 150μm. Above 150μm diameter the damage threshold remained constant as the spot-size was further enlarged. They explained this spot-size dependence as an increasing probability of encountering a defect as the spot-size is increased. They assumed that the distribution of defects can be described by a Poisson function and the diameter at which the damage level remains constant was correlated

with the determination of the average defect separation from micrographic observation. They further noticed that the mean separation between defects decrease as the deposition rate of the film increased. Figure 1.9 shows the spot-size dependence in ZrO_2 films as a typical example.

Bettis et. al[36] also presented a model for the

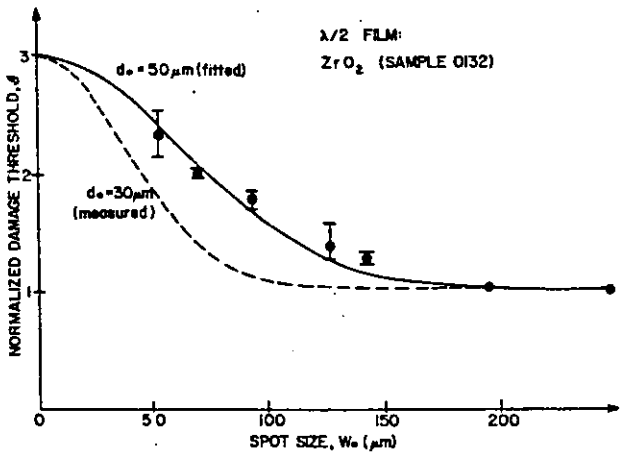

Figure 1.9: Spot-size dependence for a single half-wave thick film ZrO_2 on glass (after ref.42).

spot-size dependence, the model was later extended to bulk damage. The starting point of the model is the assumption that the surface damage threshold corresponds to the investment of a critical amount of energy in a plasma layer at the surface of the material.

Using the expression for the classical inverse bremsstrahlung absorption, they argue that the plasma absorption increases linearly with increasing laser power density, so the heating rate goes like p_o^2, where p_o is the incident power density. Thus, they arrived at a scaling law that the threshold electric field is proportional to the inverse square root of the spot-size, or the damage threshold in (J/cm^2) scales as (spot-size^{-1}). Furthermore they provided considerable evidence from the literature that for a given material the quantity (τAI^2), where A is the interaction area, and I the laser fluence is constant for a given material.

The spot-size dependence was further investigated by Tang et. al[43]. He re-examined the bulk breakdown threshold of alkali-halides using a CO_2 laser emitting 92ns bursts of mode-lacked pulses of 2.5ns long separated by 8ns. The damage threshold was recorded for both single bursts and N - on - 1 interactions, they found the same scaling law applies. Soileau et. al[44] suggested that the bulk damage threshold should be a function of the spot-size because the probability of having a starting electron present decreases as the interaction volume is decreased. Foltyn[45] presented an interesting approach to the spot-size problem based on the statistics of laser induced damage. He predicts that single pulse damage thresholds can often be interpreted to make the resultant damage threshold independent of the spot-size.

He suggested that if the damage threshold is defined to be the highest-energy density at which the sample could not be damaged then, the damage threshold is independent of the spot-size, but, if the damage threshold is defined as the average of the highest energy density which causes damage and the lowest energy density which does not cause damage, then the damage threshold is a function of the spot-size. It was assumed, however, that damage is a defect related and data for optical coatings showed that many assumptions Foltyn made are justified. Foltyn's expression for the damage probability is given by:

$$P = 1 - \left(\frac{I_{th}}{I_o}\right)^{\frac{\pi \omega_o^2 \gamma_o}{2}} \qquad (1.28)$$

where I_o is the peak fluence at the beam centre, I_{th} is the defect damage fluence, ω_o is the beam radius at $1/e^2$ amplitude and γ_o is the defect density. Figure 1.10 shows the results of testing identical reflectors at three different spot-sizes.

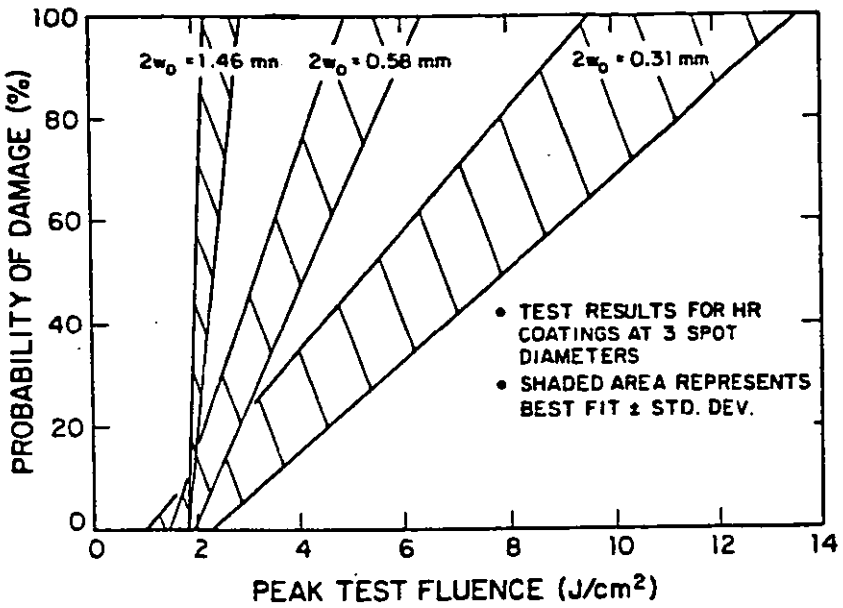

Figure 1.10: Results of testing identical reflectors at three different spot-sizes (after ref.45).

Since damage threshold in this model is defined as the maximum energy at which no damage occurs for all irradiated sites, i.e., the zero percent crossing of the damage probability curve, therefore changing the spot-size will not change the damage threshold. Only the slope of the damage probability vs laser fluence is affected as shown in Figure 1.10.

To conclude this section it should be noted that, numerous and often conflicting reports of the spot-size effects have been reported and on several occasions scaling laws have been proposed. A careful assessment of the spot-size effect must be undertaken keeping other parameters constant in order to understand this effect in more detail.

3. Frequency dependence of laser induced damage in transparent materials.

The relationship between breakdown threshold at a frequency ω and the corresponding DC breakdown threshold according to the theory of electron-avalanche is given by[7]:

$$E_\omega = E_{DC}\left(1 + \omega^2\tau_k^2\right)^{\frac{1}{2}} \qquad (1.29)$$

The experimental[46] breakdown thresholds for sodium chloride at 10.6, 1.06 and 0.694μm with a nanosecond pulse duration are 1.92 ± 0.2, 2.3 ± 0.5 and 2.2 ± 0.4MV/cm respectively. Essentially there is no increase in the breakdown threshold between 10.6μm and 0.694μm in alkali-halides. Thus, up to the electromagnetic angular frequency of $\sim 3 \times 10^{15}$Hz. The behaviour of the breakdown threshold is observed to be quite similar to the behaviour for DC fields. The reasons for this behaviour over such a remarkable frequency range are:-

1. The electron collision time τ_k in dielectric material must be very fast $< 10^{-15}$ sec.

2. In experiments up to 0.694μm, the photon energy is not a sizable fraction of the material bandgap. Eg. Figure 1.11 illustrates the frequency dependence of the breakdown threshold E_ω as predicted by the theory of electron-avalanche.

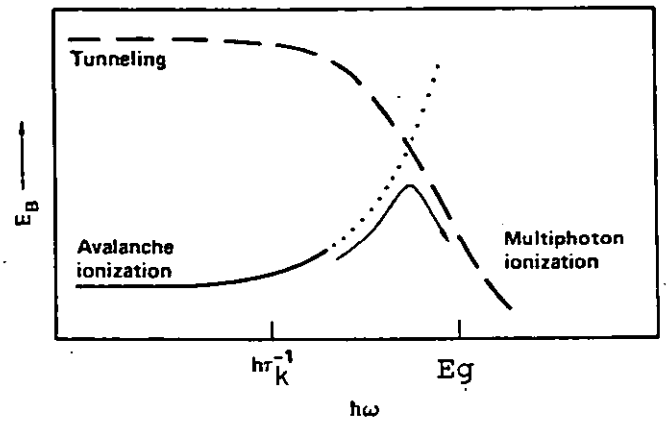

Figure 1.11: Frequency dependence of thresholds for breakdown by electron-avalanche and multiphoton ionization (after ref.7).

The dashed curve outlines the frequency dependence of the tunnelling mechanism[47] which has a threshold value of 3×10^7V/cm in alkali-halides at the low frequency limit. As the photon energy approaches that of the material bandgap, this tunnelling evolves into multiphoton ionization. Experimental data shows a frequency dependence rise in the threshold only as the wavelength is reduced to the visible part of the spectrum. This implies that the value of τ_k would be around 5×10^{-16} sec. Sparks, however, has indicated that τ_k is extremely unlikely to be this small, and, as mentioned earlier, τ_k cannot be considered to be independent of the electron energy. Therefore, different effective values of τ_k should be used at different laser

frequencies. The dependence of τ_k on the frequency is shown in Figure 1.12, and the comparison between the calculated values of the breakdown fields at 1.06μm for several alkali-halides (taking into account of the energy dependence of τ_k) with the experimental values is shown in Figure 1.7.

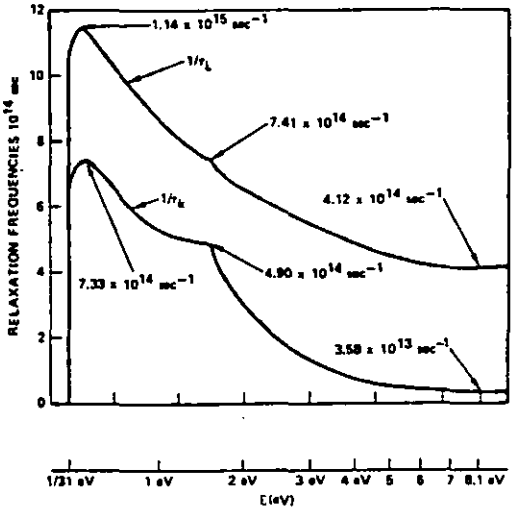

Figure 1.12: Dependence of electron relaxation frequencies on electron energy (after ref.6).

4. Manner of irradiation.

It is well known that N - on - 1 experiments yield higher damage thresholds compared with 1 - on - 1 experiments. Bass and Leung[48] have indicated that for pulsed 10.6μm laser induced surface damage in transparent materials the damage threshold depends on

the manner in which the sample is irradiated and whether a site is irradiated several times. Starting at very low intensity and increasing the intensity a few percent on successive shots until damage occurs, the threshold is often higher than if each site were irradiated only once.

The increase in the surface damage threshold in an N - on - 1 experiment might be due to either a cleaning of the surface by the laser at low intensities or smoothing out the sharp edges of polishing scratches by some form of "laser polishing".

If sharp edges are removed and "V"-like scratches become nearly cylindrical, Bloembergen[18] predicts a ratio of damage thresholds for N - on - 1 to 1 - on - 1 given by:

$$\text{Ratio} = \left(\frac{n^2 + 1}{2}\right)^2 \qquad (1.30)$$

Thus, for sodium chloride were n = 1.49, this ratio would be 2.59 and for potassium chloride with n = 1.46, the ratio is 2.54. The experimental ratios[48] are 3.06 and 2.36 respectively. Later studies[43] have also indicated that the same behaviour applies for bulk damage, but the justification is less convincing.

5. Gas Pressure.

Kovalev and Faizullov[49] have found that with a lowering in ambient gas pressure, there takes place a decrease in the surface breakdown threshold in IR-optical

materials under CO_2 - TEA laser radiation. Breakdown thresholds measured in vacuum have shown to be 1.5 to 2 times smaller than those observed at atmospheric pressure. The observed influence of the ambient gas pressure on breakdown threshold may be explained by making the assumption that the evaporation of absorbed water (which was found by the same authors[50] to be a major factor in lowering the breakdown threshold in IR-optical materials) from the surface takes place before the breakdown. Their results of the effect of the gas pressure on the breakdown threshold of sodium chloride is shown in Figure 1.13.

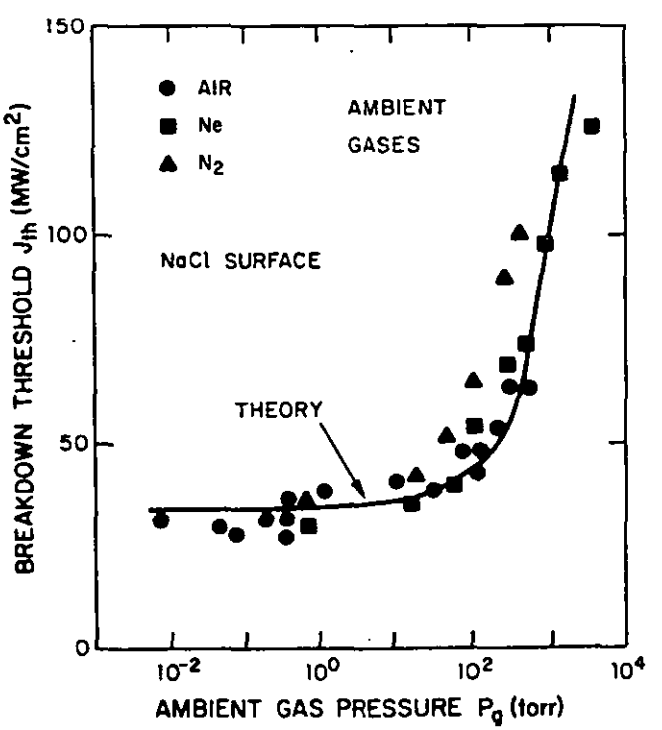

Figure 1.13: Effect of ambient gas pressure on the breakdown threshold of NaCl (after ref.49).

The same observation was made by Kardch et. al[51] for metals, but the decrease in the damage threshold was not the same as that for sodium chloride. Furthermore, Kardch has also indicated that the damage threshold in dielectric and metal components depends on the electronegativity of the ambient gas, for example, N_2 or SF_6, the more electronegative the gas, the higher the damage threshold.

6. F-centres in dielectric materials.

An F-centre is an electron bounded to a negative ion vacancy as shown in Figure 1.14. They are present in all dielectric materials naturally and acts as a source of electrons during laser induced damage. The F-centres are generally located nearer to the valance band than to the conduction band.

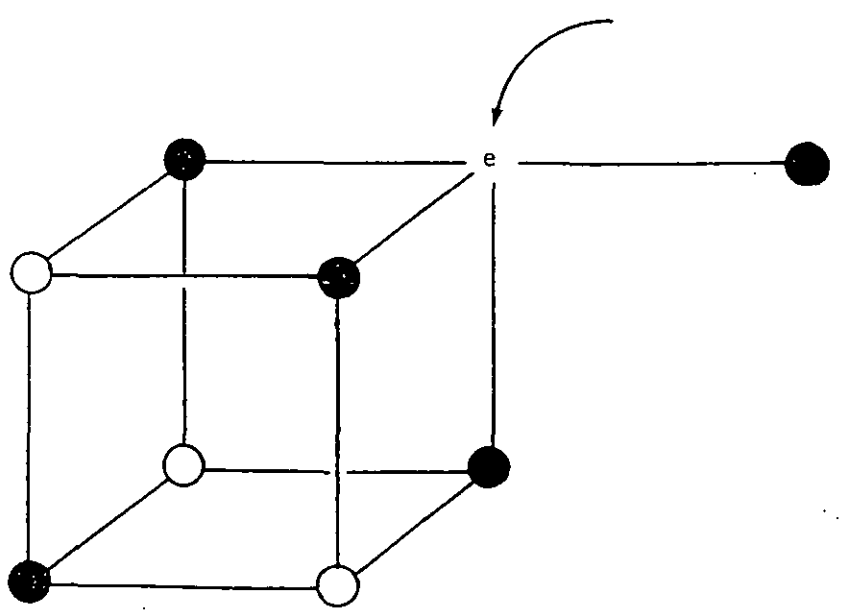

Figure 1.14: An F-centre in sodium chloride.

Yoshiyoki et. al[12] studied the effects of F-centres in KC1 and found that the damage threshold decreases with increasing the density of the F-centres. He also indicated that this decrease is greater for shorter wavelengths since the ionization rate of F-centres is larger for more energetic photons, this is shown in Figure 1.15.

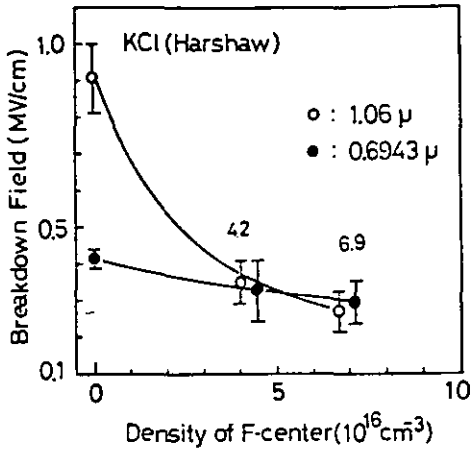

Figure 1.15: Breakdown fields in KC1 for ruby and glass lasers as a function of F-centres (after ref.12).

However, Bräunlich et. al[53] has indicated that the presence of defects in the form of F-centres, V_k^- and H-centres influences the kinetic processes involved in laser induced damage in alkali-halides and act as a drain on the free electrons and holes produced by the

laser field and as a consequence, the rate of temperature increase of the lattice by free carrier absorption is reduced. Thus the damage threshold is increased.

It should be pointed out here, that the exact influence of these F-centres in laser induced damage in alkali-halides cannot be known for sure without calculating the probability of a hole capturing an electron. This probability is now known at the present time.

7. Non-normal incidence.

In section 1.5 the theory of laser induced damage in metals was outlined assuming that the laser beam is normal to the metal surface under test, in this case the two components of the electric field vector E_s (field perpendicular to the plane of incidence and E_p field parallel to the plane of incidence) are both parallel to the metal surface and the laser beam absorption at the surface is independent of polarization.

For non-normal incidence, differences in the surface absorption arises for E_s and E_p radiation as explained below.

The intensity reflection coefficient of an electromagnetic wave at an angle of incidence θ with respect to the normal to the surface is given by[22]:

$$R_p = \frac{\hat{n} - 2n\cos\theta + \cos^2\theta}{\hat{n} + 2n\cos\theta + \cos^2\theta} \qquad (1.31)$$

$$R_s = \frac{\hat{n}\cos^2\theta - 2n\cos\theta + 1}{\hat{n}\cos^2\theta + 2n\cos\theta + 1} \quad . \tag{1.32}$$

Accordingly the abosrptances A_s and A_p are just

$$A_s = 1 - R_s \tag{1.33}$$

$$A_p = 1 - R_p \quad . \tag{1.34}$$

For metals at infra-red wavelengths where n >> 1 and K >> 1 equations (1.31) and (1.32) can be further simplified to become:

$$R_s = 1 - \frac{4n\cos\theta}{\hat{n}} \tag{1.35}$$

$$R_p = \frac{4n}{\hat{n}\cos\theta} \tag{1.36}$$

If an angular dependent absorption coefficient $A(\theta)$ is defined by

$$A(\theta) = 1 - R(\theta) \tag{1.37}$$

then we have from (1.35) and (1.36)

$$A_s(\theta) = \frac{4n}{\hat{n}}\cos\theta = A(0)\cos\theta = A_o(1 + \alpha T)\cos\theta \tag{1.38}$$

$$A_p(\theta) = \frac{4n}{\hat{n}\cos\theta} = A(0)/\cos\theta = A_o(1 + \alpha T)/\cos\theta \tag{1.39}$$

where A(0) denotes the normal incident absorption.

Therefore for a metal surface at an angle of incidence θ to the incoming laser pulse, the calculation of surface damage threshold must be modified in two respects. First, the surface fluence must be reduced by the factor $\cos\theta$ due to the increased area now irradiated. Secondly $A(\theta)$ must be modified to include electric field components both parallel and perpendicular to the metal surface. With these modifications equation (1.20) can now be corrected to include the non-normal incidence:

$$(I\tau)_s = \frac{u}{\alpha_o \alpha_1 \cos^2\theta} \sqrt{\tau KC} \qquad (1.40)$$

$$(I\tau)_p = \frac{u}{\alpha_o \alpha_1} \sqrt{\tau KC} \quad . \qquad (1.41)$$

Therefore, for the p-polarization the damage threshold is independent of the angle of incidence. For s-polarization, the damage threshold increases as $(\cos^2\theta)^{-1}$ and experimental evidence[33] has confirmed this simple model.

Presumably the above treatment for non-normal incidence will also hold true for dielectric and thin film coatings although such an observation has not so far been reported.

8. Laser damage to metals at low temperature.

In order to investigate this aspect of laser

induced damage to metals we need to re-examine equation (1.20). The parameter u is given by the function[19]:

$$f(u) = e^{u^2}(1 + \text{erf}u) \tag{1.42}$$

where $u = I\alpha\left(\frac{\tau}{KC}\right)^{\frac{1}{2}}$ and I is the laser fluence.

For values of $u \geq 1$

$$f(u) \simeq e^{u^2}\left(1 + \frac{2u}{\pi^{\frac{1}{2}}}\right) \simeq 2e^{u^2} = \frac{T_m + 1/\alpha_1}{T_o + 1/\alpha_1} \tag{1.43}$$

$$\therefore \quad u = \left(\ell n \left\{\left(\frac{T_m + 1/\alpha_1}{T_o + 1/\alpha_1}\right) \Big/ 2\right\}\right)^{\frac{1}{2}} . \tag{1.44}$$

Therefore the ratio of damage threshold for a sample at initial temperature T_1 to that at temperature T_o is given by:

$$\text{Ratio} = \frac{\left(\ell n \left\{\left(\frac{T_m + 1/\alpha_1}{T_1 + 1/\alpha_1}\right) \Big/ 2\right\}\right)^{\frac{1}{2}}}{\left(\ell n \left\{\left(\frac{T_m + 1/\alpha_1}{T_o + 1/\alpha_1}\right) \Big/ 2\right\}\right)^{\frac{1}{2}}} = \frac{\left(\ell n \left(\frac{T_m}{2T_1}\right)\right)^{\frac{1}{2}}}{\left(\ell n \left(\frac{T_m}{2T_o}\right)\right)^{\frac{1}{2}}} . \tag{1.45}$$

This ratio is always greater than one since at lower temperatures a decrease in the absorption takes place. For example, for Cu at $T_1 = 139°K$ and $T_o = 276°K$ this ratio is

$$R = \frac{\left(\ell n \frac{1356}{2 \times 139}\right)^{\frac{1}{2}}}{\left(\ell n \frac{1356}{2 \times 276}\right)^{\frac{1}{2}}} = \frac{1.258}{0.948} = 1.32 \quad .$$

The experimental[54] value of this ratio is exactly 1.32.

Although operation at very low temperatures is not desirable, in some critical applications, for example at the UV wavelengths where the damage threshold of most metals is very low, operating at low temperatures may be necessary if metal mirrors must be used.

9. Other parameters.

In addition to the parameters discussed above, there are others which affect laser induced damage such as surface roughness, refractive index, method of fabrication etc. These parameters will be discussed briefly:

1. Surface roughness:- The damage threshold has been found to vary as $E = \sigma^{-m}$ where σ is the rms surface roughness and $0.5 < m < 0.75$ for a typical example such as fused silica[55]. This relation was found to hold for σ values from 335Å to 13.75Å, for example reducing the roughness on conventionally polished fused silica in the same range increased the damage threshold ~~threshold~~ by a factor of 6.3 in the breakdown field or 40 times in fluence. For bulk

damage thresholds a value of σ equal to the lattice spacing was seen to fit the general curve. However subsequent study[56] of the surface damage threshold by 150ps, 1064nm pulses suggested that a surface roughness < 100Å rms might be less important in determining short pulse thresholds.

2. Refractive index:- It has been noted that generally, materials with a high refractive index exhibit rather low damage thresholds in comparison with lower index elements. Bettis et. al[57] showed that the threshold for transparent materials and for thin film coatings should vary as $\frac{N}{n^2-1}$, where N is the number density of the material and n is the refractive index. This scaling describes well the variation of the damage threshold for optical surfaces ranging in refraction index from 1.38 to 2.49 and similar agreement was noted for thin film coatings deposited on fused silica substrates. In addition, the surface roughness was found to modify the damage threshold by a factor of e^{-m}. Figure 1.16 shows the damage thresholds for several half wave films on fused silica and of several optical glasses.

3. Fabrication:- It is soon obvious that fabrication is the largest contributing factor in the non-reproducibility and ultimate damage resistance of high power optical elements. The major problem is

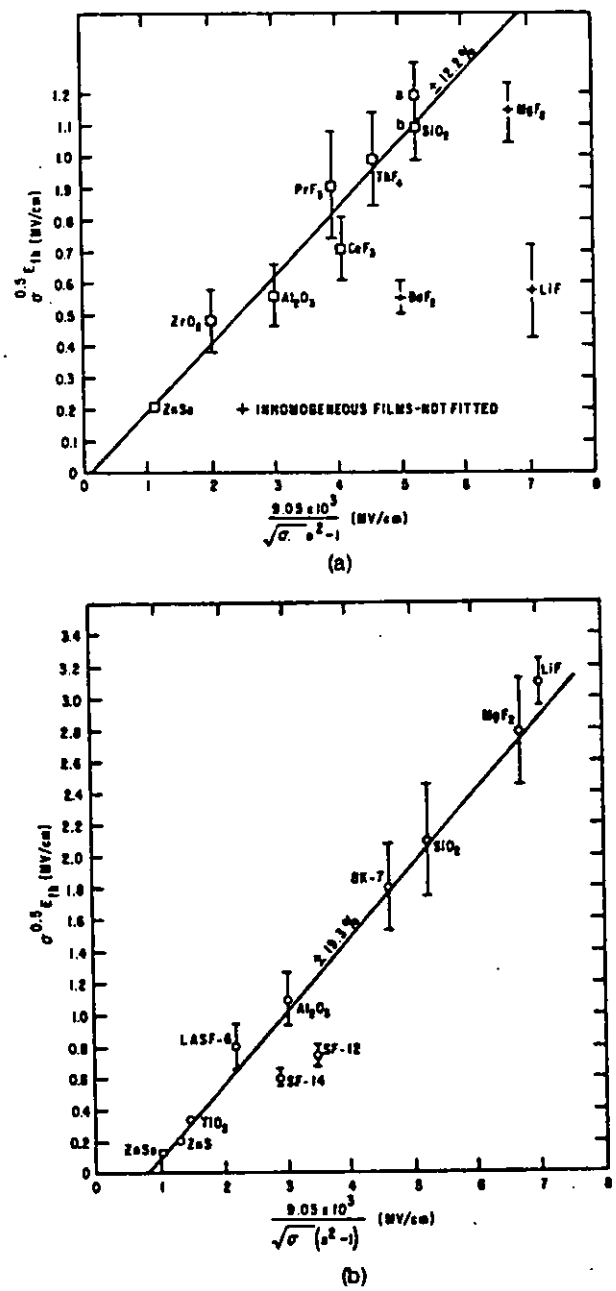

Figure 1.16: Damage thresholds for a) several half-wave films on fused silica and b) the damage thresholds for some optical glasses as a function of refractive index (after ref.57).

to produce low scatter, low absorption, damage resistance surfaces with good optical figure. Many techniques exist for surface finishing, and these varied techniques have produced mixed results. For example, standard lap polishing produces well finished surfaces having a good optical figure but the surfaces are often quite highly scratched and have high absorption. Chemical etching[58], on the other hand, produces scratch free surfaces which are laser damage resistant and with low surface absorption but with poor optical figure. Chemical/mechanical techniques have also been used to produce good optical figure surfaces with less scratches. Ion polishing has been employed to improve the surface finish of glass/metals and some dielectric materials, furthermore ion polishing of some thin films minimize contamination at the film-substrate interface and greatly improve the adherence[59]. Single point diamond turning is a relatively new technique and proved to produce good optical figure on surfaces of metals[60] and dielectrics[61]. Surfaces produced using this technique have been shown to have high damage threshold and low absorption.

The liquid phase of the grinding suspension can also affect laser damage. Bilibin et. al[62] has indicated that for KC1 samples, ethylene is better than a saturated KC1 solution since the

former gives rise to a lower destructive layer depth and therefore higher damage threshold.

4. Cleaning:- There are a number of cleaning methods in general use for optical surfaces. Surfaces can be cleaned by low pressed air or nitrogen or a variety of chemical solvents, these methods do not degrade the surfaces. On the other hand, prolonged ultrasonic cleaning can severely degrade optical surfaces, because ultrasonic cleaning can reveal sub-surface structures introduced during the grinding process as shown in Figure 1.17[63]. However a brief cleaning for a period of a minute or two can lead to an improvement in the optical surface by the removal of surface dirt.

1.8 EFFECTS ASSOCIATED WITH THE ABSORPTION OF LASER RADIATION AT A SOLID SURFACE.

1. Self-focussing.

The phenomena of self-focussing in transparent materials can be explained as follows; under certain conditions an intense laser beam passing through a material can propagate without appreciable spreading. This occurs because the high electric field associated with the laser beam increases the index of refraction of the material. Since the laser beam is most intense at its centre the increase in the index will be maximum

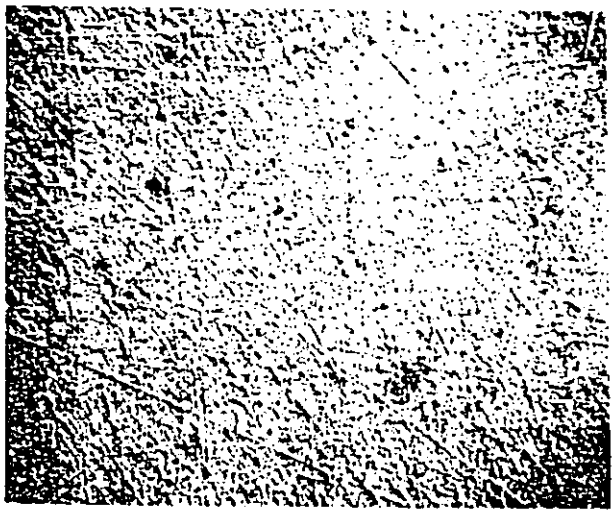

a

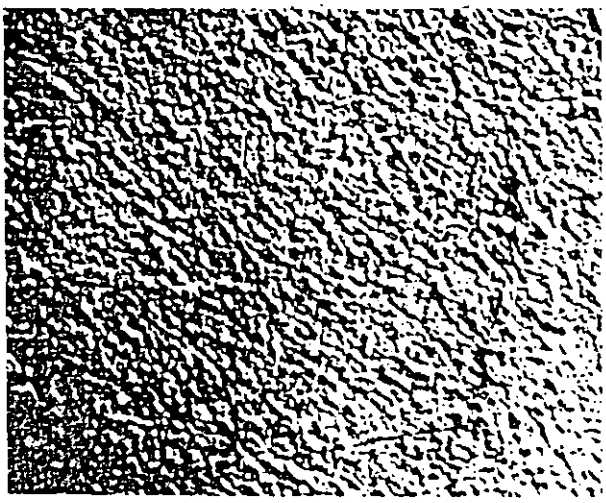

b

Figure 1.17: Effect of ultrasonic cleaning on Zirconium mirror a) before cleaning and b) after 45 minutes of ultrasonic cleaning (after ref.63).

at the centre of the beam; therefore, the propagation at the centre will be slowed down relative to the edges. This focussing effect may trap the beam and prevent it from spreading, causing extensive damage to the material. However, it is possible to avoid self-focussing if the laser power is kept below the critical power for self-focussing, given by[7]:

$$P_{cr} = \frac{c\lambda^2}{32\pi n_2} \tag{1.46}$$

where c is the speed of light, λ is the laser wavelength and n_2 is the intensity - dependent contribution to the index of refraction given by:

$$n_1 = n + n_2\left(E_{rms}\right)^2 \tag{1.47}$$

where n is the refractive index of the material.

2. Stimulated Brillouin Scattering.

Brillouin scattering involves an interaction between the optical field of the laser and the acoustic field of the crystal lattice. The electric field associated with the laser pulse produces electrostriction which in turn exerts a stress in the material and drives an acoustic wave which under appropriate conditions can induce damage to the dielectric material[64].

3. Plasma production.

A plasma is produced by vaporization of some of the target material or by some impurities on the surface of a solid. There have been many investigations of plasma production using a variety of techniques including optical interferometry, optical spectroscopic measurements, mass spectroscopy and charge collection. A wealth of experimental data has emerged from these measurements. Much of the work has been motivated by the possibility of producing high temperature plasma in which a thermonuclear reaction could occur[65]. Since here we are investigating the relation between plasma production and laser induced damage to solid surfaces, attention will be directed towards this aspect rather than the plasma itself.

The plasma ignited at a solid surface has two components[66], one is short-lived and supported in the ambient atmosphere by the laser beam itself; the direction of this component is along the laser beam, the other component extends normally to the surface and results from the vapourization caused by the deposition of energy at the surface. A plasma that results from a surface explosion would be expected to extend in a direction normal to the surface and not depend upon the angle the laser hits the surface. In optical components the occurrence of surface plasma has been taken as an indication of laser induced damage to

that surface. The connection between the surface plasma and damage was not established in the early work of laser interaction with solids, whether or not the plasma is a result or a cause of the damage or whether it is an independently occurring phenomena was not determined. This led Fersman and Khazov[67] to suggest that the surface damage is caused by the plasma interaction. On the other hand, Giuliano[68] has carried out a number of experiments in an attempt to establish the connection between surface damage and plasma production. In one experiment the sample was irradiated well above damage threshold and the plasma was observed as the power was gradually reduced, each time exposing a fresh area of the surface. Giuliano observed that the plasma is reduced in brightness and size as the power is reduced until a point is reached at which the plasma is no longer visible. Despite the absence of a plasma Giuliano was able to detect damage in the form of a number of micropits when the sample was carefully examined under the microscope. From these experiments he concluded that, while it may be true that some of the features seen on the surface of material that has been subjected to damaging laser radiation might be caused by the interaction of the plasma with the surface, the primary cause of the damage is not the plasma, but rather the plasma is a result of the mechanism or mechanisms whatever they may be that give rise to the surface damage.

4. Ripple Formation.

Many workers studying the interaction of laser beams with solids are familiar with the striking periodic damage patterns that can be produced on various surfaces when the power of the beam is at or near the damage threshold. These periodic structures or ripples have been documented since the early days of IR laser development[68]. Ever since they have been observed in laser induced damage to surfaces of dielectrics[69,70,71,72], semiconductors[73,74,75], and metals[76,77], as well as dielectric thin films[78].

A variety of explanations for the observed effect have been offered ranging from the constructive interference of the incident beam with a surface scattered wave originating at a scratch[68], short fields associated with surface defects[69] acting as dipole radiators, to surface melting with reinforcement by positive feedback from the induced surface grating[79]. In all of these theories the spacing of the surface ripples depends on the incident angle and the laser wavelength through the relation

$$\lambda_s = \frac{1}{1 \pm \sin\theta} \qquad (1.48)$$

where θ is the incident angle measured from the surface normal and λ_s is the wavelength of the induced ripple. In addition, these ripples are orientated perpendicularly to the polarization of the laser beam. Table 1.3

TABLE 1.3 : A listing of laser materials and the laser induced ripple spacing.

Material	10.6μm	3.8μm	2.7μm	1.06μm	Ref.
Cu	λ				80
Mo	λ				79
A1	λ			λ	81
Ag	λ			λ	78,81
KC1	λ/n			λ/n	81
NaC1		λ/n		λ/n	81
Si	λ			λ	79,81
KBr	λ/n			λ/n	81
ZnSe	λ	λ		λ	81
Ge	λ			λ	68,79
SiO_2		λ/n	λ/n		81
SiF_2			λ/n		81

summarises some of the materials for which ripples have been observed; note that for semiconductors and metals the ripple spacing is the laser wavelength whilst for dielectrics the spacing is λ/n where n is the refractive index of the dielectric.

1.9 METHODS OF RAISING SURFACE DAMAGE THRESHOLDS.

In actual systems, damage usually occurs first at the optical surfaces. Surfaces are characterised by a high concentration of impurities, defects and inhomogenities. Thus the resistance of an optical component to damage can be greatly improved by careful elimination of these defects. Many methods exist for raising surface damage thresholds such as ion polishing[52], acid treatment[82], laser polishing[83] and baking.

Ion polishing which has been applied most notably on glasses, metals and hard substances like sapphire, depends on using energetic ions to remove a few atomic layers from the surface leaving behind a very clean and defect-free surface. Ringlien[82] treated ED-2 glass with hot 0.4 normal nitric acid which resulted in raising the surface damage threshold from $150 J.cm^{-2}$ to $470 J.cm^{-2}$. Care must be taken in the acid treatment method to choose an appropriate acid which will not alter the optical quality of the surface, for example, nitric acid will not attack the silicate structure of

the glass and therefore can be used on glass but not other materials.

Recently it has been shown by Temple[83] that the damage threshold of mechanically polished fused silica surfaces can be increased to a value comparable to the bulk value by carbon dioxide laser polishing. Two possible explanations were given for the observed increase in the surface damage threshold of fused silica by laser polishing, first vaporization of the absorbing impurities from the mechanically polished surface and secondly healing of the surface and subsurface micro-fractures introduced by conventional grinding and polishing processes. Laser irradiation was also used by Swain et. al[84] to raise the surface damage threshold of BK-7 glass for 1ns 1064nm pulses. Swain indicated that laser cleaning is more easily accomplished using a pulse of longer duration and the maximum fluence at which the cleaning can be performed is that just below the 1 - on - 1 damage threshold.

1.10 DAMAGE THRESHOLD DEFINITION.

The laser induced damage is subject to a variety of definitions. These can range from the minute changes in the morphology or the optical properties of the sample detected by Nomarski microscopy, catastrophic damage creating a plasma, to evaporation and complete flaking. The lack of a standard definition for the laser induced

damage threshold and because of the individual approach of each laboratory testing laser induced damage as well as the lack of complete specification of the experimental conditions has led to differences in the reported data.

How the final figure has been derived also produces controversy, as well as its units, i.e. $J.cm^{-2}$, $GW.mm^{-2}$ or $MV.cm^{-1}$.

As an example, the laser induced damage could be defined as the energy density which produces damage 50% of the time[43]. Another definition[85] is the characteristic threshold energy E_{th} and the threshold fluence such that:

$$I_{th} = \frac{E_{th}}{A} = \frac{1}{2}.\frac{E_{max}(ND) + E_{min}(D)}{A} = \frac{1}{2}.\left[I_{max}(ND) + I_{min}(D)\right] \tag{1.49}$$

where $E_{max}(ND)$ is the highest nondamaging energy and $E_{min}(D)$ is the minimum damaging energy and A is the area of the incident beam on the sample taken as the $1/e^2$ points of the incident intensity. A corresponding spread is then defined as

$$S = \frac{E_{max}(ND) - E_{min}(D)}{E_{th}} \tag{1.50}$$

which is primarily defect dominated and determined from a series of shots on the sample. Example of data reported based on this definition is shown in Figure 1.18. Of course a defect free sample would have S = 0.

Hack[86], on the other hand, defines the damage threshold as the minimum energy density required to cause damage while Reichelt[87] defined damage to be the energy density which causes flash (plasma) at the surface. This definition is not adequate because later evidence[66] has indicated that damage can occur without plasma.

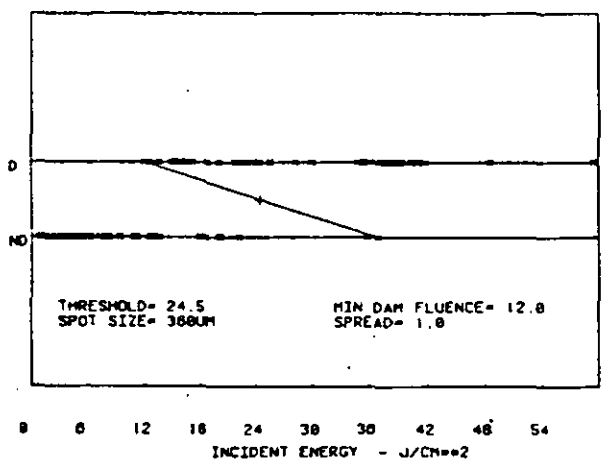

Figure 1.18: Laser induced damage data plotted in terms of energy density.

In addition to these definitions Bass and Barrett[88] observe that precisely defined damage thresholds do not exist. They found that at a particular energy density, laser induced surface damage to ten different materials could be produced with some probability per pulse, P. The measured value of P is obtained by measuring the number of pulses which produce damages at a given site divided by the total number of pulses used to irradiate that site. Accordingly damage threshold was defined as

the energy density which corresponds to the 50% damage probability.

When damage is defect dominated, the 50% damage probability overestimates the minimum damage threshold unless

1. the mean separation of the defects is small compared to the laser spot size and
2. the majority of the dominant defects fail at the same energy density.

Failure of the 50% damage probability to satisfy these two requirements is indicated by its spot-size dependence.

In some practical situations, using large spot sizes are unavoidable and in this case it is appropriate to direct attention to the lower end of the damage probability distribution, i.e., to the energy density where the damage probability first departs from zero, in this case damage threshold is defined as the absolute damage threshold.

Two approaches to determine the absolute damage threshold have been proposed. One of these has been reported by Foltyn[45] in which the damage threshold is defined as the energy density corresponding to the zero percent crossing of the probability curve. Defining damage threshold in this way will make the damage threshold independent of the spot size, the presence of defects will merely affect the slope of probability curve, the higher the defect density the steeper is the

slope of the probability curve as shown in Figure 1.10. However Foltyn assumes that all defects are degenerate, i.e., that all defects fail at the same energy density. Since in practice this situation does not exist, Foltyn's definition is of limited usefulness.

To overcome this difficulty Porteus[89], based on the concept of Foltyn's definition, used a distribution of nondegenerate defects, where the defects generally fail at different energy densities. Figure 1.19 shows the damage probability distribution for a degenerate defect ensemble for a Gaussian beam, the degenerate nature of the defects is indicated by the positive curvature of the probability curve over the extended range. As expected, the damage threshold for degenerate defects is less than the damage threshold of non-degenerate defects.

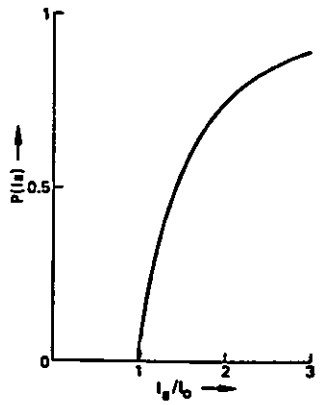

Figure 1.19: The damage probability distribution for degenerate defects for a Gaussian beam. I_a is the damage threshold and I_o is the peak energy density.

CHAPTER TWO

Piezoelectric Transducers

2.1 INTRODUCTION.

In Chapter one some effects associated with laser solid interaction are discussed. In addition to those effects, two more phenomena often occur, these are, the generation of both acoustic and thermal waves inside the solid and in the air above the solid surface. These two waves differ in two important aspects, firstly, acoustic waves have larger wavelengths than the thermal waves and, secondly thermal waves are diffuse waves that travel only one to two wavelengths before their intensity becomes negligibly small. A schematic of these two waves is shown in Figure 2.1.

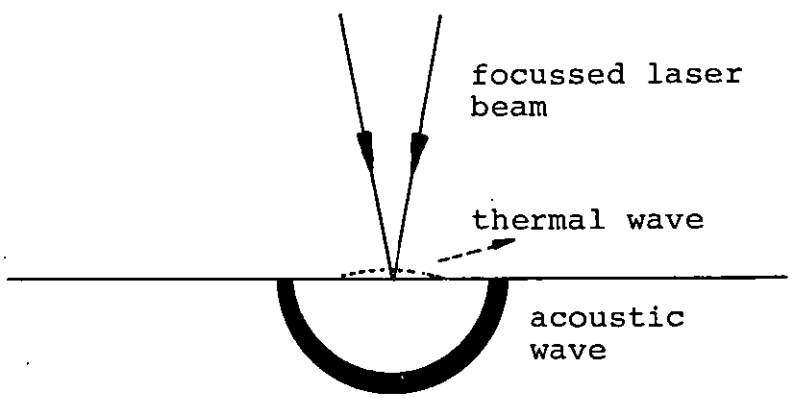

Figure 2.1: Schematic representation of acoustic and thermal waves due to the interaction of a focussed laser pulse with a solid surface.

A great deal of interest, both theoretical and experimental has been shown to these two phenomena and now a wide range of applications exist.

While acoustic waves have been used to study the mechanical and elastic properties of solid materials[1], thermal waves have been used to measure very low absorption coefficients of optical materials used in high-power laser systems[2] and for thermal imaging[3]. These waves can also be used to detect the onset of laser induced damage to optical materials.

Laser induced damage in optical materials can be detected, for example, by monitoring the amplitude of the acoustic wave generated in the sample due to the absorption of laser energy by attaching a suitable piezoelectric transducer to the sample surface. In the case of thermal waves, the damage can be detected by probing a thin He-Ne laser beam through the refractive index gradient generated near the sample surface and then monitoring the deflection of the He-Ne laser as a function of the energy of the damaging pulse. These two schemes of damage detection have been studied in this work and will be the subject of Chapter three and four respectively.

For detecting the damage using the acoustic wave we need a sensitive transducer with a wide bandwidth; this chapter will explain in a simple way the basic principles of ultrasonic transducers, their types, the

material used in constructing them and the various parameters affecting their performance. Finally, the development of two sensitive transducers used to detect the onset of laser induced damage in optical materials will be discussed.

2.2 INTRODUCTION TO PIEZOELECTRIC MATERIALS.

Piezoelectricity is the phenomena related to the production of electric charge when certain materials are deformed. Piezo is derived from a Greek word meaning to press and piezoelectricity is pressure electricity. Piezoelectricity appears only in insulating solids with no centre of symmetry. The effect was discovered by the Curie brothers in 1880 who observed that when certain materials are deformed electric charges are produced at their surfaces. Later the inverse effect was observed in which the same materials deformed when placed within an electric field. The piezoelectric effect soon found an important application in World War II in SONAR for detecting and locating submarines. However, the main application of piezoelectric materials is the field of piezoelectric transducers, these are force sensitive devices and therefore they are used for the measurement of physical quantities related to force such as pressure, stress or acceleration. The main attraction of piezoelectric transducers for measurement of these parameters is

their high mechanical input impedance (stiffness). Another advantage of piezoelectric transducers is the possibility of designing instruments with very small dimensions. Piezoelectric materials have found an important application in the field of non-destructive testing of materials in ultrasonics and the measuring of very small displacements in the picometer range[4]. Because piezoelectric materials are highly structured, any deformation will depend on the alignment of crystallographic axes with respect to the applied field. It is therefore possible to cut and section crystals in such a way that the deformation maximizes a thickness expansion or shear distortion. Taking quartz, for example, plates cut normal to the x-axis (X-cut) maximize thickness expansion, while plates cut to the y-axis (Y-cut) maximize shear distortion. These plates can then be used as a basis for design of longitudinal and shear wave transducers. The main disadvantages of piezoelectric transducers are their lack of steady-state response associated with charge leakage and the limited working temperature range in piezoelectric materials; this is in the neighbourhood of 200-250°C[5]. Although some piezoelectric materials have a Curie temperature as high as 576°C (for quartz), the loss of insulation resistance above, say 200°C sets a further practical limitation.

2.3 PIEZOELECTRIC MATERIALS.

Piezoelectric materials for use in transducers can be divided into four main groups. These are:

A - Natural crystals.

i) Quartz, SiO_2: is the most commonly used material employed in piezoelectric transducers, especially pressure sensors. The crystal structure of quartz can be described as a helix with one silicon and two oxygen atoms alternating along the helix, thus forming a hexagonal plane of view of the crystal cell as shown in Figure 2.2a. Silicon atoms carry four positive charges and the oxygen atoms two negative charges, in the unstressed arrangement all the charges are compensated and there is no net field. If, however, a force is applied to the crystal in the x-direction the balance is disturbed and the cell becomes polarized as shown in Figure 2.2b generating an electric charge on the two faces A and B (longitudinal effect). A force in the y-direction (Figure 2.2c) causes a distortion and thus a polarization of the crystal cell which leads to a charge whose polarity is opposite to that of Figure 2.2b, on the same crystal faces A and B (transverse effect). The main application of quartz is in transducers for the measurement of fast-transient pressures and accelerations.

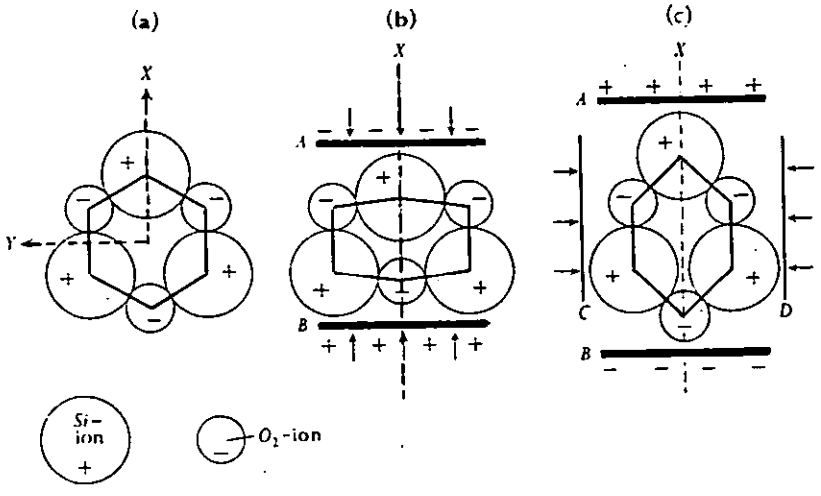

Figure 2.2: a) Simplified crystal structure of quartz, showing arrangement of atoms in neutral cell.
b) Quartz cell loaded in the x-direction.
c) Quartz cell loaded in the y-direction (after ref.5).

ii) Tourmaline: This is a naturally occurring semi-precious stone which has more limited use than quartz for pressure transducers, its main use is to measure hydrostatic pressure in fluids since tourmaline is the only material to have a large volume expansion mode.

iii) Rochelle salt: This is the only piezoelectric material that is being grown on an industrial scale because of its continuous leading role in applications such as gramophones and microphones. In addition, there are several other naturally occurring piezoelectric

crystals, notably, ammonium dihydrogen phosphate (ADP) and lithium sulphate, these piezoelectric crystals are artifically grown and have a more limited use.

B - Ceramic materials.

These are polycrystalline ceramic materials principally barium titanate ($BaTiO_3$) and lead zirconate-titanate (PZT). These materials have high dielectric constant (1000-5000). They can be visuallised as consisting of dipoles within domains of spontaneous polarization which can be partially aligned by applying a strong external electric field of about 2 $KV.mm^{-1}$, as shown in Figure 2.3, at a temperature just below the Curie temperature (Curie temperature is the temperature at which the piezoelectric properties disappear).

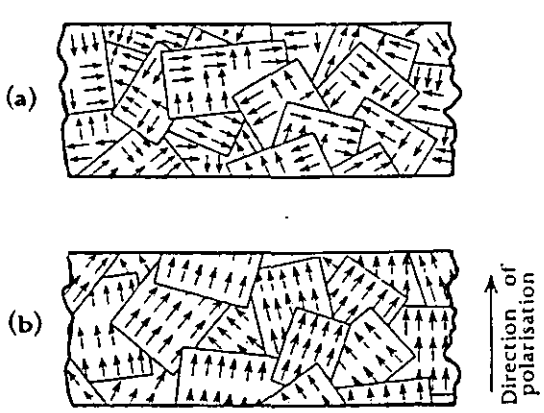

Figure 2.3: Barium titanate; a) unpolarized, b) polarized (after ref.5).

After cooling and removing the polarizing field the dipoles and domains cannot easily return to their original random positions and the material remains polarized. There is however gradual depolarization with time but this can take several years. In fact ceramic materials have largely superseded the single crystal materials for transducer use. The main advantages of ceramic materials are:

1 - They have high coupling coefficient.
2 - Remachining of the material is possible after poling.
3 - Any damage to the material can be repaired by repoling.
4 - Ceramic materials can be cast and machined into various shapes to suit a particular application.

C - Polymer materials: Many organic materials such as wood, silk and bone exhibit piezoelectric properties, unfortunately the piezoelectricity in these are too small to be used for practical devices. Polyvinylidene fluoride (PVF_2) is a polymer material which exhibits piezoelectric properties comparable to the single crystal and ceramic material. This material can be used for transducers and recently[6] PVF_2 transducers have been developed with a flat response and useful bandwidth of up to 20 MHz, depending on the thickness of the PVF_2 material. A particular advantage of the polymer material is its flexibility which allows the construction

of complex transducer shapes without machining. In many applications, for example, the ultrasonic energy has to pass through a liquid couplant before being detected by the transducer and in this respect a polymer is much more efficient than a ceramic material since the acoustic impedances are more nearly equal. These polymer materials are also suitable for use in studies involving the determination of the elastic properties of the optical materials used in laser systems and for the determination of their laser induced damage thresholds.

D - Composite materials[7].

The majority of piezoelectric materials have high acoustic impedances and are not well matched with the acoustic impedances of most of the couplants used to attach piezoelectric transducers to the structure under study. To overcome these difficulties a piezoelectric material such as PZT can be combined in some way with other material to produce a material with more suitable properties for coupling. However, the problem of producing composite piezoelectric materials with useful properties is considerably more complex than a simple mixing of the materials and the production of these materials still involves many problems.

2.4 PHYSICAL PRINCIPLES.

Suppose we have a piezoelectric crystal of cross

sectional area A, and thickness ℓ with electrodes plated on its opposite faces. Let a voltage V be applied across the electrodes to produce a field, $E = \frac{V}{\ell}$ and a constant tensile stress, T, be applied to the surfaces of the crystal. If S is the resultant mechanical strain and, provided that changes occur within the elastic limit, we have

$$S = Ts + Ed \tag{2.1}$$

$$D = Td + \varepsilon E \tag{2.2}$$

where D is the electric displacement, s is the elastic compliance of the material defined as 1/Y, Y being the Young's modulus, ε is the permittivity of the material and d is a coefficient to be defined later.

On short circuiting the electrodes so that E = 0, equations (2.1) and (2.2) may be written as:

$$S = Ts \tag{2.3}$$

$$D = Td \ . \tag{2.4}$$

Hence the electric displacement, D, becomes equal to the dielectric polarization, P, i.e., the charge per unit area. Thus,

$$P = Td \tag{2.5}$$

d is called the "d" coefficient or the piezoelectric strain constant and is defined as the charge density output per unit applied stress under short circuit

conditions. If, on the other hand, the stress, T, is removed, equation (2.1) becomes

$$S = Ed \quad . \tag{2.6}$$

The "d" coefficient may thus be defined alternatively as the mechanical strain produced by unit applied field under conditions of no load and is expressed either in coulomb newton^{-1} or meter volt^{-1}. In the absence of the piezoelectric effect, the term d disappears from equation (2.2) and we have the known relation

$$D = \varepsilon E \quad . \tag{2.7}$$

In addition to the "d" coefficient, two other constants, the "g" and "h" coefficients are sometimes used to describe the behaviour of piezoelectric crystals. The "g" coefficient is the electric field produced per unit applied stress and the "h" coefficient is the electric field produced per unit strain, in both cases under conditions of open circuit, i.e.

$$E = gT \tag{2.8}$$

$$E = hS \quad . \tag{2.9}$$

The unit of "g" coefficient is volt meter newton^{-1} and the unit of the "h" coefficient is newton coulomb^{-1}.

Up to now, it has been assumed that the changes in E, T, S and P have been in thickness direction of the crystal. In general one must take into account

variation which may occur in any direction. A stress applied to a solid in a given direction may be resolved into six components; three tensile stresses T_1, T_2, T_3 along the x, y, z axes respectively and shear stresses T_4, T_5, T_6 about these axes. Therefore the corresponding components of the strain are, S_1, S_2, S_3, S_4, S_5, S_6 and equation (2.3) can be rewritten in general as:

$$S_i = s_{ij} T_j \quad . \tag{2.10}$$

Since $c_{ij} = 1/s_{ij}$, c_{ij} being the stiffness of the material, equation (2.10) can be written in the following form:

$$T_i = c_{ij} s_j \quad . \tag{2.11}$$

This gives 36 values of c_{ij} as follows:

$$\begin{aligned}
T_1 &= c_{11}S_1 + c_{12}S_2 + c_{13}S_3 + c_{14}S_4 + c_{15}S_5 + c_{16}S_6 \\
T_2 &= c_{21}S_1 + c_{22}S_2 + c_{23}S_3 + c_{24}S_4 + c_{25}S_5 + c_{26}S_6 \\
T_3 &= c_{31}S_1 + c_{32}S_2 + c_{33}S_3 + c_{34}S_4 + c_{35}S_5 + c_{36}S_6 \\
T_4 &= c_{41}S_1 + c_{42}S_2 + c_{43}S_3 + c_{44}S_4 + c_{45}S_5 + c_{46}S_6 \\
T_5 &= c_{51}S_1 + c_{52}S_2 + c_{53}S_3 + c_{54}S_4 + c_{55}S_5 + c_{56}S_6 \\
T_6 &= c_{61}S_1 + c_{62}S_2 + c_{63}S_3 + c_{64}S_4 + c_{65}S_5 + c_{66}S_6
\end{aligned} \tag{2.12}$$

From the principle of conservation of energy it can be seen that

$$c_{ij} = c_{ji} \quad \text{and} \quad s_{ij} = s_{ji} \tag{2.13}$$

so that the number of these constants are reduced to 21. Symmetry of axes will reduce this number still further.

Another common relation is the coupling coefficient K, this coupling coefficient represents the square root of the mechanical energy converted to electrical energy, to the input mechanical energy and vise versa. The value of the coupling coefficient can be represented by the following relation:

$$k_{ij} = (d_{ij} \times h_{ij})^{\frac{1}{2}} . \tag{2.14}$$

For frequencies well below the mechanical resonance frequency of the crystal, the coupling coefficient is simply a measure of the efficiency of the crystal as an energy converter. The value of K is the theoretical maximum, but in practical transducers the conversion is usually lower especially at frequencies far from resonance. Table 2.1 lists the values of some peizo-electric coefficients for various types of piezoelectric ceramics.

2.5 WAVE PROPAGATION IN SOLIDS.

In solids a variety of waves can be generated.

TABLE 2.1*: Properties of some important piezoelectric materials.

Coefficient	PZT-4	PZT-5A	PZT-5H	PZT-8
K_{33}	0.70	0.70	0.75	0.64
K_{31}	0.33	0.34	0.39	0.30
d_{33} ($cm.V^{-1}$)	285×10^{-10}	374×10^{-10}	593×10^{-10}	225×10^{-10}
d_{31}	-122×10^{-10}	-171×10^{-10}	-274×10^{-10}	-97×10^{-10}
g_{33} ($V.cm.dyne^{-1}$)	24.9×10^{-6}	24.8×10^{-6}	19.7×10^{-6}	25.4×10^{-6}
g_{31}	-10.6×10^{-6}	-11.4×10^{-6}	-9.1×10^{-6}	-10.9×10^{-6}
Thermal conductivity ($W.m^{-1}.°C$)	2.1	1.5	1.5	2.1
Mechanical Q	500	75	65	10000
Curie point °C	325	365	195	300
Tensile strength (psi)	11000	11000	11000	11000
Density ($Kg.m^{-3}$)	7.5	7.75	7.5	7.6

* Source Moderen Piezoelectric Ceramics, Vernitron Ltd., 1976.

The first propagation mode is the longitudinal wave or P wave, in these waves the direction of propagation and the vibration are collinear and the wave represents a series of compressions and rarefactions in the solid. The second of these waves is the shear wave which can only exist in solid materials and some highly viscous liquids. In shear waves the propagation and displacement vectors are at right angles. Another important wave motion is the surface waves, and there are two types of these surface waves. The first, polarized in the plane of the surface and at right angles to the direction of motion, is called Love waves and the other is Rayleigh waves. For Rayleigh waves the wave vector has two components, one longitudinal and the other is transverse, at right angles to the surface. Surface waves do not penetrate appreciably into the interior of the solid and propagation thus takes place in only two dimensions. The attenuation of these waves is consequently very much less than that of waves which do penetrate into the solid.

In thin plates or in tubes it may be impossible for any of the above waves to propagate without interacting with both surfaces, this interaction results in a complex series of waves arising from reflections, refractions and interference of different modes. Table 2.2 compares the longitudinal, surface and shear wave velocities for some materials.

TABLE 2.2 : Comparison of waves velocities in some materials which may be used with transducers.

Material	Longitudinal wave ms^{-1}	Shear wave ms^{-1}	Surface wave ms^{-1}
Aluminium	6374	3111	2906
Glass	4372	2100	1964
Stainless steel	5980	3297	3049
Quartz	5970	3765	3410
Tungsten	5221	2887	2668
Perspex	2700	1330	1242

2.6 REFLECTION AND REFRACTION OF ACOUSTIC WAVES AT A BOUNDARY.

When an acoustic wave travels in one medium with a given specific impedance (defined as the ratio of acoustic pressure to particle velocity , in analogy to the electric impedance) and meets a boundary with a medium with a different impedance, part of the incident energy is reflected and the other part is transmitted, the ratio of the reflected energy to the transmitted energy depends on the acoustic impedances

of the two media and on the angle of incident of the acoustic wave with respect to the normal to the boundary separating the two media. The reflection and refraction of the acoustic waves at the boundary between the two media is governed by Snell's law as in optics, however, the difference is that when a longitudinal wave is reflected, it is made of longitudinal and transverse waves. This is called a mode conversion. For normal incidence, the intensity of the acoustic wave reflected or transmitted can be calculated using the following equation for the intensity reflection coefficient being the ratio of the reflected to the incident intensity,

$$R = \left(\frac{Z_2 - Z_1}{Z_2 + Z_1} \right)^2 \qquad (2.15)$$

and for the transmitted intensity,

$$T = \frac{4Z_2}{(Z_2 + Z_1)^2} \qquad (2.16)$$

where Z_1 and Z_2 are the acoustic impedances of the two mediums respectively. It is therefore important for coupling a piezoelectric transducer to the surface to be investigated that the impedance of the transducer will match that of the surface for maximum transmission of the acoustic energy across the boundary.

2.7 BACKING OF PIEZOELECTRIC TRANSDUCERS.

Transducers are devices which, for the purpose of measurement, turn physical input quantities into electrical output signals[5]. The use of suitable backing materials can be a major factor in shortening or broadening the bandwidths of piezoelectric transducers. The ideal backing material is one for which the transfer of ultrasonic energy from the piezoelectric to the backing material is efficient so that reflections do not occur in the piezoelectric material. In addition, the ultrasonic wave once in the backing should be rapidly absorbed or attenuated so that the backing material does not act as a source of delayed sound waves. Plastics are strongly attenuating and therefore good absorbers of ultrasound, however, the problem in using plastics is that their acoustic impedance are low compared to most piezoelectric materials, for example, the acoustic impedance for PZT material is 2.7×10^7 kg m^2 sec^{-1} compared to 3.2×10^6 kg m^{-2} sec^{-1} for perspex. The impedance mismatch of metals and unpoled piezoelectric materials is much higher and consequently they are more often used as a backing material. Thus stainless steel which has acoustic impedance of 4.6×10^7 kg m^{-2} sec^{-1} would be fairly closely matched to the PZT. In this case the PZT would be coupled to the steel via at least one layer of coupling fluid such as water. The acoustic impedance (Z_L) of the load

(couplant and steel) as seen by the PZT is given by[8]:

$$Z_L = Z_w \left(\frac{Z_s + Z_w \tanh(\phi t)}{Z_w + Z_s \tanh(\phi t)} \right) \qquad (2.17)$$

Where $\phi = \alpha + i\,(2\pi f/v)$, v is the ultrasonic velocity in water, Z_w is the acoustic impedance of water, Z_s is the acoustic impedance of steel and t is the thickness of water layer, f is the ultrasonic frequency and α is the absorption in water. If it is assumed that the water layer is thin and that absorption is negligible then, equation (2.17) can be rewritten in the following form:

$$Z_L = Z_w \left(\frac{Z_s + Z_w(2\pi t/\lambda)}{Z_w + Z_s(2\pi t/\lambda)} \right) \qquad (2.18)$$

where λ is the ultrasonic wavelength. For $t = 0$ the load is equal to Z_s as expected but the load falls rapidly as t increases. However, the disadvantage of using metals, as a backing material is that of forming an acceptable bond between the backing and the piezoelectric material since most of the commercially available bonding agents have acoustic impedances less than 10% of that of the piezoelectric material and backing metals. At the present time the most favoured backing material in use with common piezoelectric materials is metal-loaded organic materials[8]. These materials are suspensions of a suitable metal powder in an organic base usually a bonding material. The usual

choice for metallic components is tungsten which has both a high acoustic impedance and is relatively inert. The purpose of the metal suspension is to increase the acoustic impedance of the total assembly so that to match the acoustic impedance of that of the piezoelectric material. Figure 2.4 shows the acoustic impedance of tungsten in araldite as a function of tungsten concentration.

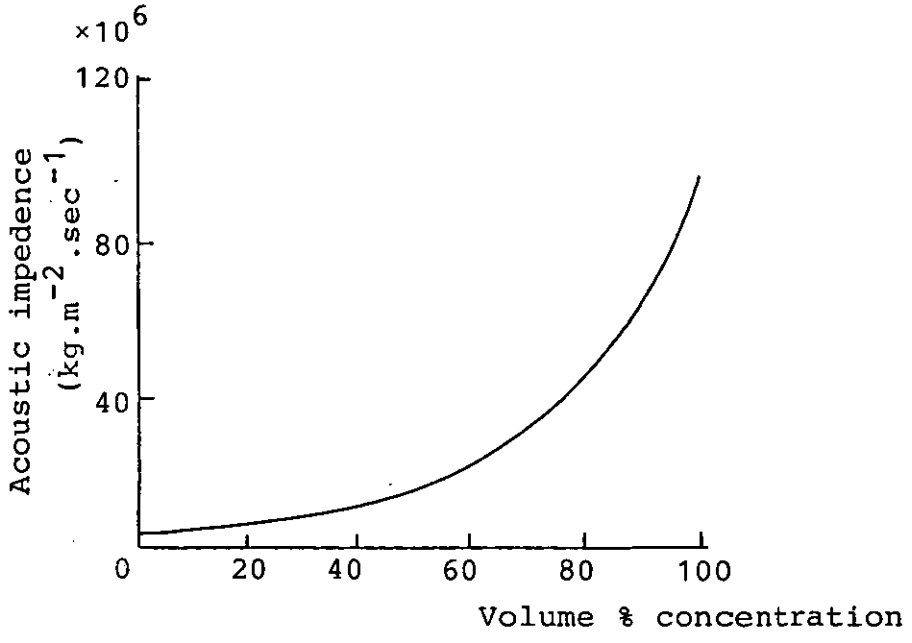

Figure 2.4: The acoustic impedance of tungsten suspensions in araldite. (after ref. 8).

2.8 COUPLING OF PIEZOELECTRIC TRANSDUCERS.

Piezoelectric transducers are usually coupled to the structure under study using a suitable material such as wax, silicon grease or even water as shown in

Figure 2.5. Ideally the transducer face material, the couplant and the structure should have a good acoustic impedance match. Usually some compression is needed and the couplant layer should be kept as thin as possible in order not to introduce acoustic reflections in the couplant layer. Moreover in order to ensure a uniform thickness of the couplant between the transducer and the structure and to eliminate bubbles in the interface, both the transducer and the structure must normally have a good degree of polish.

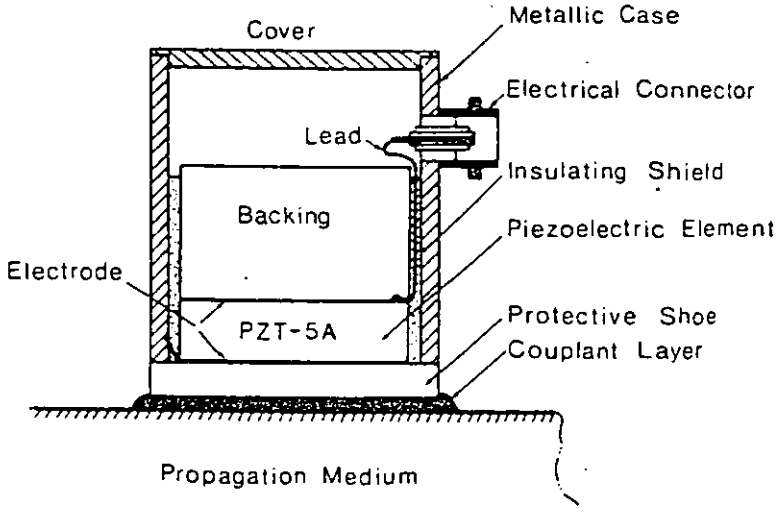

Figure 2.5: Coupling of a piezoelectric transducer to the load.

Figure 2.6a shows the response of a well bonded transducer, while Figure 2.6b shows the response of a badly bonded transducer, the ringing correspond to

reflections within the couplant layer. Silk[9] has predicted that a couplant thickness greater than a few percent of the acoustic wavelength can completely alter the performance of the transducer.

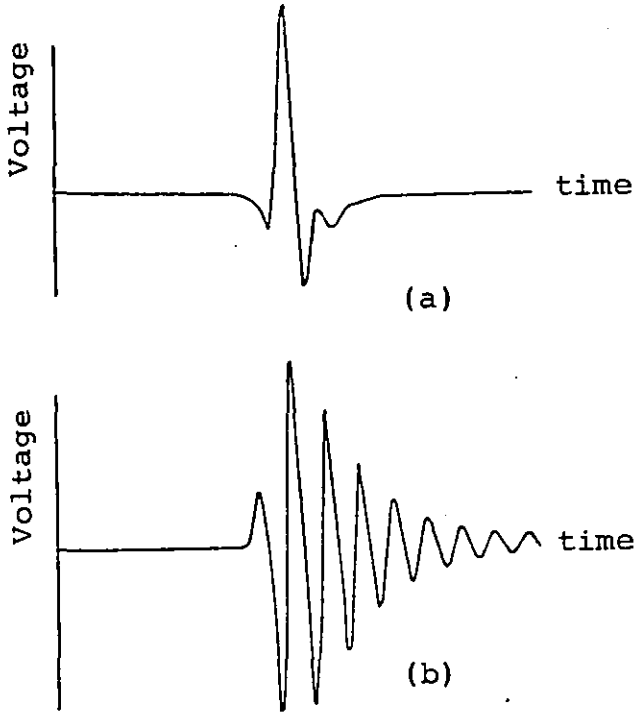

Figure 2.6: a) The response of a well bonded transducer.
b) The response of a badly bonded transducer (after ref.8).

2.9 TRANSDUCER TYPES.

A wide variety of transducers are in recent use. There are, for example, electromagnetic transducers, the main application being in loudspeakers and microphones, while strain-gauge transducers are used for

measuring pressure, acceleration and force.

Many piezoelectric transducers have been designed for use in the generation and reception of ultrasonic waves. The piezoelectric material and the transducer design depend on the intended application[5]. Since the application of piezoelectric transducers in this work involved the detection of acoustic emission associated with radiation interaction with solid surfaces, the emphasis in what follows will be on the different types of transducers available and designed for the detection of acoustic emission. Acoustic emission transients contain a wide range of frequencies and consequently useful transducers must be sensitive over wide bandwidth in order to study the entire wave form. Quartz is a popular choice as a transducer material because of its high Q value (the Q value is defined as $\frac{f_o}{f_1 - f_2}$, where f_o is the resonance frequency, f_1 and f_2 are the frequencies at which the radiated power has fallen to half that at resonance), but it is clearly inappropriate to use quartz for acoustic emission studies because of the limited bandwidth. Ceramic materials such as PZT on the other hand, have low Q value due to internal damping and for this reason piezoelectric ceramics are often used for acoustic emission applications. Figure 2.7a shows a conventional design[10] for the detection of acoustic emission signals. The construction of these transducers is particularly

simple. The two faces of the piezoelectric element are coated with a conductive layer usually a heat cured silver paint, the upper face is connected to a backing or damping block and a lead from this face goes to the BNC lead. The front face is connected to a thin metal foil resting on a wear plate usually made of plastic or matching PZT ceramic which is in turn coupled to the surface under study. The backing block as discussed above is designed to absorb acoustic waves over the range of interest and consists of metal or, mixture of tungsten powder and epoxy. The backing disc also has the property of broadening the ceramic element resonance leading to a broad bandwidth of the disc[5]. Although this kind of transducer can have a reasonable bandwidth, they are not free from mechanical and electrical resonances and when used for acoustic emission detection in solids the information they yield is modified by the response characteristic of the transducer itself as well as by that of the medium which acoustically couples the transducer to the surface under study. A further disadvantage of this construction is that the diameter of the sensitive area of the transducer is typically >10 mm, this means that the upper frequency of the device is limited to wavelength $>$ 20 mm. For example, for a surface wave in steel, this corresponds to 0.3 MHz. This upper frequency cutoff is associated with the apperture effect. Finally, these transducers

are not easy to calibrate being partially resonant in operation, furthermore, they tend to have large variations in the sensitivity over the frequency range of interest.

In order to overcome these difficulties, various types of transducers have been proposed. One particular solution is the capacitive transducer shown in Figure 2.7b. This transducer has been reported by Scruby et. al[11], although the physical principle upon which it is based is well established[12]. The capacitive transducer consists of two parallel plates of area A, separated by a small air gap ζ. One plate is the polished surface of the test-piece, and this is earthed. The other plate in the transducer is maintained at a potential V. Thus oscillation of the surface due to the arrival of the elastic wave causes the capacitance C of the transducer to change. Provided the potential difference between the plates is kept constant, then a charge δq is induced on the plates, which is given by

$$\delta q = V\delta C \tag{2.19}$$

since

$$C = \varepsilon A/\zeta \tag{2.20}$$

then

$$\delta q = - \varepsilon VA \, \delta\zeta/\zeta^2 \tag{2.21}$$

and the sensitivity of the transducer to surface displacement is thus given by

$$\frac{dq}{d\zeta} = - \frac{\epsilon VA}{\zeta^2} \quad . \qquad (2.22)$$

From equation (2.22) it can be seen that the sensitivity is increased by increasing the plate area A, decreasing plate separation and increasing the potential difference between the plates. Recently Boler and Spetzler[13] have designed a capacitive transducer with a capacitive probe diameter of only 0.1 mm. This is 50 times smaller than the capacitive transducer of Figure 2.7b. The transducer, shown in Figure 2.7c, is capable of detecting a minimum displacement of 10^{-11}m, which is equivalent to 7mV/nm.

The capacitive transducers described above have a flat frequency response over a wide frequency range, making possible a faithful reproduction of the surface displacement. They are however, directional, of low sensitivity, and require a highly polished mounting surface. While they are an excellent transducer for laboratory work, a need for a transducer without these limitations is evident.

One particular solution shown in Figure 2.8a and suggested by Proctor[14], this design is based on the following criteria;

1 - The design has been kept simple.

2 - The transducer contact area has been kept as small as possible.

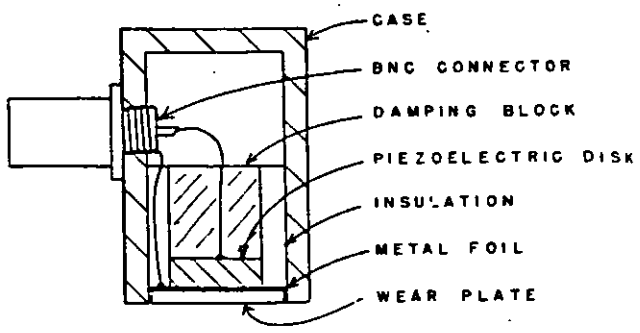

(a)

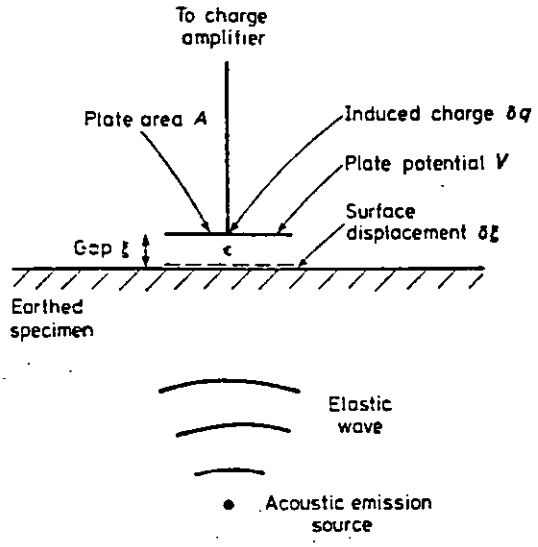

(b)

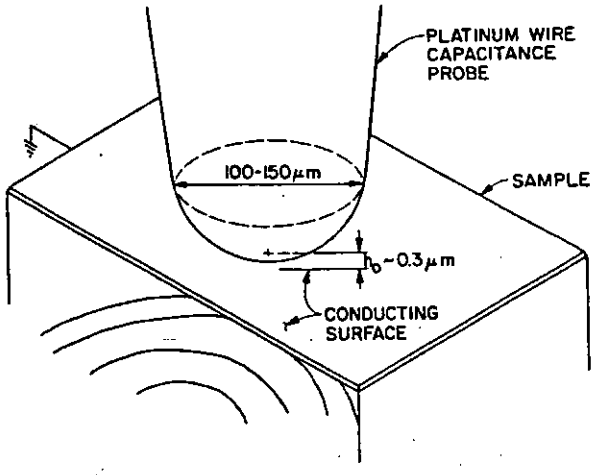

(c)

Figure 2.7: a) A conventional transducer,

b) the capacitive transducer and

c) is a point-like capacitive transducer.

3 - No wear plate has been used.

4 - The backing has been extended both radially and axially.

The transducer consists of only two pieces. The active element is a cone of PZT material. The truncated end of the conical element is about 1.5 mm in diameter, this is small compared to the frequency range of interest (normally 100 kHz - 1 MHz). The backing is a brass cylinder which is large compared to the PZT element. A silver electrode is attached to the small area of the active element and the piezoelectric element is fixed to a small flat area on the brass backing with heat cured epoxy resin. Proctor used brass which has acoustic impedance of 3.7×10^7 kg m^{-2} sec^{-1} compared to 3.87×10^7 kg m^{-2} sec^{-1} for the PZT. The large dimension of the brass backing also means that reflections are delayed and reduced by attenuation in the block. In use the transducer is mounted directly on the surface with no couplant and is surrounded by a box which houses the matching amplifier. Electrically, the backing block acts as the non-grounded electrode for signal detection. The small contact size of the PZT element makes the transducer an approximation to a point receiver. Proctor's transducer which was developed at the National Bureau of Standards in Washington has a flat frequency response from 50 kHz up to 1 MHz

and has a sensitivity of 2×10^8 V/m which is the sensitivity of the PZT element itself. Furthermore, the upper frequency limit can be extended by reducing the thickness of the PZT element. The problems associated with this type of transducer are, its large mass and any reduction in the size of the backing block will steadily diminish the frequency response of the transducer. In addition, unless special arrangements are taken, the transducer cannot be used on non-metallic surfaces because earth return is through the subject. Another practical disadvantage is that with frequent use of the transducer, the silver paint on the contact area will wear away and have to be painted again.

Another approach to wideband transduction has also been described by Niewish and Krämmer[15], this transducer, shown in Figure 2.8b consists of a piezo-electric platelet (PZT) with dimensions 10 mm × 10 mm × 0.5 mm embedded in damping material made from epoxy resin such that the diagonal of the platelet is perpendicular to the surface under inspection. This arrangement results in a very small contact area. The backing material consists of a relatively large steel cylinder on the other side of the diagonal.

A completely different form of transducer which is growing in use is based on optical interferometry[16]

is shown in Figure 2.8c, this transducer has a large bandwidth (up to 10 MHz) and can be further increased by improving the associated electronics. The advantages of the optical transducer are:

1 - Very high resolution, the light source, usually a laser, can be focussed on to a small spot on the surface of the subject.

2 - The transducer does not disturb the quantities being measured and is therefore non-invasive.

3 - Freedom from mechanical resonances.

4 - No couplant is needed.

5 - Optical transducers are inherently calibrated via the wavelength of light used.

The main disadvantages of the optical transducers are:

1 - Optical transducers are at least an order of magnitude less sensitive than the piezoelectric transducers, for example, in the optical interferometer the minimum detectable displacement is given by the following expression:

$$S_{min} = \frac{\lambda}{4\pi\ V_{max}} \times \text{noise} \qquad (2.23)$$

where λ is the laser wavelength and V_{max} is the maximum voltage measured by the detector. For λ = 632nm, V_{max} = 1.7 volt and for a noise level of 0.5 mV the minimum displacement is

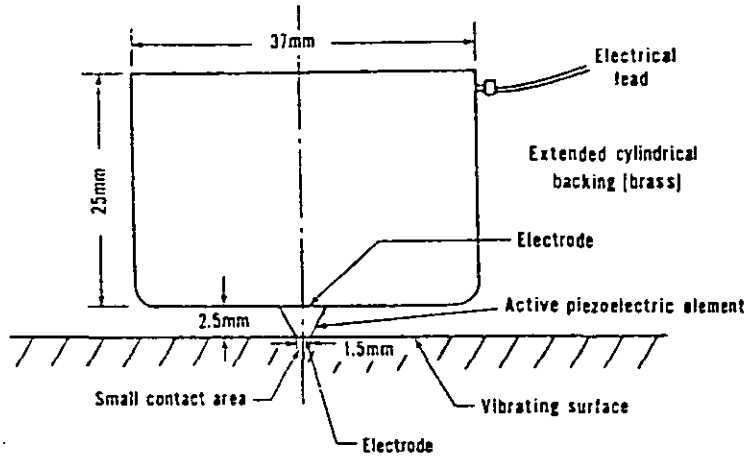

(a)

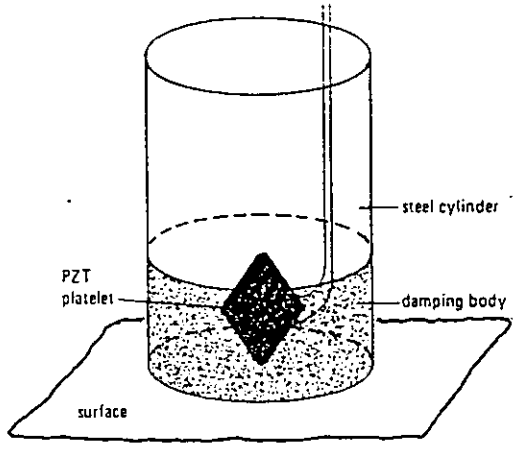

(b)

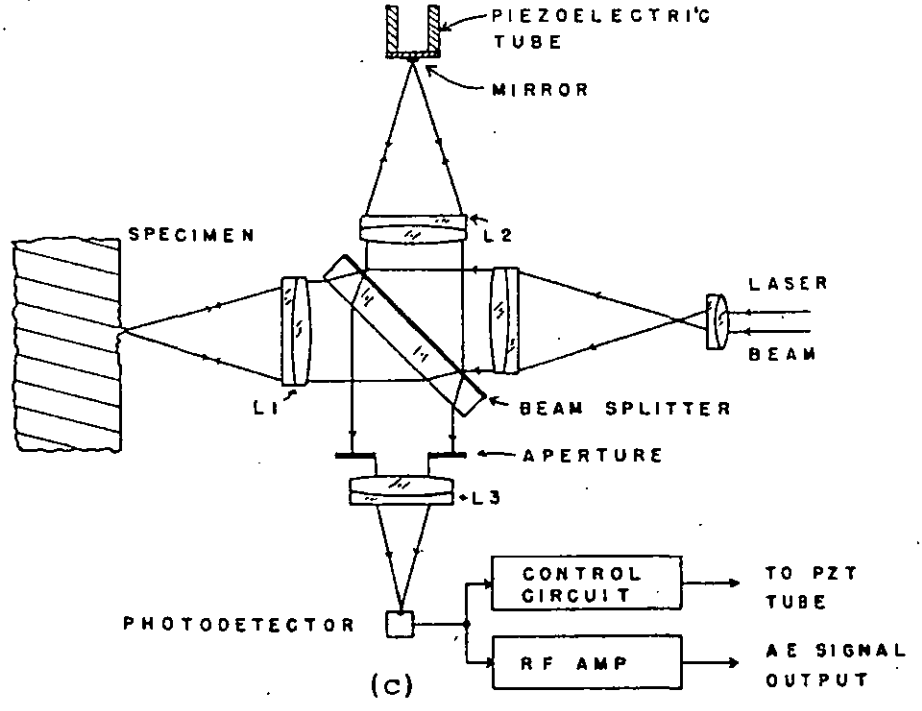

(c)

Figure 2.8: a) The conical transducer,

b) Niewish transducer, and

c) is the optical transducer.

$$S_{min} = 14.7 \text{ pm} .$$

This minimum displacement is to be compared with the minimum detectable displacement of 2.5 pm for the conical piezoelectric transducer.

2 - The interferometric paths must be stabilized in order to ensure high sensitivity all the time, this requires the use of complicated electronics.

3 - They are relatively bulky and expensive compared to piezoelectric devices.

4 - Optical transducers are normally only sensitive to vertical displacements.

2.10 THE DESIGN OF TRANSDUCERS USED FOR LASER INDUCED DAMAGE DETECTION.

Transducers discussed in section 2.9 are not simple and they are not suitable for studying the acoustic impulse which may be associated with the onset of damage in optical components. The laser interferometer would seem to offer the best technique in terms of non-contacting and consequently could probe a test surface during laser impact but it is the least sensitive of all the transducers. Optical techniques are the subject of Chapter four and further references will be made there.

The capacitive probe, on the other hand, does not lend itself to the application of small optical components

and furthermore requires that the test sample to be metallic or have a conducting coating to act as a plate of the capacitor; it is therefore not considered further.

Undoubtably the most widely used transducer is based on piezoelectric material, unfortunately most of the sensitivity in practical systems is associated with the resonant nature of most commercial devices and in turn these tend to be large and cumbersome to use. It was planned to try and detect damage during the time scale of the irradiating laser pulse ($\sim$ 60 ns) and so a wide bandwidth is a necessary prerequisite of the transducer coupled with the maximum sensitivity.

The conical or point contact transducer was shown to offer a wide bandwidth with the inherent sensitivity of these ceramic materials. However, the only designs available at the onset were not suitable, mainly on grounds of size and coupling methods.

Two approaches to these problems were considered:

a) The design and construction of small resonant transducer and,

b) application of point contact transducer to the detection of laser damage.

The first of these transducers is shown in Figure 2.9a and is based on that of Figure 2.7a. The heart of the transducer is a lead zirconate-lead titanate

(PZT-5A) disk that is poled axially and silvered on both ends. PZT-5A was chosen because of its low Q value which results in a reduced ringing, in spite of that, a small amount of ringing was observed but this did not constitute a major problem for the intended application in our studies. Since the aim was to miniaturise the transducer, the radius of the disk was chosen to be 2 mm while the thickness was 1 mm resulting in a fundamental resonance frequency of 2.5 MHz. This disk was then mounted in a brass casing cylinder with dimensions 30 × 10 mm to provide a shielded earth return and to minimize electrical pick-up from the laser discharge. The front diaphragm of the casing was less than 1 mm to reduce ringing. Furthermore, a thin layer of silicon grease was applied between the PZT disk and the casing to ensure good acoustical coupling. The backing of the PZT disk was a brass cylinder. The backing and the PZT were spring loaded against the diaphragm, a thin layer of silicon grease was also applied between the PZT disk and the backing. To prevent short circuiting between the backing cylinder and the brass casing, the backing cylinder was incased in PVC insulation. Since the outside surface of the brass casing was not optically polished, it was wrapped with thin aluminized film to reflect most of the stray light especially CO_2 radiation for which aluminium has a strong reflection coefficient. Finally, the signal was led through a wire

to the BNC connector.

The second transducer was a small conical transducer, Figure 2.9b, similar to that of Figure 2.8a, but, on a smaller scale. This transducer was mounted inside a stainless steel casing and was loaded against the diaphragm by using two small screws. The backing of the PZT was insulated from the casing by insulation tape.

2.11 METHODS OF TRANSDUCER CALIBRATION.

A - Calibration systems: An important consideration in selecting a transducer is its frequency response. This information is critical to determining optimum signal to noise ratios for specific applications. Historically an ultrasonic back-to-back calibration technique has often been used for transducer calibration. This method is based primarily on underwater far-field reciprocity calibration techniques[17]. The transducer to be calibrated is excited into continuous plane-wave thickness-mode vibration by a standard ultrasonic sending transducer. The output of the transducer is measured and presented as an amplitude versus frequency plot. For waves travelling transverse to the transducer base, such as in the case of surface wave, the response curve is quite different. Later, several methods were employed using helium-jet method[18], grinding powder[19], etc.. All of these methods lack rigorous theoretical

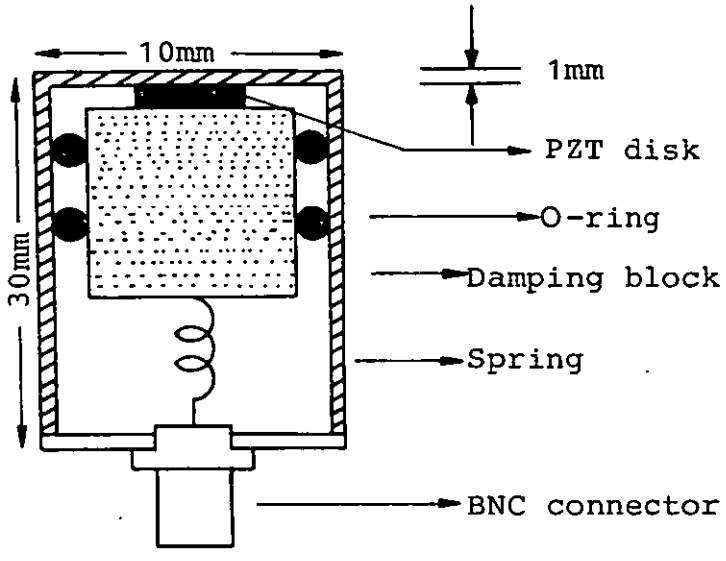

(a)

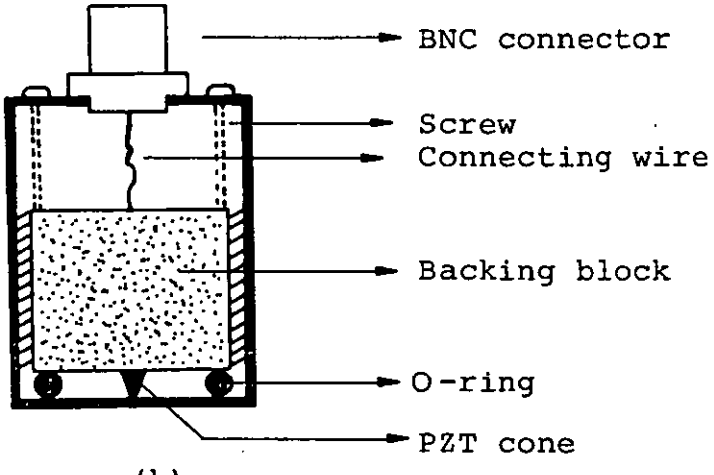

(b)

Figure 2.9: Details of the transducers developed for the detection of laser induced damage in optical materials.

backgrounds which are essential for an absolute calibration.

The most widely used method of transducer calibration is the so-called surface pulse method. The development of the basic principles of this technique was done by Breckenridge, Tschiegg and Greenspan[20]. This calibration technique functions in the following way: A step-function force event is generated on the plane surface of a large elastic block by the sudden release of a nearly static force applied by breaking a standard source. The resulting dynamic displacements of all points on this surface can be expressed by the elastic theory up until the arrival time of reflections from other boundaries of the block. The normal component of the displacement is measured using a standard transducer, i.e., capacitive or interferometric transducer. Figures 2.10 and 2.11 show the theoretically calculated displacement and the average of 10 measured displacement waveforms using a capacitive transducer. To perform the calibration, the standard transducer and the transducer to be calibrated are placed at the plane surface of the block equally distant from the source. The transient electrical outputs of both the standard transducer and the unknown transducer are recorded digitally and then computer processed to extract the response of the unknown transducer.

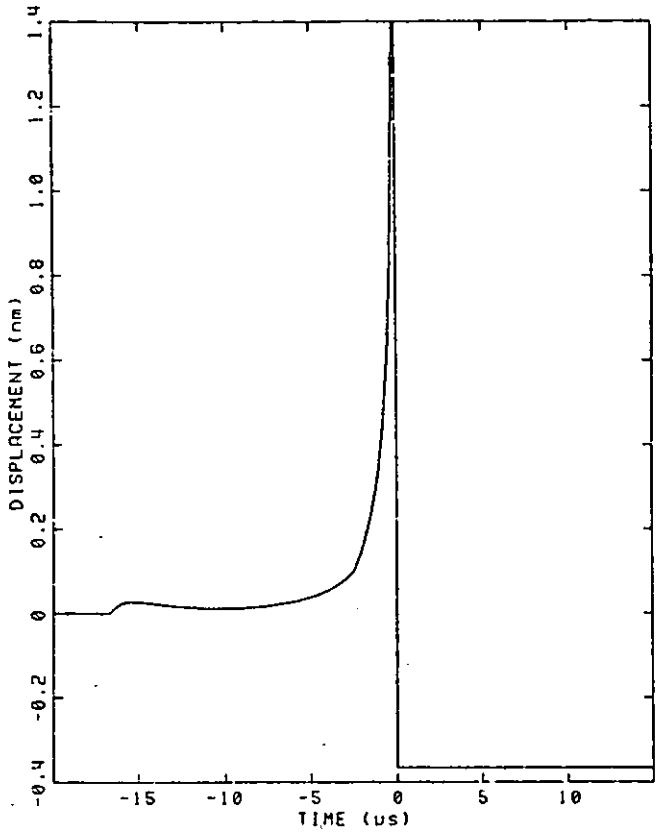

Figure 2.10: Calculated surface pulse wave form for steel block at the location of the transducer (101nm from the source)(after ref.20).

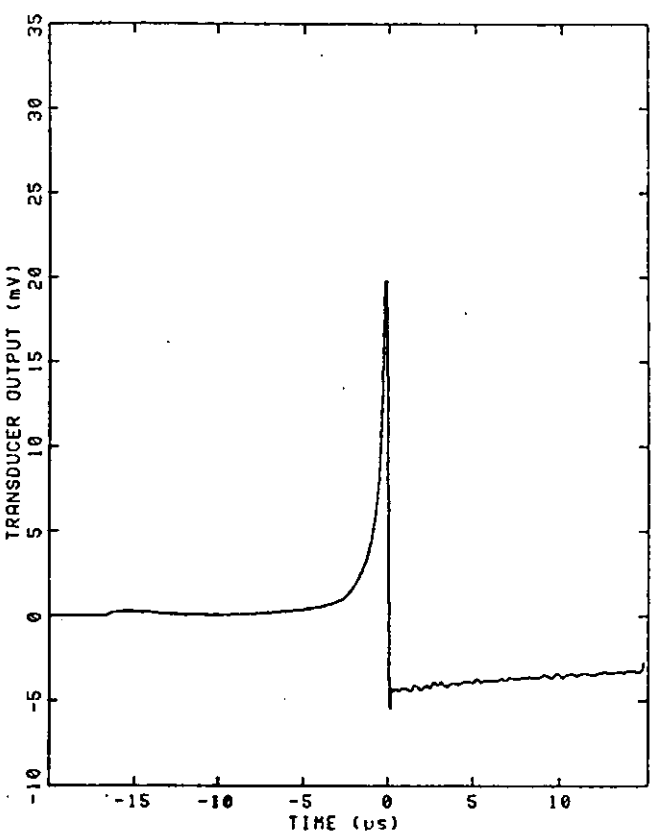

Figure 2.11: Experimental surface pulse waveform obtained by averaging 10 waveforms from a capacitive transducer (after ref.20).

B - The source: An ideal source for use in calibrating acoustic emission transducers is a surface wave of delta function time history. Several methods have been tried and evaluated to generate a suitable source. Mechanisms such as ball bearing impact on a solid, an electric spark, a piezoelectric pulsar, etc., all have resulted in some success. However, they are far from ideal because of the non-delta type surface waves generated. The first simulated acoustic emission reported by Breckenridge, Tschiegg and Greenspan[20] is based on squeezing glass capillary ($\sim$ 0.2 mm diameter) between the top of a loading screw and the upper face of a large elastic block. When the capillary breaks, the sudden release of force is a step function whose risetime is of the order of 0.1 μs. Hsu[21] has extended the approach with a technique based on the breaking of a pencil lead shown in Figure 2.12, this is a self-contained push-buttom type mechanical pencil with high quality pencil leads. The process of lead breaking is initiated by pressing the bottom of the pencil repeatedly until a bit of lead protrudes. The end of the lead is then levelled with the end of the guide tube of the pencil by pressing the tip of the pencil perpendicularly towards the test block while the bottom is pressed down. Then the button of the pencil is pressed 6 times causing the lead to protrude 3 mm. The pencil is guided obliquely towards the test block surface until the guide

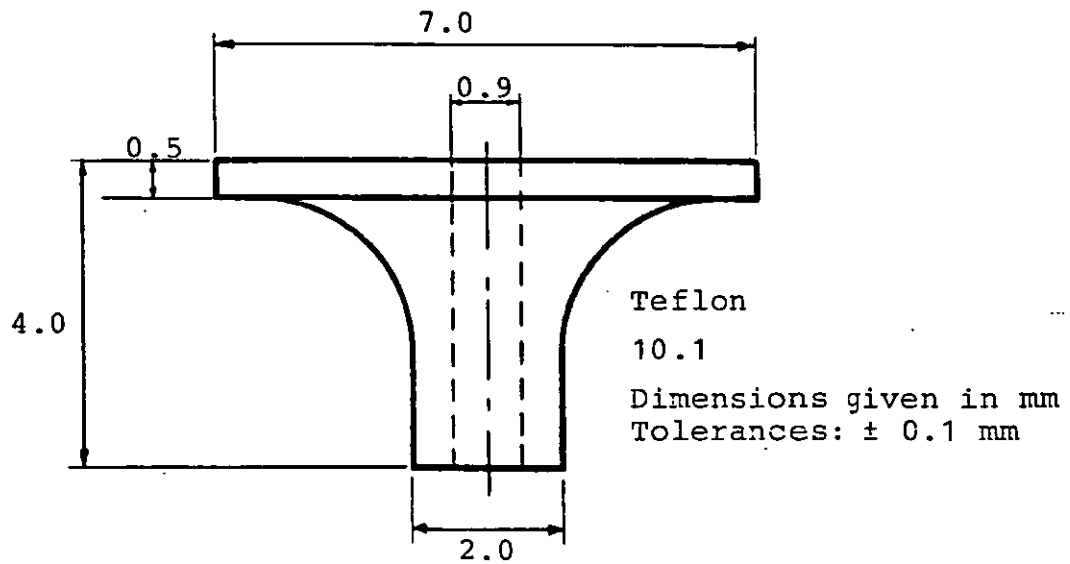

GUIDE RING

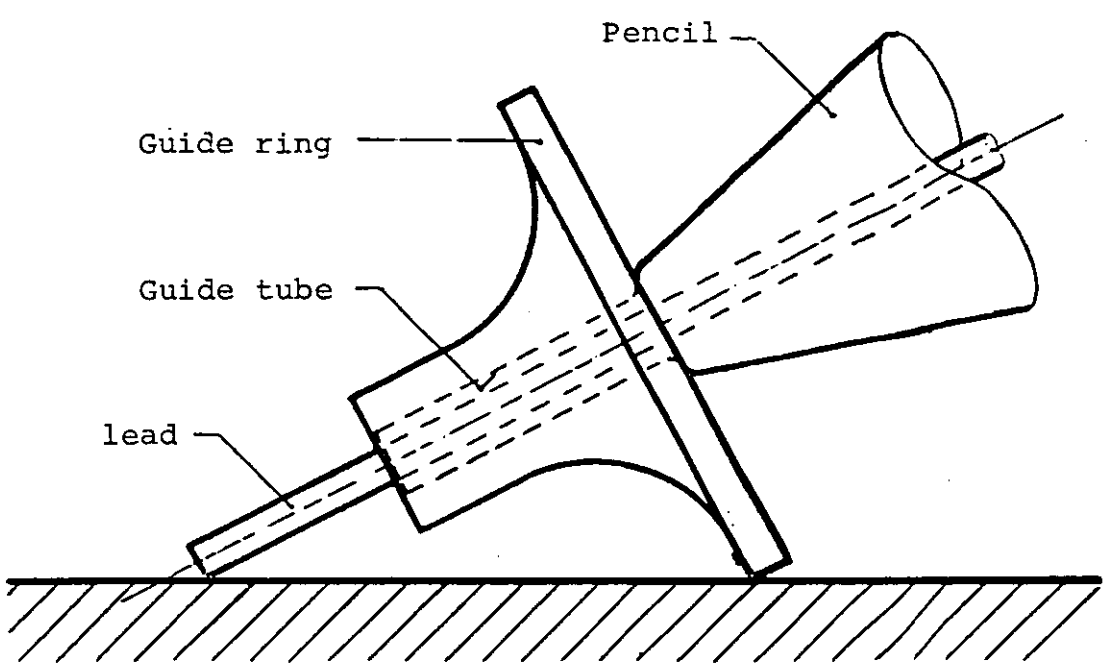

Figure 2.12: PENCIL LEAD acoustic emission source (after ref.22).

ring is resting on the surface. The pencil is then turned around the point of contact towards a steeper position; the lead will inevitably break by this movement thereby generating a step function force unloading on the test block. The magnitude of the force can be selected by the choice of pencil lead. This simple technique has become the standard method throughout the world for calibrating transducers.

More recently[23] a Nd.YAG laser has been used to produce predictable, repetative thermoelastic dipole sources to generate elastic waves but this technique is expensive and hazardous compared to the portability, simplicity and low cost of pencil lead.

2.12 CALIBRATION OF THE TRANSDUCERS USED FOR LASER INDUCED DAMAGE.

The two transducers used for laser induced damage detection were calibrated using the optical interferometer as a standard transducer and the pencil lead breaking was used as a standard source of acoustic emission. The calibration proceeded according to the block diagram shown in Figure 2.13. The response of the optical transducer and the response of the transducer to be calibrated for the pencil lead break were recorded by a fast transient recorder (Gould biomation model 4500 digital oscilloscope). The two waveforms then transferred to a computer by IEEE488 or GPIB where a fast Fourier

transform (FFT) was carried out on these waveforms in order to find their frequency contents. Since the optical transducer is inherently calibrated against the wavelength of the light used, therefore by dividing the frequency response of the optical transducer by the frequency response of the unknown transducer, we get the frequency response of the transducer in terms of displacement and voltage, i.e. $nm.V^{-1}$. Figure 2.14a shows the response of the optical transducer to the pencil lead break while Figure 2.14a and b gives the response of the first and second transducer to the same event. The frequency response of the optical transducer and that of the first and second transducer are shown in Figure 2.15a, b and c. The constant on the y-axis in Figure 2.15a is due to the mathematics involved in the Fourier transformation.

The frequency response of these transducers compare well with that of the optical transducer. The sensitivity of the first and second transducer is calculated to be 3.2 pm and 8.6 pm respectively for a noise level of 1 mV.

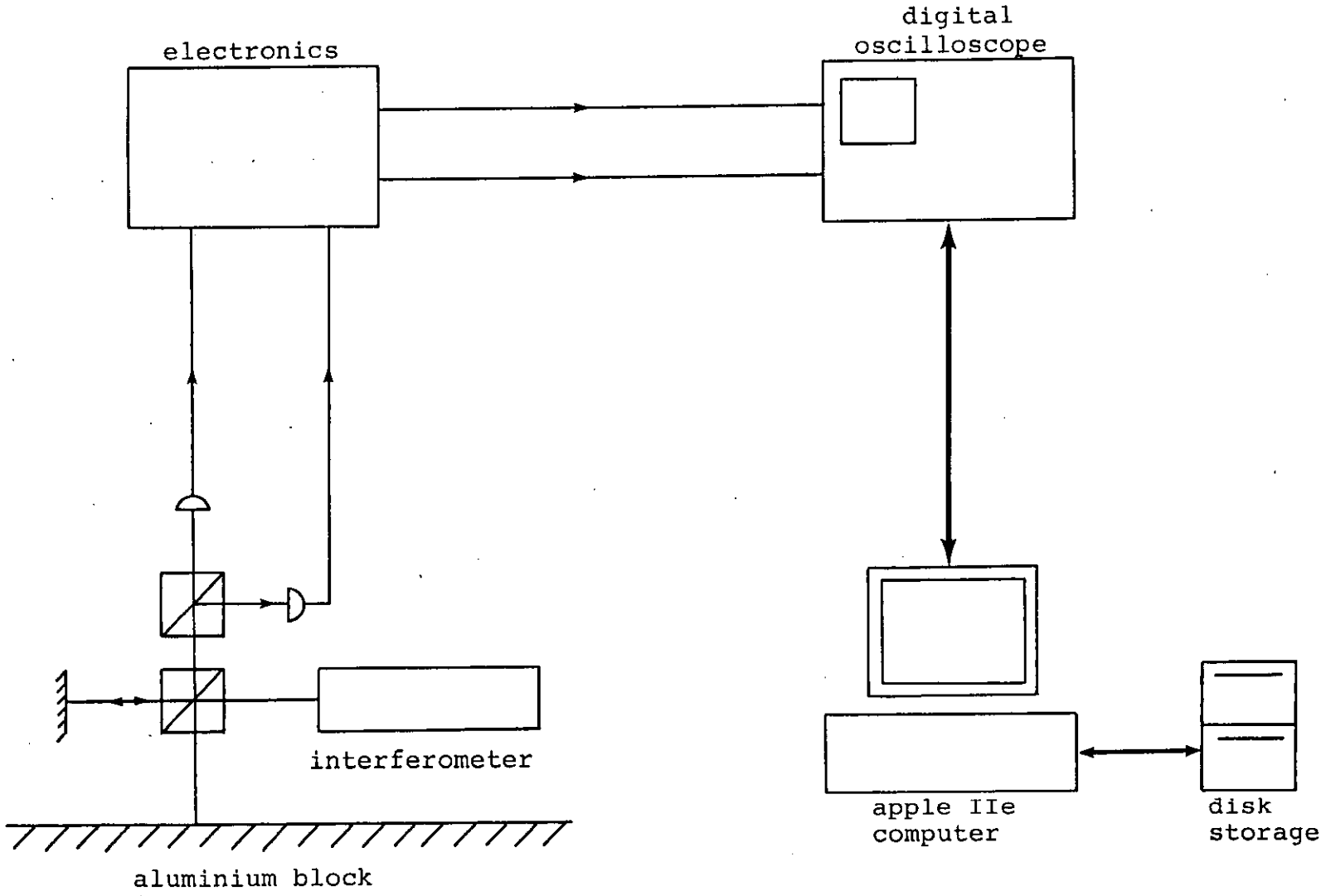

Figure 2.13: System used for the calibration of transducers used in laser induced damage studies.

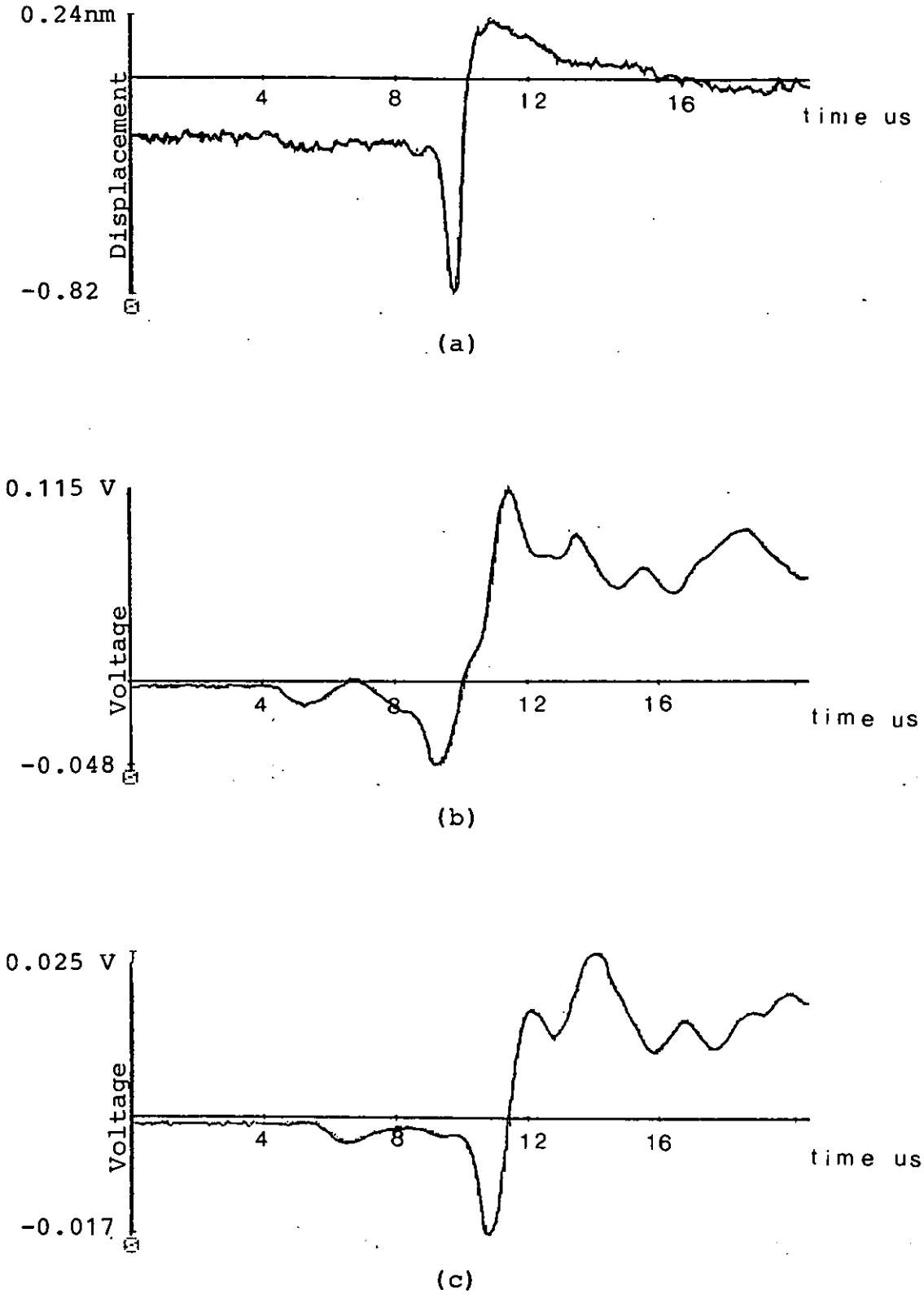

Figure 2.14: a) The response of optical transducer to pencil lead break.
b) and c) The response of first and second transducer to the same event.

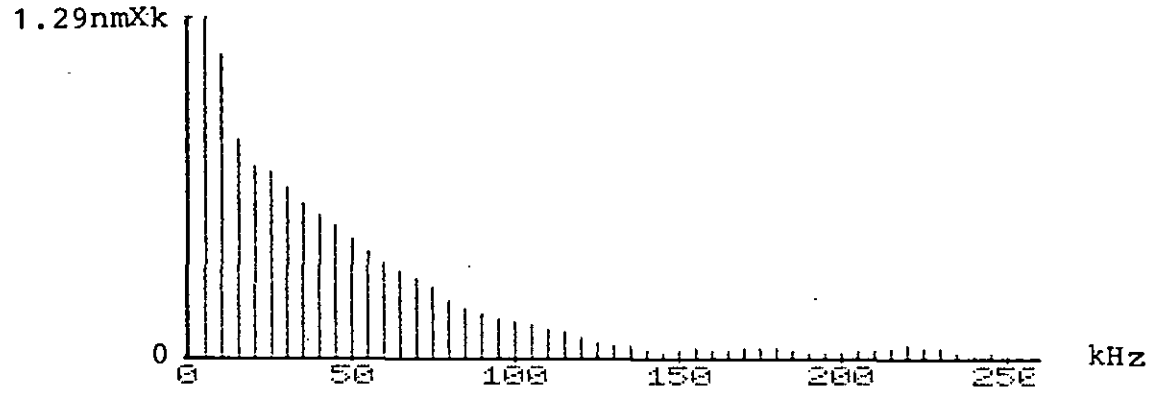

(a)

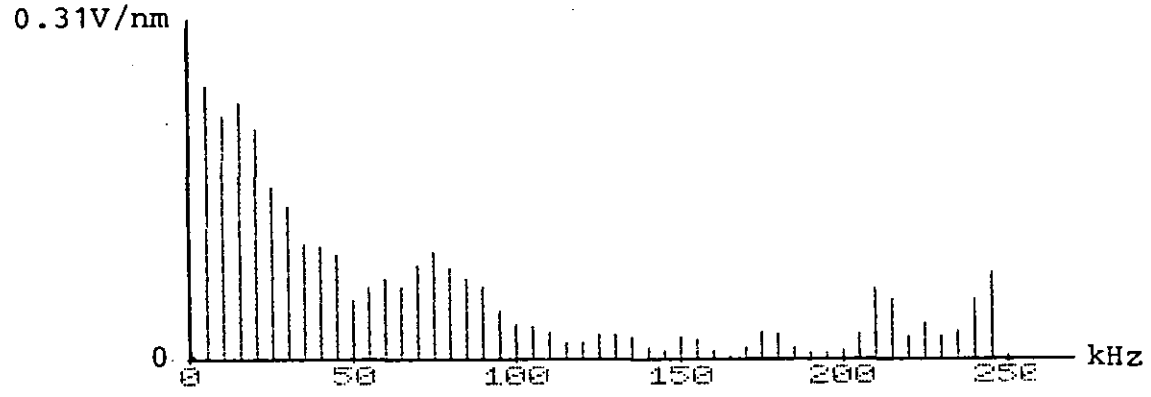

(b)

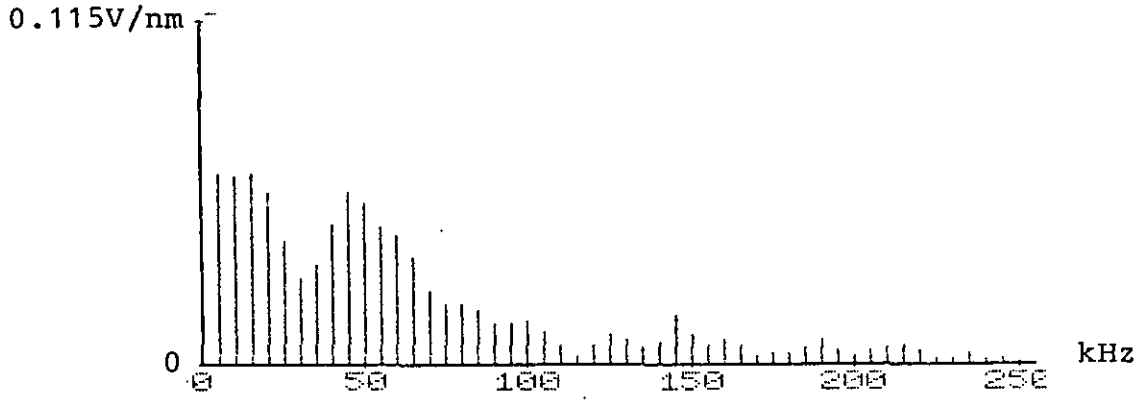

(c)

Figure 2.15: a) The frequency response of the optical transducer.

b) and c) The frequency response of the first and second transducer.

CHAPTER THREE

Photoacoustic Detection of Laser Induced Damage in Optical Materials

3.1 INTRODUCTION.

The photoacoustic effect, is the production of an acoustic signal when a sample of matter is exposed to a beam of intensity modulated radiation or a transient heating. The concept on which the photoacoustic effect is based is quite old and the analogous effect commonly referred to as the optoacoustic effect has been used for many years in the study of optical absorption phenomena in gases. The change of name from optoacoustic to photoacoustic has been instituted to reduce confusion with the acoustooptic effect in which light interacts with acoustic or elastic waves in solids.

The photoacoustic effect was discovered in the nineteenth century and was first reported in 1881 by Alexander Graham Bell[1]. After the initial flurry of interest generated by Bell's original work, experimentation with the photoacoustic effect apparently ceased. The effect was obviously considered as being no more than an interesting curiosity of no great scientific or practical value. Furthermore, the experiments were difficult to perform since they required the investigator's ear to be the signal detector. The photoacoustic effect was forgotten for nearly 50 years, until the advent of the microphone, since then a progressive improvement and development has occurred. It should be mentioned, however, that the strong rebirth of the photoacoustic effect was limited to studies in gases only; it was not until 20

years ago that the photoacoustic was applied to non-gaseous matter. The advent of the laser provided a major impetus to the photoacoustic effect with applications especially in spectroscopy.

In the following sections the physical principles of the photoacoustic effect will be explained briefly before some of the important applications are reviewed.

3.2 THE PHYSICAL PRINCIPLES OF THE PHOTOACOUSTIC EFFECT.

The photoacoustic effect arises when an intensity-modulated light or some other form of electromagnetic radiation, impinges on a sample surface, the sample will absorb some of the incident energy, this absorbed energy is (α E), where α is the absorption coefficient and E is the incident energy on the sample surface. Energy levels within the sample medium are excited and when the energy is subsequently released it is through non-radiative or heat-producing processes. Thus the absorption of electromagnetic radiation at any point on the sample surface will give rise to a localized heating of the sample.

When localized heating occurs in a material, the heat energy will be transferred to the surrounding matter through two mechanisms. Firstly, there is a transfer by means of heat conduction and diffusion. The rate of energy transfer is determined by the material thermal diffusivity, $\alpha = \frac{K}{\rho C}$, where K is the thermal conductivity,

ρ is the density and C is the specific heat. When the heating is periodic, at a frequency f, the distance over which the periodic heat will transfer to the surrounding medium is given by the thermal diffusion length $\ell_{th} = \left(\frac{2\alpha}{f}\right)^{\frac{1}{2}}$. Energy transfer through thermal diffusion is a dissipative process in which the individual atoms or molecules within the material are vibrationally excited. This energy transfer is referred to as the thermoacoustic mode.

The second mechanism for energy transfer is by means of coupling of the heat energy to the vibrational modes of the material itself, that is, through the coupling to the sample's acoustic phonons. This is a thermoelastic process which is generally nondissipative. The rate of this energy transfer depends on the speed of sound in the material and the distance over which the energy can be transferred is limited by the dimensions of the sample except at very high frequencies where ultrasonic attenuation is appreciable. In this second mode of energy transfer, there are two regimes:

If the electromagnetic energy is absorbed relatively slowly a thin layer of the surface will expand in such a way that the adjacent layers of the material can relax and an acoustic wave is generated. If, however, the energy is deposited very rapidly as it would be the case for a short high power laser pulse, the heated material will again expand and exert a force on adjacent

material which leads to a particular form of acoustic impulse known as a shock wave. There is no sharp boundary between the two regimes, both being thermo-elastic in origin.

The first analysis of how the acoustic waves are generated by a laser pulse was described by White[2]; he considered in detail the way in which the temperature of a solid changes, both as a function of time and depth in the material from the surface. Ready[3] carried out a study along a similar line, with later work indicating the type of acoustic pulse likely to be developed from temperature gradients within the irradiated solid[4]. Experiments on laser induced acoustic waves in both solids and liquids have been reported. In liquids these experiments were carried out by Askaryan et. al[5], Bell and Landt[6], Emmony[7], Sigrist and Kneubühl[8], Sladky[9] and many other authors.

In solids, investigations have tended to use high power laser pulses[10,11,12,13]. These have included experiments to study the effect of constraining layers on the surface of a solid[14], when enhancement over a generation of ultrasound at a free surface, is observed. Enhancements have been produced by the application of coatings to solid surfaces. O'Keefe and Skeen[15] have used coatings of transparent relatively volatile materials to produce an order of magnitude increase in the acoustic wave over bare targets. It has also been shown

by Fox[16] that a thin coat of a black paint or drops of distilled water can produce results comparable with constraining techniques. Studies on free surfaces have been conducted mostly with Q-switched lasers producing light pulse duration in the range 10-50ns. Since solid surfaces are capable of supporting transverse vibrations in addition to the longitudinal vibrations, three types of acoustic waves are therefore expected, shear, longitudinal and surface waves. All of these waves have been produced by a pulsed laser[17] although most of the work has concentrated on the production of longitudinal pulses with applications of the technique to the non-destructive testing[18,19,20,21,22,23].

3.3 SOME ASPECTS OF LASER-SOLID INTERACTION.

When a laser pulse is incident normally on a solid surface some of the incident energy is absorbed. As mentioned earlier the fraction of the energy ΔE absorbed depends on the laser energy E and the absorption coefficient α, i.e.

$$\Delta E = (1-R)E \quad . \tag{3.1}$$

Where R is the reflectivity of the surface, the rest of the laser energy will be reflected. The screening by conduction electrons is such that most of the absorption and reflection takes place very close to the surface within what is called the "skin depth" and

generally denoted by δ. At long wavelengths in the infrared the skin depth is given by the following expression[24]:

$$\delta^2 = \frac{1}{\pi\sigma\mu\mu_o f} \tag{3.2}$$

where σ is the electrical conductivity and μ is the permeability of the solid, μ_o is the permeability of the free space and f is the frequency of the incident laser radiation. The skin depth is dependent on the wavelength of the light used, for example, for aluminium at 10.6 μm δ = 9.2 nm while at the KrF excimer laser wavelength (λ = 248 nm), δ = 6.73 nm.

The reflection coefficient of a solid surface is given by the following equation[24]:

$$R = \left| \frac{Z_2 - Z_1}{Z_2 + Z_1} \right|^2 \tag{3.3}$$

where Z_1 is the electrical impedance of free space and Z_2 is the electrical impedance of the solid. For a good conductor $Z_2 = (1+j)/\sigma\delta$ while for free space $Z_1 = \mu_o c$, where c is the velocity of light. Thus the reflection coefficient can be expressed by the following equation:

$$R = \left| \frac{(1+j) - \mu_o \sigma c\delta}{(1+j) + \mu_o \sigma c\delta} \right|^2 \tag{3.4}$$

where the complex value shows that there is a phase

change even at normal incidence. If we write t for the quantity $\mu_o \sigma c \delta$ equation (3.4) becomes:

$$R = \frac{2 + t^2 - 2t}{2 + t^2 + 2t} . \qquad (3.5)$$

For metal, where $\sigma \cong 10^7$ ohm^{-1}.m^{-1}, $t \cong 4 \times 10^9 \delta$, therefore t is much greater than unity at all frequencies up to that of visible light. Hence equation (3.5) can be approximated and becomes:

$$R = 1 - \frac{4}{t} = 1 - 2.1 \times 10^{-5} (\mu f/\sigma)^{\frac{1}{2}} . \qquad (3.6)$$

This formula shows that metals should be almost perfect reflectors of electromagnetic radiation for all frequencies up to those of visible light. Upon substituting equation (3.6) into equation (3.1) we get the following expression for the absorbed energy:

$$\Delta E = \frac{4E}{\mu_o \sigma c \delta} = (1-R)E \qquad (3.7)$$

$$\therefore \quad \alpha = \frac{4}{\mu_o \sigma c \delta} . \qquad (3.8)$$

The absorption coefficient calculated by the above expression may be higher than the experimentally determined values since the reflectivity may be reduced by surface roughness, contamination or surface oxidization.

If the laser pulse is very short in duration, it will act as a transient heat source at the solid surface

and the absorption of energy will occur very rapidly in such a way that the heat generated will not have a chance of being transferred to the bulk of material, therefore, the deposition of energy will be confined to a very small volume determined by the surface area A and the skin depth δ. The absorbed energy causes a rise in the temperature, ΔT given by:

$$\Delta T = \frac{\Delta E}{C\rho A\delta} \tag{3.9}$$

where C is the specific heat and ρ is the density. Substituting for ΔE we get:

$$\Delta T = \frac{4}{\mu_o C\rho\sigma c\delta^2}\left(\frac{E}{A}\right) \quad . \tag{3.10}$$

The rise in temperature is, as might be expected, directly proportional to the incident energy density. Although the incident energy density might not be uniform, the common assumption from the point of an acoustic wave generation view is that the energy distribution is unform. The rise in temperature is naturally accompanied by an equally rapid thermal expansion and if a volume V is involved in this process, it will expand to a new volume $V + \Delta V$ where

$$\frac{\Delta V}{V} = 3\beta T \tag{3.11}$$

where β is the coefficient of linear thermal expansion of the material. Thermal expansion of the surface

element leads to horizontal and vertical stresses in the solid. The vertical stress relaxes to near zero very fast via a small outward displacement of the free surface, the magnitude of the displacement may be $\sim$1 μm or less. This displacement, although small, has been used to deflect an optical probe beam and is made use of in photodisplacement spectroscopy of solids[25]. On the other hand, since displacement in direction parallel to the free surface is inhibited by the inertia of the surrounding material, very large compressive stresses can be induced in these directions. They will exceed the elastic limit of the solid if the temperature rise and the coefficient of thermal expansion are large enough. In this situation the solid suffers plastic compressive deformation. This is a permanent strain that will remain even after the solid has cooled down to the intinal ambient temperature.

So far it has been assumed that the heat energy is distributed only in the interaction region. In practice, however, the generated heat will immediately start to diffuse into the surrounding solid, the diffusion process can lead to the distribution of the absorbed energy over a volume large compared with the interaction volume, that is to a depth greater than the skin depth. This problem has been treated by Carslaw and Jaegar[26]. They showed that for a surface source constant in time for which the temporal variation of the

pulse is given by:

$$P(t) = \begin{cases} P_o , & t > 0 \\ 0 , & t < 0 \end{cases}$$

then the variation of temperature with depth is given by:

$$T(z,t) = \left(\frac{2\alpha P_o}{K}\right) (kt)^{\frac{1}{2}} \text{ ierfc}\left[z/2(kt)^{\frac{1}{2}}\right] \qquad (3.12)$$

where K is the thermal conductivity, k is the thermal diffusivity, α is the absorption coefficient, P is the laser pulse power density,

$$\text{ierfc } x = \int_x^\infty \text{erf } s\,ds \quad \text{and} \quad \text{erfc } x = (2/\pi)^{\frac{1}{2}} \int_x^\infty e^{-s^2} ds. \qquad (3.13)$$

The surface temperature T(0,t) is seen to be proportional to $t^{\frac{1}{2}}$:

$$T(0,t) = \left(\frac{2\alpha P}{K}\right)\left[\frac{kt}{\pi}\right]^{\frac{1}{2}} . \qquad (3.14)$$

We see that there is no limiting surface temperature; if the laser power were maintained indefinitely at P, $T(0,\infty) \longrightarrow \infty$.

If the radiation is applied in the form of a pulse

$$P(t) = \begin{cases} P_o , & 0 < t < \tau \\ 0 , & t < 0,\ t > \tau \end{cases}$$

then T(z,t) is as given by equation (3.12) while the pulse is applied, but the temperature subsequently varies as:

$$T(z,t)_{t>\tau} = \frac{2P_o k^{\frac{1}{2}}}{K} \left\{ t^{\frac{1}{2}} \text{ iertc } \frac{z}{2(kt)^{\frac{1}{2}}} - (t-\tau) \text{ ierfc } \frac{z}{2[k(t-\ )^{\frac{1}{2}}]} \right\} \quad (3.15)$$

The solution given by equations (3.12) and (3.15) will be approximately valid for the situation where heating proceeds only over a limited area of the free surface of a semi-infinite slab provided that the dimension of the heated area is greater than $(4kt)^{\frac{1}{2}}$.

The problem ofapulsed surface source which is variable in time has been treated by Carslaw and Jaeger[26], White[2] and Rykalin et. al[27]. The simplest solution is obtained when the source generates a series of rectangular pulses as shown in Figure 3.1a. White[2] has shown that the resulting temperature distribution can be obtained by superimposing single pulse solutions from equations (3.13) and (3.15). Figure 3.1b shows the temperature rise on the surface of a semi-infinite solid irradiated with such rectangular pulses.

The case in which the intensity distribution in the focal area can best be described by a Gaussian function has been treated by Ready[3], this is the situation in the case of a laser operating in the TEM_{oo}

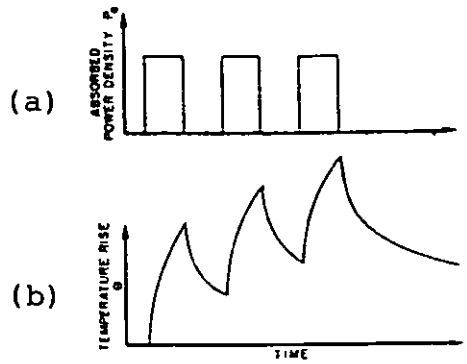

Figure 3.1: Variation of temperature with time for a semi-infinite half space on irradiation with a series of pulses (after ref.2).

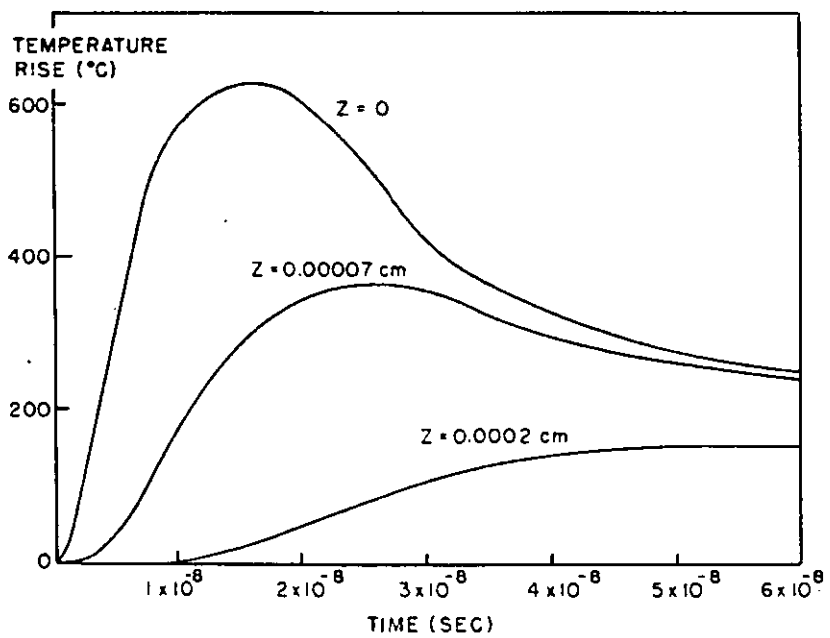

Figure 3.2: Calculated temperature rise as a function of time at the centre of laser irradiated area for an aluminium sample, stuck by an unfocussed Q-switched 30ns duration laser pulse. Depth z as a parameter (after ref.3).

mode and focussed with distortionless optics. The intensity on the surface of material can be written:

$$P(r) = P_o \exp(- r^2/\omega_o^2) \qquad (3.16)$$

where P_o is the power density at the centre of the spot and ω_o is the Gaussian beam radius. Ready[3] showed that the temperature $T(r,z,t)$ at a depth z, radial position r and after a time t is given by

$$T(r,z,t) = \frac{P_o\ \omega_o^2}{K} \left(\frac{k}{\pi}\right)^{\frac{1}{2}} \int_o^t \frac{p'(t-t')}{t^{\frac{1}{2}}(4kt' + \omega^2)} \exp\left[- \frac{z^2}{4kt'} - \frac{r^2}{4kt'+\omega^2}\right] dt' \qquad (3.17)$$

In the above equation p'(t) is the temporal profile of the laser pulse on the surface normalized to its maximum value. Ready used equation (3.17) to calculate the temperature rise as a function of time at the centre of the laser spot for an aluminium sample irradiated by a Q-switched 30ns laser pulse from the sample surface, the result of such calculation is shown in Figure 3.2 As shown the heating is very rapid with the maximum surface temperature being reached soon after the peak intensity of the laser pulse. Below the surface, the maximum temperature is delayed by the diffusion process.

3.4 APPLICATION OF THE PHOTOACOUSTIC EFFECT.

A - Spectroscopy: the photoacoustic effect has shown itself to be a very good research and analytical tool.

It has found application in physics, chemistry and biology. One of the most important applications is in the field of spectroscopy in what has come to be known as photoacoustic spectroscopy[28]. This new type of spectroscopy has been used to provide spectral information on solids and liquids which cannot be readily measured using conventional techniques of reflection and absorption spectroscopy due to nonspecular surfaces like powders and amorphous compounds. In photoacoustic spectroscopy or (PAS) as it is commonly abreviated, the sample is placed inside a specially designed closed cell containing air or other suitable gas and a sensitive microphone. The sample is then illuminated with a chopped monochromatic light. If the sample absorbs any of the energy incident on it, then some energy level in the sample will be excited. The most common mode of deexcitation is through nonradiative or heating mode, and thus the periodic optical excitation of the sample results in a periodic heating of the sample and a subsequent heat into the surrounding gas. This in turn results in a periodic pressure oscillation within the cell, which is detected by the microphone as an acoustic signal. A photoacoustic spectrum is obtained by recording the microphone signal as a function of wavelength of light incident on the sample. The strength of the acoustic signal is porportional to the amount of light absorbed by the sample, and thus, there is a close

correspondence between a photoacoustic spectrum and a conventional optical absorption spectrum. Furthermore, since only absorbed light can produce an acoustic signal, scattered light, which often presents serious problems in conventional spectroscopy, presents no serious problems in PAS although scattering of the exciting radiation can give rise to signals due to absorption on the wall of the cell, these can be avoided by phase sensitive detection techniques making use of time delay between the scattered light and the signal.

When the solid is placed inside a cell as described above, the technique is usually referred to as solid gas microphone (SGM). When the solid is immersed in a liquid, the technique becomes more sensitive than the (SGM) and referred to as solid liquid microphone (SLM). However, both arrangements are not quite sensitive because of the coupling medium between the solid and microphone. It has been found that the poor coupling between the solid-gas/liquid- and microphone can be overcome by attaching a piezoelectric transducer directly to the solid and therefore increase the sensitivity appreciably[29].

Using photoacoustic microscopy, absorption coefficients as low as 10^{-8}-10^{-9} cm^{-1} are now routinely measured for gases[30]; in liquids, absorption as low as 2×10^{-5} cm^{-1} has been measured[31], while in solids the lowest absorption

measured was 10^{-5} cm^{-1} [32].

In addition to its sensitivity, photoacoustic spectroscopy is easier to perform and quicker than laser calorimetry or other forms of conventional spectroscopy particularly for low levels of absorption.

B - Production of short acoustic pulses in solids:
Low energy short duration laser pulses imply high power and laser energies of $\lesssim$ 1mJ and pulse duration of 10 ns have been used to generate extremely short duration acoustic pulses in solids[33]. These short pulses are useful for accurate measurement of the velocity of longitudinal, shear and surface waves. Furthermore the observed photoacoustic signal provides a means of substrate defect detection (ultrasonic imaging) deep inside the solids because ultrasonic waves are attenuated less than thermal waves.

The production of acoustic waves in solid can be divided into two power density regimes. At low power densities less than the plasma threshold ignition, the generation of the acoustic waves is thermoelastic. In this regime the resultant acoustic pulse is proportional to the incident laser energy but independent of the energy density[34]. The theoretical treatment of such a process is given by Dewhurst et. al[34]. Figure 3.3a shows the acoustic waveform detected by a capacitive transducer at the rear of 25 mm thick aluminium sample

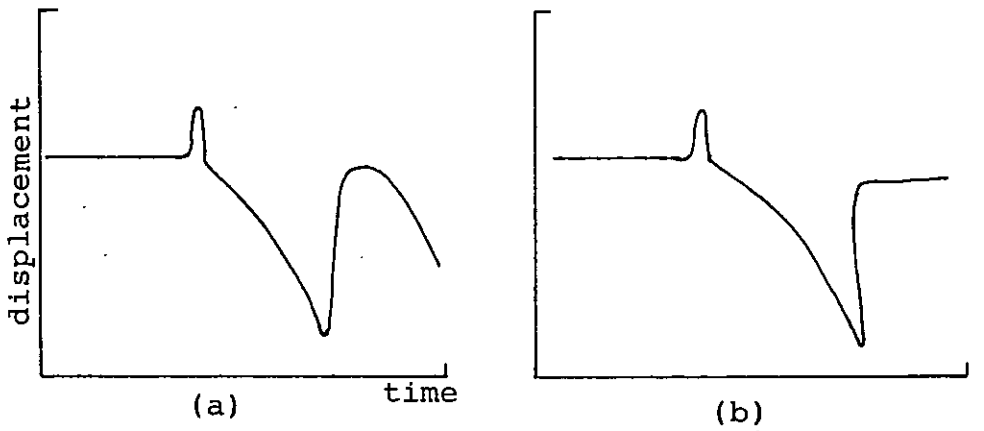

Figure 3.3: a) Experimental waveform measured by a capacitive transducer,
b) The theoretical waveform (after ref.34).

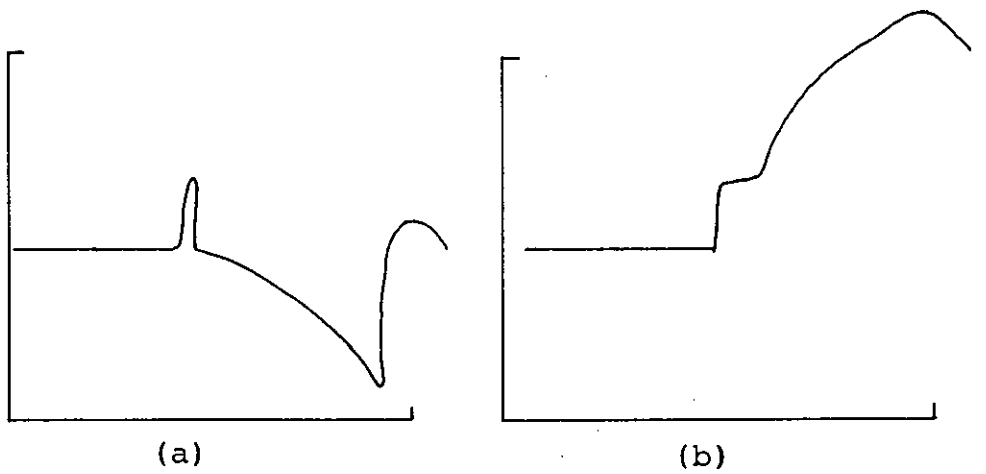

Figure 3.4: a) The waveform for low density plasma,
b) is the waveform for high density plasma (after ref.34).

irradiated with 35 mJ laser pulse from a Q-switched Nd:YAG laser. This signal agrees quite well with the theoretical pulse shape shown in Figure 3.3b.

The second regime is achieved when the power density on the surface of material is increased until plasma is formed on the surface. The generation mechanism in this regime is essentially a recoil process or momentum transfer[34] and the generated acoustic pulse changes in shape and amplitude, both being dependent on the laser power density. Figure 3.4a shows the generated waveform on the same aluminium sample for a low density plasma formed on the surface while Figure 3.4b represents the waveform for a high density plasma. At low plasma densities the waveform consists of a longtitudinal wave with some thermoelastic effect still remaining, at high plasma densities the generation mechanism is completely dominated by the momentum transfer.

C - Photoacoustic measurement of ultrashort laser pulse temporal profiles: Temporal profile in the nanosecond range can be measured either by streak camera or fast photodiodes[35]. For picosecond and femtosecond laser pulses another method which depends on the optical delay line is normally used[36]. In this case the laser pulse is divided by a beam splitter and the two replica pulses travel different path lengths, then the two pulses with a variable time delay travel collinearly

through a nonlinear KDP crystal. By measuring the autocorrelation function as a function of the time delay, the temporal profile of the laser pulse can be obtained. This technique requires special complex instrumentation and is not easy to perform. The photoacoustic effect has been used for this kind of measurement[37]. In the photoacoustic technique the laser pulse is again divided in two and a variable time delay is imposed on one of the pulses. The two pulses are then recombined in a nonlinearly absorbing crystal such as KDP located at one focus of a truncated fused quartz ellipse as shown in Figure 3.5. A transducer located at the other focus of the ellipse will measure

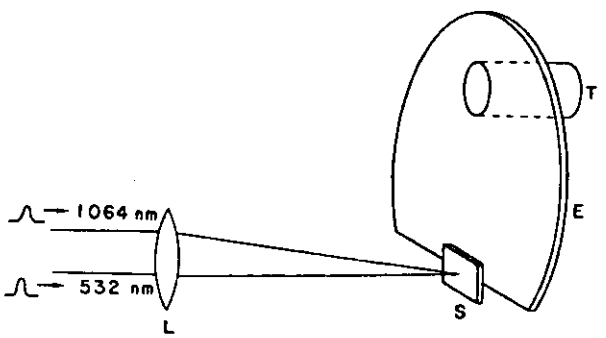

Figure 3.5: Experimental set-up for measuring ultrashort laser pulses, E is truncated fused quartz, T is a transducer and S is nonlinear crystal (after ref.35).

the acoustic pulse generated in the crystal and provide the necessary correlation function to obtain the laser pulse profile.

D - Application in chemistry: The photoacoustic effect has found important applications in chemistry, one of these is an experiment performed with thin layer chromotography (TLC)[38]. TLC is widely used and a highly effective technique for the separation of mixtures into their constituent components. This technique is of considerable importance in the chemical, biological and medical fields. However, the identification of the TLC-separated compounds directly on the TLC plate can be fairly difficult procedure. Conventional spectroscopic techniques are unsuitable because of the optical properties of the silica gel on the TLC plate. Photo-acoustic spectroscopy offers a simple and very sensitive means for performing non-destructive compound identification directly on the TLC plate. Figure 3.6a shows the PAS spectra taken on five different compounds that were separated and developed on TLC plates. These PAS spectra were taken directly on the plates themselves and were run in the ultraviolet region of 200-400 nm. The five compounds starting from the top of Figure 3.6a are p-nitroaniline, benzylidene acetone, salicylaldehyde, 1-tetralone and fluorenone. Figure 3.6b shows, for the sake of comparison the published UV absorption spectra

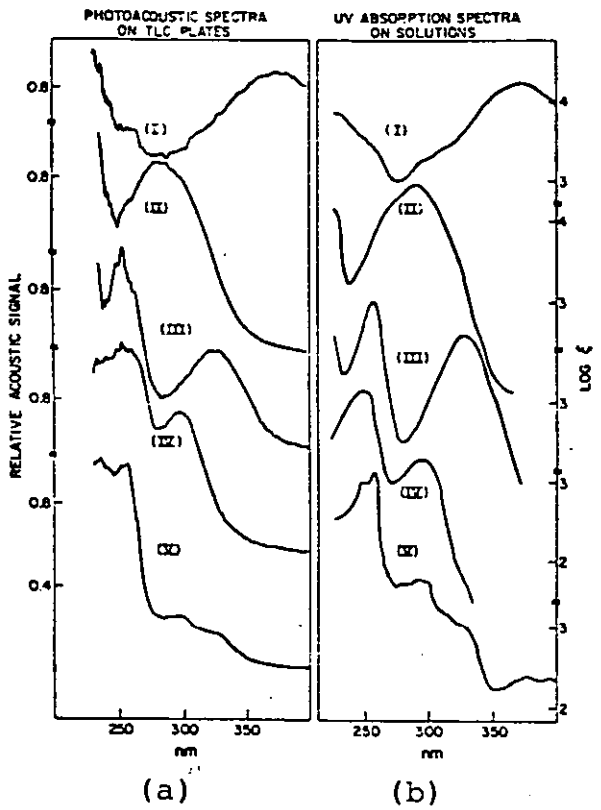

Figure 3.6: A photoacoustic study on thin-layer chromotography. In a) are shown the UV PAS spectra of five compounds, p-nitroanaline (I), benzylidene-acetone (ii), salicylaldehyde (III), 1-tetralone (IV), and fluorenone (V). These spectra were taken directly on a thin-layer chromotography plates. In b) are shown the UV absorption spectra of the same five compounds in solution (after ref.38).

of these compounds in solution. The strong similarity of the photoacoustic spectra and the optical absorption spectra permit a rapid identification of the compounds.

E - Applications in biology and medicine: In biology photoacoustic studies has been performed on materials which are often difficult if not impossible to study by any other means. An example of the use of PAS in biology is in the identification of bacterial states. Although conventional methods can be used to monitor bacterial growth on various substrates, the light scattering makes it most difficult to obtain spectroscopic data on the bacteria and thus to identify them. However, bacterial samples are quite suitable for study by PAS. The PAS spectrum of Bacillus subtilis var.niger, a common airbone bacterium, contains a strong absorption band at 410 nm[39] when this bacterium is its spore state. Thus, PAS enables the detection and discrimination of various bacterial states and allows one to monitor and detect bacteria in various stages of development.

In medicine the PAS has been used in the study of animal and human tissues both hard tissues such as teeth and bone and soft tissues such as skin and muscle[39].

F - Laser induced damage in optical materials: As the absorption of radiation is characterized by the emission of the acoustic signal, it is reasonable to assume that

when a material changes its absorption as for example in damage process then the acoustic signal would change also. Rosencwaig and Willis[40] have demonstrated the possibility of using the photoacoustic effect for monitoring laser induced damage in optical thin films. In their experiment, a pulsed Nd:glass laser, operating at nominally 1J at 1ns is used in a single shot mode to excite a transient photoacoustic signal in the sample. A piezoelectric transducer is then acoustically bounded to the rear surface of the sample and the photoacoustic signal is monitored as the energy density at the sample surface was gradually increased until damage is occurred. The damage in their experiment, was then related to the change in the photoacoustic signal when damage starts to occur. They showed that before damage the photoacoustic signal shows an essentially linear dependence on the laser energy, after damage the photoacoustic appeared to be proportional to E^n where n depends on the thin film material. The value of n was found to be in the range of 3-5 for high reflection dielectric films, while for high reflection metallic films the value of n did not differ appreciably from 1.

3.5 PHOTOACOUSTIC DETERMINATION OF LASER INDUCED DAMAGE TO METALLIC AND TRANSPARENT MATERIALS.

In this work, the application of the photoacoustic effect to damage threshold measurement has been extended

to cover metallic and transparent optical materials using sensitive piezoelectric transducers. In the following sections the experimental procedure for the determination of laser induced damage in optical materials will be explained and results will be given. In addition, the technique is shown to provide a sensitive way of studying spot-size dependence. It is also shown that the energy transfer to the sample after damage depends on the manner in which the sample is irradiated.

3.6 EXPERIMENTAL PROCEDURE.

A - The CO_2 laser:-

It is now more than twenty years since the CO_2 laser was developed. During that time the CO_2 laser has become well established as a tool in the laboratory, cutting, drilling and welding. The high efficiency and the relative simplicity of the CO_2 laser makes it a leading contender for eventual use in power-producing plants. Furthermore, the long wavelength of 10.6 μm and the gas phase active media preclude series effects from self-focussing and the resultant permanent damage. The laser used in our study is shown in Figure 3.7. The laser is a flowing gas version of the sealed system described fully elsewhere[41]. Briefly, the laser is a transversely excited atmospheric laser (TEA) in which a uniform pulsed electrical discharge is produced in the

slowly flowing gas at atmospheric pressure between two parallel Rogwski profiled electrodes. The gas is a mixture of carbon dioxide, nitrogen and helium in a ratio approximately 1:1:5. In the sealed system, additives are used to reduce the build up of CO which will otherwise react with the electrodes, material (nickel) to form $Ni(CO)_4$. The presence of nitrogen is to increase the efficiency of the energy transfer from the first vibrational level of the ground state of nitrogen to the (00°1) level of the CO_2 molecules which lies at an energy level coincident with that of the first vibrational level of the ground state of the nitrogen molecules. Helium is usually added to increase the power output. The increase is understood in terms of two effects: (1) the increased rate of de-excitation of the lower vibrational levels of the carbon dioxide molecules and (2) the increase in the rate at which carbon dioxide molecules are excited to the 00°1 level (the upper laser level).

The natural tendency to arc between the cathode and the anode is countered by the use of subsiduary discharges between trigger wires and the anode. These wires provide ultraviolet radiation of the cathode surface, so producing the diffuse photoemission of the electrons necessary for the creation of a uniform discharge at high pressures. Table 3.1 shows the typical operation conditions of this laser together with some physical dimensions of the laser.

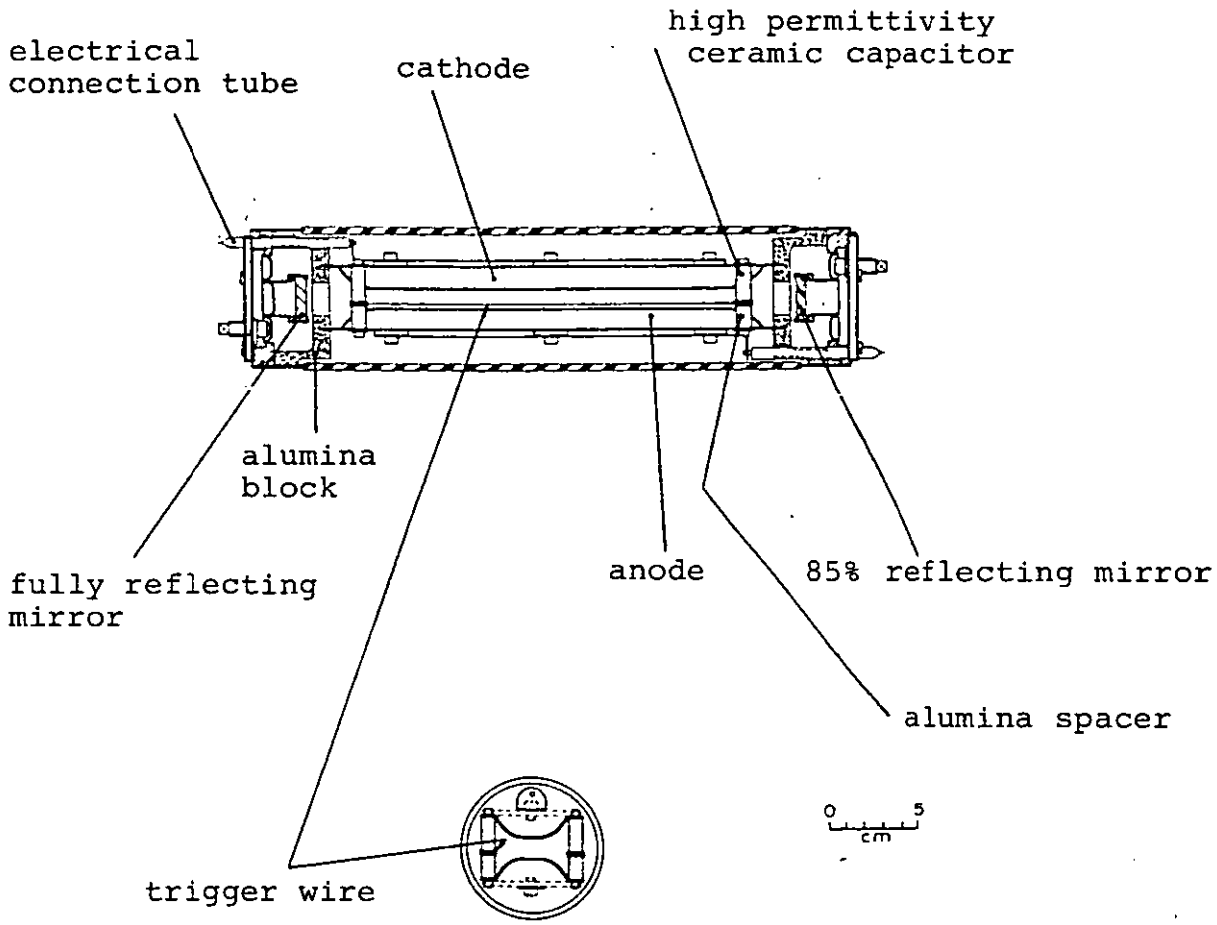

Figure 3.7: Details of the CO_2-TEA laser (after ref.41).

TABLE 3.1 : Dimensions and the typical operating conditions of the CO_2-TEA laser.

Length of the laser cavity	380 mm
Diameter of the laser	81 mm
Discharge volume	200 × 10 × 10 mm^3
Optical cavity length	281 mm
Reflectivity of the output mirror	85% (multi-layer dielectric coated flat Ge)
Main storage capacitance	12 nF
Charging voltage	20-27 KV
Input energy	2.4 - 4.4J

The laser is capable of supplying of up to 75 mJ in a pulse 60 ns (FWHM) long in the TEM_{oo}. The main operating wavelength is 10.56 μm although no longitudinal mode selections are present. The temporal profile was measured by a germanium photon drag detector, while the spatial profile of the neat beam was measured using pinhole/oscilloscope combination, the pinhole 100 μm size, was scanned across the CO_2 pulse in 200 μm steps, the spatial profile was found to be gaussian as shown in Figure 3.8 together with temporal profile of the CO_2 pube. The total energy of the pulse was measured by two

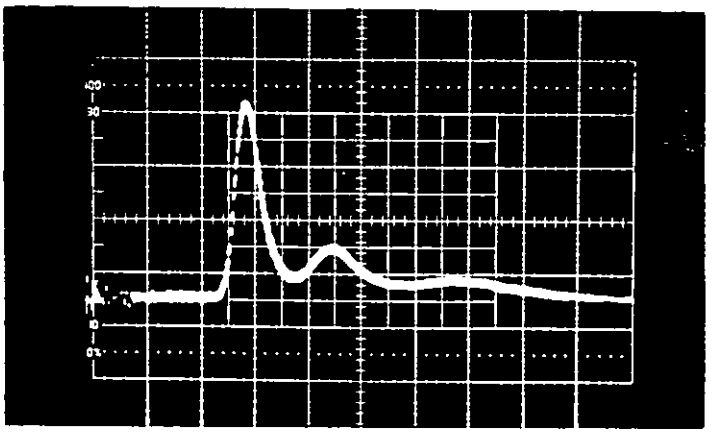

(a) 100 ns/div

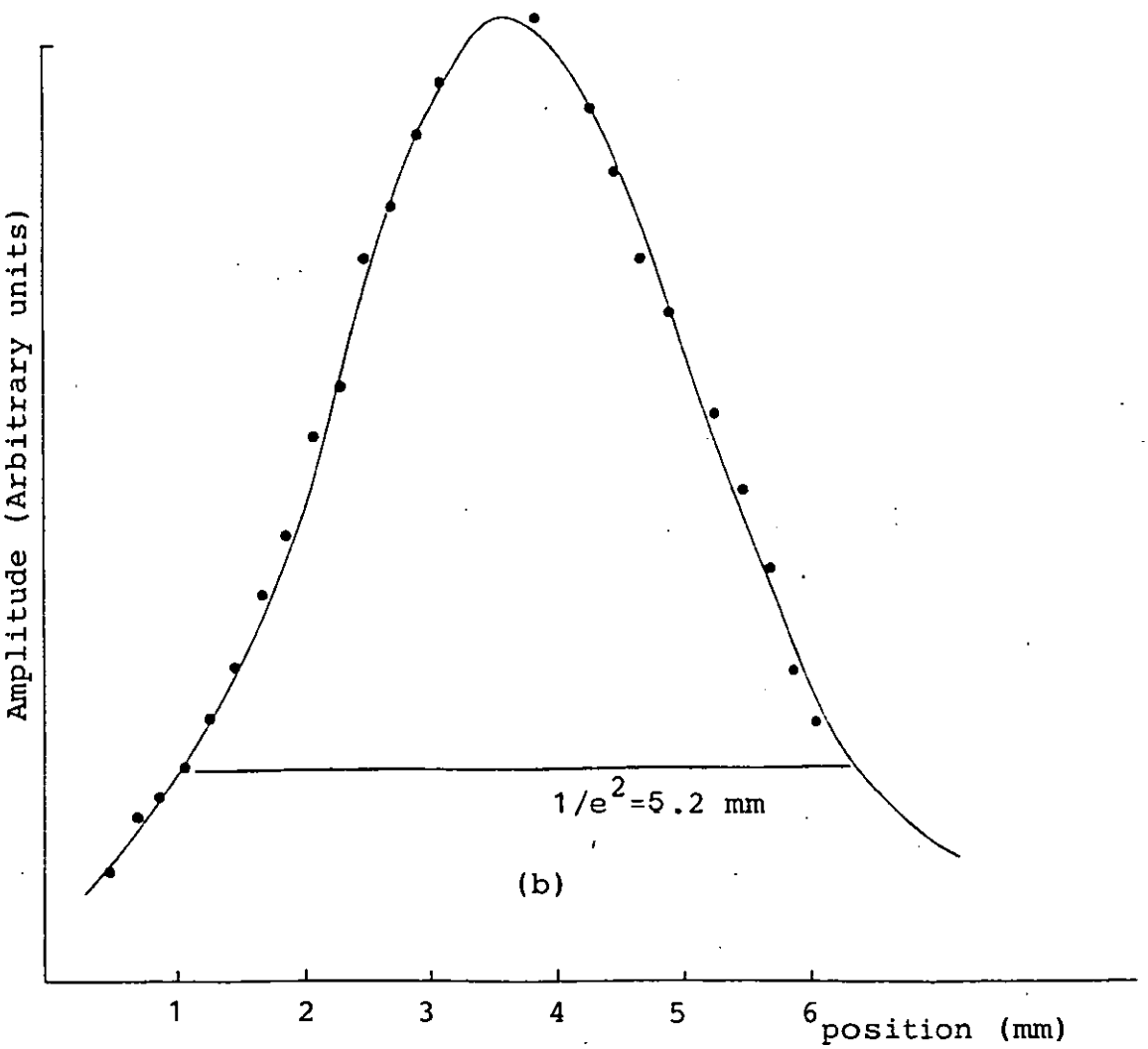

Figure 3.8: a) The temporal profile of the CO_2 laser pulse.
b) The spatial profile of the CO_2 laser pulse.

calorimeters, Gentact ED-500 and laser instrumentation 17AN, the measured energy was found to be identical and the pulse to pube repeatability was less than 10%.

B - Experimental set-up:-

This is shown in Figure 3.9. The CO_2 pulse was focussed to a spot size of (0.2 - 0.3) mm on the sample surface by short focus germanium lenses, while the energy density at the sample surface was varied using thin polythene sheets which, experimentally found to attenuate the laser independent of the energy as shown in Figure 3.10. This sort of attenuation allows laser operating conditions (gas mixture, discharge voltage... etc.) to remain unchanged and eliminate any change in the temporal behaviour or focussed spot size.

The samples were circular discs 50 mm in diameter and 5 mm thickness, always placed at the focus of the laser beam. One of the transducers described in Chapter two was acoustically bonded to the rear surface of the sample under test with a viscous fluid such as silicon grease, the sample-transducer assembly was mounted on a holder which permitted the rotation of the sample about its axis with the transducer being on axis so that the distance to the transducer for each illuminated site is the same. Part of the laser energy was diverted by a sodium chloride flat plate acting as a beam splitter for the purpose of energy measurement.

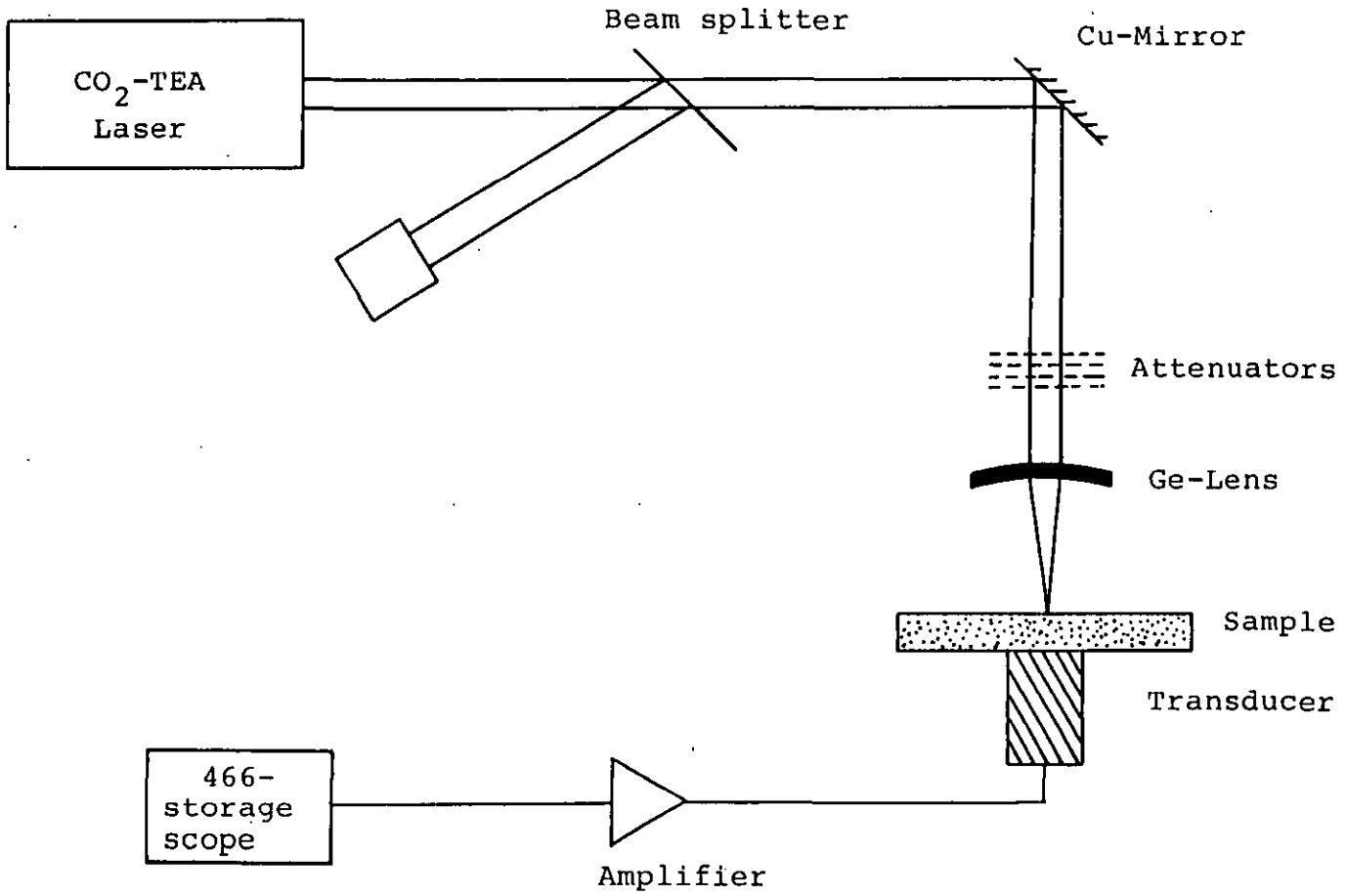

Figure 3.9: The experimental set-up.

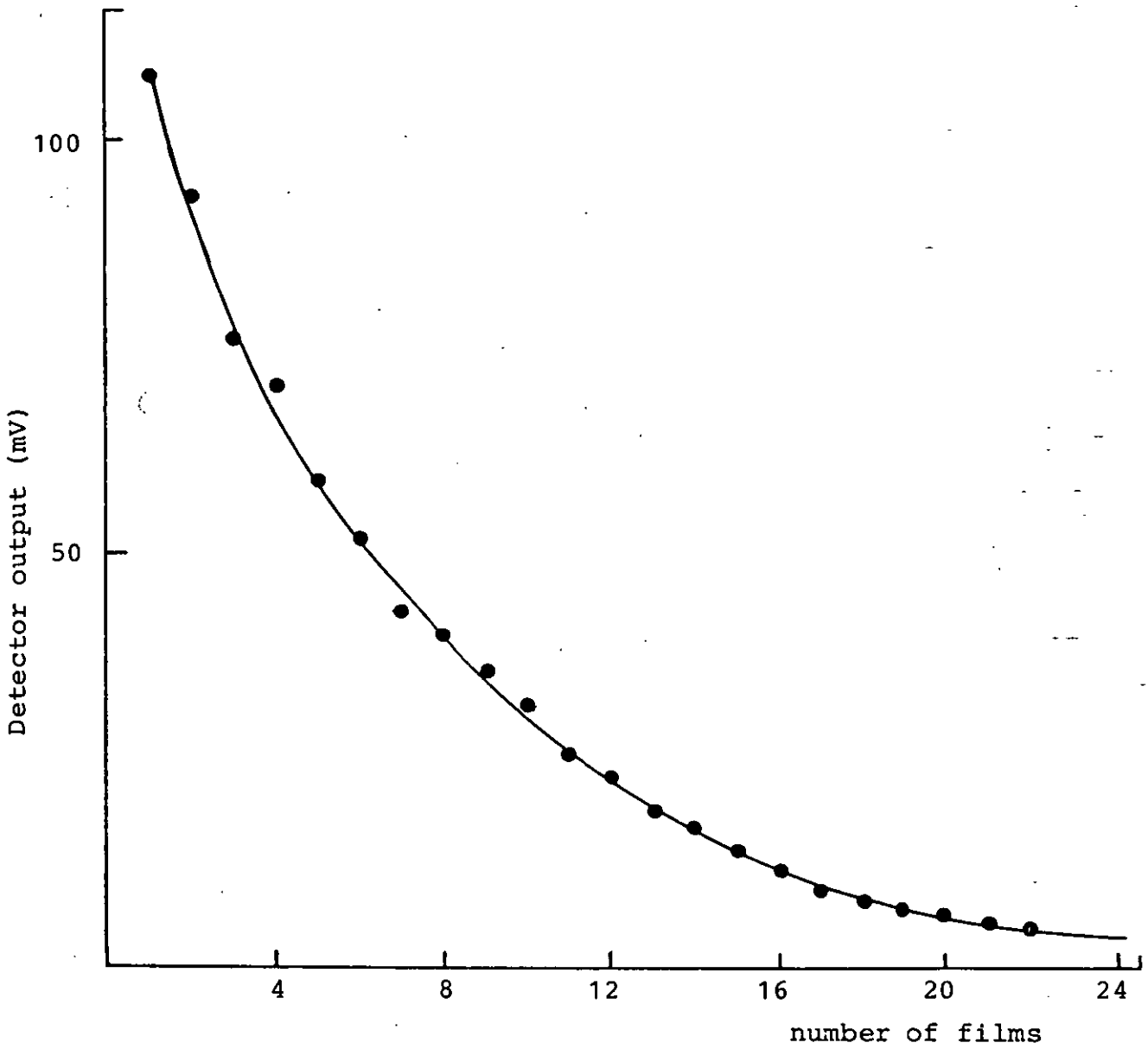

Figure 3.10: The attenuation of thin polythene films.

The energy of each shot was calculated using the following expression:

$$E = \left[\frac{x + R_1 x}{D} \cdot \frac{100}{R_2} - \frac{x + R_1 x}{R_2}\right] \left[0.8568\right]^n \qquad (3.18)$$

where x is the calorimeter reading (Gentact ED-500) in mV,

R_1 is the reflectivity of the calorimeter at 10.6 μm,

D is the calibration constant of the calorimeter in $V.J^{-1}$,

R_2 is the reflectivity of sodium chloride,

0.8568 is the transmission of the attenuators,

n is the number of polythene sheets inserted.

After substituting the numerical values the above expression reduces to the following form:

$$E = 4.28 \left[0.8568\right]^n \quad . \qquad (3.19)$$

The energy density at the sample surface was gradually increased until the signal detected by the transducer increased in magnitude. The detected photoacoustic signal was then amplified by a Dunegan-Endevco acoustic emission amplifier model (1081-450B) which has a voltage gain of 40 dB. The signal was finally displayed on a storage oscilloscope (Tektroniks 466).

3.7 RESULTS AND DISCUSSION.

A range of samples were damage tested, these included, metallic samples, dielectric and thin films. The metallic samples were:

1 - High purity copper.

2 - Aluminium, type BS1474/HE30TF consisting of 99% aluminium.

3 - Stainless steel, type BS325S21.

4 - Molybdenum, purchased from Specac.

These first three samples underwent roughing on a grinding machine before being wet polished on a circular lap with a 0.25 μm particle abrasive to an optical finish. The dielectric samples were sodium chloride and potassium chloride purchased from Specac. While the thin film samples included high reflecting films on germanium, copper-nickel mirror with hard gold coating, gold film on glass substrate and aluminium film on glass substrate.

Laser induced damage was detected by gradually increasing the energy density on the sample surface until a big increase in the magnitude of the photoacoustic signal was recorded by the transducer. Each data point is obtained at a different site on the sample surface by rotating the sample about its axis. Since the transducer is on this axis, the time delay of the acoustic signal from each spot is the same. Table 3.2 lists the measured damage thresholds of samples tested, also shown in the table are the published damage thresholds, for the

TABLE 3.2 : Measured damage thresholds compared to the published damage thresholds.

Substance	Damage thresholds ($J.cm^{-2}$)	Published damage thresholds ($J.cm^{-2}$)	Ref.
Stainless Steel	4.07	4.6(58)	42
Aℓ	11.9	14 (100)	43
Cu.	63.69	67 (58)	42
Mo	24.06	25 (58)	42
Ge	14.6	-	
GeHR	16.17	-	
KCℓ	51	55.2(92)	44
NaCℓ	68	92 (92)	44
Ni/Cu	20.9	-	
Au/Glass	21.20	-	

sake of comparison. The pulse lengths at which the published damage thresholds were carried out are indicated in parantheses.

A typical form of the photoacoustic signal in sodium chloride is shown in Figure 3.11, the scope was triggered by the CO_2 laser pulse, the delay to the first peak is associated with the time for the photo-acoustic wave to travel to the transducer from the illuminated spot. The height of the first peak which corresponds to the longitudinal wave, and travels directly to the transducer is taken as a measure of the absorbed energy to avoid any reflection and mode conversion arriving at the transducer later on. Care was taken to prevent any scattered light from reaching the transducer, this was done by wrapping the transducer

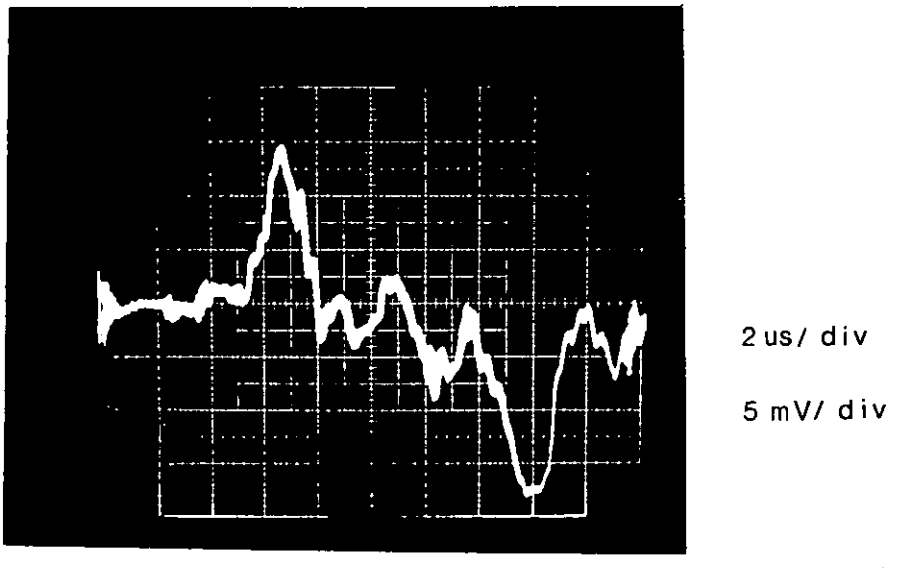

Figure 3.11: Typical form of the photoacoustic signal in sodium chloride, incident energy is 10.52 mJ.

with thin aluminized film as described in Chapter two. In addition we can discriminate against the scattered light signal by its time delay. Figures 3.12 - 3.14 shows the photoacoustic signal as a function of laser pulse energy for sodium chloride, polished molybednum and a HR film on germanium substrate respectively. The slopes in these figures were measured and found to be 1 ∓ 0.05, 1.17 ∓ 0.24, 1.02 ∓ 0.003 respectively, therefore the photoacoustic signal shows an essentially linear dependence on the incident energy density below damage, this behaviour is expected for linear absorption process. When damage starts to occur the photoacoustic signal increases noticeably and for energy densities greater than the damage threshold of the sample, the photoacoustic signal appears to follow a simple power law behaviour with the laser pulse energy, i.e.:

$$S = A\ E^{n} \tag{3.20}$$

where S is the photoacoustic signal and n is the power dependence of the signal. The magnitude of n depends on the nature of the sample, its value is generally less than 3 for metals while for dielectric materials n is greater than 3. The measurement of the energy density at the point where the graph between the incident energy and the measured photoacoustic signal change its gradient marks the damage threshold of the optical sample under damage test.

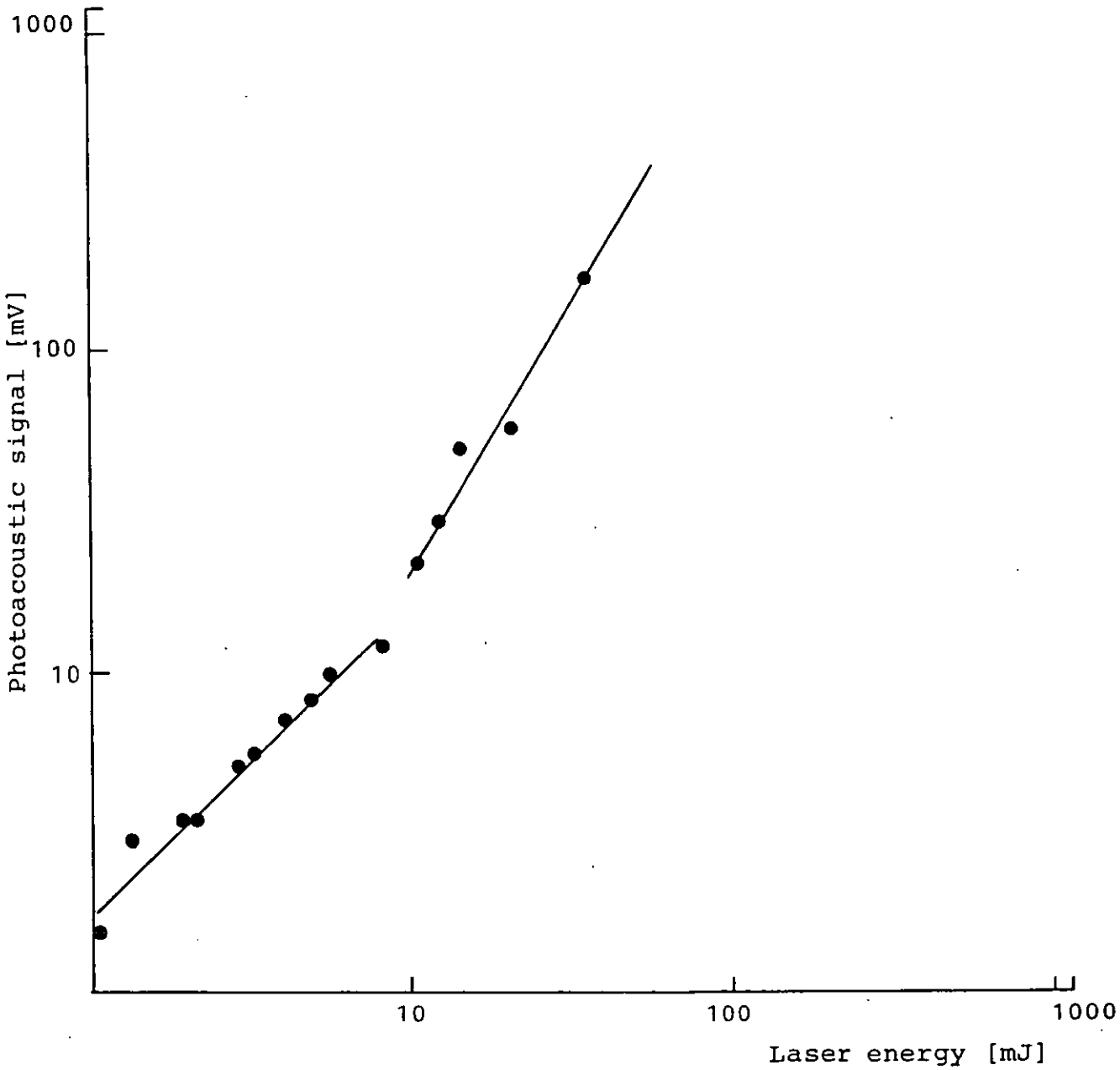

Figure 3.12: Photoacoustic signal as a function of laser energy in Sodium Chloride.

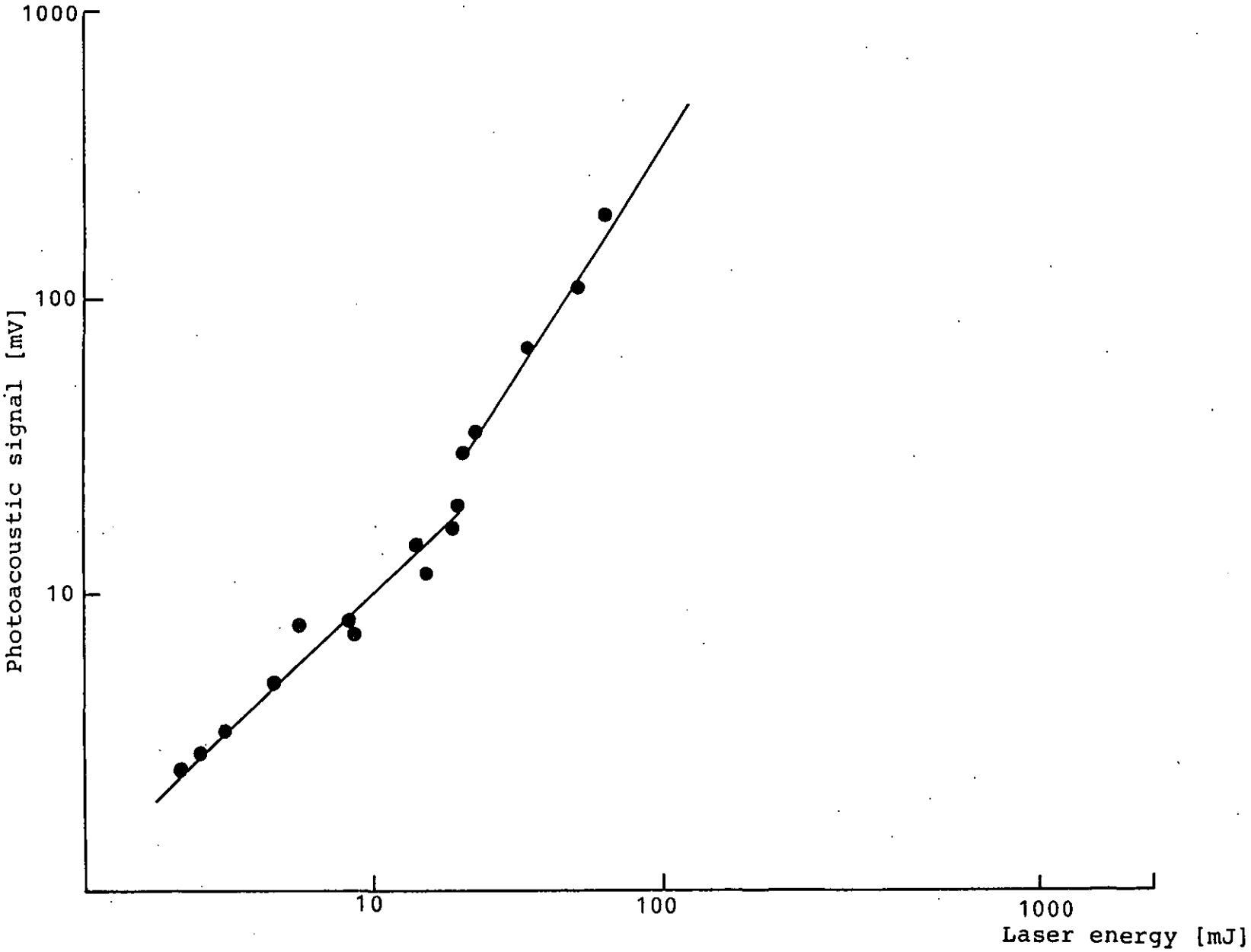

Figure 3.13: Photoacoustic signal as a function of laser energy in Molybednum.

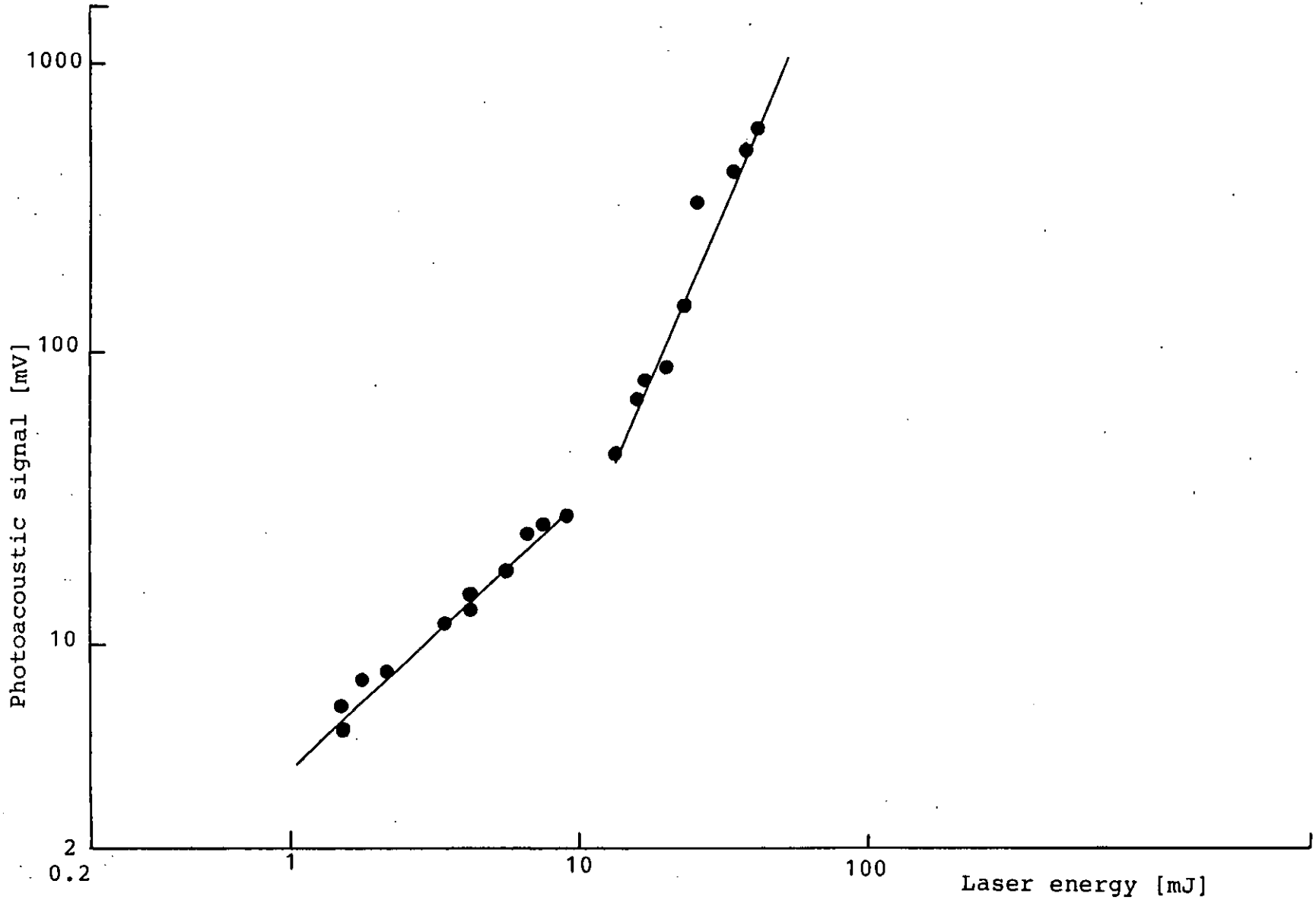

Figure 3.14: Photoacoustic signal as a function of laser energy in HR-germanium.

A photoacoustic signal is always produced whenever any of the laser pulse is obsorbed by the sample under damage test. This signal is always detected by the transducer since the wavelength of the photoacoustic signal generated is considerably larger than the focussed spot size of the laser, for example, the transducer used has a resonant frequency of about 2.5 MHz and if the sample is sodium chloride in which the sound travels at 3890 $m.sec^{-1}$, then the photoacoustic signal would have a wavelength of 1.55 mm, this is large compared to the focussed spot size of the laser, (0.3 mm). The transducer, however, will not be able to detect the photoacoustic signal if the focussed spot size of the CO_2 laser pulse is larger than the wavelength of the generated signal since there will be a destructive phase interference at the transducer because signals originating from different positions in the illuminated area will have different phases at the transducer.

Figures 3.12 - 3.14 shows that the photoacoustic signal suffers a major change when damage occurs. One might think that the increase in the signal is due to acoustic emission associated with the mechanical damage. This, however, is not the case. It must be kept in mind that below damage, most of the absorbed energy will be converted to heat at the sample surface and a photoacoustic signal will be produced immediately. When damage starts, some of the absorbed energy will

be used in breaking bonds and some will be used for melting and therefore less energy will be available for the production of the photoacoustic signal and a decrease in the signal should be expected rather than an increase. The increase in the signal therefore, is not due to the increased acoustic emission, it is due to the increased absorption via some mechanism at the damage site itself during damage process. It is well known, for example, that the reflectivity of most metals is reduced when they are subjected to high intensity laser pulses[45,46,47,48], or the metal may undergo anamolous absorption[49] for which analysis has shown that the thermal emission from the laser heated plasma, the peak of which lies in the near ultraviolet (where metals have much higher absorptance) is responsible for the increased absorption and consequently this process can be an efficient thermal coupling process. However, beyond the damage threshold, the increase in the photoacoustic signal does not continue at the same rate and, at very high energy densities far above the threshold the rate of increase falls as shown in Figure 3.15. There are two possible explanations for this behaviour at high energy densities:

1 - Some of the energy goes into either melting or increasing the temperature of the vaporized material. During this stage the input energy is divided between

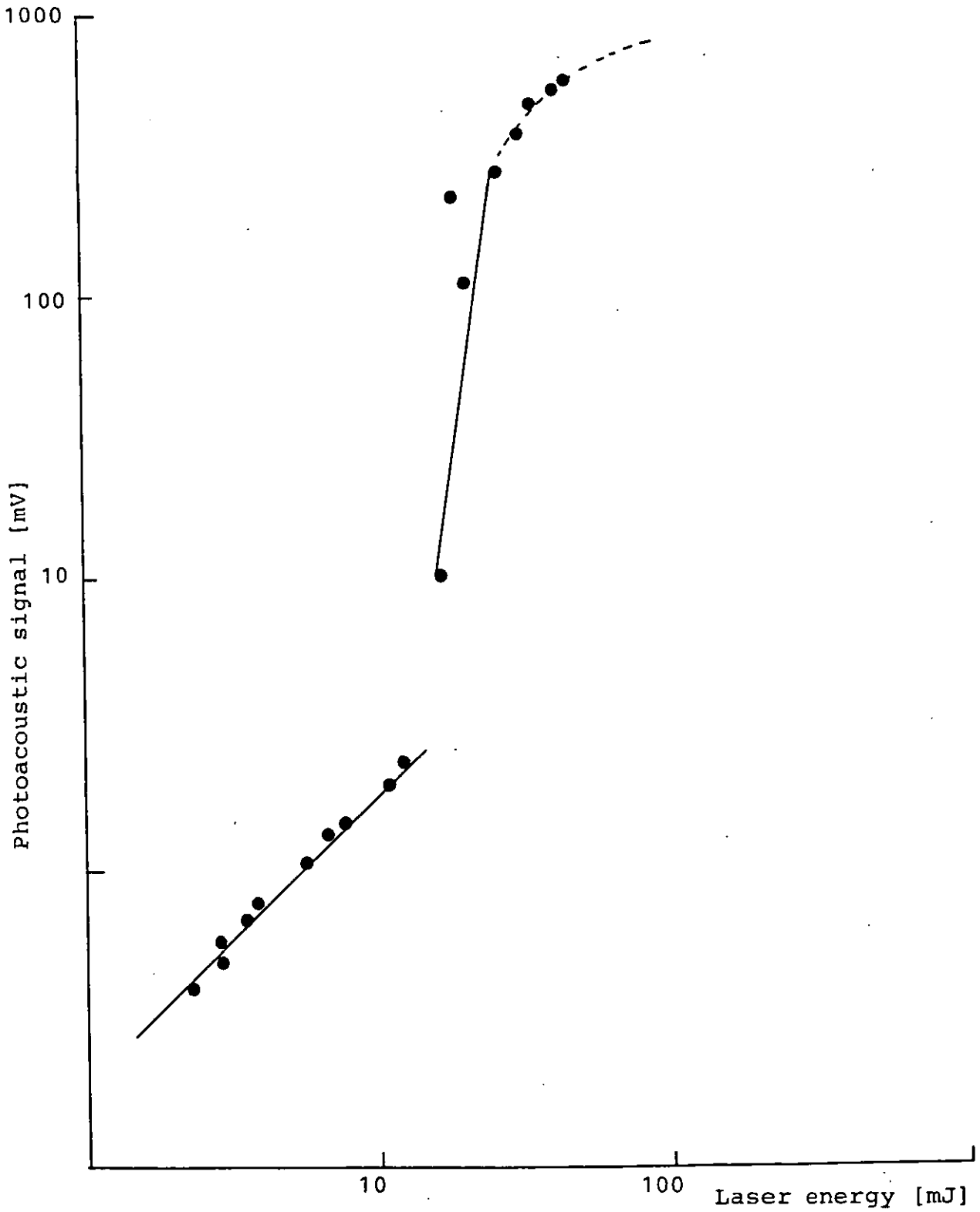

Figure 3.15: Photoacoustic signal as a function of laser energy for Au film on glass.

direct acoustic generation process and simply heating the vaporized material.

2 - A plasma is formed on the sample surface and at energies slightly higher than the plasma threshold intensity, a laser - supported combustion (LSC) wave is usually ignited. LSC waves are often seen at intensities around $2 \times 10^4 W.cm^{-2}$ for 10.6 μm[50] with both pulsed and continuous laser beams. The ignition of an LSC wave initially takes place in the target vapour, as a consequence of the ignition process and the presence of the sample surface, a precursor shock wave proceeds the LSC wave. The LSC wave propagates into the shocked air with subsonic velocity, the mass flow through the LSC wave is very low and therefore the plasma temperature is high, leading to a strong radiation from the plasma to the surface. When the laser energy is increased further, a transition from LSC wave to laser-supported detonation wave (LSD) takes place, the LSD wave propagates with supersonic velocity and the mass flow through the LSD wave is high, therefore some of the energy will be used to increase the temperature of the plasma rather than being coupled to the sample surface. This in turn will reduce the magnitude of the photoacoustic signal detected by the transducer. Another way of expressing this is to say the plasma processes shield the sample surface from the laser radiation.

The technique described above for the accurate determination of damage threshold lends itself to further study of the damage process, in particular it enables the spot-size dependence to be investigated. Figures 3.16 and 3.17 shows the spot-size dependence of laser induced damage in copper and HR coating on germanium substrate. As the spot-size increases, the damage threshold decreases. The reduction in the damage threshold is due to the increased probability of finding a defect in a large spot-size illuminated area. Both curves have nearly $(\text{spot-size})^{-1}$ dependence in agreement with previous studies[51].

Damage to optical materials also depends on the manner in which the sample is irradiated. It was found that the damage threshold in the case of N - on - 1 (many shots on the same site) is higher than the damage threshold in the case of 1 - on - 1 test (one shot per site). The ratio of the two tests was 2.64 in molybednum and 1.67 in the copper nickel mirror with hard gold coating being typical examples of the samples tested. The increase in the damage thresholds in the N - on - 1 test might be explained to be either due to cleaning of the surface by the laser at low intensity or, smoothing out of the sharp edges of the polishing scratches by some form of laser polishing. Moreover, after damage has occurred in the sample, it was found that the energy transfer to the sample surface in the

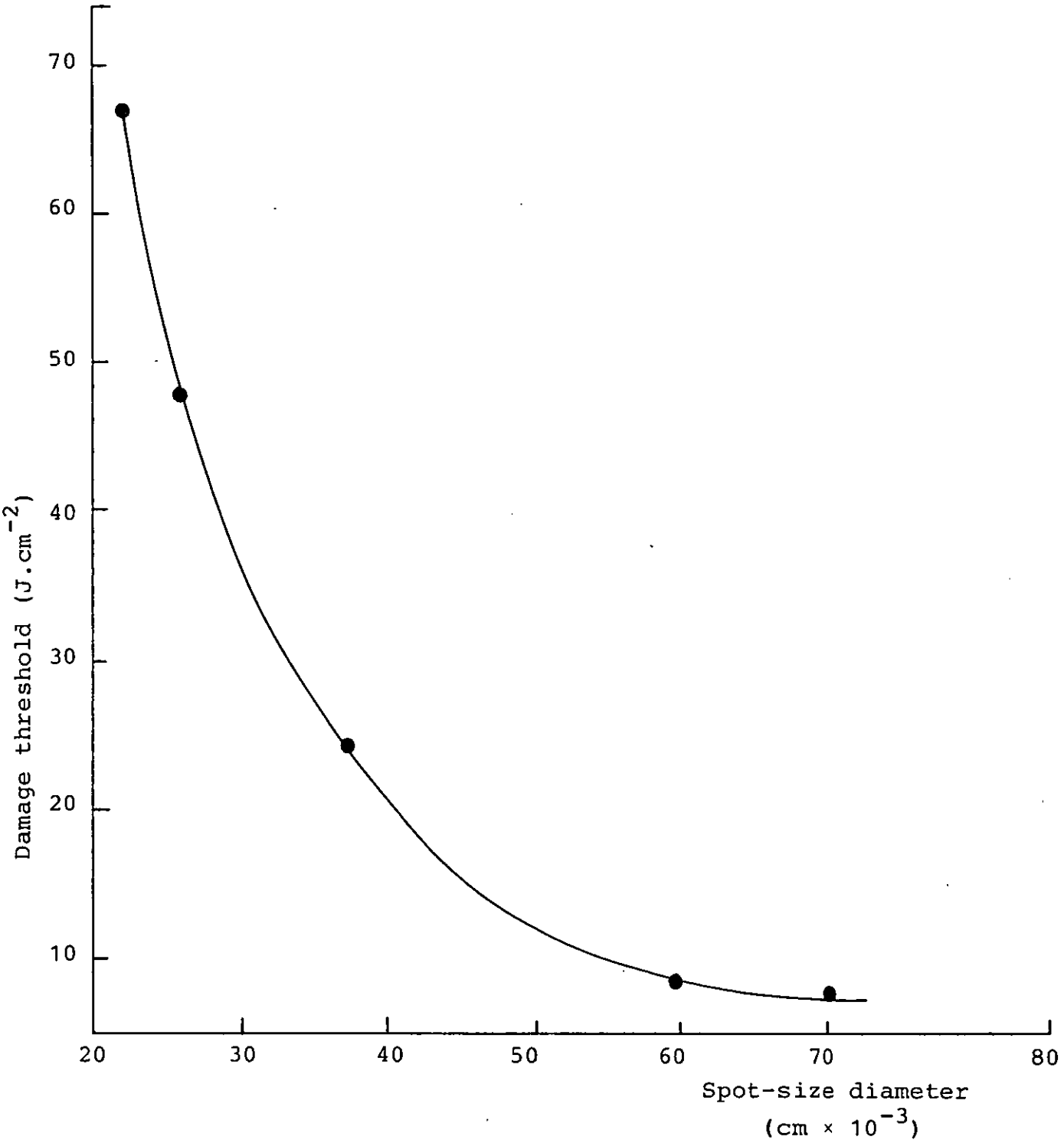

Figure 3.16: Spot-size dependence of damage threshold in copper.

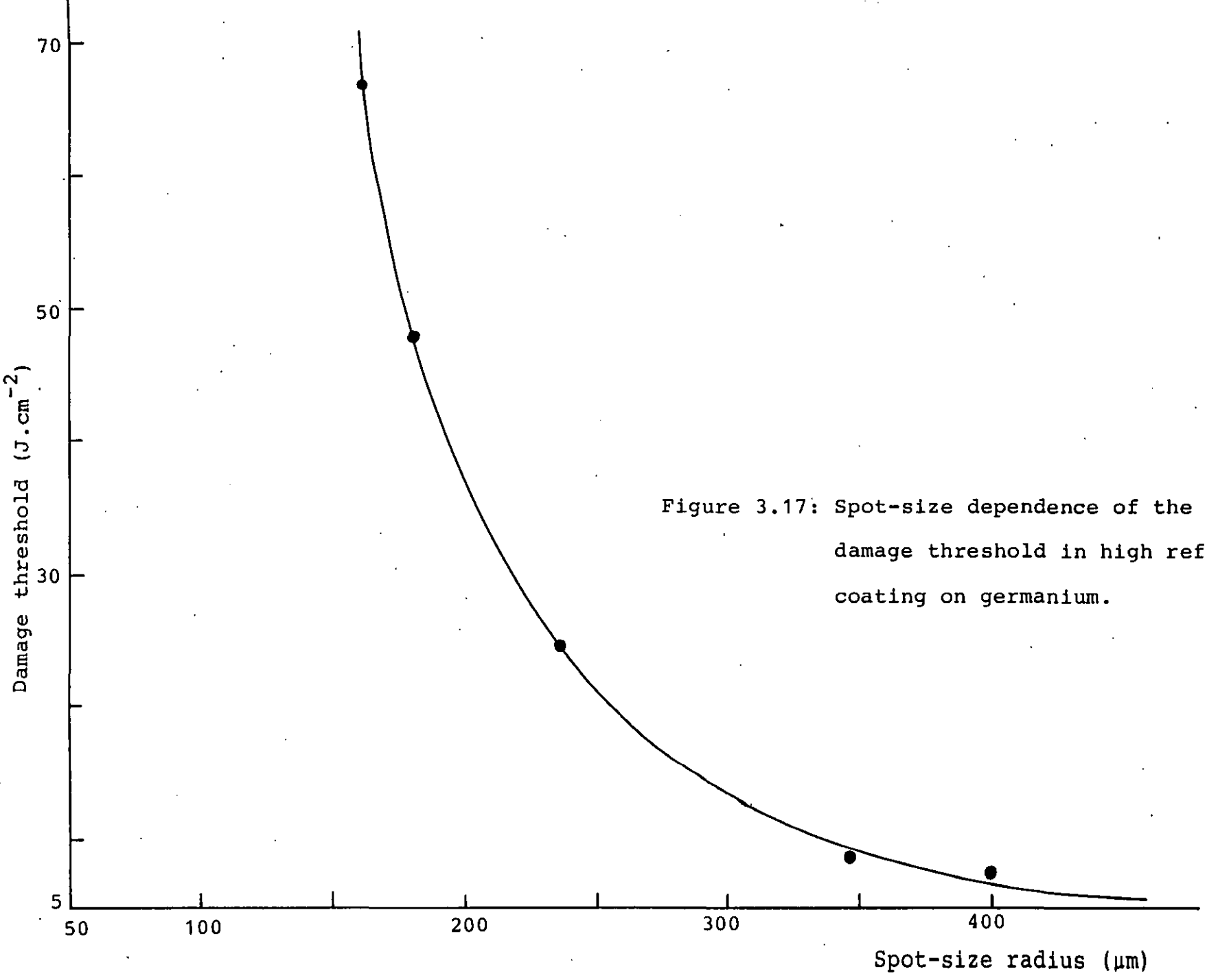

Figure 3.17: Spot-size dependence of the damage threshold in high reflection coating on germanium.

case of N - on - 1 test is steeper than in the case of 1 - on - 1 test as shown in Figures 3.18 and 3.19 respectively.

The magnitude and shape of the photoacoustic signal depends on many parameters, these include:

i) Size of the illuminated area:

It was mentioned in section 3.4 that below plasma threshold the magnitude of the photoacoustic signal is independent of the energy density. To investigate this behaviour, the laser spot-size on an aluminium surface was varied keeping the energy falling on the sample constant. The result of such an investigation is shown in Figure 3.20, which is a good confirmation of the fact that the photoacoustic signal in the thermoelastic regime is dependent only on the energy.

ii) Energy density:

Figure 3.21a shows the photoacoustic signal produced on an aluminium surface at energy density well below the plasma threshold formation, while in Figure 3.21b, the photoacoustic signal in the presence of plasma is shown. The big increase in the magnitude of the photoacoustic signal and the change in the shape is a direct result of the change in the generating mechanism from the thermoelastic to momentum transfer mechanism in accordance with previous studies[34].

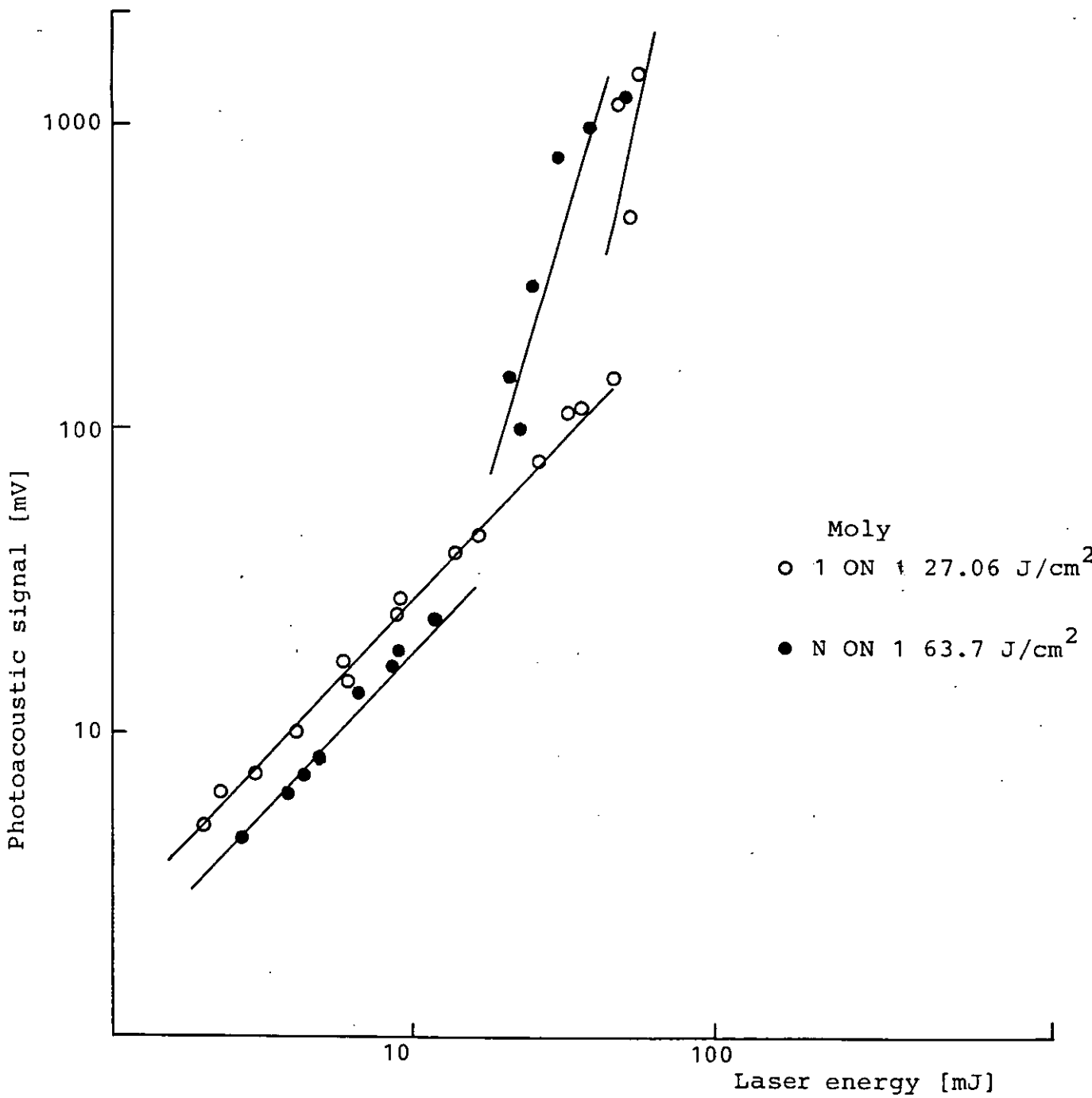

Figure 3.18: Damage dependence on the method of irradiation in Moly

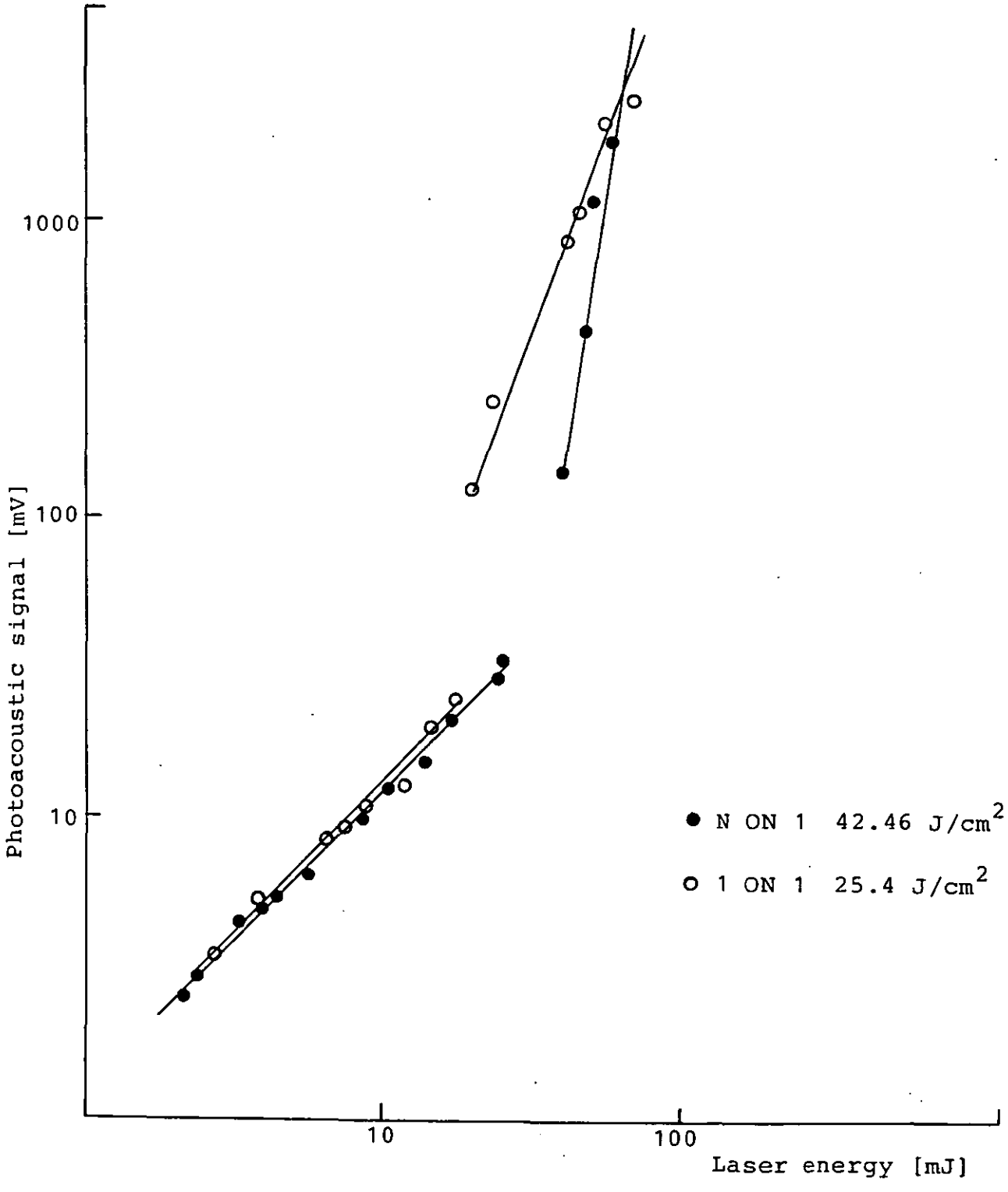

Figure 3.19: Damage dependence on the method of irradiation in Cu-Ni/Au.

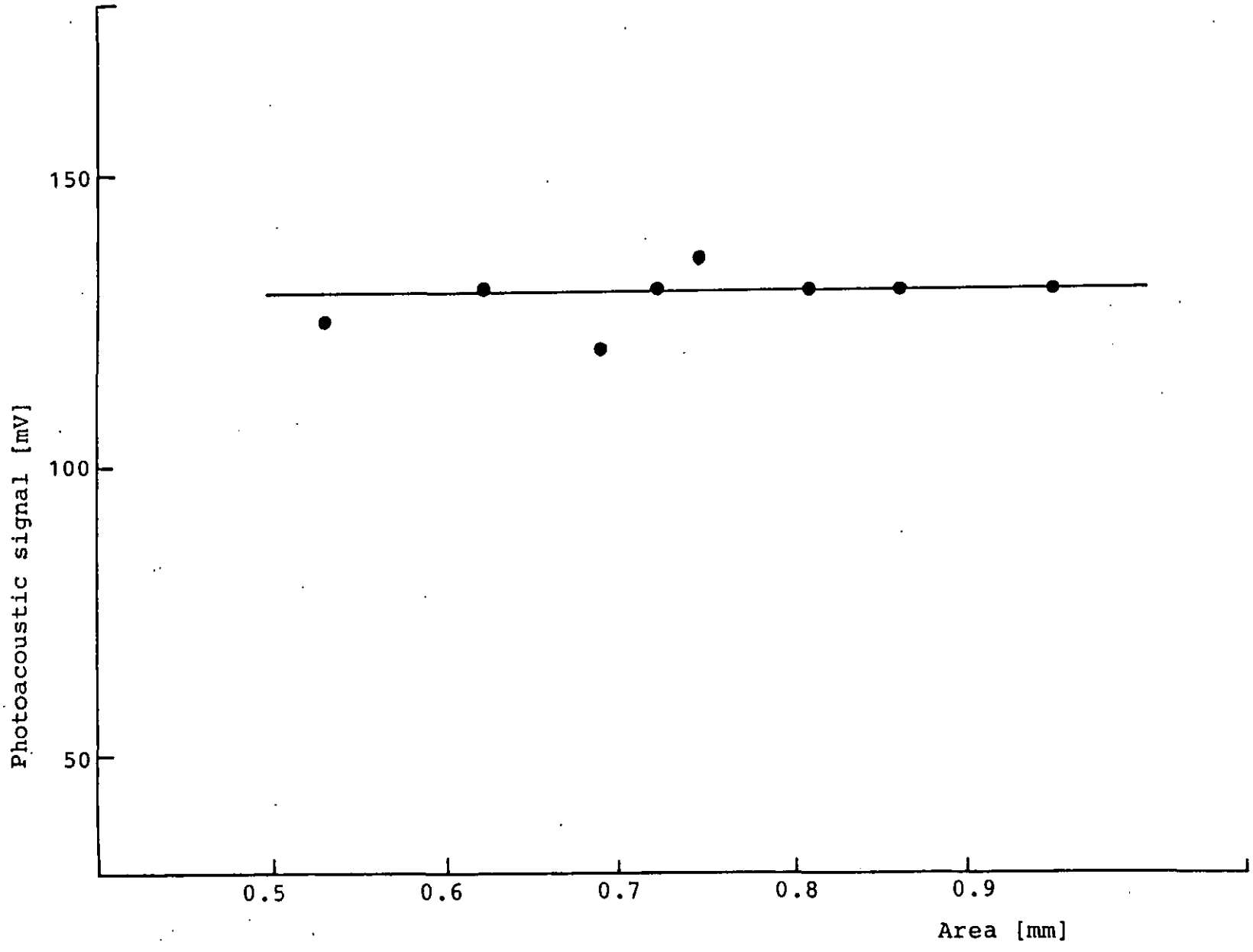

Figure 3.20: Photoacoustic signal as a function of the illuminated area.

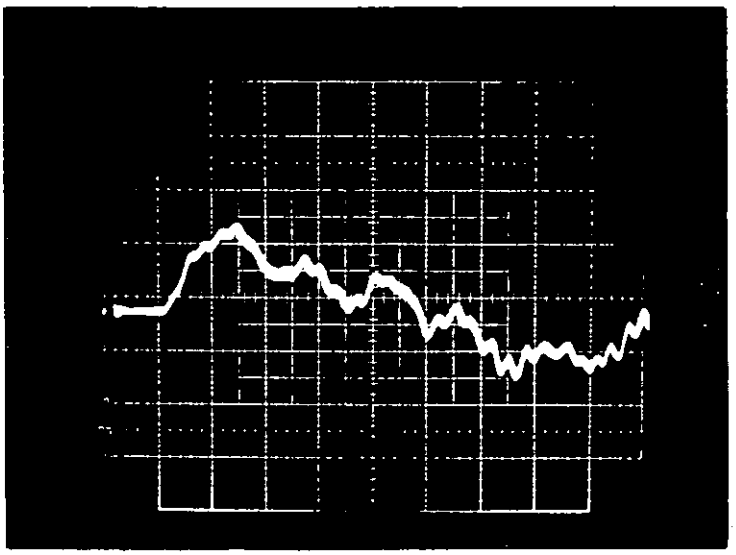

50mV/div.

2μs/div.

(a)

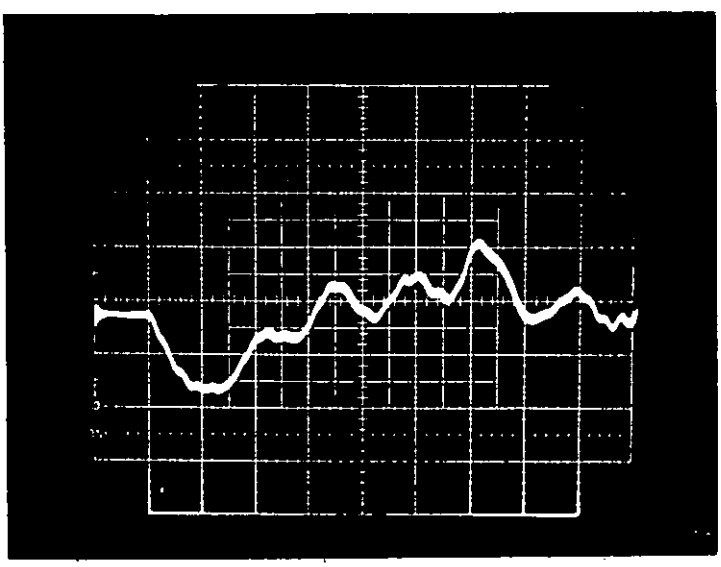

1V/div.

2μs/div.

(b)

Figure 3.21: Photoacoustic signal in aluminium,

a) below plasma threshold,

b) after plasma threshold.

3.8 CONCLUSION.

Since laser induced damage to optical materials is often responsible for a large share of the operation costs, there is a need for a detection method which can sense the early stage of laser induced damage, before damage becomes catastrophic and before the optics fracture or melt and consequently before the laser is put out of commission.

Most of the damage thresholds measured in this work are less than those reported in the literature. In addition, when damage sensed photoacoustically it was often very difficult to find any traces of damage under an optical microscope even at 400X magnification. Photoacoustic thus appears to provide several important advantages, these can be summarized in the following points:

1 - It can see damage threshold very precisely and, it provides an opportunity for performing on-site automatic detection of the damage in the optical components of high energy laser systems.

2 - It is relatively simple since piezoelectric transducers can be readily mounted on optical components or indeed on the support structure and, the photoacoustic signal can be remotely monitored.

3 - It provides new information on the energy transfer in the presence of damage and possibly new information on the damage mechanism itself.

4 - Reduction in the laser system's necessary costs by offering a technique for the early detection of the onset of damage thus allowing the laser to be switched off and components repolished before damage has progressed to a state where the component is permanently damaged.

5 - If damage is detected in its early stages, a new component can be prepared or obtained ahead of time to minimize laser down time.

6 - When the optical component constitutes one of the walls of a laser cell under vacuum conditions, for example, in an excimer laser, early detection of the damage can prevent a serious leakage of air into the cell or hazardous gases out into the environment.

CHAPTER FOUR

Laser Induced Damage Detection by the Optical Deflection Technique

4.1 INTRODUCTION.

The growing interest in the application of lasers in various fields and the continuous progress in the development of high power lasers has motivated the development of sensitive techniques to measure low absorption losses in highly transparent solids, metals and thin film coatings. The photothermal deflection technique or "mirage effect" for measuring ultralow absorption coefficients was developed originally by Boccara and co-workers[1,2,3,4,5]. The principle of the photothermal deflection is shown in Figure 4.1. The surface of a sample is illuminated by a modulated (chopped) light source of the wavelength of interest. Some of this radiation is absorbed and heats the surface which in turn is coupled into the surrounding gas. The refractive index of the gas changes. A probe beam directed along and just above the sample surface will be deflected by the refractive index gradient. This deflection can be detected by laser beam position sensors. These position sensors, usually two photodiodes placed symetrically in the beam, have the capability of measuring deflections down to 10^{-9}- 10^{-10} radians. Alternatively a knife edge which blocks half of the probe beam diameter followed by a single detector can be used. The sensitivities of these two deflection schemes are almost the same[4].

Photothermal deflection has found some important

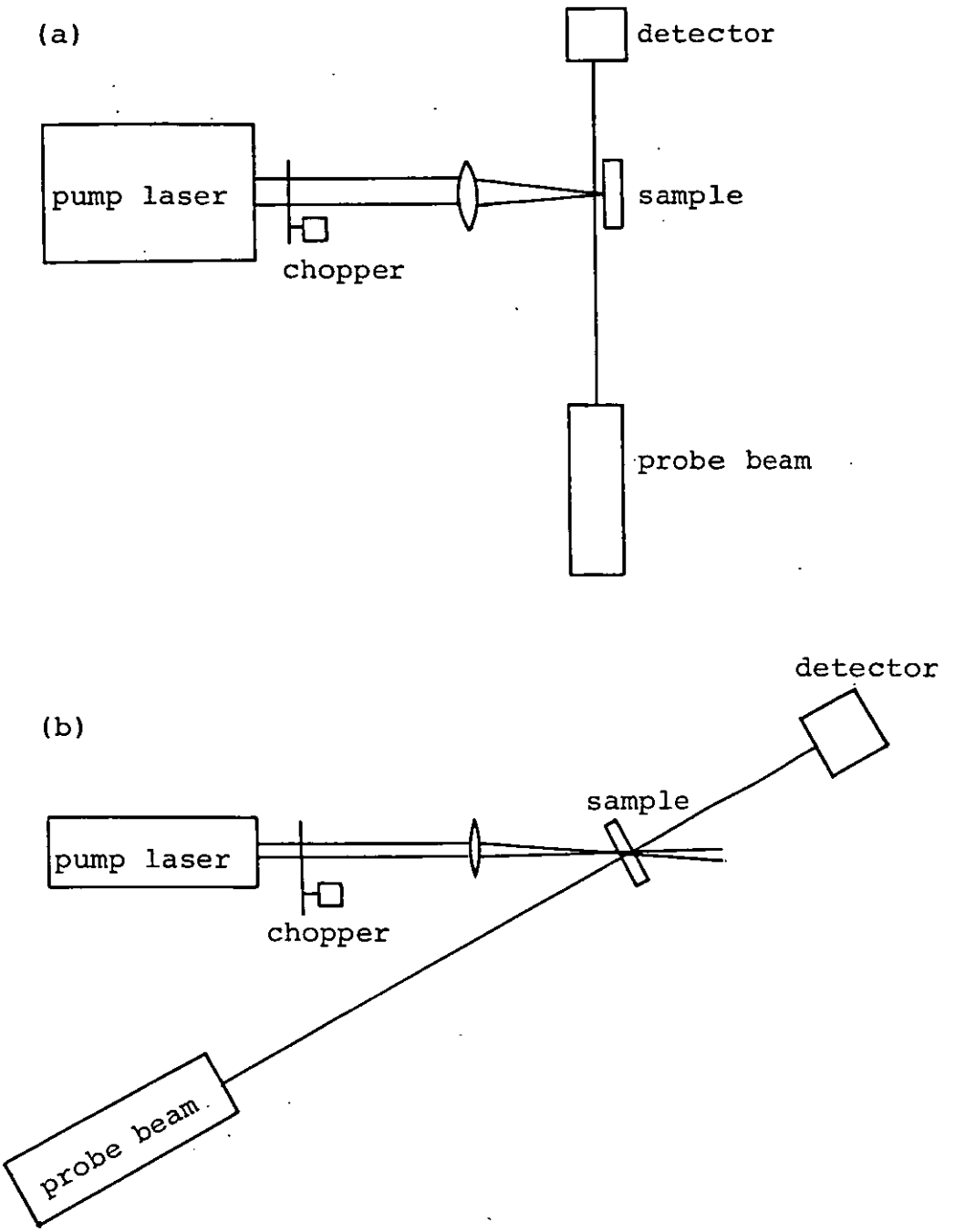

Figure 4.1: a) Transverse photodeflection spectroscopy.
b) Collinear photodeflection spectroscopy.

applications. A few of these applications will be explained briefly.

A - Measurement of optical absorption coefficients.

Calorimetric methods[6] and emission spectroscopy[7] are the common methods of measuring the optical absorption coefficient. In the calorimetric method, a laser beam of constant intensity is incident on the sample for a certain period of time, after the laser beam is switched off the sample cools down. The slopes of the heating and cooling curves can be used to calculate the absorption coefficient. Calorimetric methods are usually not sensitive enough for making measurements below 10^{-2} cm^{-1} unless high laser powers are used and the ambient temperature must be controlled carefully. On the other hand, the photoacoustic technique can be used to measure absorption coefficients in the range 10^{-4} - 10^{-5} cm^{-1}. The most sensitive measurements down to 10^{-6} cm^{-1} have been made using incident laser powers of $\sim$ 100 mW[8]. Jackson et. al[2] has recently shown that for modulation of the pump beam at low frequency (up to 10 kHz) the amplitude ϕ of the probe beam deflection is given by:

$$\phi = \frac{dn}{dT} \frac{P}{K\pi^2 x_o} \left[1 - \exp(-\alpha \ell)\right] \left[1 - \exp\left(\frac{-x_o^2}{\omega_o^2}\right)\right] \qquad (4.1)$$

where $\frac{dn}{dT}$ is the temperature coefficient of the refractive

index, P is the power of the modulated pump beam, K is the thermal conductivity of the surrounding gas, x_o is the distance between the intensity maxima of the probe and pump beam as shown in Figure 4.1b, α is the optical absorption coefficient, ℓ is the interaction length of the pump and probe beam and ω_o is the radius of the pump beam at 1/e intensity. Thus, for small $\alpha\ell$ the amplitude of the deflection is proportional to $\alpha\ell$ and to the power and inversely proportional to the modulation frequency. The photothermal deflection technique is capable of measuring absorption coefficients as low as 10^{-7} cm^{-1} for thin films[5] and 10^{-8} cm^{-1} for liquids[5], it has the advantage that there is no mechanical contact with the sample and there are no light scattering problems. In addition, the measurement can be carried out in hostile environment, however, laser noise (intensity fluctuations) of the probe beam may limit the sensitivity.

One has two choices in performing photodeflection, i.e,:

1 - Collinear photothermal deflection: where the gradient of the index of refraction is both created and probed within the sample.

2 - Transverse photothermal deflection: where the probing of the gradient of the index of refraction is accomplished in the thin layer adjacent to the sample surface. This

approach is normally used for opaque samples and for materials of poor optical quality such as powders.

B - Thermal wave imaging[9,10,11,12].

In thermal wave imaging, macroscopic and microscopic thermal features on or beneath the sample surface can be detected and imaged. This technique is a development of the photoacoustic technique. In thermal wave imaging a laser beam is focussed and scanned across the surface of the sample. This beam is intensity modulated at a frequency which can be in the range 10 Hz - 10 MHz. The laser energy is absorbed at or near the surface. A periodic surface heating results; this heating is a source of thermal waves which progagate away from the interaction region. These thermal waves travel only one or two wavelengths before their amplitudes become negligibly small. In spite of this small range, thermal waves can interact with thermal features in a manner equivalent to the scattering and reflection of ordinary electromagnetic waves. Thus any features on or beneath the surface of the sample that is within the range of these thermal waves and has thermal characteristics different from their surroundings will reflect and scatter, and thus become visible. Several techniques have been developed for the detection of the scattered and reflected thermal waves arising from these thermal features. The earliest was scanning photoacoustic

microscopy (SPAM)[13,14], in which a gas microphone is used to monitor variations in the local surface temperature. The surface temperature oscillations produce variations in the gas pressure inside a closed photoacoustic cell as a result of the periodic conduction of heat from the sample surface to the gas in the cell. Another technique known as photothermal imaging[15,16,17], involves detection of the infrared radiation emitted from the periodically heated spot on the sample. A third technique referred to as the "mirage effect" or as optical beam deflection is based on periodic heat conduction from the heated spot on the sample surface to the local layer of gas or liquid adjacent to it. This technique measures the deflection of a laser beam traversing the periodically heated gaseous or liquid layer. All these techniques detect the thermal waves that are scattered or reflected from the local thermal features through the effect of these waves on the surface temperature. However, all these surface temperature monitoring methods are impractical at frequencies exceeding 10 KHz, and thus are severely limited in imaging resolution[18].

The resolution obtainable in thermal wave imaging is set by both the spot-size of the incident energy beam[19] and the thermal wavelength[20]. The thermal wavelength is given by:

$$\lambda_{th} = 2\pi \left(\frac{2K}{\rho C f}\right)^{\frac{1}{2}} \qquad (4.2)$$

where f is the modulation frequency of the pump beam, K, ρ, C are the thermal conductivity, density and heat capacity of the sample respectively. Thus the thermal resolution for thermal conductors at 10 KHz is only 20 to 30 μm and a micrometer range resolution requires beam modulation frequencies of 1 MHz, which is not practical for the surface temperature detection technique described above. To overcome this resolution limitation, Rosencwaig[19] suggested that the scattered and reflected thermal waves can be detected through their effect on the thermoelastic signals generated in the bulk of the sample. Such signals can be detected at high frequencies by using ultrasonic transducers in acoustic contact with the sample. It should be noted, however, that thermal wave imaging is not the same as thermoelastic ultrasonic imaging. In thermal wave imaging it is the interaction of the thermal waves with the thermal features in the sample that produces the main image features, while in thermoelastic ultrasonic imaging it is the interactions of the acoustic waves with the elastic features in the sample that produces the principal image features.

Thermoelastic signals occurs in any sample with a nonzero thermal expansion coefficient, thus a 1 MHz thermal wave gives rise to 1 MHz acoustic waves. These

thermoacoustic waves are propagating waves of much longer wavelengths being typically a few millimeters at 1 MHz compared to a few micrometers for thermal waves at the same frequency. The magnitude and phase of the thermoacoustic waves are directly related to the temperature profiles in the heated volume and thus are directly affected by the presense of scattered and reflected thermal waves. An example of thermal wave imaging is shown in Figure 4.2. This image is taken with a scanning electron microscope equipped with a thermal wave imaging system. Figure 4.2a shows the back scattered image of a silicon integrated circuit with no visible sign of defects. Figure 4.2b is the thermal wave image of the same region and clearly shows a subsurface microcrack running vertically down the right hand side of the imaged area. Figure 4.2c shows the back scattered electron image of another silicon circuit which shows no obvious defects. The thermal wave image in Figure 4.2d, however, shows the presense of local film delamination (irregular white regions in the upper central area).

C - Application to photoelectrochemical structures.

Photoinduced redox reactions at the surface of microscopic ($\lesssim 1\mu m$), partially metalized, semiconductor powders have been a focus for much recent work on photocatalysis for energy storage. Recently a new

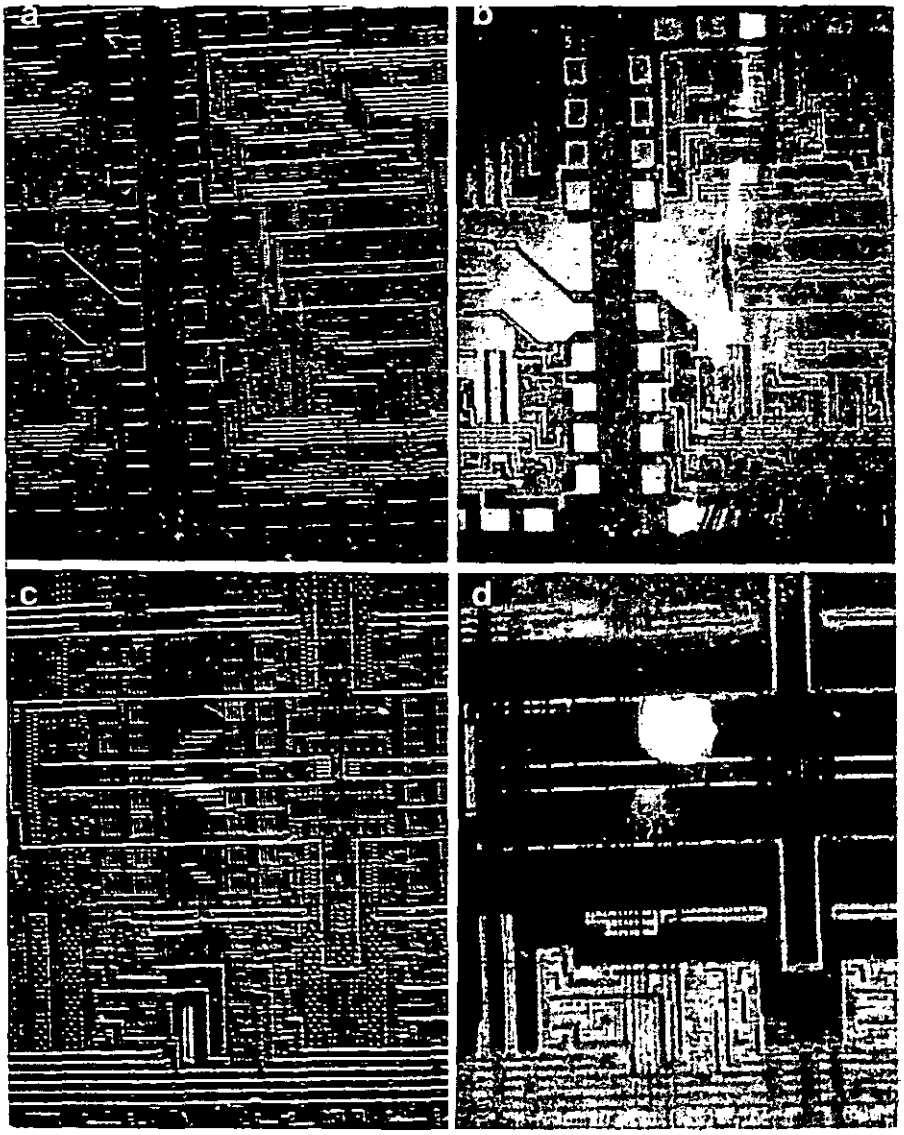

Figure 4.2: Examples of subsurface mechanical defects in silicon circuits: (a and c) backscattered-electron images exhibiting no visible signs of defects; (b and d) thermal-wave images of the same areas, showing (b) a subsurface microcrack and (d) local subsurface delaminations (irregular white regions in upper center). (after ref.18).

planer photoelectrochemical (PEC) structure has been reported[21] in which nonmetallized powder such as TiO_2 or WO_3 is incorporated in a thin, porous layer on a metallized substrate. The conventional techniques of specular reflection, transmission and ellipsometry cannot be applied for characterization of such porous structures. Because photothermal deflection spectroscopy can be applied to any state of matter, Tamor and Hetrick[21] have used this technique to obtain the absorption spectra of these PEC materials. If there is any unreduced material, it will show as strong absorption bands. These bands can also be correlated with the electronic structure of the PEC materials.

D - Application to combustion diagnostics[22].

There is considerable interest in the development of combustion diagnostic techniques for minority species concentration measurement. The basic idea behind the application of photothermal deflection spectroscopy in combustion studies is quite simple. Two laser beams, a pump beam and a He-Ne laser beam (probe beam), intersect in the region where the molecules of interest are to be detected. The pump beam is tuned to an absorption line of the molecule of interest. Laser energy is absorbed by the molecules which loses most of the energy by quenching collisions with other molecules. Most of this energy eventually appears as heat in the flame

gases, thereby changing the refractive index of the medium. The probe beam suffers a deflection due to the refractive index gradient that is produced. The amplitude of the signal is proportional to the concentration of the molecules of interest. Spatial resolution is obtained because the intersection of the pump and probe beams localizes the region where the signal is observed and the temporal resolution is obtained by using a pulsed laser. Based on photothermal deflection technique a number density of NO_2 molecules of about 3×10^{14} molecules cm^{-3} (50 ppm) has been obtained[22].

E - Application to thin film thickness measurement.

Normally direct measurement of the geometrical thickness of a film requires either microscopic examination of a cross sectioned sample or stylus measurement of a step height as in the Talystep device. Both of these techniques may be destructive procedures. Several non-contact, non-destructive methods are also available; these methods include optical interferometry and optical ellipsometry for optical transparent films, eddy current and resistivity probe for metallic films. None of these non-contact methods are widely applicable and none are suitable for both transparent and opaque films. A new method based on the use of thermal waves has been devised for thin film measurement which is

applicable for both optically transparent and opaque films[23,24]. The method consists of using highly focussed laser beams for both generating and detecting thermal waves, both the pump and probe beams incident normal to the sample surface and the two laser spots are displaced ∿ 2 μm from each other at the sample surface. Using three dimensional model of thermal wave propagation in layered media Opsal et. al[24] has derived an expression which relates the deflection signal as a function of the film thickness. This new technique is capable of measuring film thicknesses in the range 500 - 25000Å with an accuracy of ± 2%, this implies a sensitivity of 10Å.

F - Thin film characterization.

The production of adequate coatings for high power lasers, especially excimer lasers operating in the U.V must meet several criteria. The first of these, is the single shot damage threshold of the coating which in the U.V is generally lower than in other parts of the spectrum. Next is the increase in the scattering cross section at shorter wavelengths. These problems largely centre around small absorbing and scattering sites in the coatings which results from substrate and film preparation procedures. Photothermal deflection spectroscopy has proved to be a useful tool in characterizing thin films[25,26] and in providing high

spatial resolution maps of these impurities in thin film optical coatings. Those absorption maps can reveal flaws or micron-size defects which could become damage sites when exposed to high energy laser radiation.

G - The optical monitoring of photoacoustic pulse propagation in solids.

Piezoelectric transducers are commonly used to monitor elastic waves in solids. However, the information they yield is modified by the response characteristics of the transducers themselves as well as by those of the medium which acoustically couples the transducer to the work piece. Interferometric techniques have also been employed to measure elastic waveforms in solids and although the interferometric techniques are non-contact, they have to be stabilized, this requires the use of fairly complicated electronics. Recently, Sontag and Tam[27] have demonstrated a simple, non-contact method based on optical deflection principles for direct and fast detection of elastic waves propagating in thin silicon wafers. In their experiment a nitrogen laser with a pulse energy $\lesssim$ 1 mJ was weakly focussed onto the sample surface without causing any damage. A He-Ne laser beam is then focussed on the opposite surface of the water and detected by a fast photodiode-amplifier combination with a bandwidth of 100 MHz. When the nitrogen laser pulse is absorbed

at the silicon wafer surface, longitudinal and surface elastic waves are produced. These waves cause surface distortions at the opposite surface which can be detected by the probe beam deflection. The advantages of this simple technique is that it is ideally suited for measurement in high temperature, hostile, or inaccessible environments. It should be noted however, that this technique differs from the previous applications of the "mirage effect" in that the surface distortions cause the deflection of the probe beam and not the refractive index gradient generated by the laser pump beam.

4.2 THE DETECTION OF LASER INDUCED DAMAGE IN OPTICAL MATERIALS USING THE OPTICAL BEAM DEFLECTION TECHNIQUE.

When an intense laser pulse interacts with a solid surface some fraction of the incident laser energy will be absorbed. In metals, the absorption is mainly by free electrons. Interband absorption can also contribute but they are small and can be ignored. In insulators, the absorption is due to the excitation of lattice vibration, for example, photons of infrared radiation rarely have enough energy to excite electrons in pure insulators. They can, however, excite lattice vibrations if the wavelength is appropriate. In common salt and other alkali halides the positive and negative ions oscillate naturally in the lattice at frequencies about 10^{13}Hz,

corresponding to wavelengths of 20 - 100 μm. As a result such infrared radiation is strongly absorbed by these crystals. Absorption, may also arise from defects in these crystals, these defects introduce electronic levels in the band gab just like the denars and accepters in semiconductors. The absorption coefficient of a solid which is caused by defects is proportional to the concentration of defects.

The energy absorbed by a solid will eventually be converted to heat. Some of this heat will be lost by radiation, convection and conduction. One can generally assume that the energy lost from the surface through reradiation is negligible, however, if the laser pulse is too long so that heat can be conducted over a larger area, then a large area contributes to reradiation and even though the power per unit area may be small, the total power reradiated may approach the power absorbed. The amount of heat lost by radiation can be estimated by calculating the temperature profile on the surface as a function of time and position and numerically integrating the thermal radiation from the surface using the calculating temperature profile and Stefan's law. An approximate estimate of the heat lost by radiation can be calculated roughly as follows:

The thermal diffusion length $\ell \simeq (\kappa\tau)^{\frac{1}{2}}$, where κ is the thermal diffusivity and τ is the laser pulse length, can be used to calculate how far the heat will

diffuse during a laser pulse of duration τ. For aluminium, for example, and for a laser pulse duration of 60 ns

$$\ell = (1.03 \times 60 \times 10^{-9})^{\frac{1}{2}} = 2.4 \times 10^{-3} \text{ mm}$$

if the laser pulse is focussed to a spot radius, ω_o of 0.5 mm, then the heated volume is

$$V = \pi \omega_o^2 \ell$$

$$= 3.14(0.5)^2 \times 2.48 \times 10^{-4}$$

$$= 1.19 \times 10^{-9} \text{ mm}^3$$

the mass involved in the heating process is

$$m = \rho V \quad , \qquad \rho \text{ is the density}$$

$$= 2700 \times 1.19 \times 10^{-9} = 5.13 \times 10^{-6} \text{ gm.}$$

The rise in the surface temperature can now be calculated with the aid of the following equation

$$\Delta T = \frac{\alpha E}{mC} \quad , \quad \text{where } \alpha \text{ is the optical}$$

absorption coefficient, therefore the temperature rise for $\alpha = 0.05 \text{ cm}^{-1}$ and $E = 20$ mJ is

$$\Delta T = \frac{0.05 \times 20 \times 10^{-3}}{5.13 \times 10^{-6} \times 0.83} = 230°C$$

the heat lost by radiation can now be calculated using Stefan's law

$$E_{rad} = \sigma A(T - T_o)^4, \quad \text{where } \sigma \text{ is constant}$$

T_o is the surrounding temperature and A is the interaction area,

$$\therefore E_{rad} = 1.7\ \mu J.$$

This energy is only 0.17% of the energy absorbed.

The energy lost by convection is proportional to 1.25 power of the temperature difference between the surface and the surrounding gas and can be calculated using the following equation:

$$E_{convection} = 20.9 \times 10^{-5}(T - T_o)^{1.25}$$
$$= 7.869 \times 10^{-5}\ \mu J.$$

This loss due to convection is even much more smaller than the energy loss due to radiation and can be ignored completely.

The only effective mode of heat transfer to the adjacent air is conduction. This heat, although small, can be used to deflect a narrow probe beam skimming of the surface. Below the damage threshold of the surface, this deflection will be proportional to the laser energy absorbed. When damage starts to occur at the surface, changes in the optical properties of the surface takes place, this leads to an increased absorption due to the increased carrier concentration. The amplitude of the probe beam deflection will increase leading to a non-linearity in the deflection versus incident laser energy. This deviation has been found experimentally

to indicate the onset of laser induced damage to the optical specimen under test.

4.3 PRINCIPLES OF THE PULSED OPTICAL DEFLECTION OR "MIRAGE EFFECT".

A schematic view of the geometry of the pulsed optical deflection experiment is shown in Figure 4.3a, the heated sample lies in the xz plane and the focussed probe beam is y_o above the surface, when the irradiating laser pulse is incident on the sample surface, a time dependent rise in the temperature of the sample surface causes a corresponding temperature rise in the gas layer adjacent to the surface. This temperature rise leads to a temperature gradient and therefore a transient refractive index gradient in the gas layer which in turn deflects the probe beam. The probe beam will also be deflected by the acoustic wave generated due to the laser absorption, this wave will propagate from the interaction region to the probe beam where it generates a temperature rise by adiabatic compression. The gradient of this temperature rise deflects the probe beam. The acoustic wave also deflects the probe beam through the pressure dependence of the index of refraction. These two contributions are small compared to the deflection generated by the temperature gradient as a result of heat conduction from the heated sample surface and can be ignored[2].

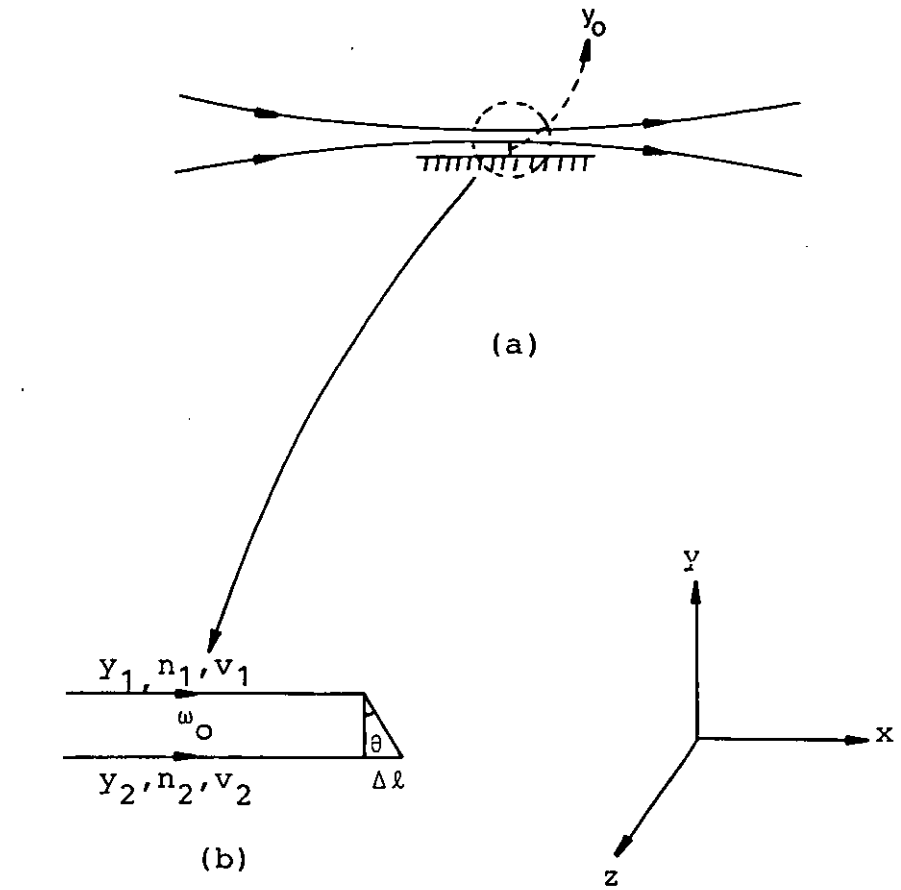

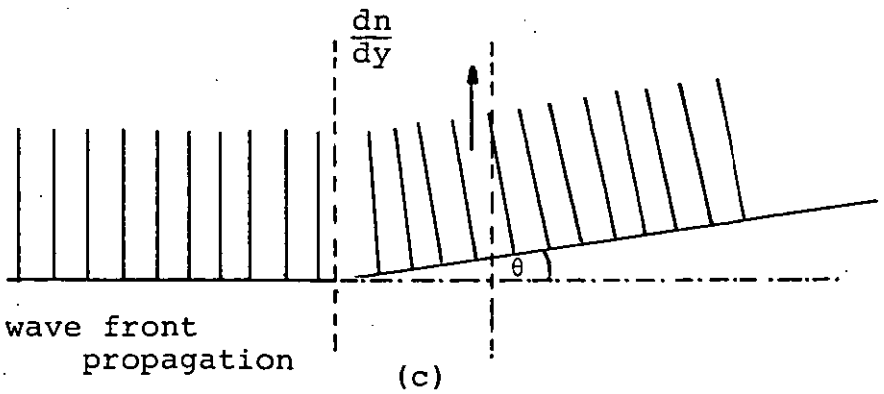

Figure 4.3: Geometry of the optical deflection experiment.

The refractive index for a gas having a temperature T°C can be written in the following form[28]:

$$n_T = 1 + \frac{n_o + 1}{1 + \sigma_o T} \tag{4.3}$$

where n_o is the index of refraction at 0°C and σ_o is a slowly varing function of the wavelength. This wavelength dependence can be ignored and σ_o can be considered constant and is equal to 0.0003/°C for air near room temperature. As the probe beam passes through the heated region near the sample surface, the direction of the beam is bent. Since the value of σ_o is very small, the corresponding bending is also small, thus with no significant error, the average path of the probe beam can be assumed to be a straight line, i.e.

$$y = y_o + mx \tag{4.4}$$

where m is the slope. Because the probe beam has a finite beam waist which is determined by the F-number of the focussing lens, the index of refraction will cause the upper part of the probe beam to travel with less velocity than the lower part of the beam, according to this the upper part of the beam will travel with a velocity v_1 and the lower part of the beam will travel with a velocity v_2 and therefore the lower part of the beam will travel a $\left(\frac{v_2}{v_1}\right)dx$ while the upper part will travel only dx, where dx is the incremental path length

as shown in Figure 4.3b, therefore the path difference between the two beams is:

$$\Delta = \left(\frac{v_2}{v_1} - 1\right) dx \ . \tag{4.5}$$

This path difference will tilt the wavefront of the probe beam through an angle θ (see Figure 4.3c) given by

$$\theta = \tan\theta = \frac{\Delta}{\omega_o} \tag{4.6}$$

$$= \left(\frac{v_2}{v_1} - 1\right) \frac{dx}{\omega_o} \tag{4.7}$$

where ω_o is the probe beam width. In terms of indices of refraction the deflection becomes:

$$\theta = - \left(\frac{n_2}{n_1} - 1\right) \frac{dx}{\omega_o} \tag{4.8}$$

but

$$n_1 = n_2 + \frac{dn}{dy} (y_2 - y_1) \tag{4.9}$$

where y_2 and y_1 represent the distances of the upper and the lower part of the probe beam above the sample surface. This is approximately equal to ω_o, the probe beam waist

$$\therefore \quad n_2 = n_1 - \frac{dn}{dy} \omega_o \tag{4.10}$$

$$\therefore \quad \theta = - \left(\frac{n_1 - \frac{dn}{dy} \omega_o}{n_1} - 1\right) \frac{dx}{\omega_o}$$

$$\theta = - \left(\frac{n_1}{n_1} - \frac{1}{n_1} \frac{dn}{dy} \omega_o - 1 \right) \frac{dx}{\omega_o}$$

$$\theta = \frac{1}{n_1} \frac{dn}{dy} dx \quad . \tag{4.11}$$

Since n_1 is approximately equal to n_o, the ambient refractive index, therefore,

$$\theta = \frac{1}{n_o} \frac{dn}{dy} dx \tag{4.12}$$

but $$\frac{dn}{dy} = \frac{dn}{dT} \cdot \frac{dT}{dy}$$

$$\therefore \quad \theta = \frac{1}{n_o} \frac{dn}{dT} \frac{dT}{dy} dx \sim \frac{\ell}{n_o} \frac{\partial n}{\partial T} \cdot \frac{\partial T}{\partial y} \tag{4.13}$$

where ℓ represents the interaction path length of the probe beam.

The quantity $\frac{\partial T}{\partial y}$ for the case of pulsed optical beam deflection has been solved by Jackson et. al[2]. They showed that a pulsed laser beam of Gaussian radius ω_o and energy E and a pulse duration τ produces a temperature gradient in an infinite medium with a weak absorption coefficient α as follows:

$$\frac{\partial T}{\partial y} = \frac{-\alpha E}{2\pi K \tau y} \left[\exp\left(\frac{-2y^2}{\omega_o^2 + 8\kappa t} \right) - \exp\left(\frac{-2y^2}{\omega_o^2} \right) \right] \tag{4.14}$$

$$\text{for} \quad 0 \leq t \leq \tau$$

$$\frac{\partial T}{\partial y} = \frac{-\alpha E}{2\pi K \tau y}\left[\exp\left(\frac{-2y^2}{\omega_o^2+8\kappa t}\right) - \exp\left(\frac{-2y^2}{\omega_o^2+8\kappa(t-\tau)}\right)\right] \qquad (4.15)$$

for $t > \tau$.

In the above two equations, K is the thermal conductivity of the medium, κ is the thermal diffusivity, t is the time after the start of the laser pulse and y is the distance of the probe beam from the sample surface. Upon substituting equation (4.13) we get:

$$\theta = -\frac{\ell}{n_o}\frac{\partial n}{\partial y} \cdot \frac{\alpha E}{2\pi K \tau y}\left[\exp\left(\frac{-2y^2}{\omega_o^2+8\kappa t}\right) - \exp\left(\frac{-2y^2}{\omega_o^2+8\kappa(t-\tau)}\right)\right] \qquad (4.16)$$

$$\therefore \quad \theta = B\,\frac{\alpha E}{y}\left[\exp\left(\frac{-2y^2}{\omega_o^2+8\kappa t}\right) - \exp\left(\frac{-2y^2}{\omega_o^2+8\kappa(t-\tau)}\right)\right] \qquad (4.17)$$

where $B = \frac{1}{2\pi K \tau} \cdot \frac{\ell}{n_o}\frac{\partial n}{\partial T}$ is a constant.

The last equation shows that α can be measured as a function of the wavelength. The thermal diffusivity can also be measured by fitting the observed signal shape to the form in the square bracket in equation (4.17).

4.4 EXPERIMENTAL DETERMINATION OF LASER INDUCED DAMAGE USING THE OPTICAL BEAM DEFLECTION TECHNIQUE.

A - The parallel geometry: A schematic of the

experimental arrangement is shown in Figure 4.4. The CO_2-TEA laser is fully described in Chapter 3, and has a maximum energy of about 50 mJ in 60 ns pulse duration (full width at half maximum). This laser was directed so that it was normal to the sample surface and was focussed by a short focal length germanium lens. A sodium chloride flat was used to divert a portion of the beam for the purpose of energy measurement in each pulse. The output from 2.0 mW He-Ne laser (Spectra Physics 136) is spatially filtered and then made parallel by a 50 mm camera lens to generate the probe beam. The probe beam is then focussed by 200 mm small diameter lens. After leaving the interaction region above the sample surface, the probe beam was made parallel again by 100 mm lens. A knife-edge was inserted into the parallel section to intercept half of the probe beam. The probe beam was then focussed by 20 mm camera lens on the photodetector (RCA solid state detector model C30816 with 35 ns rise time). The signal was finally displayed on a digital scope with a band width of 60 MHz. Both the sample and the focussing germanium lens were held on one optical assembly in such a way that they can be moved together with respect to the probe beam at the same time, keeping the spot-size unchanged. The movement of the assembly was controlled by a micrometer with one micron resolution.

The minimum offset of the probe beam is controlled

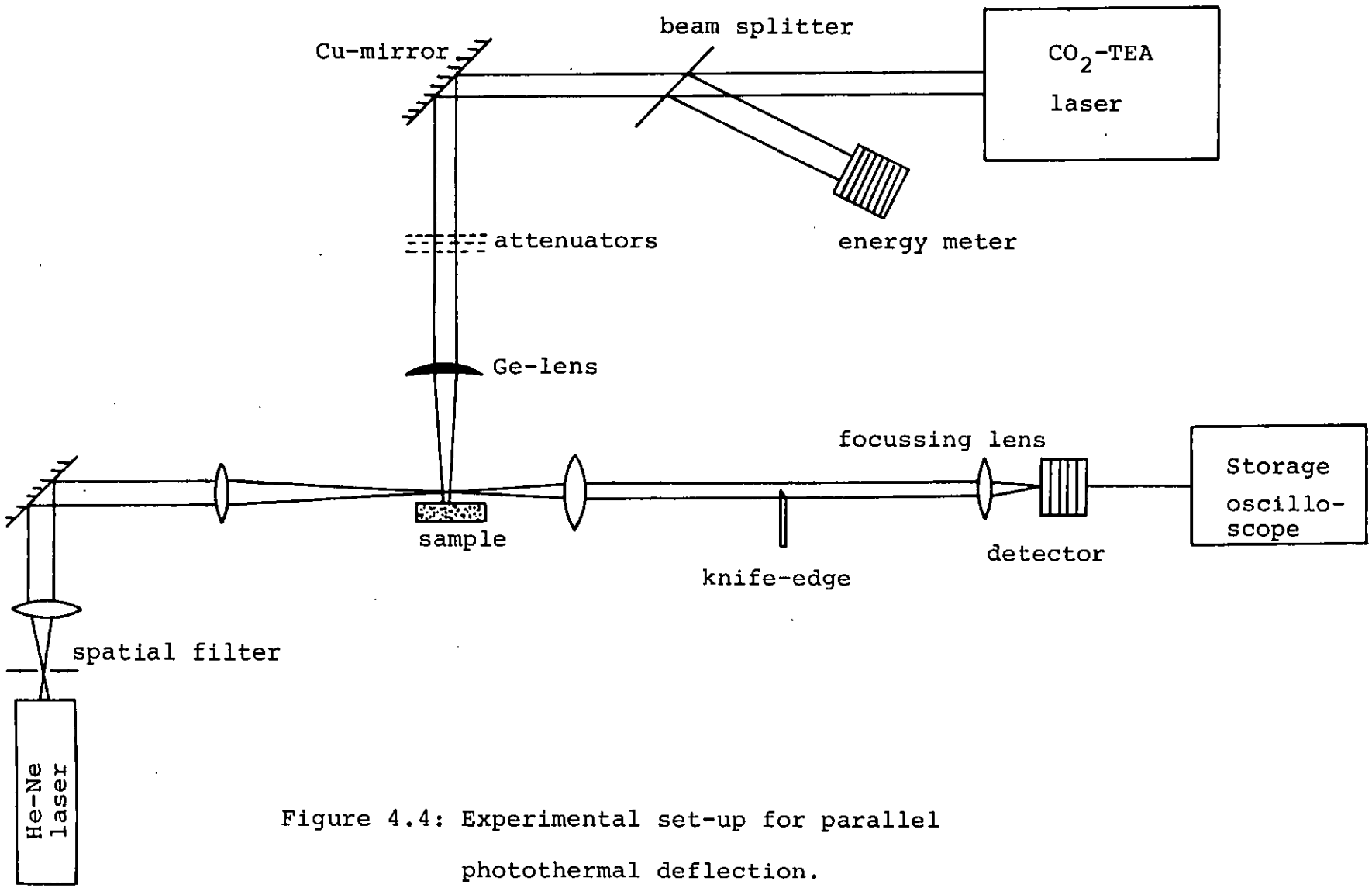

Figure 4.4: Experimental set-up for parallel photothermal deflection.

by the F-number of the focussing lens and the sample length L, this offset can be calculated with the aid of Figure 4.5. The minimum offset is given by the following equation:

$$y_o = \frac{L}{2} \tan \frac{\psi}{2} \qquad (4.18)$$

but $$\frac{\psi}{2} = \frac{f}{2D} = \frac{1}{2F} ,$$

where f is the focal length of the focussing lens, F is the F-number and D is the diameter of the focussing lens. Since $\frac{\psi}{2}$ is normally very small, therefore, equation (4.18) can be simplified to become:

$$y_o = \frac{L}{2} \tan \frac{1}{2F} \simeq \frac{L}{4F} \quad . \qquad (4.19)$$

The minimum offset as a function of the F-number is shown in Figure 4.6a.

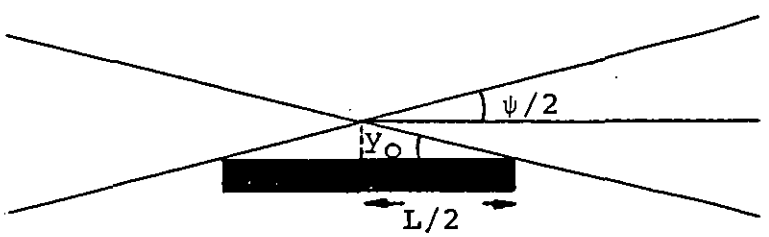

Figure 4.5: Geometry for minimum offset.

If the test sample is raised beyond this distance, the sample edges will start to block the edges of the probe beam, this results in a decrease in the sensitivity.

There are two possible ways of reducing the minimum offset. Firstly, the y_o can be reduced by increasing the F-number but the problem here is that there will be an increase in the probe beam waist as indicated by the following relationship[29]:

$$\text{beam waist} = 0.8 \times 10^{-3} F(\text{mm}) \qquad (4.20)$$

this increase in the probe beam waist is shown in Figure 4.6b. The second alternative is to reduce the sample length L.

Many samples were damage tested, Figures 4.7 - 4.10 show the optical beam deflection signal as a function of the incident laser energy for aluminium, aluminium coating on glass, high reflection coating on germanium and stainless steel respectively. In each figure the damage threshold to the sample is indicated by the sudden change in the deflection signal. As can be seen, the relation between the deflection signal and the laser energy is linear before the onset of laser damage to the sample under test. After damage the signal appears to follow a power dependence with the energy, i.e. E^n in agreement with the results presented in Chapter Three.

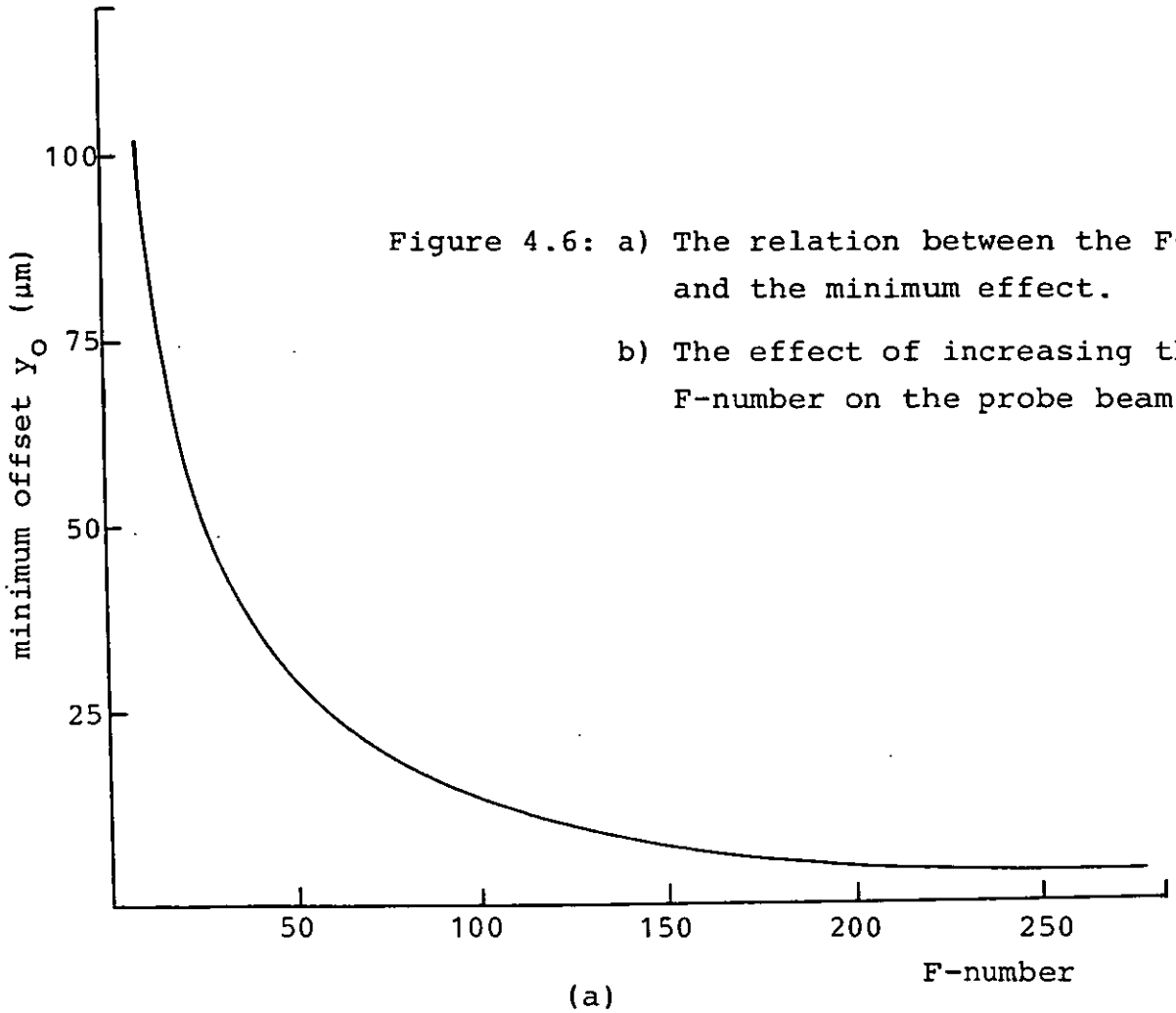

(a)

Figure 4.6: a) The relation between the F-number and the minimum effect.

b) The effect of increasing the F-number on the probe beam waist.

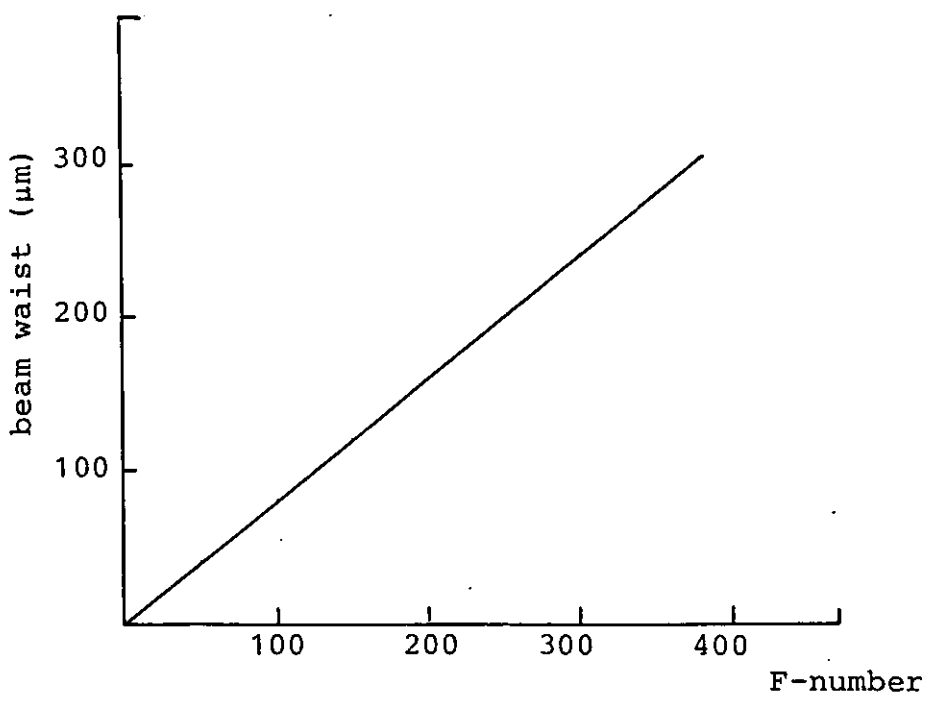

(b)

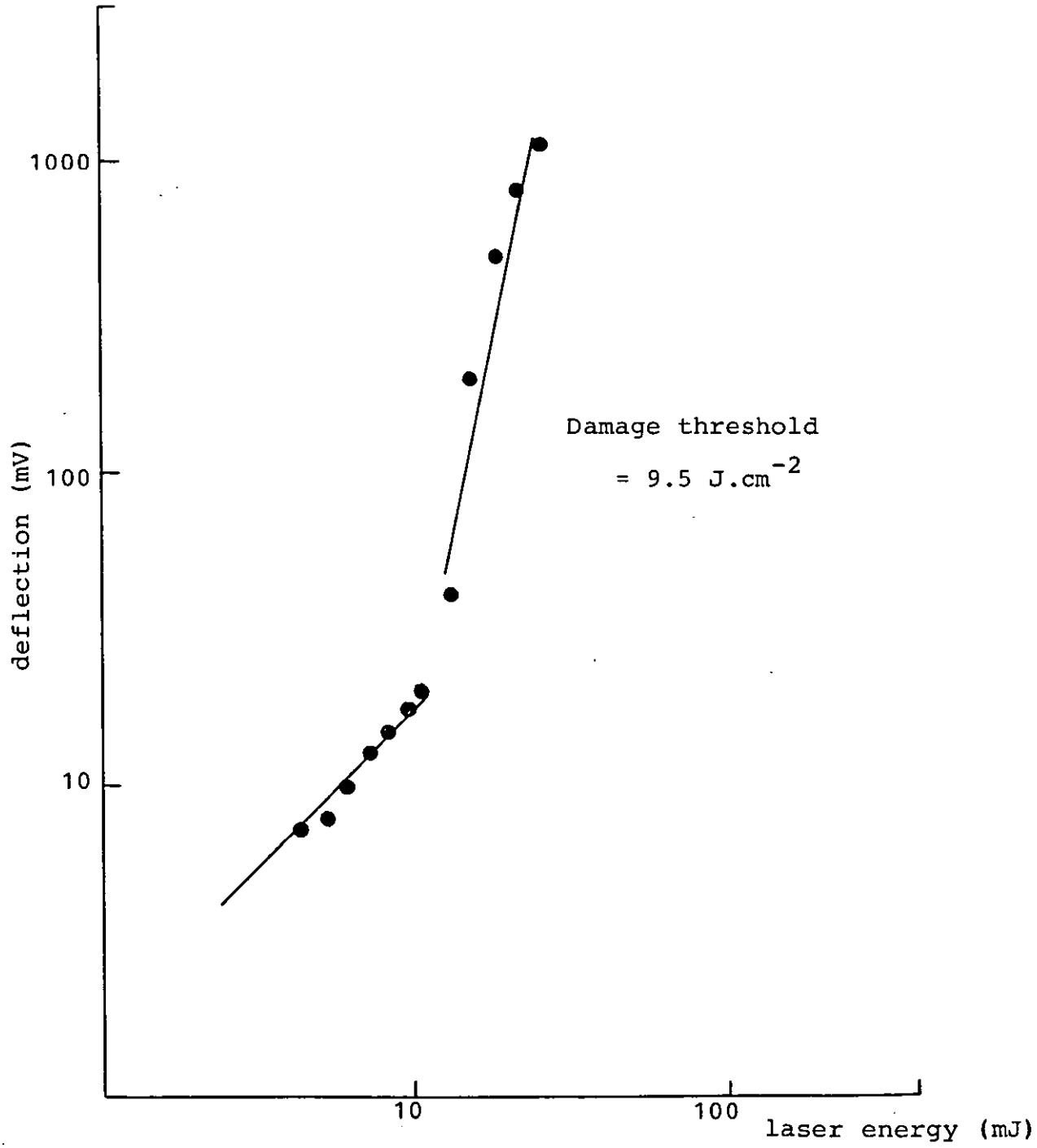

Figure 4.7: Deflection signal as a function of the incident laser energy for an aluminium film on glass substrate.

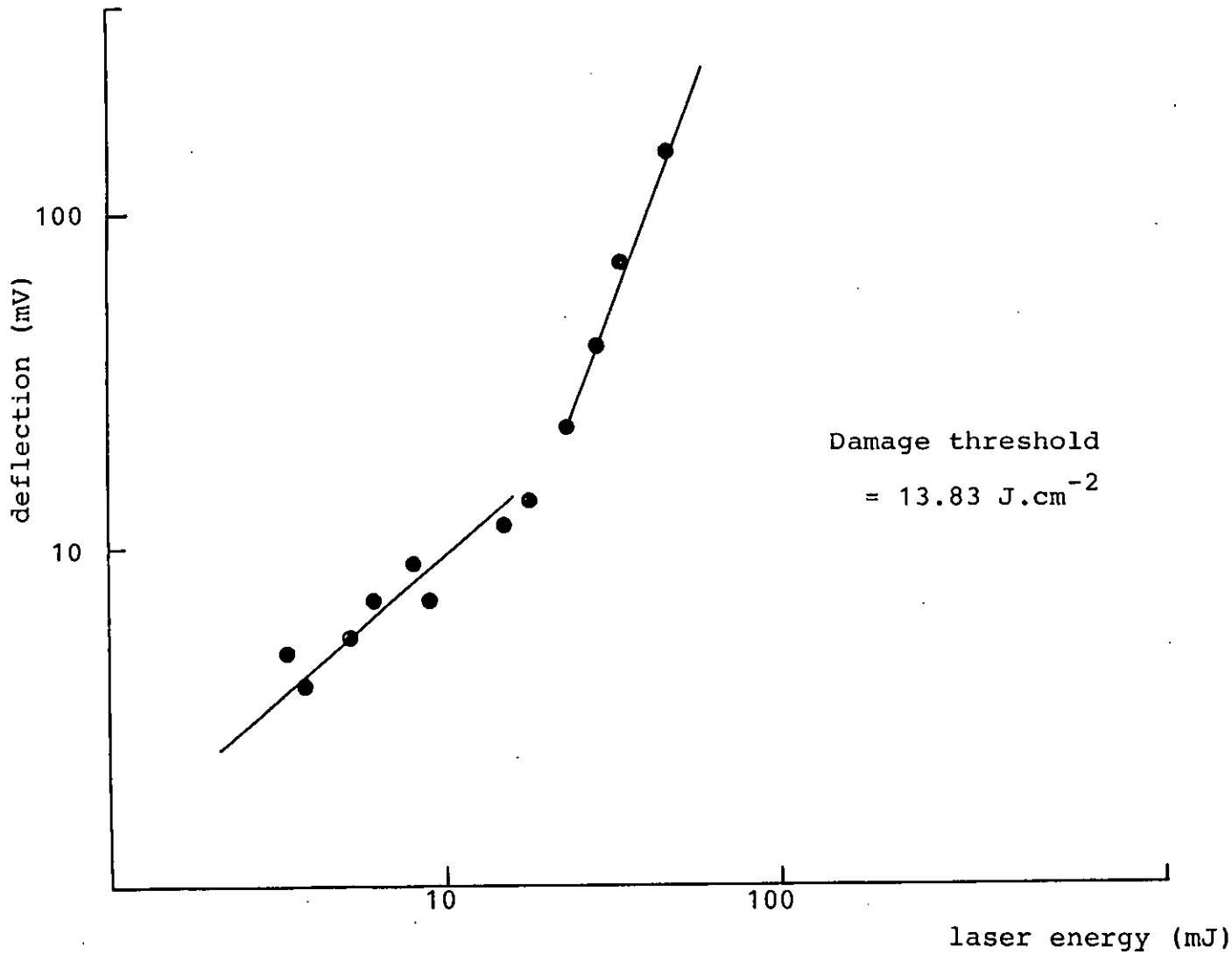

Figure 4.8: Deflection signal as a function of the incident laser energy for Aluminium.

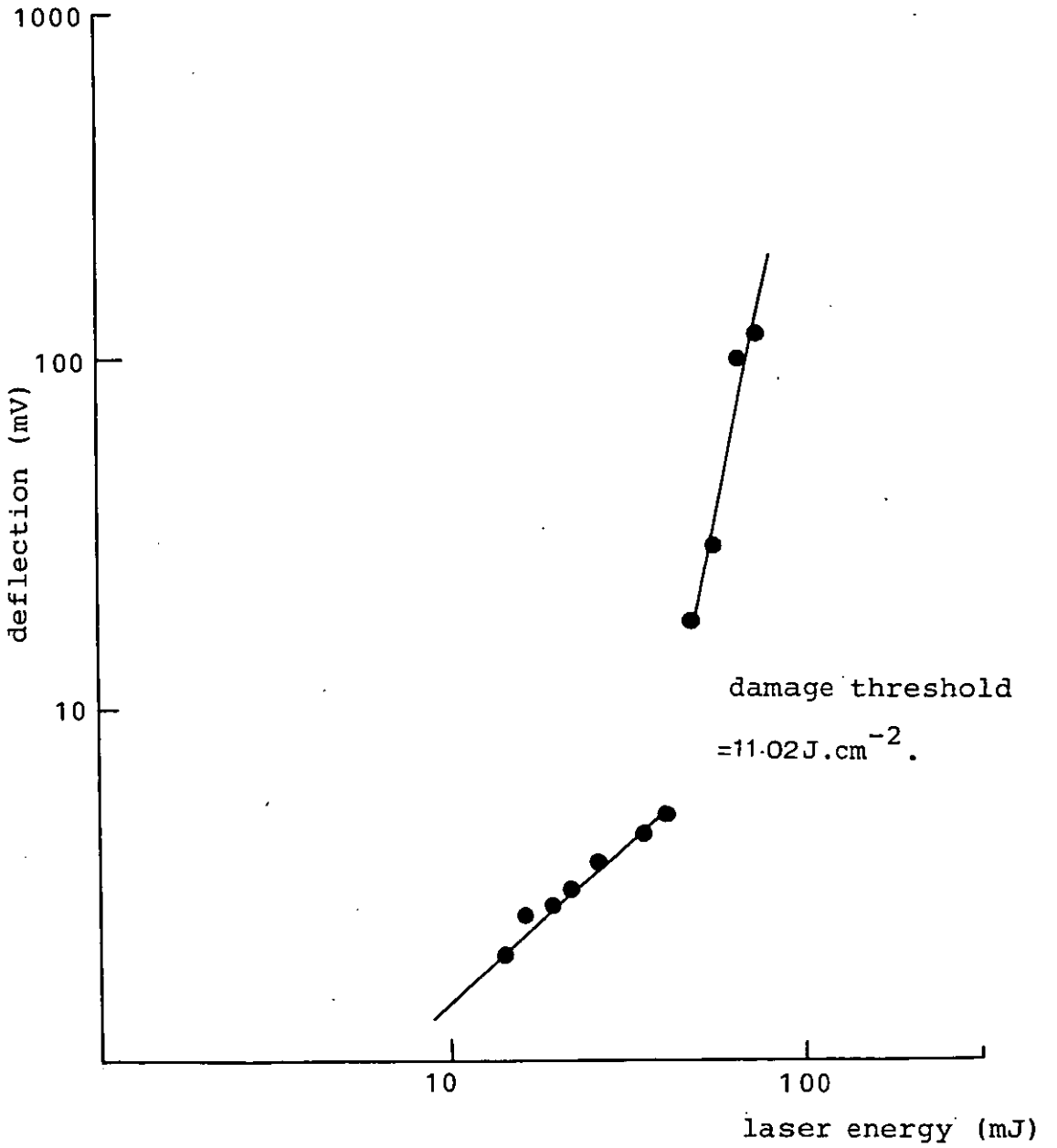

Figure 4.9: Deflection signal as a function of the incident laser energy for high reflection coating on germanium substrate.

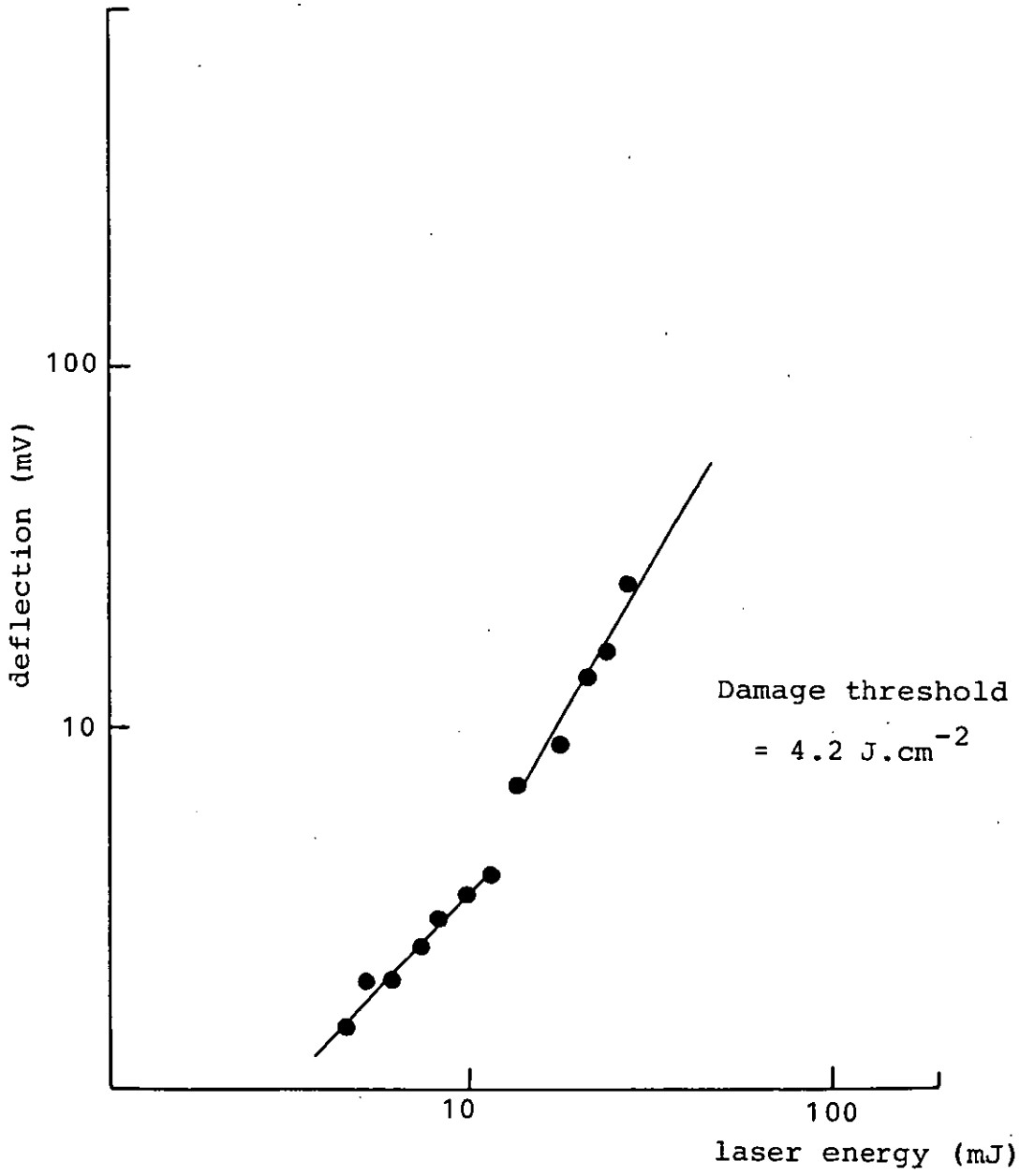

Figure 4.10: Deflection signal as a function of the incident laser energy for stainless steel.

B - Reflection geometry: The experimental set-up used in this case is shown in Figure 4.11. The angle of incidence was nearly 20°. The deflection signal for a typical example of an aluminium film on a glass substrate is shown in Figure 4.12. The calculated damage threshold is 9.22 $J.cm^{-2}$ compared to 9.55 $J.cm^{-2}$ for the case of parallel geometry. This difference might be due to the increased sensitivity for the reflection geometry compared to the parallel geometry. In the parallel geometry, the probe beam is deflected by the refractive index gradient set-up when the pump beam is absorbed locally in the sample. This effect is also present in the reflection geometry, but here the probe beam is also deflected by the "bump" caused by the local heating and resulting thermal expansion of the interaction region.

4.5 DISCUSSION.

It was found that the optical deflection signal depends on many parameters which is explained below.

1 - Signal dependence on the probe beam offset y_o: Figure 4.13 shows the deflection as a function of the probe beam offset for a sample length of 5 mm. The solid curve represents the deflection signal calculated by using equation (4.17). As shown, the deflection signal decreases very rapidly with increasing the probe beam offset, this behaviour is expected to arise

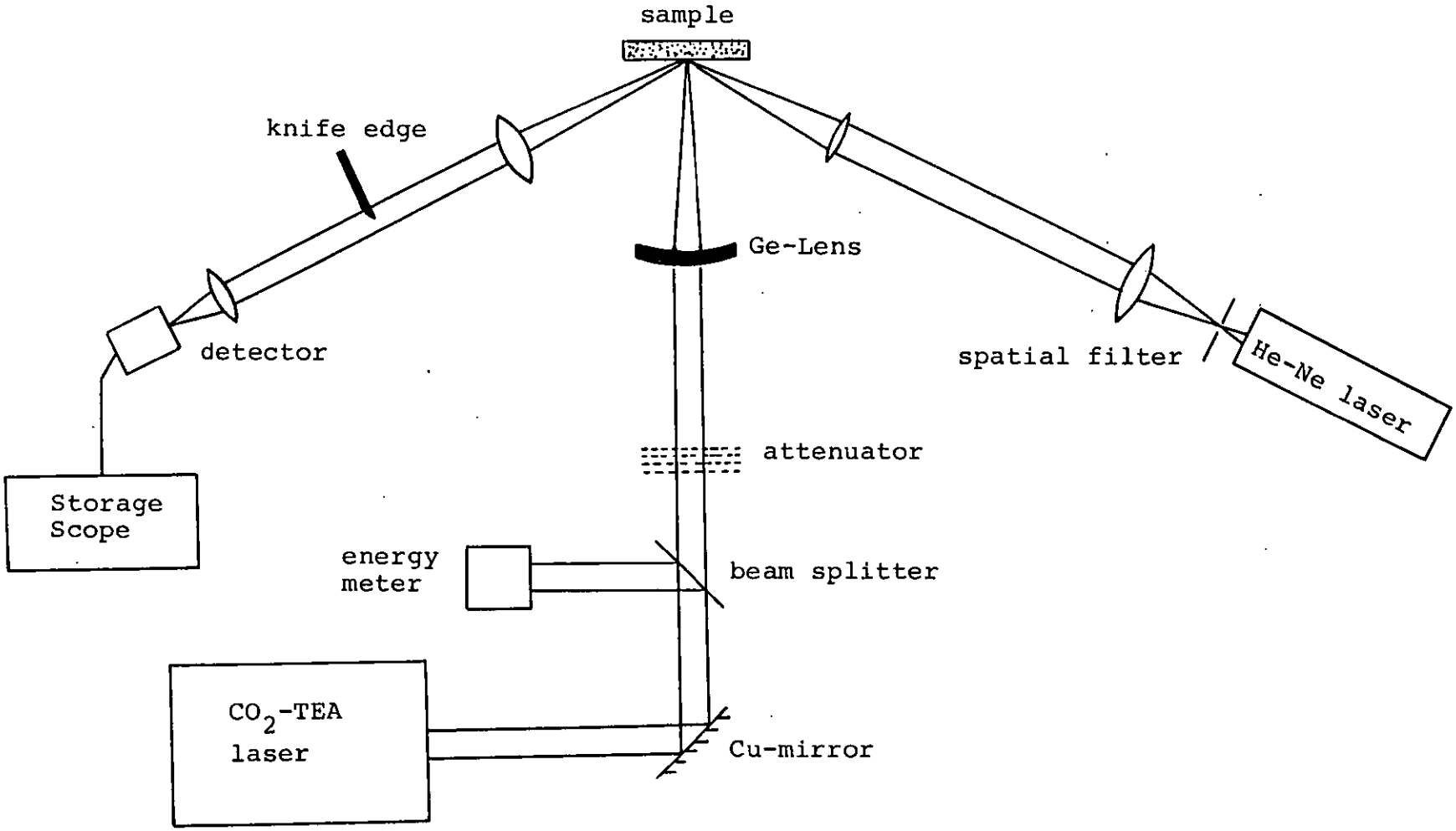

Figure 4.11: The experimental set-up for the reflection geometry.

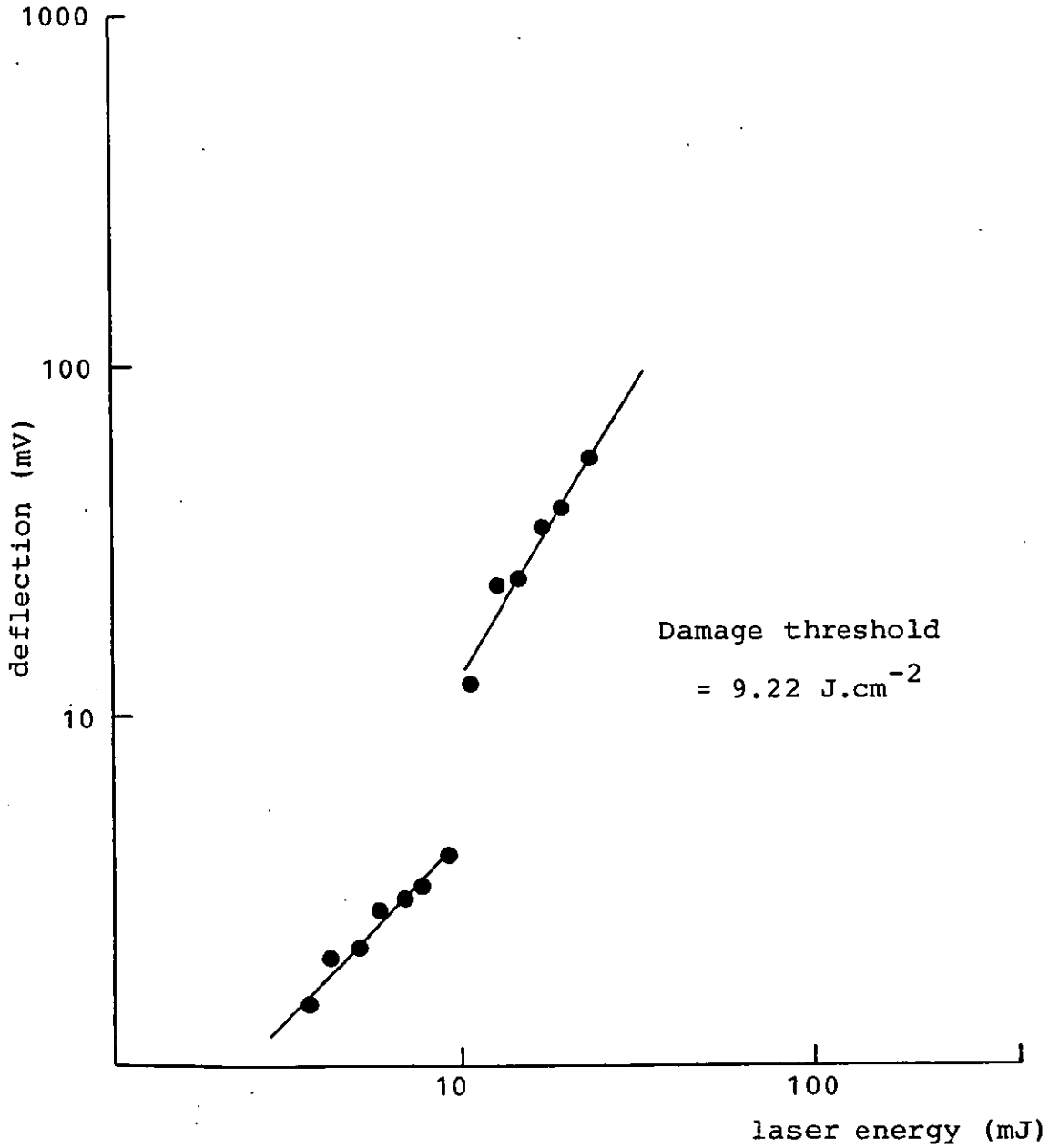

Figure 4.12: Deflection signal as a function of the incident laser energy for an aluminium film on a glass substrate using reflection geometry.

from the damped nature of the thermal waves. The signal shape for a different offset is shown in Figure 4.14. The total energy incident on the sample (an aluminium film on glass substrate) was 31 mJ.

2 - Angle of incidence: For small angles the probe beam will graze the sample surface for a long distance and therefore the deflection will be large. For large angles, the probe beam will graze the sample surface for a smaller distance and consequently less signal is expected, as shown in Figure 4.15.

3 - Signal dependence on the distance between the interaction region and the detector: Since the probe beam after leaving the interaction region was made parallel before being focussed on the detector, the deflection signal did not depend on the distance between the interaction region and the detector, as shown in Figure 4.16.

4 - Signal dependence on the probe beam waist: In order to keep the offset distance y_o constant during this experiment, a small stainless steel ball bearing of 8 mm diameter was used as a sample. The ball bearing was mounted on a vertical translator and the probe beam waist was varied by changing the F-number of the focussing lens. Each time the height of the ball bearing was adjusted until the ball was just

touching the probe beam, this was easily done by observing the diffraction pattern on a distant screen, the waist was then calculated using equation (4.20). Figure 4.17 shows the deflection signal as a function of the probe beam waist. It is evident that the sensitivity can be increased by reducing the probe beam waist. This is in agreement with a previous investigation[30].

5 - Signal dependence on the lateral separation: It has been shown by Aamdt et. al[31] that when the probe beam passes through the centre of the index of refraction gradient, only a normal component is present. For rays on either sides of the centre, a reduced amplitude normal deflection component and a transverse deflection component, i.e., deflection parallel to the plane of the sample and normal to the probe beam, are observed. The presence of a reduced normal component could be used to confirm that the temperature profile generated by a Gaussian beam, is also a Gaussian. Figure 4.18 shows the deflection signal as a function of the lateral separation, this is nearly Gaussian since the CO_2 pulse is also Gaussian, while Figure 4.19 shows the deflection signal shape for different lateral separations. It should also be noted that for a maximum sensitivity one must make sure that both the probe and the pump beams must lie in one plane normal to the sample surface.

6 - Deflection signal as a function of the pump laser energy: Figure 4.20 shows the effect of varying the pump laser energy for a constant offset. The signal increases as the energy is increased, this increase is linear as long as the damage threshold of the sample is not exceeded. In figure 4.21 the shape of the deflection signal for different values of the pump laser energy are presented for an aluminium film on a glass substrate.

4.6 CONCLUSION.

It has been shown that the photothermal deflection of a small probe beam can be used as a precursor for the detection of the early stages of laser induced damage in optical components. In many of the samples which were damage tested using this technique, it was very difficult to see any signs of damage even at high magnification. The technique also has the following advantages over the photoacoustic technique.

1 - It is at least as sensitive.

2 - It can be employed in a hostile environment.

3 - There is no light scattering problem.

4 - There is no contact between the sample and the probe beam.

On the other hand, the disadvantages of the optical beam deflection technique can be summarized in the

following points:

1 - Alignment is more difficult.

2 - For transparent materials it may be difficult to find a probe beam that is transmitted by some materials.

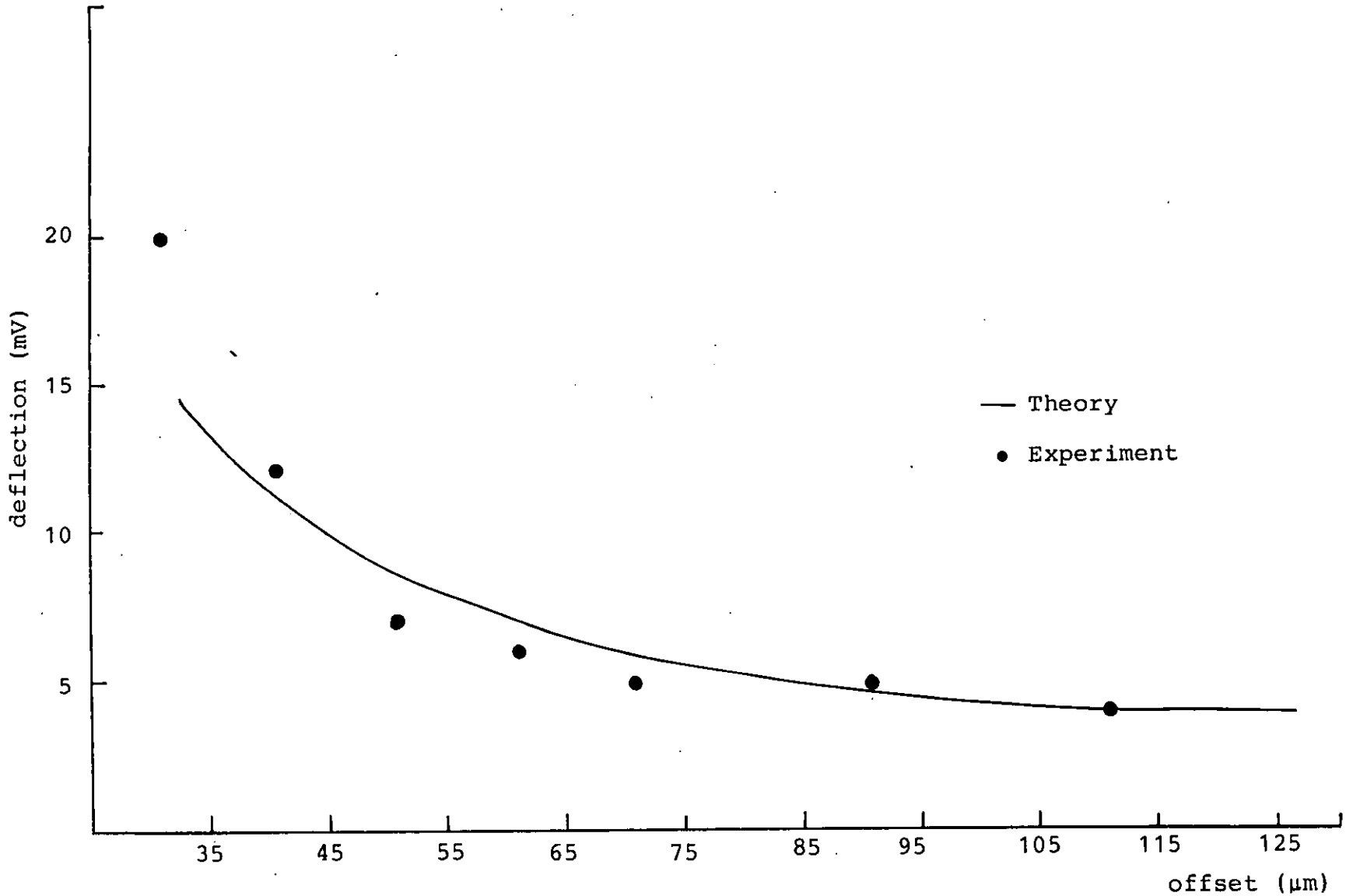

Figure 4.13: Deflection signal as a function of the offset y_o for a sample length of 5 mm.

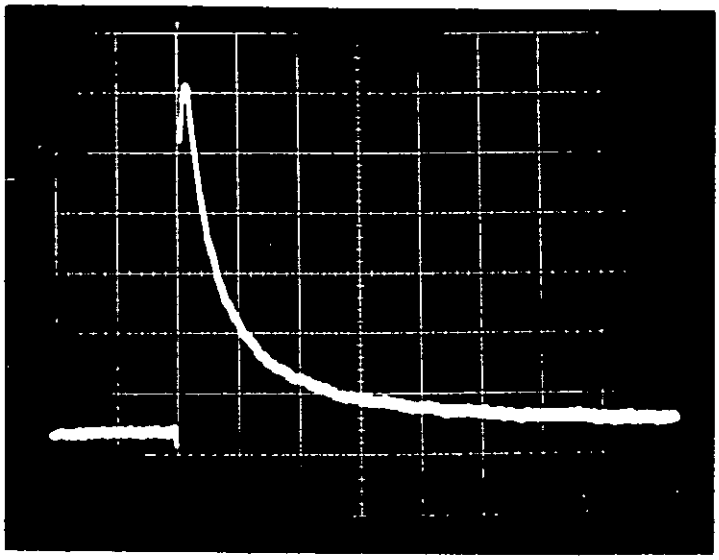

15 μm

0.1 msec/div

20 mV/div

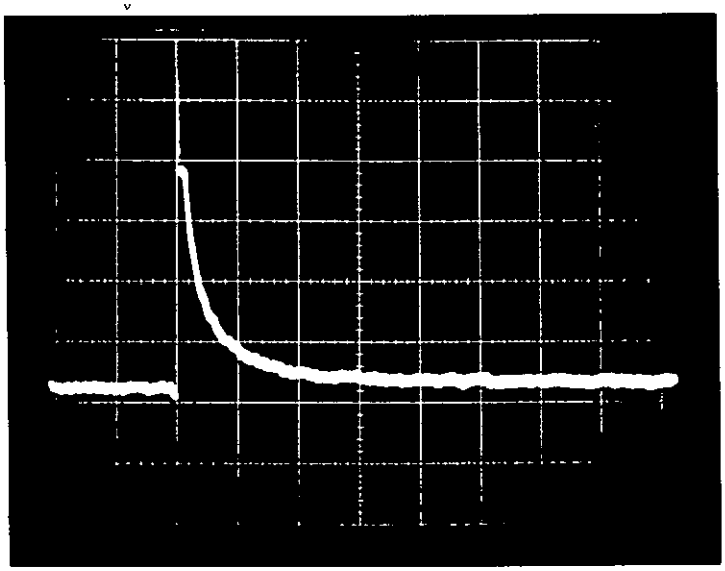

20 μm

0.1 msec/div

20 mV/div

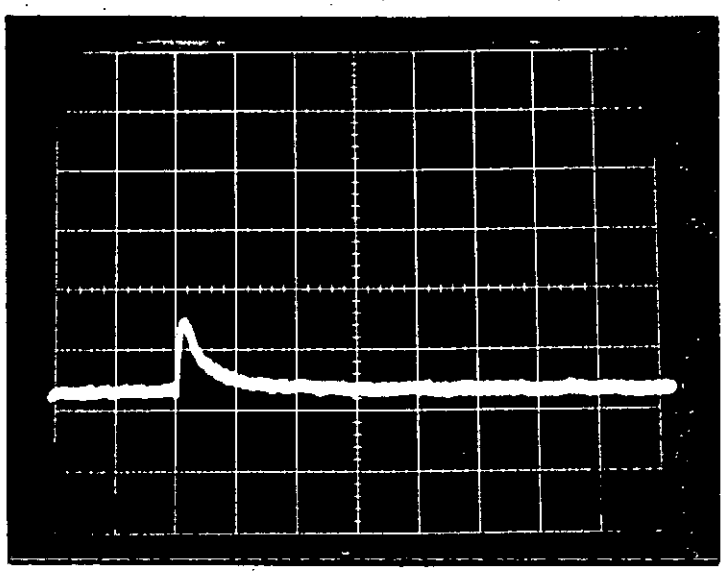

25 μm

0.1 msec/div

20 mV/div

Figure 4.14: Deflection signals for different offsets.

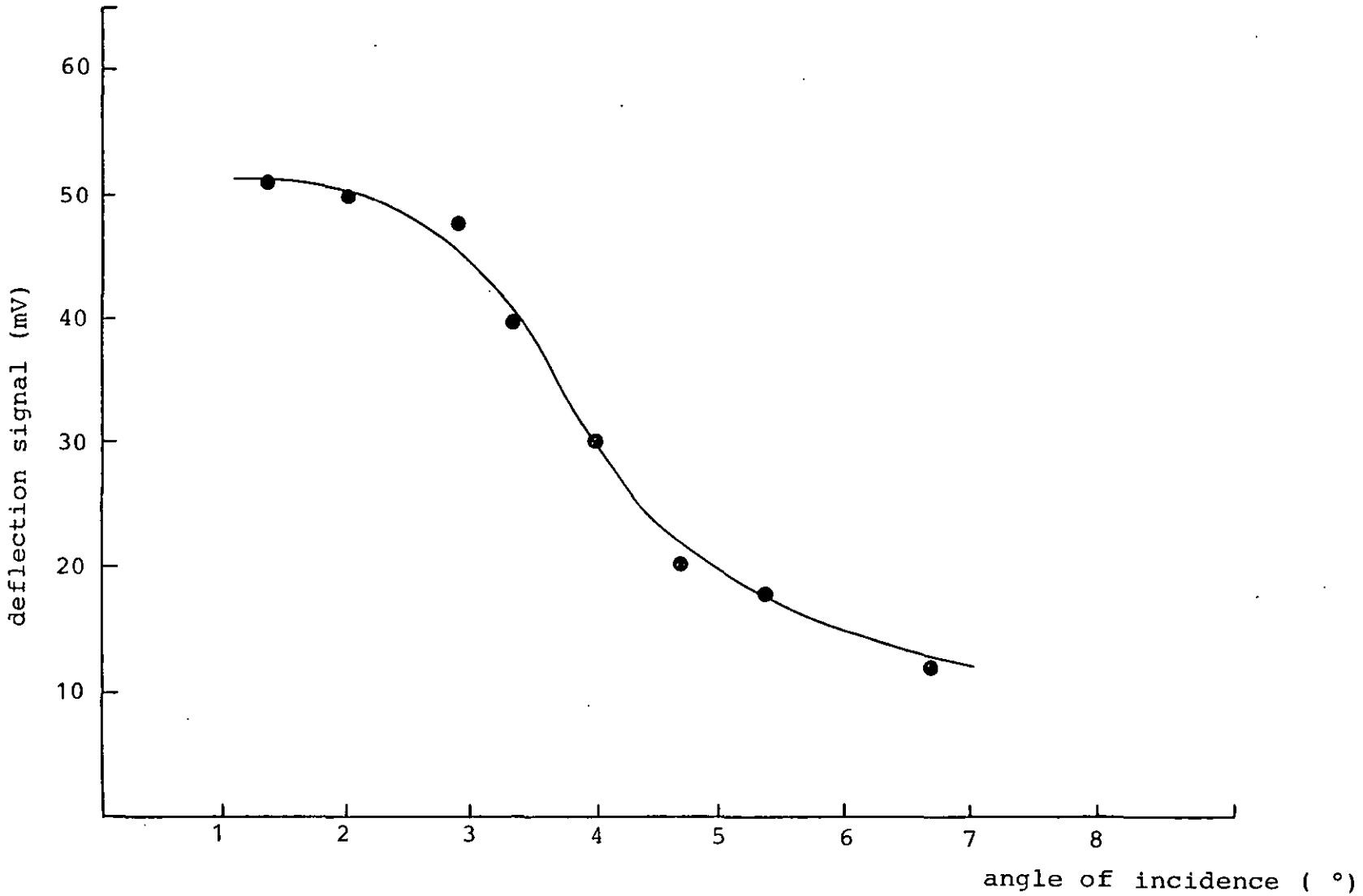

Figure 4.15: Deflection signal dependence of the angle of incidence in case of the reflection geometry.

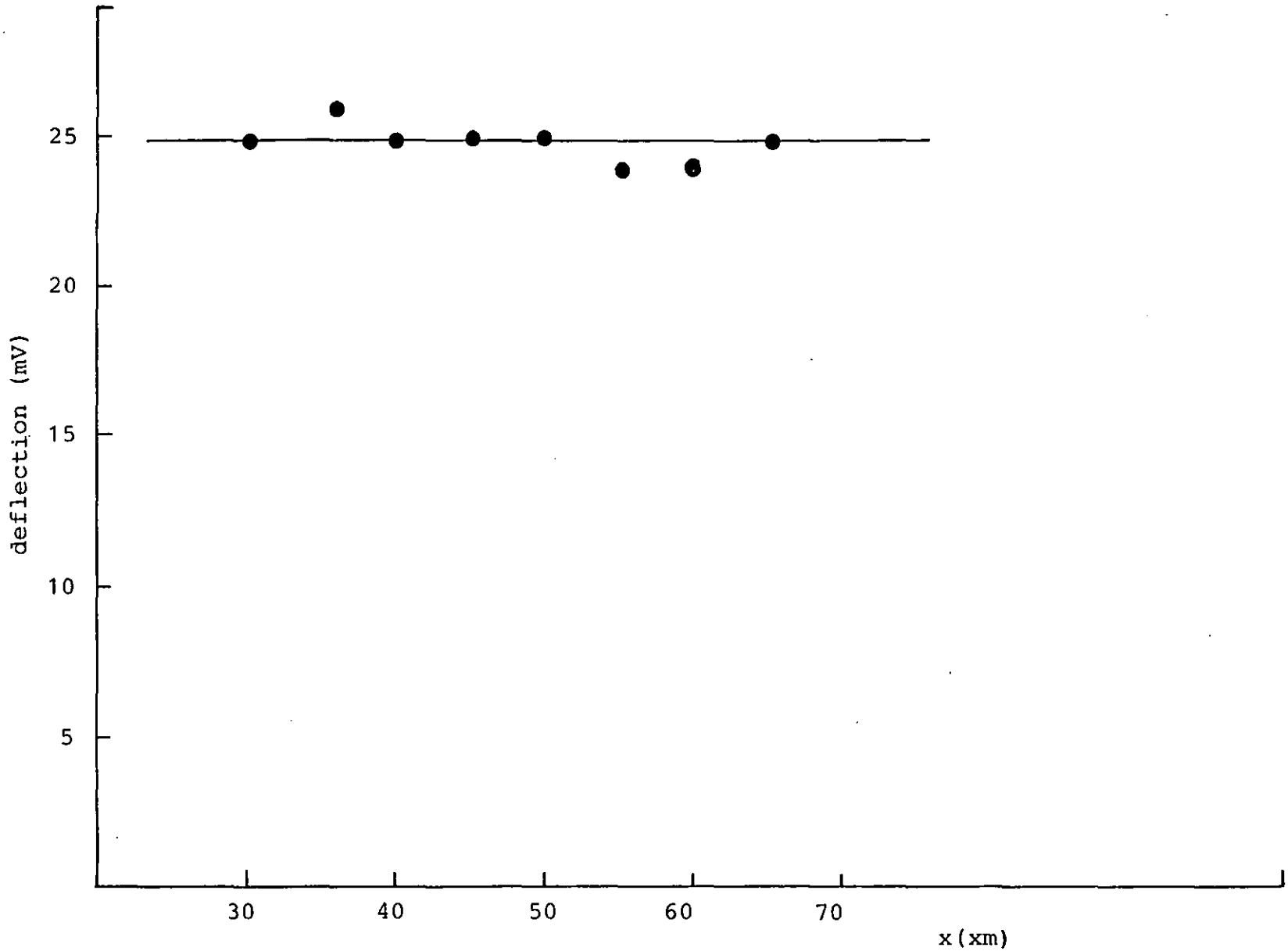

Figure 4.16: The relation between the deflection signal and the distance between the interaction region and the detector.

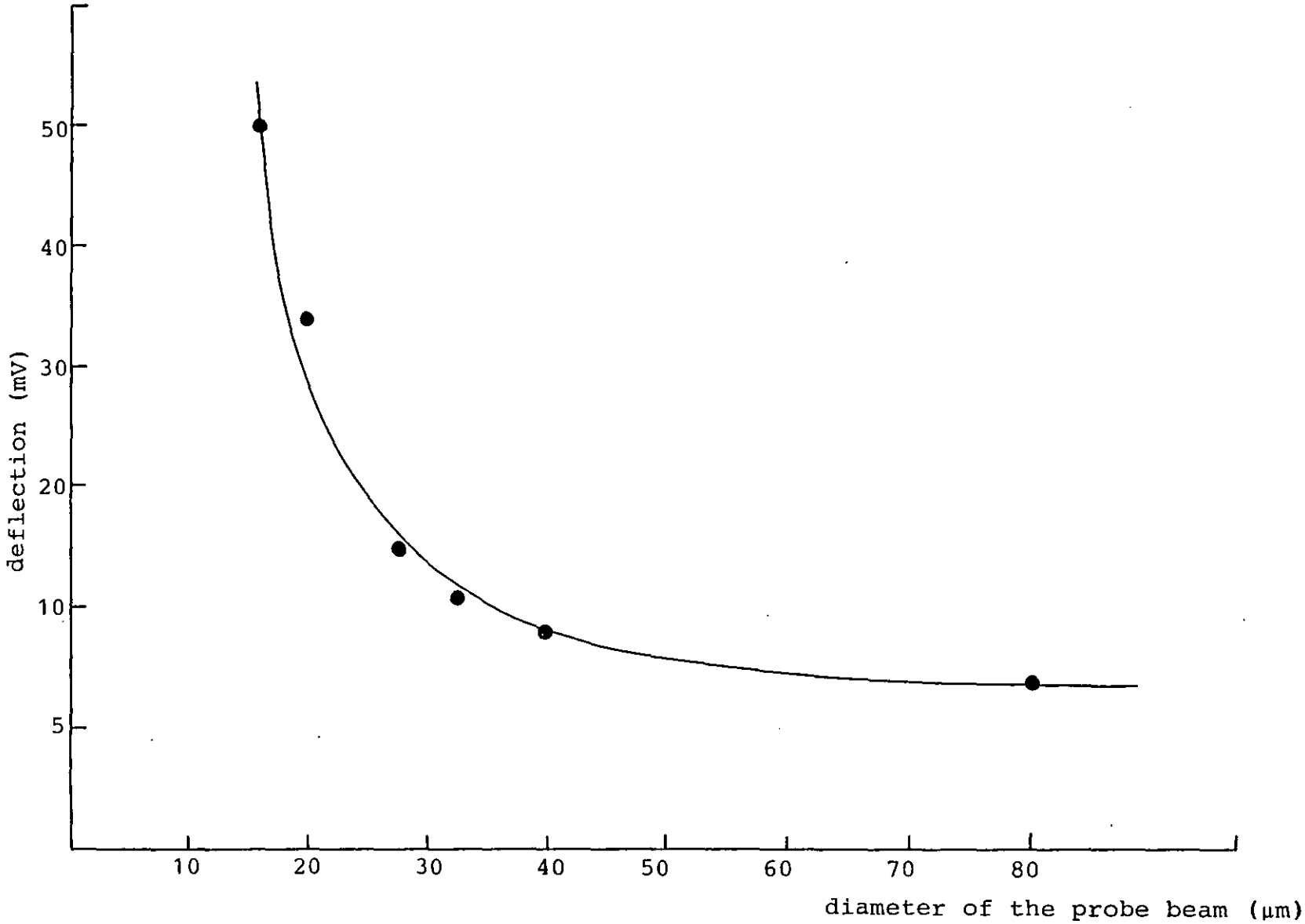

Figure 4.17: The deflection signal as a function of the probe beam diameter.

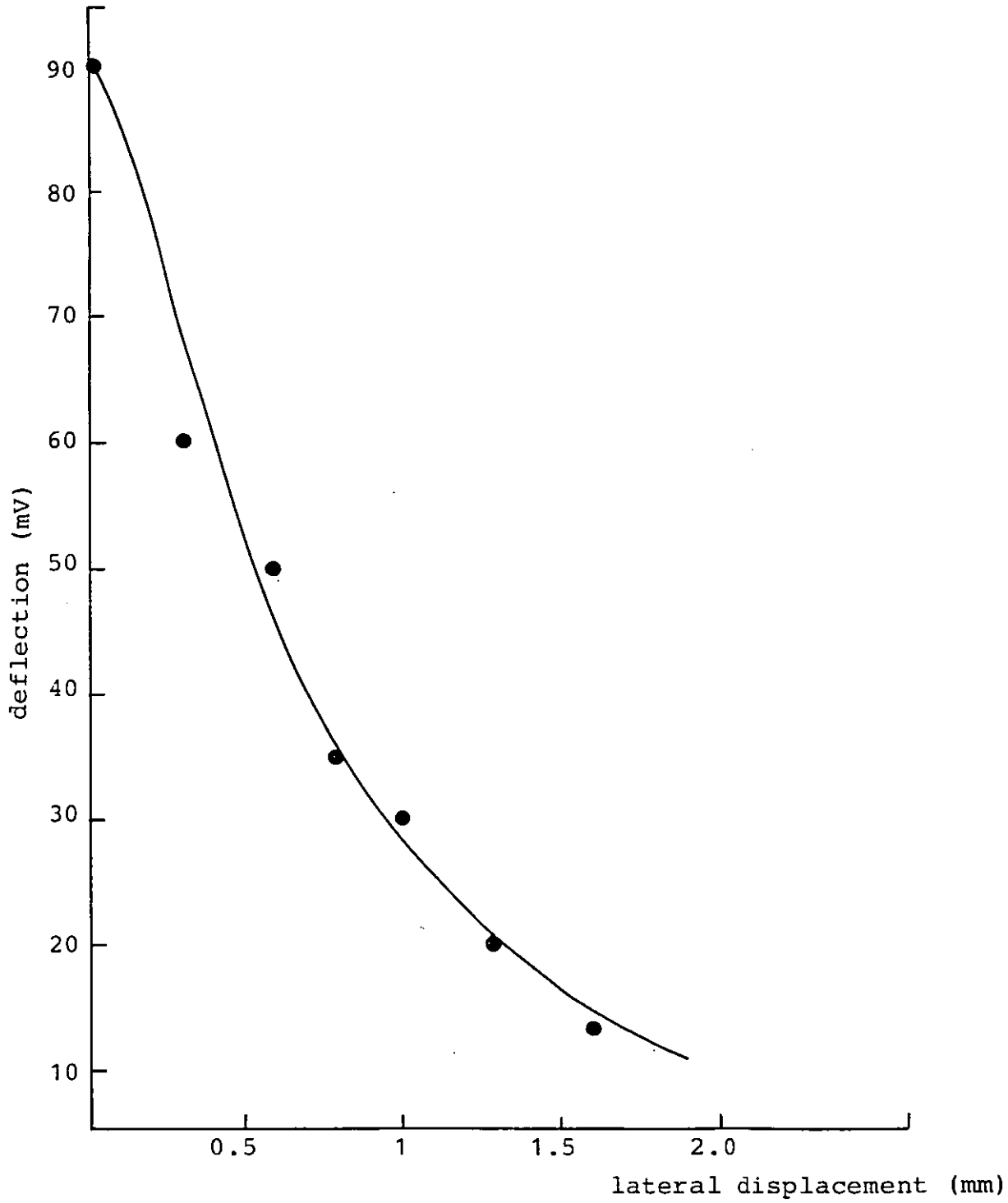

Figure 4.18: The deflection signal as a function of the lateral displacement.

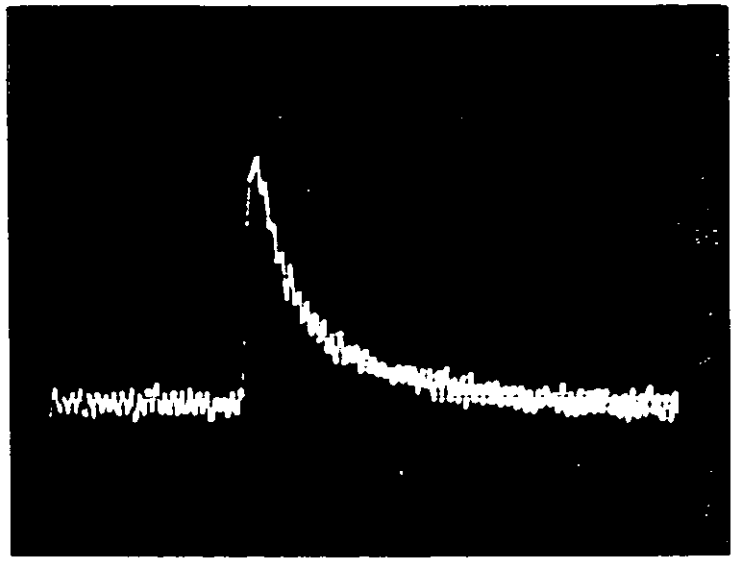

50 µs/div
4 mV/div
0 mm

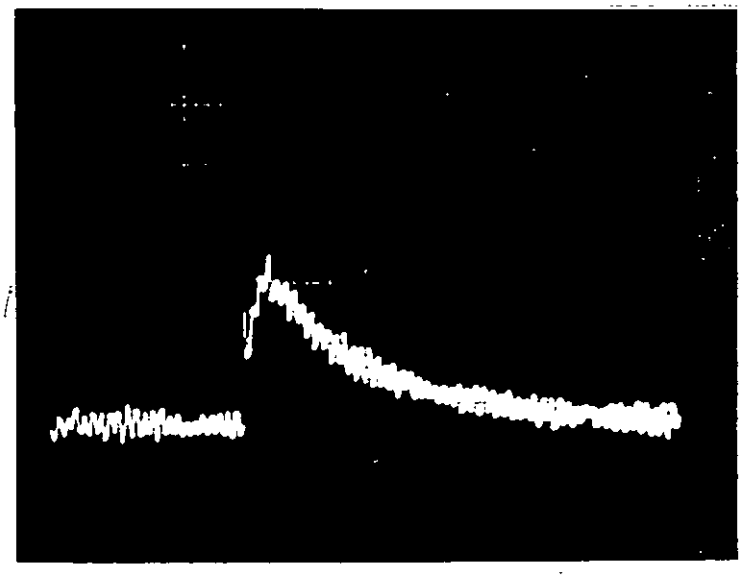

50 µs/div
4 mV/div
0.5 mm

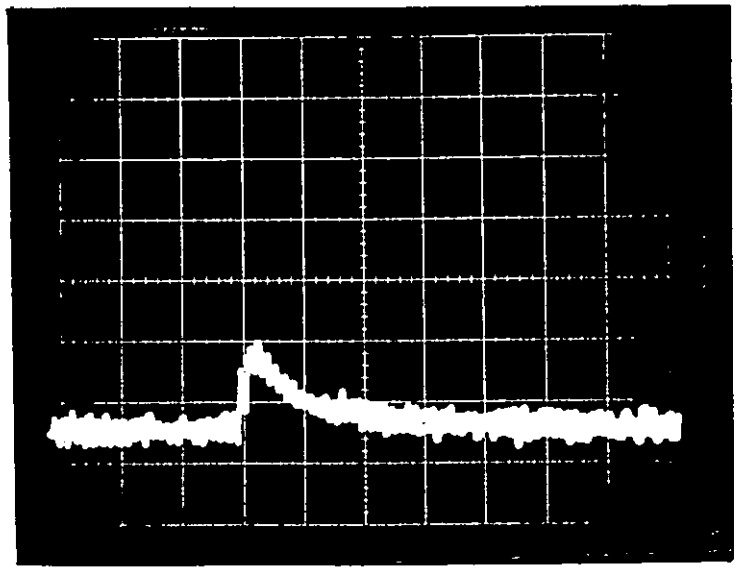

50 µs/div
4 mV/div
0.5 mm

Figure 4.19: Deflection signal shape for different lateral displacements.

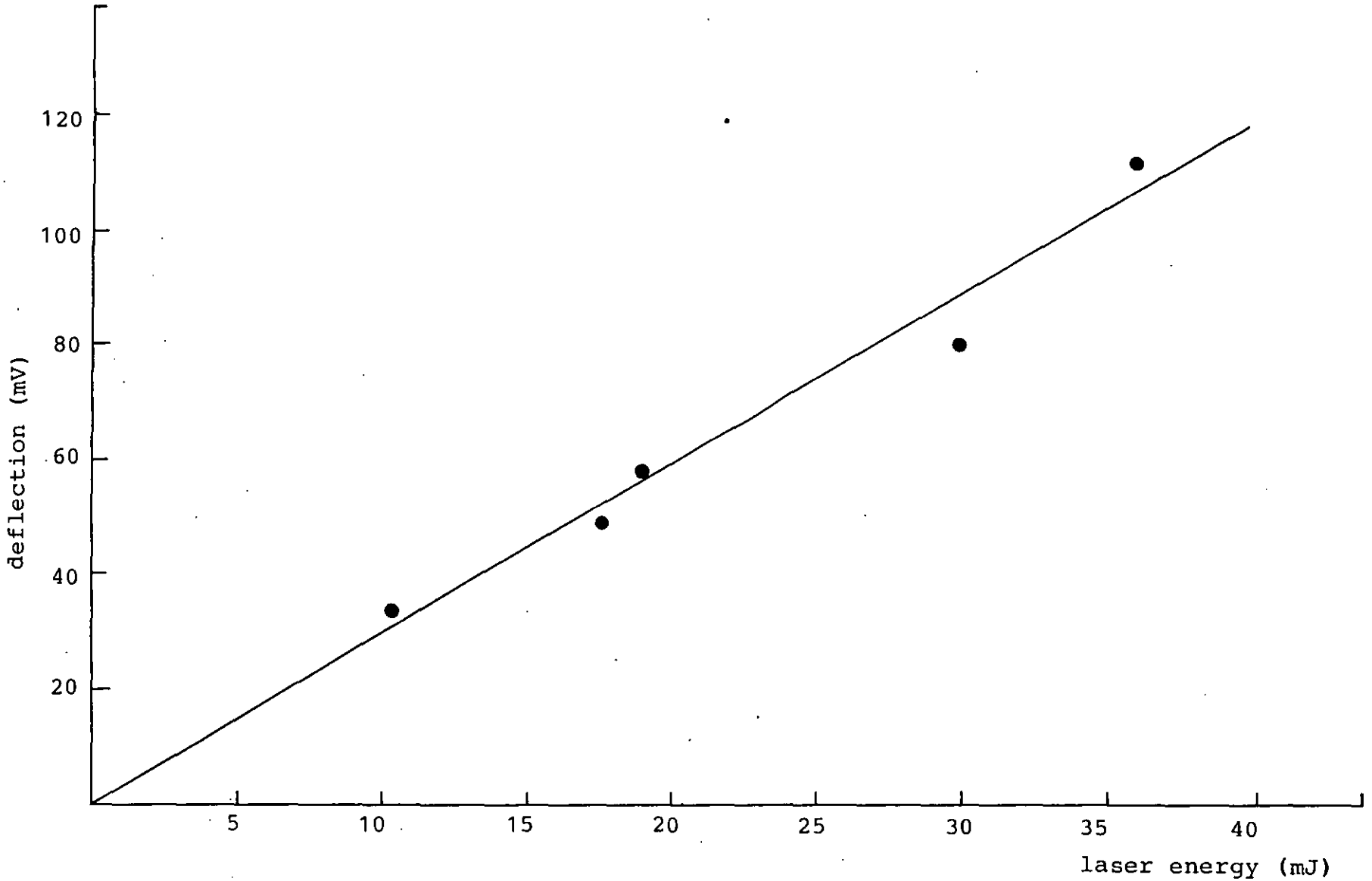

Figure 4.20: Dependence of the deflection signal on the laser energy for a constant offset.

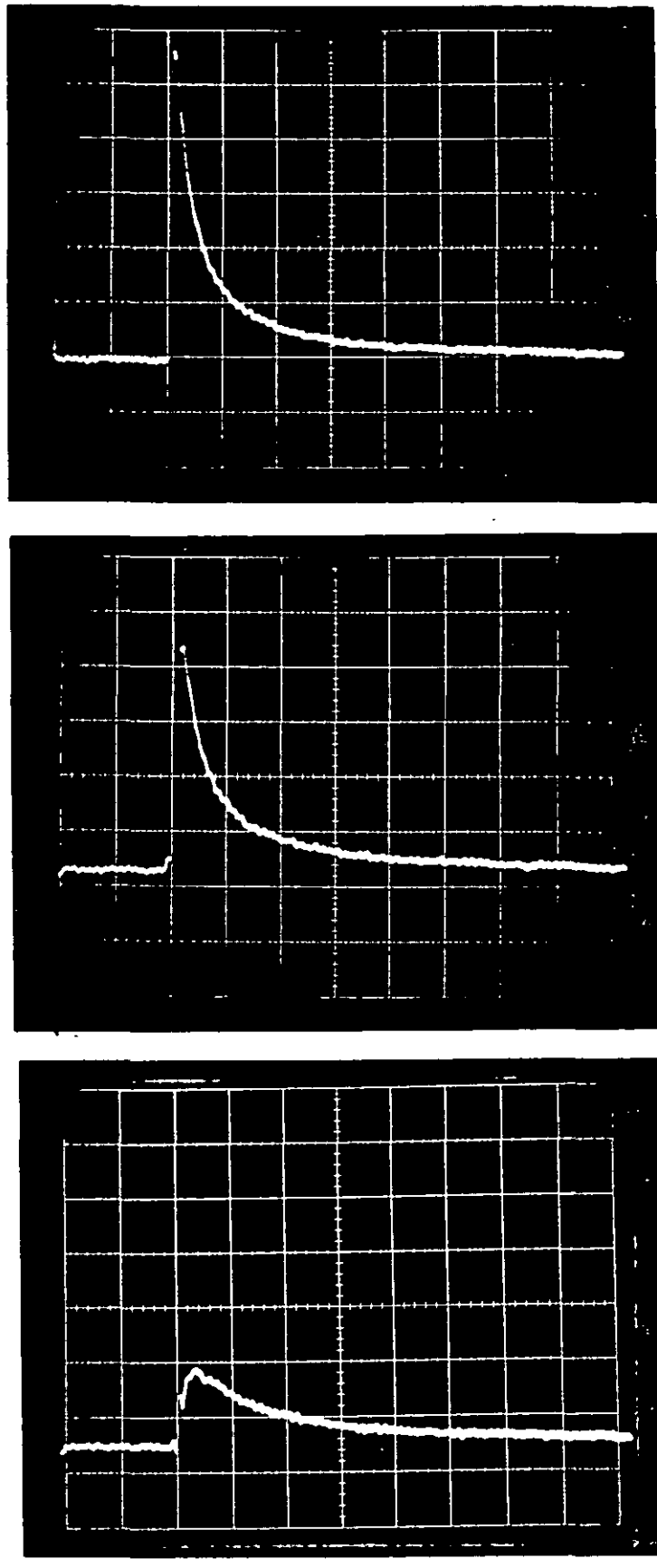

Figure 4.21: Deflection signals for different values of pump laser energy.

CHAPTER FIVE

The Detection of Laser Induced Damage by Laser Scattering

5.1 INTRODUCTION.

When an electromagnetic wave impinges on an atom or molecule, it interacts with the bound electrons transferring energy to the atom. This effect can be pictured as if the lowest ground state of the atom were set into vibration, the frequency of the vibration will be equal to the frequency of the incoming electromagnetic wave. At resonance the electrons vibrating with respect to the nucleus may be regarded as oscillating electric dipoles and as such, they will reradiate electromagnetic energy at a frequency which coincides with that of the incident wave. This reradiation of electromagnetic wave is called scattering, and the combined effect of absorption and scattering is called extinction. It is the scattering which underlines the physical mechanism operative in reflection, refraction and diffraction.

When scattering occurs off a surface which is smooth the scattered light is often confined to one direction and it is called specular reflection. The specular reflection depends on many factors such as, wavelength of the electromagnetic wave, the angle of incidence and the electrical properties such as permittivity and conductivity of the two adjoining media. As a matter of fact, the laws of reflection by a plane boundary are so well understood that, conversely the electrical properties of the material are often determined by

measuring its reflection coefficient according to equation (3.6) of Chapter Three. What happens, however, if the boundary is not plane, but irregular with some sort of variations of height measured from some mean level. Perhaps the most striking difference in the behaviour of a smooth and a rough surface is the fact that a smooth surface will reflect the incident light specularly into a single direction, while a rough surface will scatter into various directions. For a randomly rough surface the scattered light will be continuously distributed in angle, while for a periodically rough surface, the scattered light will be bunched into numbers of diffracted orders located at discrete angles. For example the location of the diffracted orders for a sinusoidally rough surface, as shown in Figure 5.1, are given by the usual grating equation:

$$\sin \theta_m = \sin \theta_i + m \frac{\lambda}{d} \qquad (5.1)$$

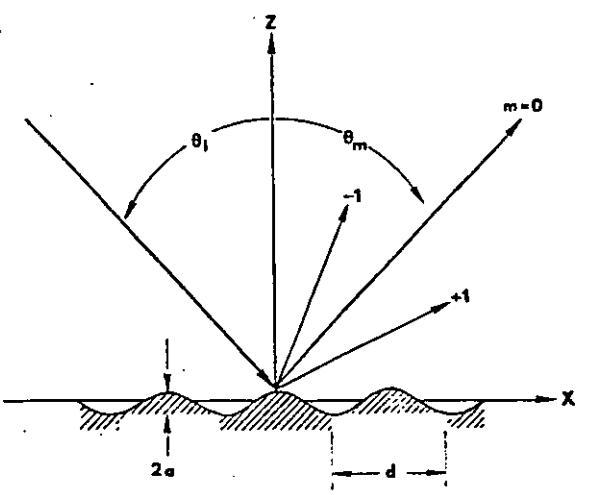

Figure 5.1: Schematic of the scattering from a simple sinusoidal reflecting surface.

where θ_m is the angle of diffraction, θ_i is the angle of incidence and m = ±1, ±2, ±3 ± ... is the diffraction order, λ is the wavelength of light and d is the wavelength of the grating. The positions of the diffracted orders are independent of the depth of the grading but the intensities of the diffracted orders depend strongly on the grating depth. On the other hand, if light traverses a homogeneous medium, it will not be scattered, only inhomogeneities causes scattering. In fact any material medium has inhomogeneities as it consists of molecules each of which acts as a scattering centre, but it depends on the arrangement of these molecules whether the scattering will be effective. In a perfect crystal at zero absolute temperature the molecules are arranged in a very regular way and the waves scattered by each molecule interfere with the light scattered by other molecules in such a way that the net result is that no scattering will occur but only a change in the overall velocity of propagation of the incident light.

5.2 LIGHT SCATTERED BY OPTICAL COMPONENTS.

Light scattered by optical components arises from several sources. In the visible and ultraviolet regions of the electromagnetic spectrum the dominant source of scattered light from optical components is the surface scattering by microirregularities. In general, surface scattering is more important than scattering from

inhomogeneities in the bulk material for transparent optical components. Volume scattering in thin films is important in multilayer reflective and antireflective coatings but even here surface scattering plays the major role. Since, for metallic surfaces, the optical penetration depth is only of the order of hundreds angstroms which can be calculated from equation (3.2), viz,

$$\delta = \left(\frac{\lambda}{\pi\sigma c\mu\mu_o}\right)^{\frac{1}{2}} ,$$

the scattered light is entirely a surface effect. Surface scattering may arise from:

(i) Scratches and digs larger than the wavelength of the viewing light.

(ii) Isolated irregularities which are comparable in size or smaller than the wavelength of the light.

(iii) Correlated irregularities which have heights small relative to the wavelength.

Scattering from correlated irregularities is often the dominant one for optical components used in the near infrared, visible and ultraviolet. Scattering from digs or scratches is only important at longer wavelengths.

Generally the microirregularities cover the entire optical surface statistically and their distribution can be described by a height distribution function which is found experimentally to be Gaussian to a

good approximation. It has been found that in regions where scattering from microirregularities is dominant the fraction of the reflected light which is scattered into directions other than the specular one is well described by a simple scalar scattering theory based on the Kirchhoff diffraction integral. For normal incident light, the dependence of the total integrated scattered light (TIS) on wavelengths is given by[1]:

$$TIS \cong 1 - \frac{R}{R_o} = 1 - \exp\left[-\left(\frac{4\pi\delta}{\lambda}\right)^2\right] \cong \left(\frac{4\pi\delta}{\lambda}\right)^2 \qquad (5.2)$$

where R_o is the fraction of the incident light which is reflected into all angles including the specular direction, R is the specular reflection of the surface and δ is the rms height of the surface microirregularities. The scattered light as a function of the wavelength for different values of δ is shown in Figure 5.2.

Equation (5.2) describes the observed scatter from optical surfaces quite well in the visible, ultraviolet and near infrared regions of the spectrum. However, if the surface is heavily scratched, the height distribution is no longer Gaussian and the above equation is no longer valid since, in this case, the scattered light will be independent of the wavelength.

Since the TIS is a function of the height but not the lateral dimensions of the microirregulatities, it is possible to determine the rms value of the roughness,

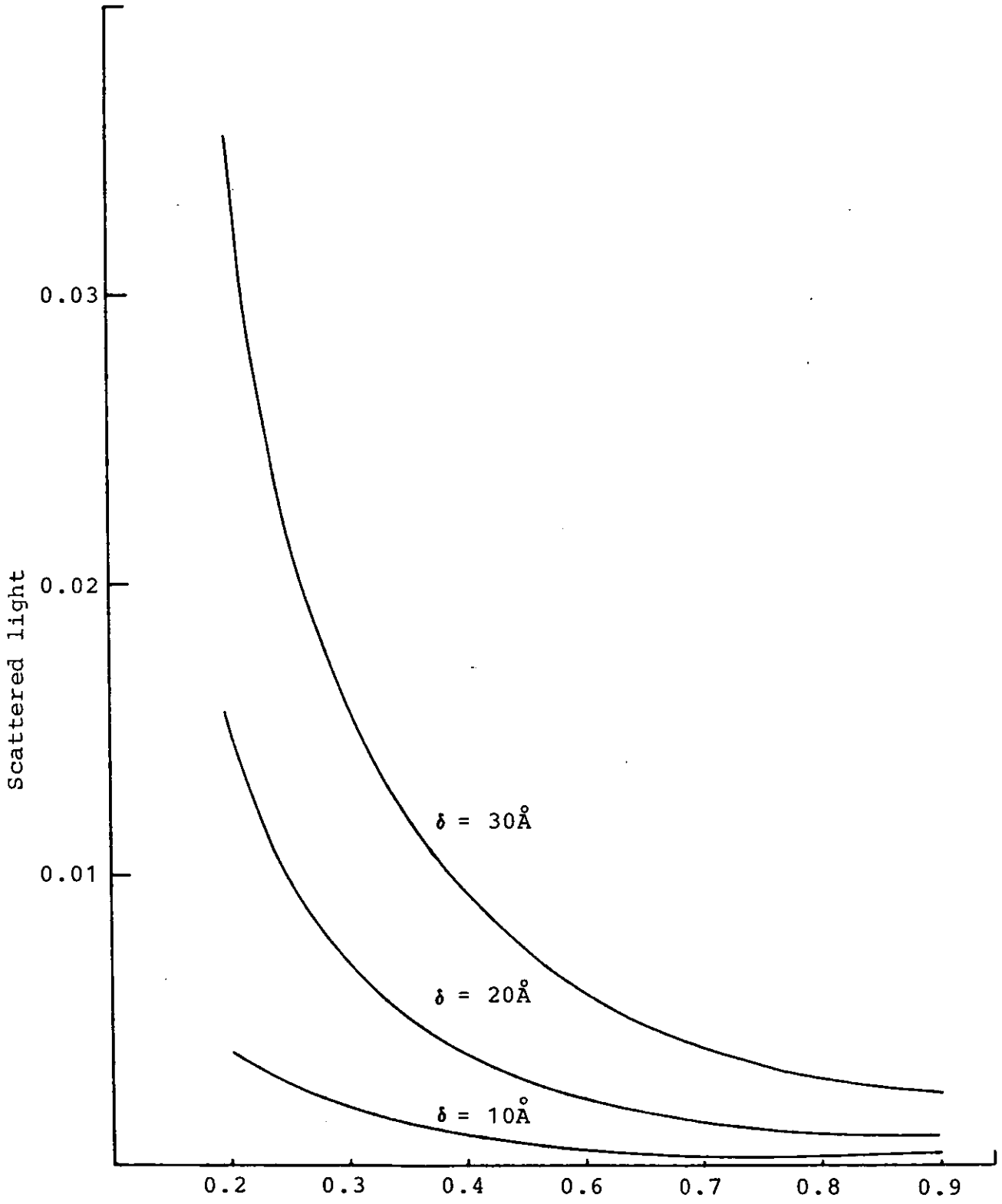

Figure 5.2: Wavelength dependence of the total scattered light from an arbitrary surface at normal incidence as a function of the surface roughness.

δ, uniquely from TIS measurement. This technique is increasingly widely used for this purpose.

5.3 TYPE OF SCATTERING.

Scattering can be divided into two main categories:

A - Rayleigh scattering.

This mechanism is associated with particles whose diameters are small compared to the incident wavelength. For a small dielectric sphere and dielectric constant ε_1 embeded in a medium with dielectric constant ε_2, the scattering of light can be explained as follows:

The isolated sphere is illuminated by a parallel beam of linearly polarized light. The sphere becomes polarized in the electromagnetic field due to the displacement of electrons with respect to the nuclei. Since the particle is small compared to the wavelength, the instantaneous field which it experiences due to the electromagnetic wave is uniform over its volume. If only the effect of the electric vector is considered the problem will be reduced to the standard electrostatic problem of an isotropic, homogeneous, dielectric sphere in a uniform field. The solution is well known[2]. Within the sphere, the field is uniform and parallel to the external field (see Figure 5.3) with the electric field intensity given by[2]:

$$E_{inst} = \left[3\varepsilon_2/(\varepsilon_1 + 2\varepsilon_2)\right] E_o \qquad (5.3)$$

where ε_1 and ε_2 are the dielectric constants of the sphere and the external medium, respectively. Outside the sphere the field is composed of two parts; the initial uniform field E_o, that would have existed in the absence of the particle, and superimposed upon this is an induced field identical with that which would be given by a simple dipole oriented parallel to the incident field with dipole moment

$$p = 4\pi\varepsilon_2 a^3 \left[(\varepsilon_1 - \varepsilon_2)/(\varepsilon_1 + 2\varepsilon_2)\right] E_o \qquad (5.4)$$

where a is the radius of the particle. If the incident field oscillates harmonically, then to a close approximation the induced dipole will follow synchronously so that

$$pe^{i\omega t} = 4\pi\varepsilon_2 a^3 \left[(\varepsilon_1 - \varepsilon_2)/(\varepsilon_1 + 2\varepsilon_2)\right] E_o\, e^{i\omega t} \qquad (5.5)$$

where the exponential factor describes the time dependence. Thus, the spherical particle acts as an oscillating electric dipole which now radiates secondary or scattered waves in all directions. The geometry can be visualized with the aid of Figure 5.4. The linearly polarized incident wave propagating along the positive z-axis has its electric field vector parallel to the x-axis. The induced dipole is at the origin and is also orientated along the x-axis. The scattering

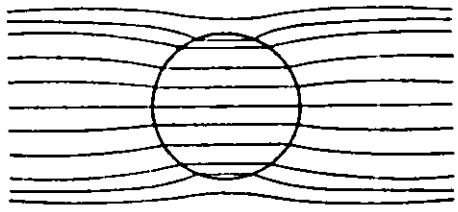

Figure 5.3: Perturbation of a uniform electric field by a homogeneous sphere. The field within the sphere is uniform.

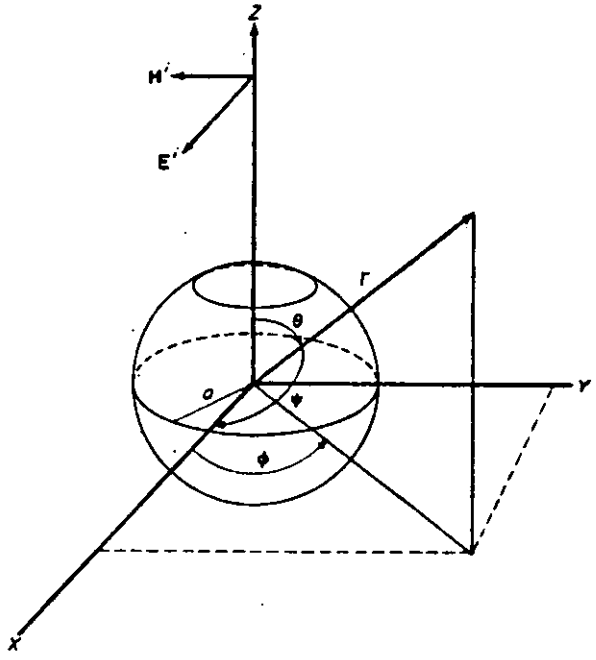

Figure 5.4: Geometry for Rayleigh scattering. Incident wave travels along positive z-axis. Particle with radius a has its centre at the origin. Direction of scattered wave is defined by the polar angle θ and ϕ.

direction is taken from the origin through the point defined by the polar coordinates r, θ, ϕ.

$$x = r\sin\theta\cos\phi,$$
$$y = r\sin\theta\sin\phi, \qquad (5.6)$$
$$z = r\cos\theta$$

The angle measured from the scattering direction to the dipole is ψ. The angle of observation, θ, is measured from the forward to the scattered directions and defines the scattering plane or the plane of observation. The intensity of the scattered wave at a distance r from the particle is given by[3]:

$$I_{sca} = \frac{16\pi^4 a^6}{r^2 \lambda^4}\left(\frac{\varepsilon_1 - \varepsilon_2}{\varepsilon_1 + 2\varepsilon_2}\right)^2 \sin\psi \quad , \qquad (5.7)$$

since $n \cong \sqrt{\varepsilon}$, $n_2 \simeq 1$, then

$$I_{sca} = \frac{16\pi^4 a^6}{r^2 \lambda^4}\left(\frac{n_1^2 - 1}{n_1^2 + 2}\right)^2 \sin^2\psi \qquad (5.8)$$

where n_1 is the refractive index of the particle and λ is the wavelength of the light used.

There are two special cases of interest. For Case 1 where the scattering is in the yz-plane and $\psi = 90°$, the incident beam is perpendicularly polarized with respect to the scattering plane. The

scattered radiation, also perpendicularly polarized, has an intensity

$$I_1 = \frac{16\pi^4 a^6}{r^2 \lambda^4}\left(\frac{n_1^2 - 1}{n_1^2 + 2}\right)^2 \quad . \tag{5.9}$$

This is independent of the angle of observation since all directions in this plane are equivalent with respect to the dipole.

Case 2 if for scattering in the xz-plane. Here the polarization is parallel to the scattering plane and ψ, which may now take on all values, is related to θ by

$$\psi = \pi/2 - \theta$$

so that

$$I_2 = \frac{16\pi^4 a^6}{r^2 \lambda^4}\left(\frac{n_1^2 - 1}{n_1^2 + 2}\right)\cos^2\theta \quad . \tag{5.10}$$

The main features of Rayleigh scattering are now apparent, including the dependence of the scattering upon the inverse fourth power of the wavelength and the complete polarization at 90°. The polarization is often described by a polar diagram of the scattered intensity as shown in Figure 5.5.

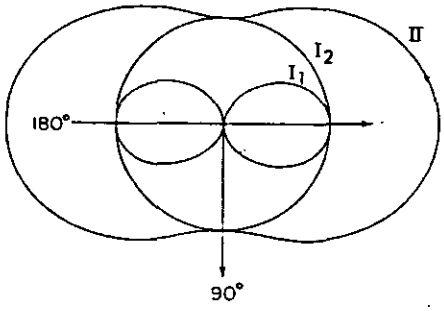

Figure 5.5: Radiation diagram for Rayleigh scattering. The radius vector to each curve is proportional to the intensity scattered at the corresponding angle. Curve I_1 is for Case 1; curve I_2 is for Case 2; curve II is for unpolarized light.

The radius vector to the curves designated I_1 and I_2 gives the intensity scattered in the direction θ for incident beams polarized vertically and horizontally, respectively, each of equal intensity. The curve labelled II is for unpolarized light.

B - Mie scattering.

When the particle is comparable in size or large relative to the wavelength of the incident radiation, the scattered light will be the resultant of the light waves originating from various parts of the particle, the phase and intensities of such waves are related in a complicated manner. The Mie equation can be written

in the following form[4]:

$$I_{sca} = \frac{\lambda^2}{2\pi} \sum_{\nu=1}^{\infty} \left(\frac{a_\nu^2 + p_\nu^2}{2\nu + 1} \right) \qquad (5.11)$$

where a_ν and p_ν are functions of x and β and $x = 2\pi a/\lambda$, $\beta = 2\pi an/\lambda$ .... , a being the radius of the particle.

5.4 DEPENDENCE OF THE SCATTERED LIGHT ON THE SIZE OF THE PARTICLE.

Unless the conductivity is very large in which case most of the incident light is radiated in the backward direction, the polar diagram in the limit of a vanishing small sphere ($a \longrightarrow 0$), is symmetrical about the plane through the centre of the sphere at right angles to the direction of propagation of the incident light as shown in Figure 5.6a. There is an intensity maximum in the forward direction ($\theta = 0°$) and in the reverse direction ($\theta = 180°$), and there is a minimum in the plane of symmetry. As the radius of the sphere is increased there is a departure from symmetry, more light being scattered in the forward direction, Figure (5.6b,c), than in the backward direction. As the radius is increased further, practically all the scattered light appears around the forward direction ($\theta = 0°$). When the radius of the sphere is very large compared to the wavelength used

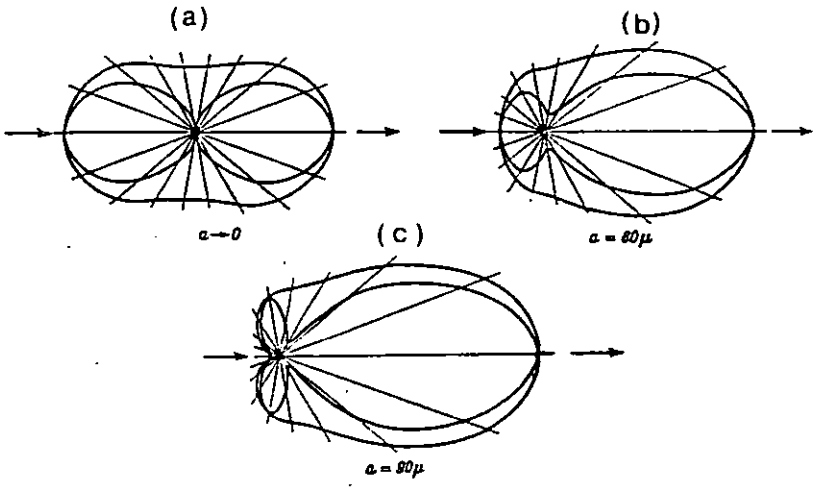

Figure 5.6: Polar diagram for the scattering of linearly polarized light by a spherical gold particle (after ref.6).

most of the incident light will be reflected according to geometrical optics.

5.5 EFFECTS DUE TO ABSORPTION OF LASER RADIATION.

Melting, fracture, ripple formation or slip plane distortion are some of the effects observed when a high power laser pulse interacts with a solid surface. However, if the energy density of the laser is below the damage threshold of the surface, there will be a progressive deterioration of the surface upon increasing the energy density. This will lead to changes in the optical properties of the surface and some of these changes could be permanent like the reduction in the reflectivity of the surface[5]. The systematic change

in the optical properties of a stainless steel surface subjected to increasing laser energy density is shown by a series of scanning electron micrograph (SEM) in Figure 5.7. Each micrograph represents a different site on the surface. There is a progressive increase in the surface pitting which acts as a source of scattering centres. When the energy in the laser pulse is just enough to damage the surface, the damage usually occurs in the form of small areas of isolated micro damage caused by surface imperfections remaining from the polishing process or due to airborn dust particles. It is these microdamage sites together with the surface pitting which could be used in the early detection of laser induced damage in optical materials since pitting and microdamage sites act as a source of increased scatter from the optical surface.

5.6 EXPERIMENTAL DETERMINATION OF THE LASER INDUCED DAMAGE THRESHOLD AT 10.6 μm.

The experimental set-up is shown in Figure 5.8. The CO_2-TEA laser is fully described in Chapter Three. The sample was mounted on an xy-translator and the CO_2 laser was focussed on the sample surface by 12.7 cm antireflection coated germanium lens to a spot 0.03 cm diameter, this best focus corresponds to the diffraction limit of this lens. The probe beam was 5 mW He-Ne laser. The diameter of the probe beam measured by a

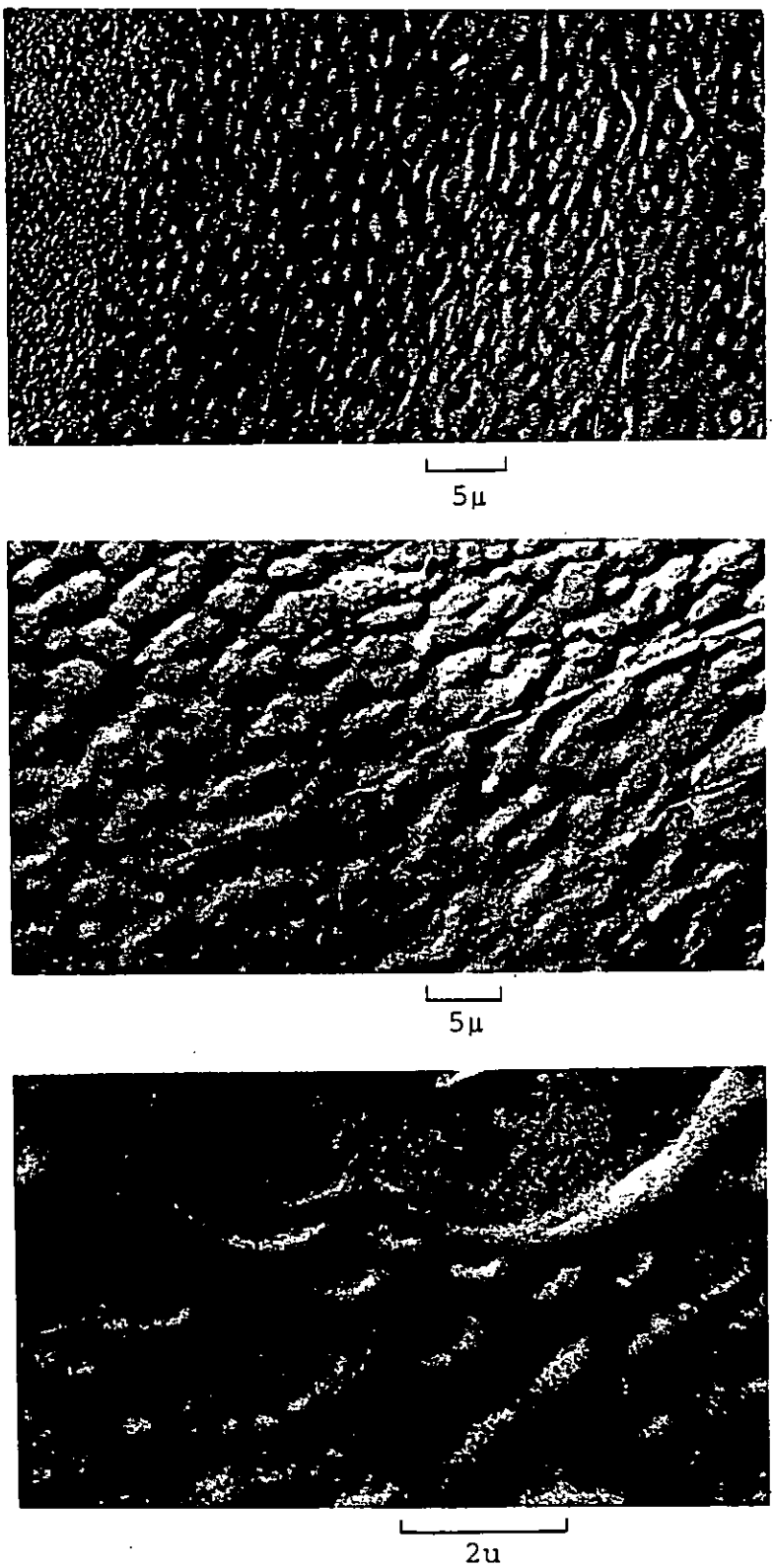

Figure 5.7: Change of the morphology of stainless surface subjected to CO_2 laser pulse with increasing energy.

scanning knife-edge, detector and oscilloscope combination, the results of this measurement are shown in Figure 5.9. The diameter was found to be a 0.85 mm. This diameter was then reduced by a factor of 1/4.2 by using two lenses with focal lengths 50 mm and 12 mm respectively. The narrow probe beam resulted in an increased sensitivity. The probe beam was then chopped using a Rofin-Sinar light chopper serial No. 20236, the chopper was used to make the measurement of the scattered light much simpler compared with a D.C. signal. The probe beam after being reflected off the sample surface was stopped by a small circular stop painted on the surface of the imaging lens. This means that only scattered light reaches the detector. A He-Ne band pass interference filter was placed in front of the detector to prevent any light coming from the electrical discharge inside the He-Ne laser from reaching the detector as well as excluding room light. The detector used to record the scattered light was an RCA solid state detector Model C30816 with a typical rise time of 35 ns and a responsibility of 1×10^4V/m at 900 nm. The scattered light received by the detector was displayed on a Phillips storage oscilloscope PM3311 with a bandwidth of 60 MHz. A 20 cm focal length lens was used to collect the scattered light, this lens must have a large diameter in order to collect as much scattered light as possible. The lens was placed near

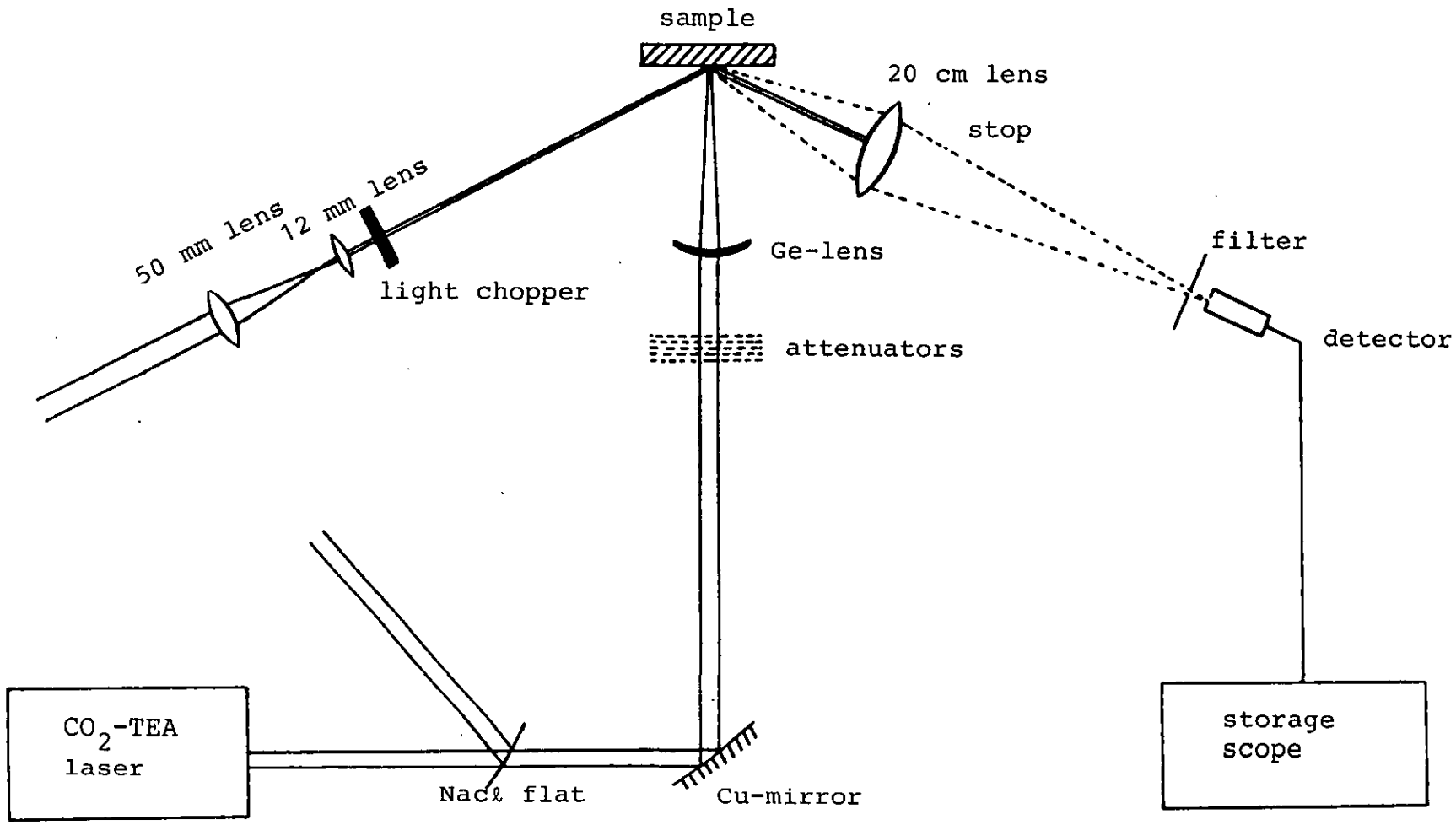

Figure 5.8: The experimental set-up used for laser induced damage at 10.6 μm.

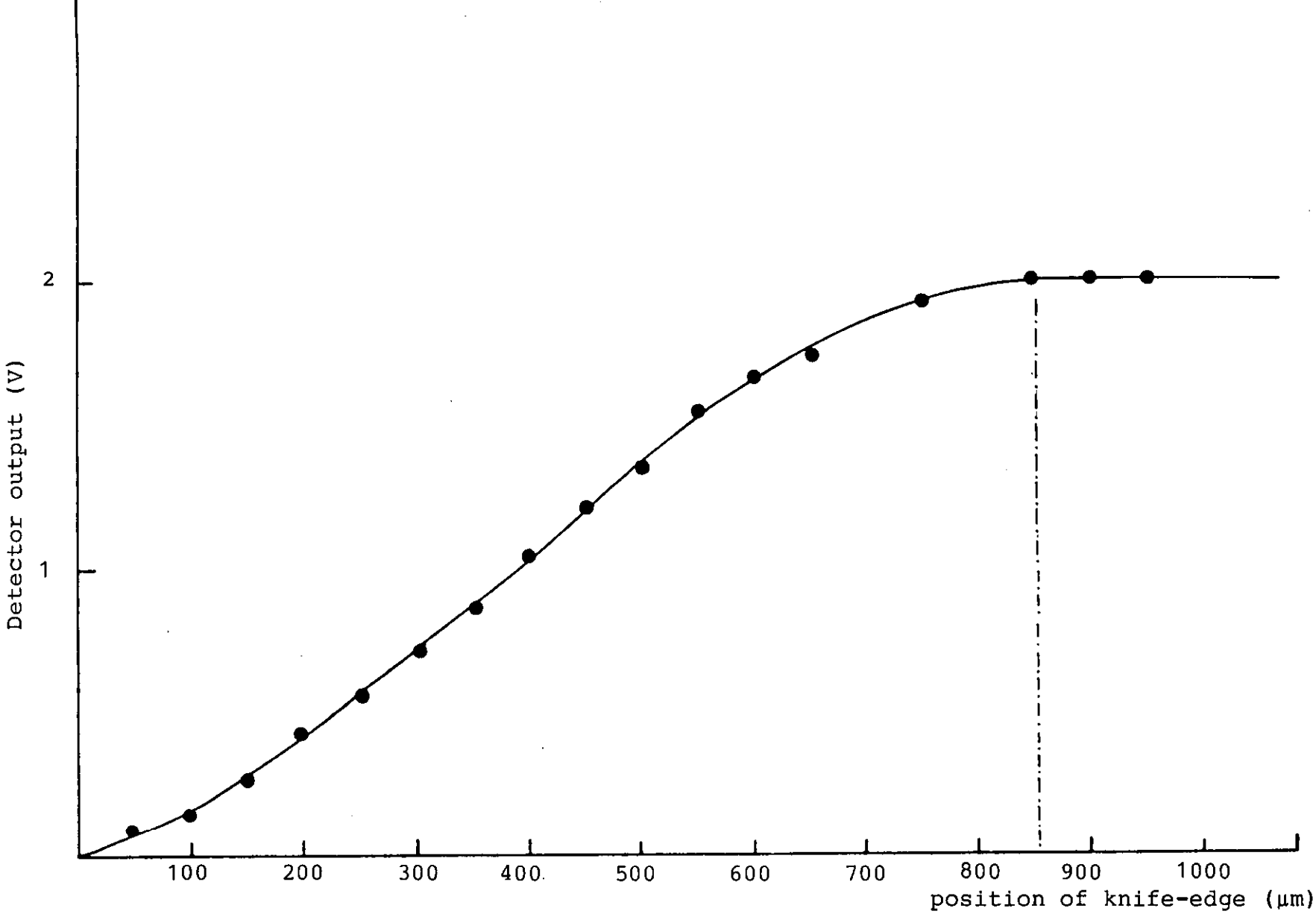

Figure 5.9: Detector output as a function of the position of the knife-edge.

the sample to keep the aperture (F-number) as high as possible while imaging the damage spot on the photo-detector. The energy density at the sample surface was varied using previously calibrated polythene sheets and the energy in each pulse was measured using a pyroelectric calarometer. Damage was associated with an increase in the scatter of the He-Ne laser and a range of samples were damage tested, some of these are shown in Table 5.1 together with the measured damage thresholds. These figures are estimated to have ± 10% error resulting from the measurement of the spot-size and the laser pulse energy.

TABLE 5.1 : List of samples damage tested.

Sample	Damage threshold $J.cm^{-2}$
Germanium	23.92
HR on germanium	11.89
Au on glass	16.71
Enhanced aluminium	3.85
Stainless steel	4.81
Aℓ on glass	9.22
Moly	22.58

Figure 5.10 - 5.13 shows the scattered light signal as a function of the incident laser pulse energy for

germanium, gold on glass substrate, HR coating on germanium and stainless steel respectively. In each of these figures the signal remained at the same value until damage occurred. Damage occurred at the points indicated by the arrows. After damage the scattered signal increases linearly with the incident laser pulse energy. Figure 5.14 shows the damage morphology for an Aℓ film on a glass substrate, (a), correspond to the first increase in the scatter of the He-Ne laser. The micrographs suggest that localized microdefects in the coating are responsible for the first damage to be seen. Reliable nondestructive methods for identifying these defects and predicting damage threshold levels are not fully developed yet. When damage is defect-dominated, however, the probability of damage in an individual test shot often varies significantly over a wide range of energy densities and under fixed conditions of wavelength and pulse duration, the damage probability within this range depends on the irradiated spot-size, this is shown in Figure 5.15 for an aluminium film on a glass substrate. The spot-size dependence scales approximately with the $(\text{spot-size})^{-1}$.

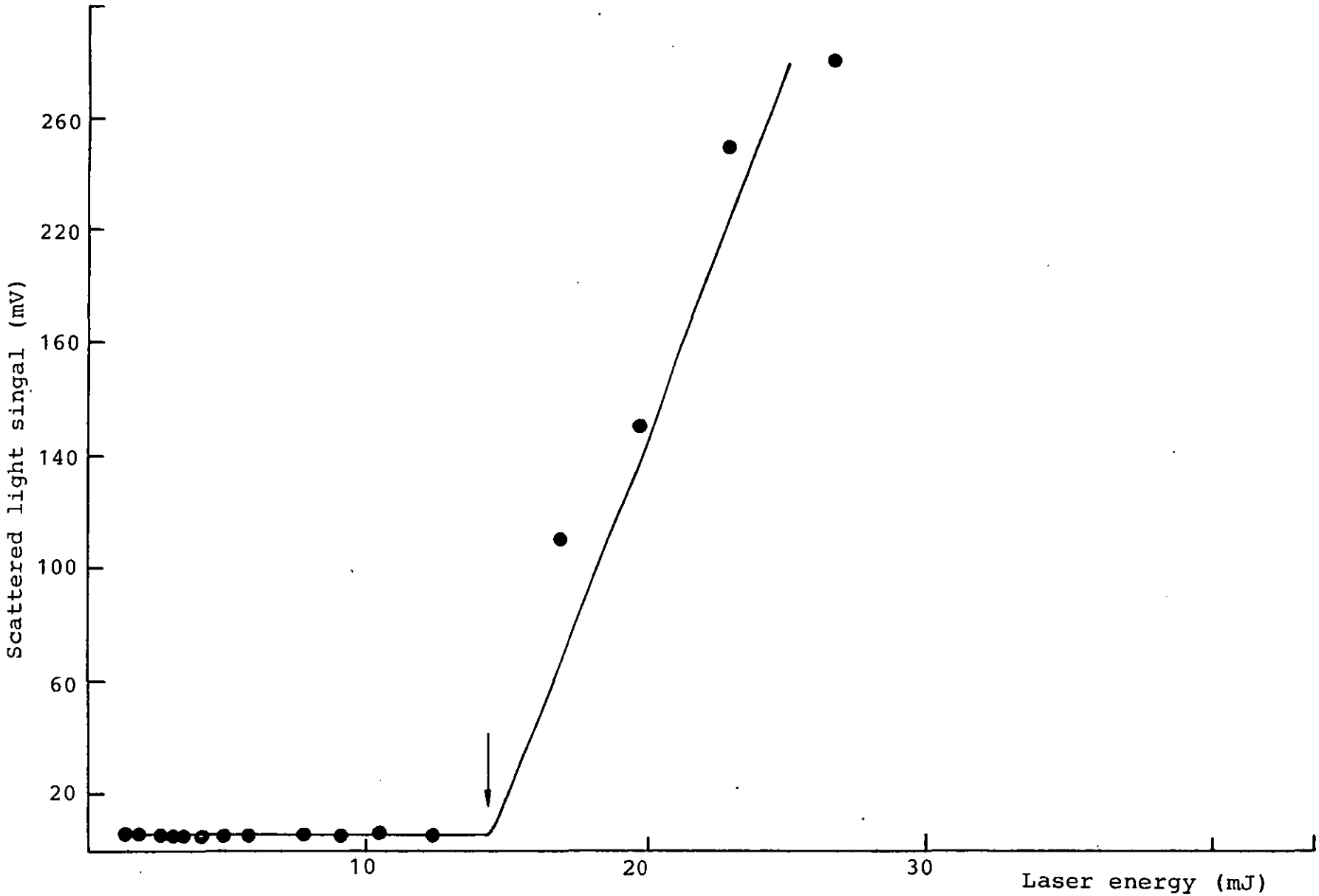

Figure 5.10: Scattered light signal as a function of laser energy for germanium.

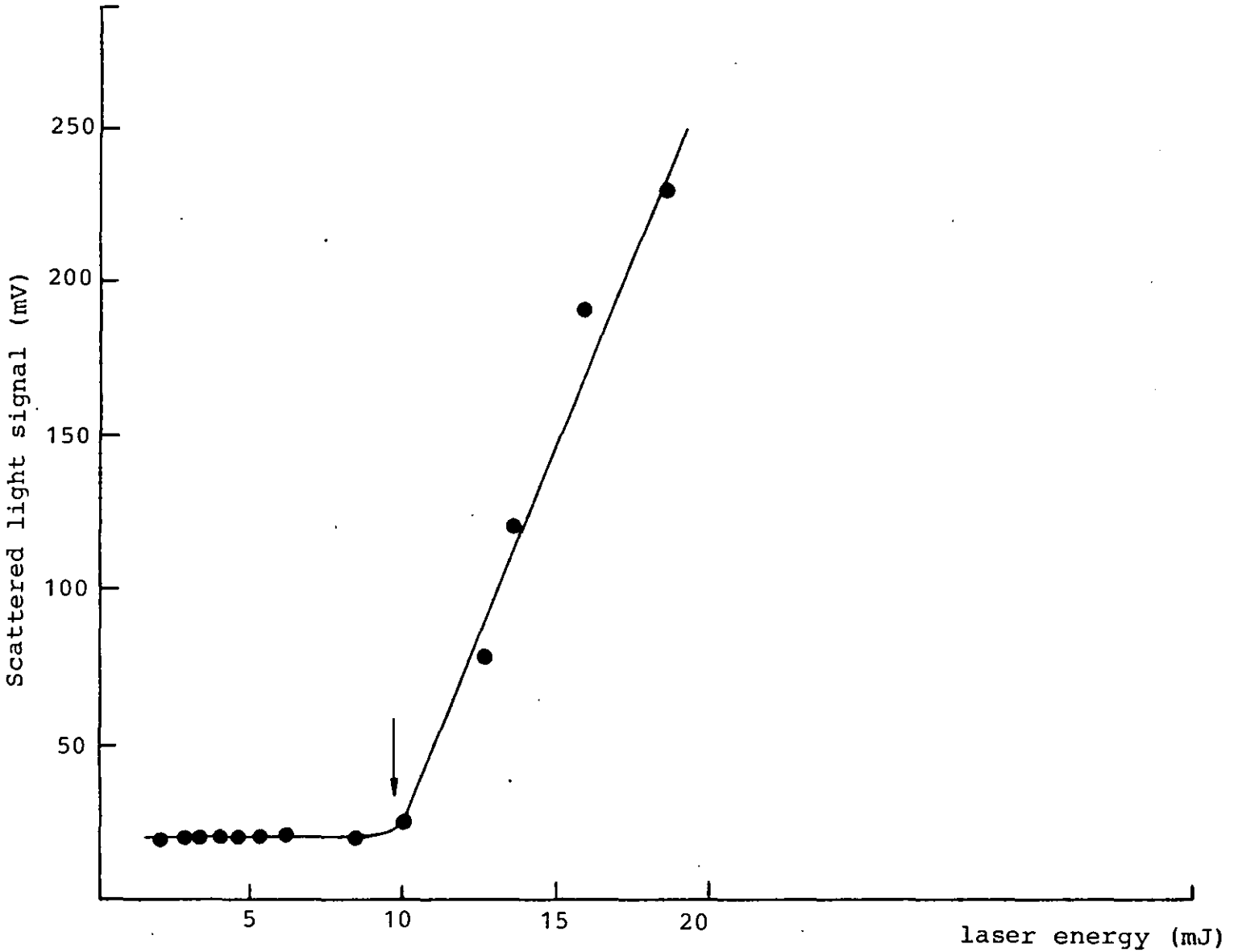

Figure 5.11: Scattered light signal as a function of laser energy for gold film on glass substrate.

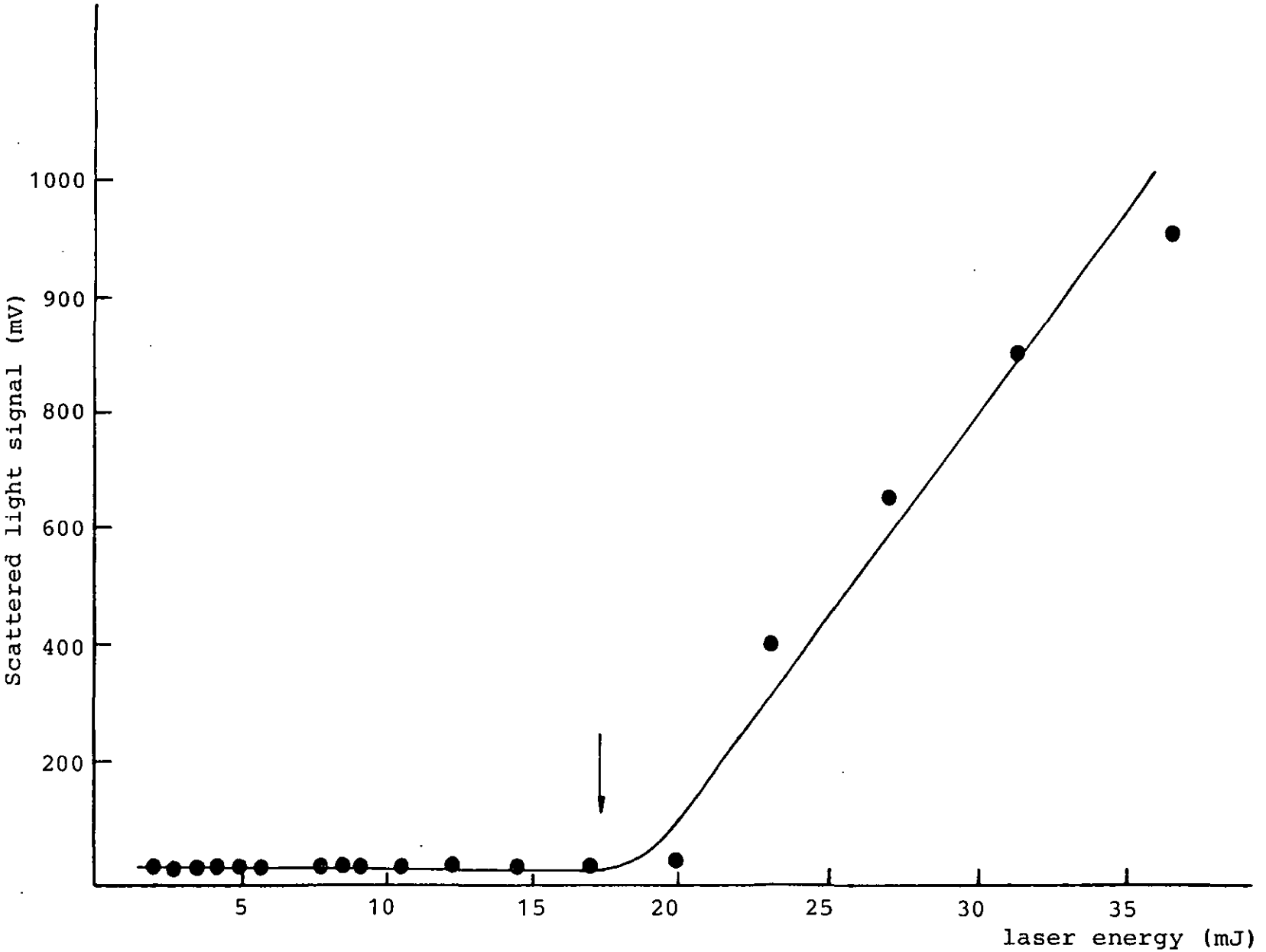

Figure 5.12: Scattered light signal as a function of laser energy for HR coating on germanium.

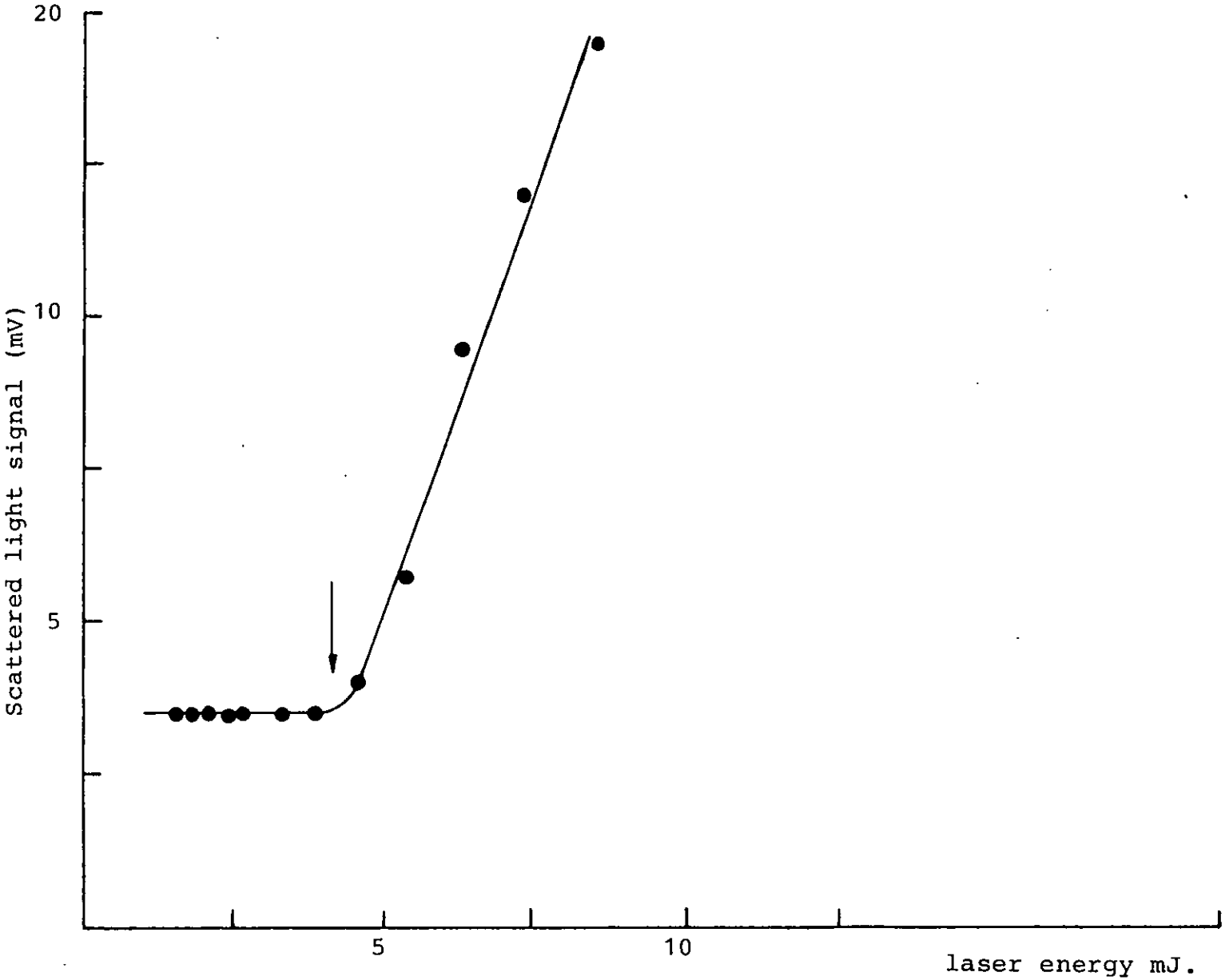

Figure 5.13: Scattered light signal as a function of laser energy for stainless steel.

(a)

(b)

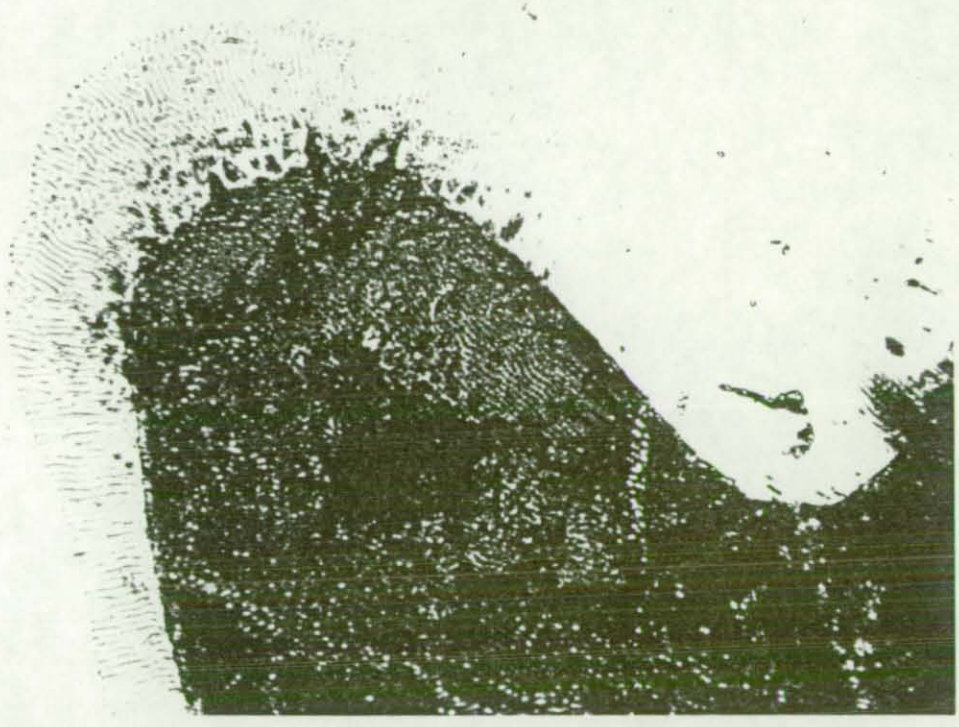

Figure 5.14: Morphology of damage for an aluminium film on glass substrate; (a) corresponds to the first increase in the scatter of the He-Ne laser while (b) corresponds to a severely damaged area.

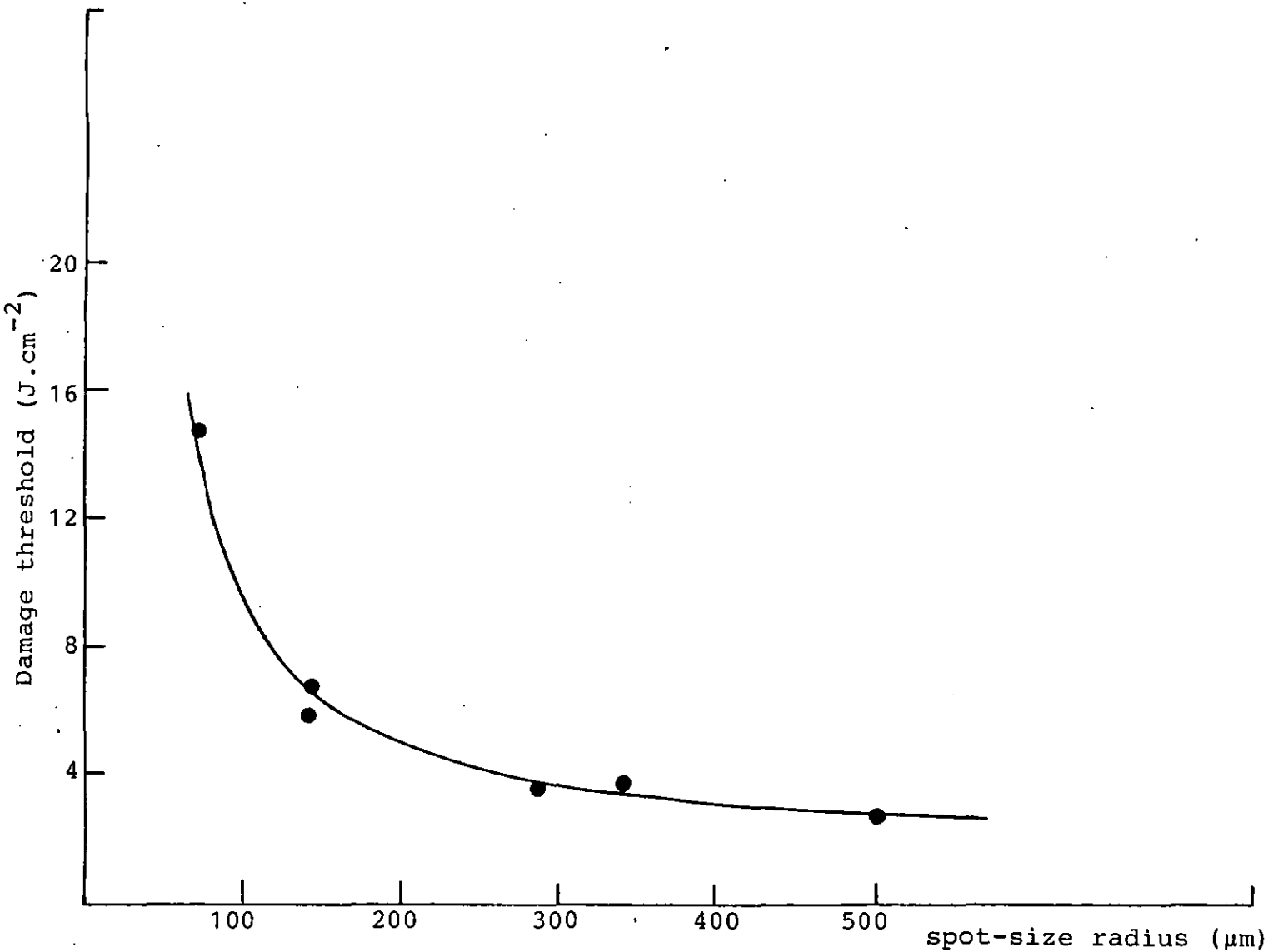

Figure 5.15: Spot-size dependence of laser induced damage for aluminium film on glass sunstrate.

5.7 DAMAGE AT 248 nm.

For damage in the U.V., the experimental arrangement shown in Figure 5.16 was employed. The discharge pumped KrF laser (Lamda Physik EMG200) produces a maximum output of about 500 mJ. The energy in the pulse was measured with a laser instrumentation calorimeter (model 17AN) and the shot to shot variation in the energy was 5%. The temporal profile was measured with a vacuum photodiode (EMI Gen.Con.PD 1912-5S), the width at half maximum was 30 ns. A pinhole/detector combination was scanned through the focussed beam to measure the spatial profile of the pulse in plane at which the test sample was subsequently located. The spatial profile in both the horizontal and vertical directions are shown in Figure 5.17 together with the temporal profile, the beam area is defined in terms of the half-widths at the $1/e^2$ intensity points, these were 3.68 mm × 0.85 mm giving an effective area of 3.128 mm^2. The test sample was placed in the focal region of a 30 cm focal length fused silica lens. A variable length liquid cell using aqueous solutions of Cobalt and Nickel Sulphate or Rhodamine 6G was used to act as uniform laser attenuator.

In addition to the scattering arrangement, a solid state video camera was also used to monitor damage. The output from the camera was connected to a video recorder and finally displayed on a T.V. monitor, the overall amplification was approximately 70. The energy density

at the sample surface then gradually increased until there was an increase in the He-Ne scatter or any noticeable change on the T.V. monitor. Figure 5.18 shows the scattered light signal as a function of the energy in the laser pulse for antireflection coating on a silica substrate, this coating had a reflectivity, R < 1% at 248 nm, the composition of the film was unknown to us.

When a clean site was chosen for damage, the signal remained the same until damage started whereas if a dirty site was chosen the signal first decreased and then remained at the same value until damage occurs, the decrease was attributed to the removal of debris and dust particles. The dirty site was always found to have a lower damage threshold. The measured damage threshold ranged from 1.31 $J.cm^{-2}$ for an unclean site to 1.7 $J.cm^{-2}$ for a clean one. Figure 5.19 shows two micrographs for the morphology of the damage in this sample, (a), corresponds to the first increase in the scatter while (b) corresponds to a severely damaged area.

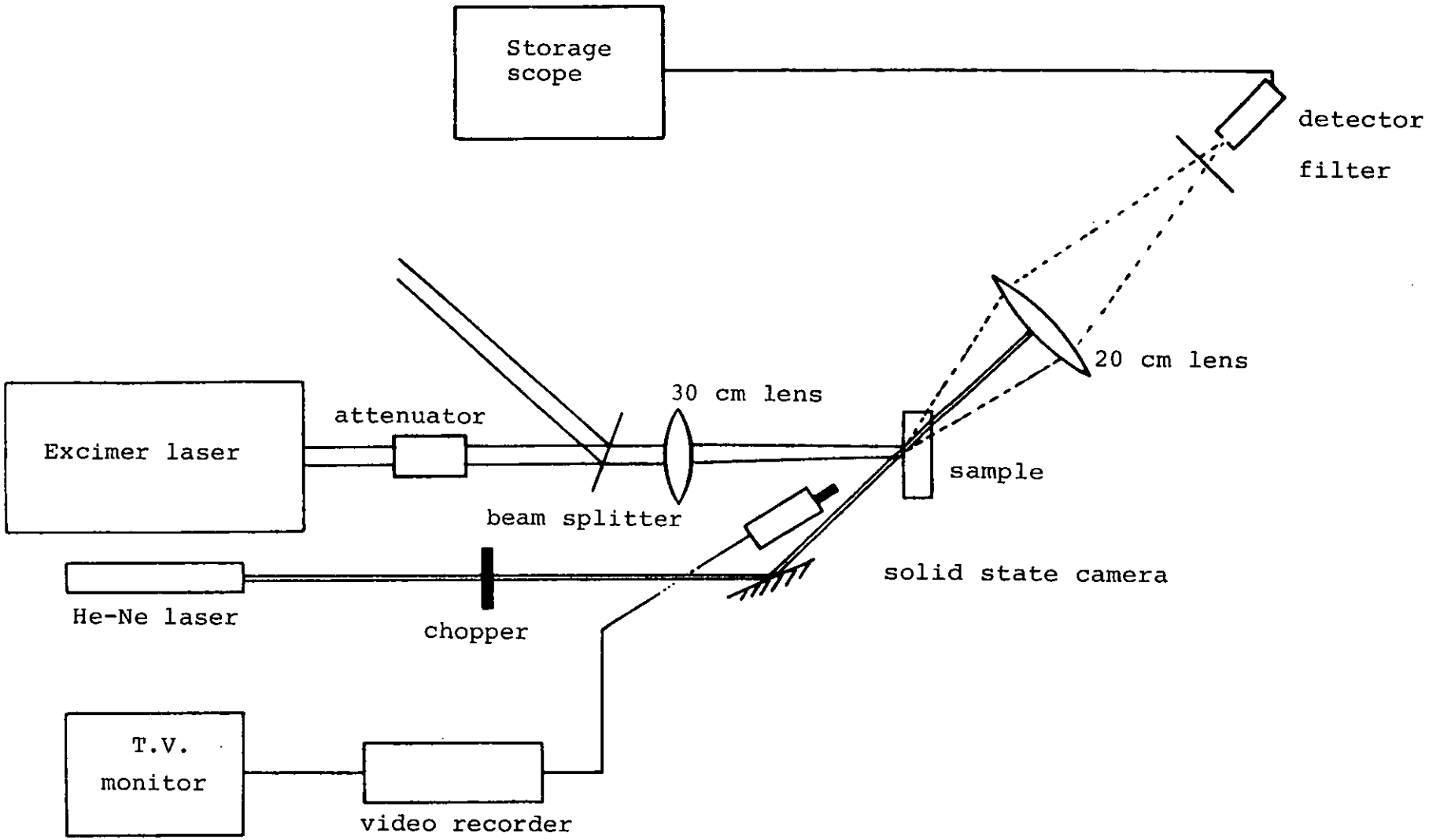

Figure 5.16: Experimental set-up used for damage in the U.V.

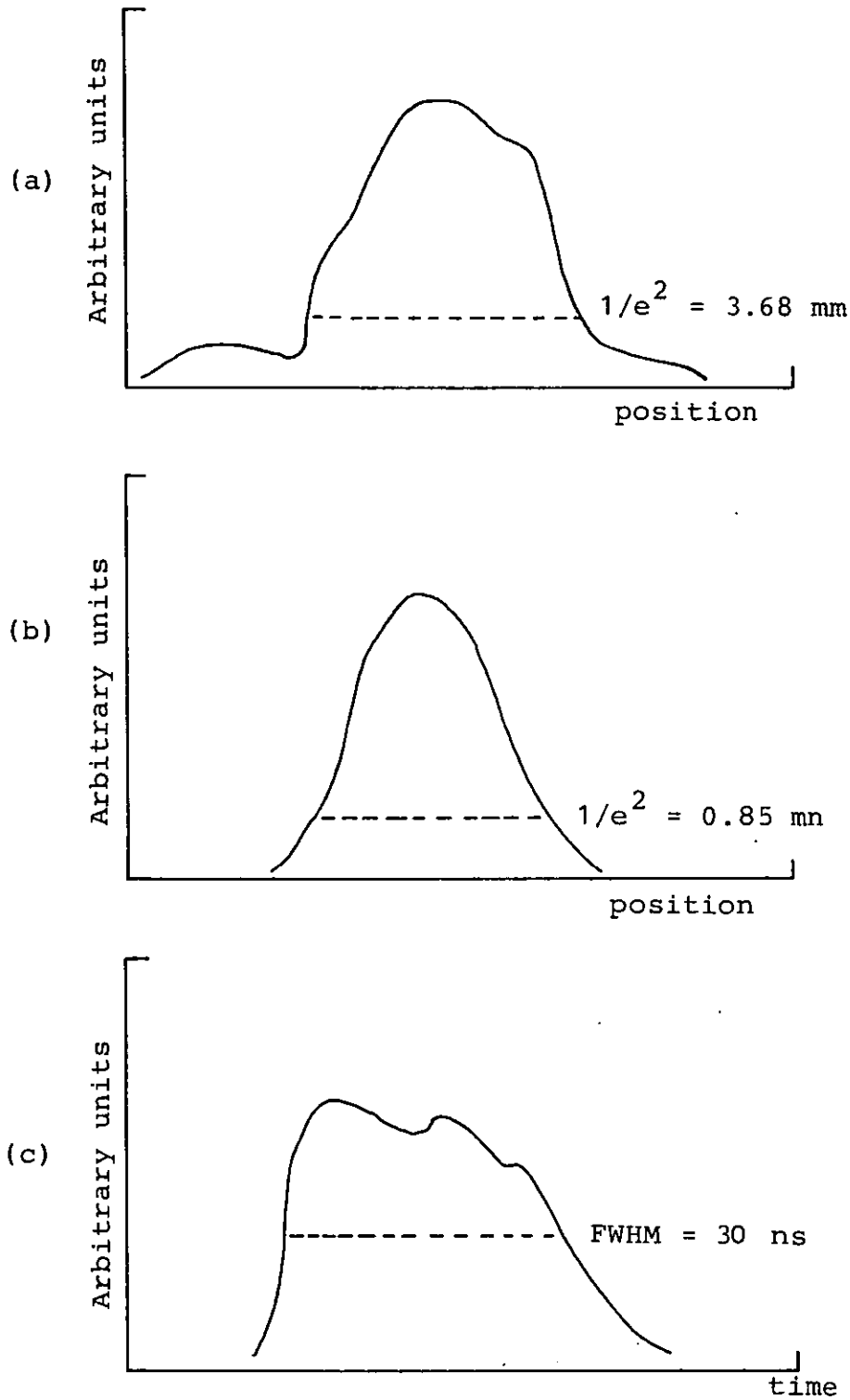

Figure 5.17: (a) Spatial profile in the horizontal direction.
(b) Spatial profile in the vertical direction.
(c) The pulse temporal profile.

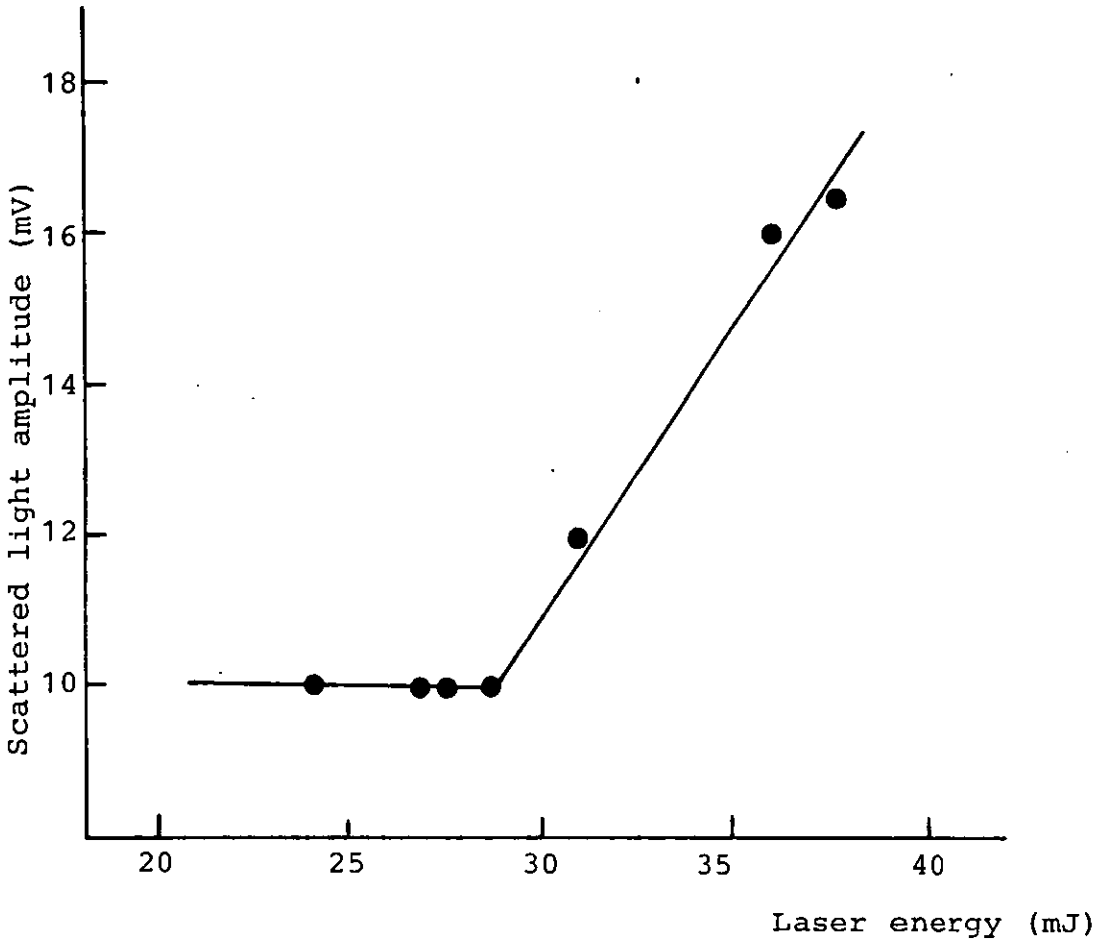

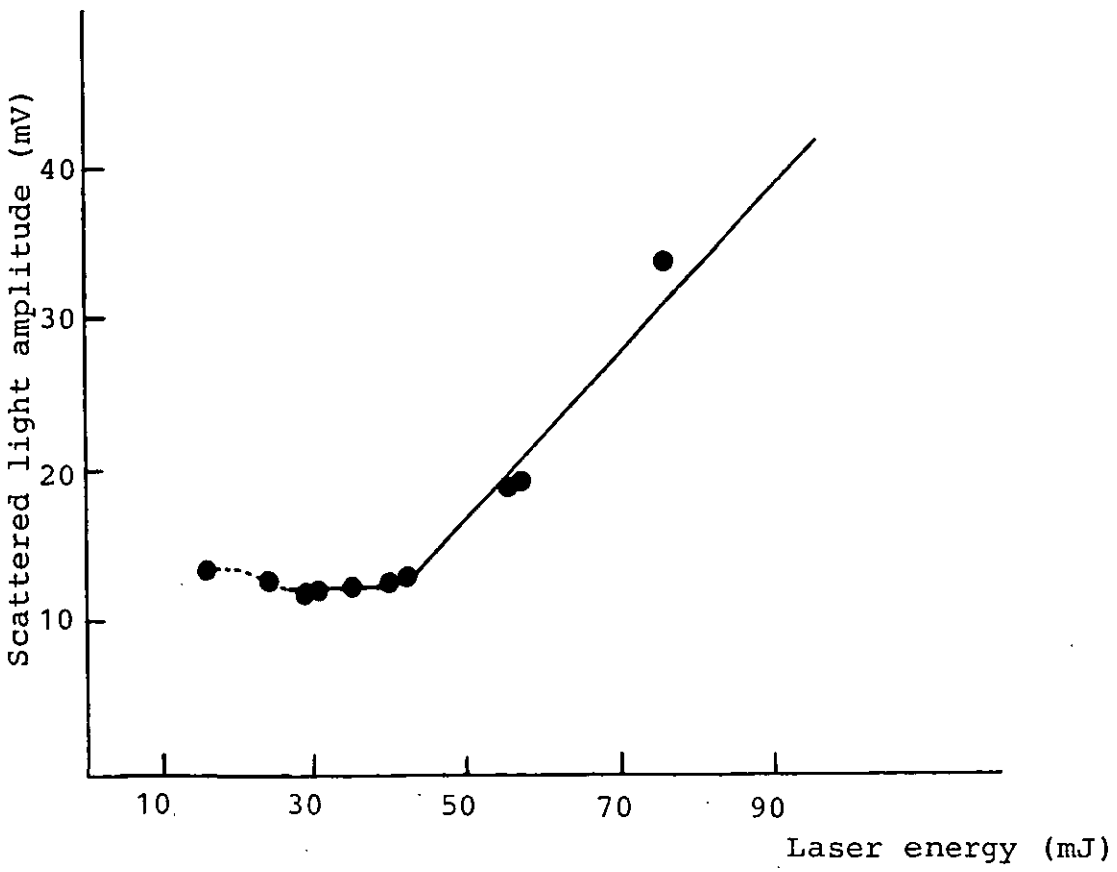

Figure 5.18: Scattered light signal as a function of the laser energy. (a) represents a clean site while (b) represents a dirty site.

(a)

(b)

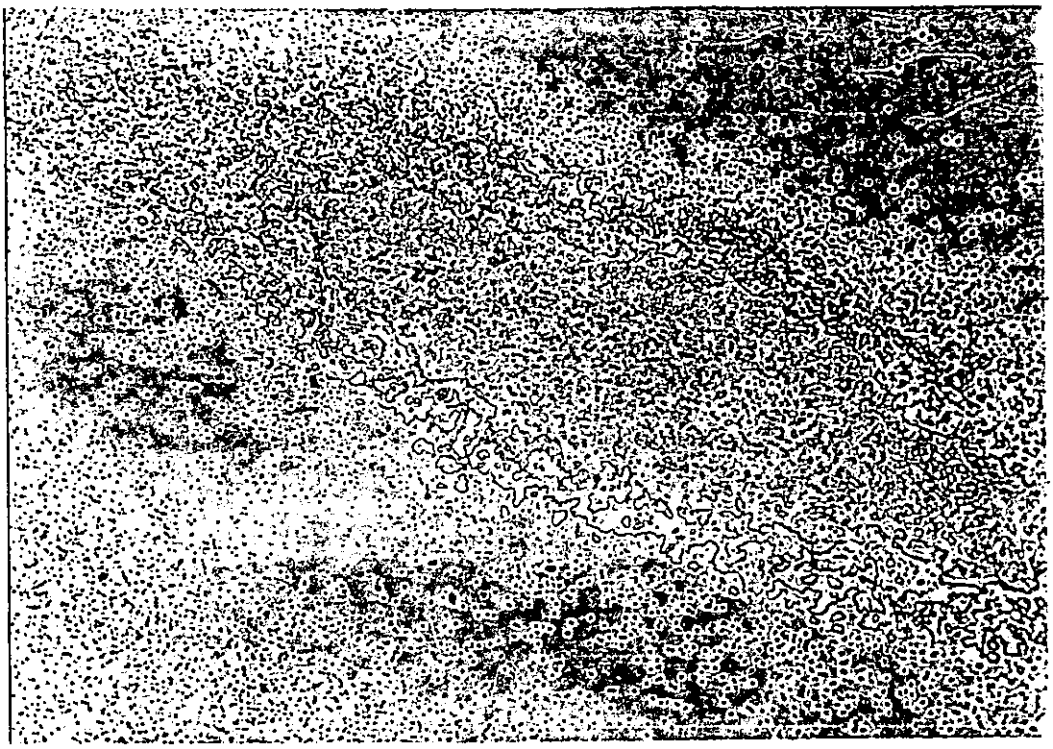

Figure 5.19: Damage morphology for antireflection coating on silica substrate, (a) corresponds to the first increase in the scatter while (b) shows a severely damaged area.

5.8 THE SENSITIVITY OF THE SYSTEM.

In order to get the maximum sensitivity the following requirements should be fulfilled:

1 - The collecting lens should be placed near the sample, the lens should also be of a large diameter in order to collect as much scattered light as possible.

2 - Since most of the scattered light is in the forward direction as shown in Figure 5.6, the detector must be placed on axis with respect to the scattered light. It should also be noted that working slightly off axis should not make a great loss in the sensitivity.

3 - The shape of the stop should be circular since in the early stages of damage the scattered light will be diverged to a very small angle. The difference between using a circular stop and a strip stop, for example, could be calculated easily as follows:

Let r be the radius of the circular stop as shown in Figure 5.20a, if the scattered light is diverged to a new radius, R, then the amount of scattered light reaching the detector will be proportional to the change in the area, i.e.:

$$\Delta A = \pi R^2 - \pi r^2 = \pi (R^2 - r^2) \quad . \tag{5.12}$$

In the case of a strip stop of width 2r, the amount of scattered light reaching the detector will be

proportional to the shaded area in Figure 5.20b, this area is equal to the area of the sector minus the area of the two triangles, i.e.:

$$2A = \frac{1}{2} R^2\theta - r(R^2 - r^2)^{\frac{1}{2}}, \tag{5.13}$$

and $$\theta = 2(90 - \sin^{-1}\psi)/57.3 \tag{5.14}$$

$$\therefore \quad 2A = R^2\left[2(90 - \sin^{-1}\psi)/57.3\right] - 2r(R^2 - r^2)^{\frac{1}{2}}. \tag{5.15}$$

The loss in the amount of scattered light reaching the detector is therefore equal to:

$$\text{Loss} = \Delta A - 2A \tag{5.16}$$

$$\therefore \quad \text{Loss} = \pi(R^2 - r^2) - R^2\left[2(90 - \sin^{-1}\psi)/57.3\right] - 2r(R^2 - r^2)^{\frac{1}{2}}. \tag{5.17}$$

The percentage loss as a function of the diverged scattered light radius is shown in Figure 5.21. For small changes in the radius, the loss in the sensitivity is maximum, this loss is quite significant since we are interested in the early stages of laser induced damage.

4 - Size of the stop: Ideally one would like to use a stop equal to the probe beam diameter but due to diffraction effects, scattering in the optical train and the divergence of the probe beam itself, there will be still some light reaching the detector. Therefore, the optimum size of the stop was found experimentally,

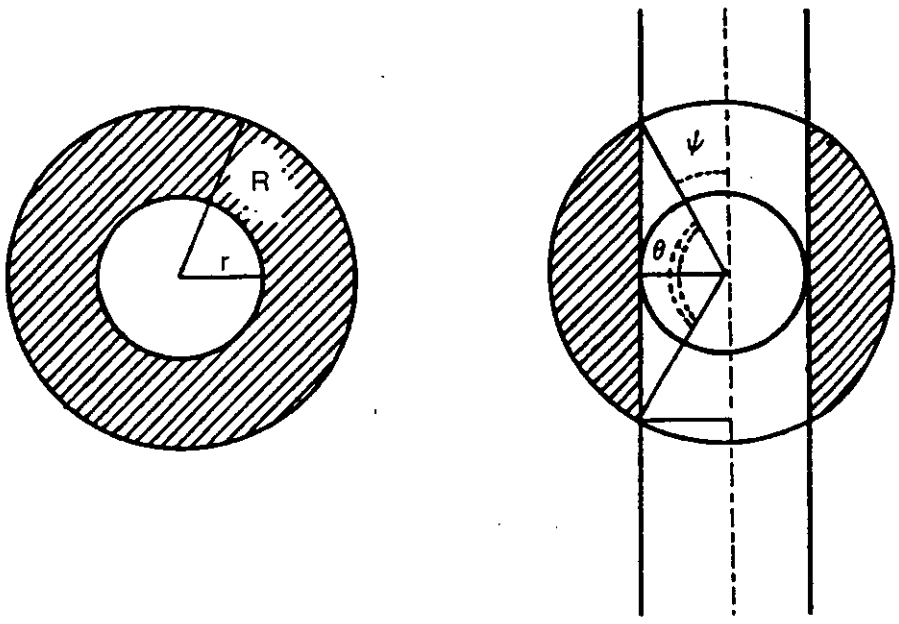

(a) (b)

Figure 5.20: Representative geometries for a circular stop,(a), and a strip stop, (b).

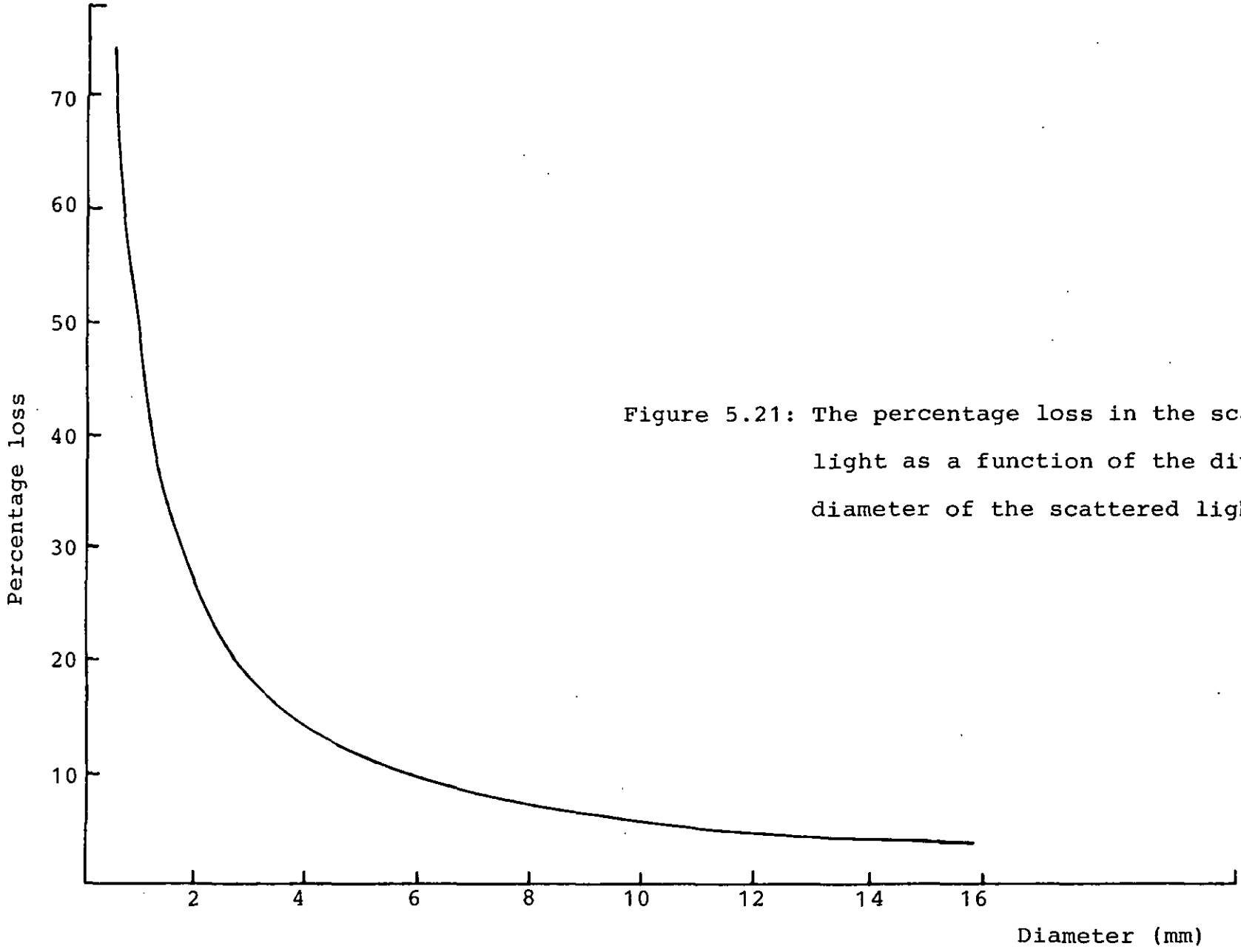

Figure 5.21: The percentage loss in the scattered light as a function of the diverged diameter of the scattered light.

this was achieved by putting different stop sizes until a situation is reached in which increasing the diameter of the stop in one direction reduced the amount of light reaching the detector while decreasing the diameter of the stop in the opposite direction increased the light received by the detector, as shown in Figure 5.21. Any stop with a diameter value within the linear portion of Figure 5.21 could be used without sacrificing in the sensitivity.

5 - Size of the probe beam and method of illumination: If the neat probe beam is used, the magnitude of the scattered light signal will be limited by the spot-size of the pump laser pulse. The spot-size of the CO_2 laser pulse is only 0.03 cm while the probe beam diameter is 0.085, so only an area of 0.03 cm diameter will contribute to the scattered light signal. Therefore the probe beam width must be reduced to a size comparable to that of the CO_2 laser pulse. Putting the collecting lens far from the sample, as shown in Figure 5.23a, will result in a loss in the sensitivity due to the fact that less scattered light will be collected. On the other hand, if the probe beam is focussed on the sample surface, the sensitivity is fixed, (see Figure 5.23b). It was found experimentally that the experimental set-up shown in Figure 5.23c, gives the maximum sensitivity. In this case the collecting lens is as near as possible

to the illuminated sample so much of the scattered light will be collected.

6 - Position of the detector: Since most of the scattered light is in the forward direction as shown in Figure 5.24 in which the scattered light signal is plotted as a function of the angle measured with respect to the normal to the sample surface, the best position of the detector is on axis with respect to the probe beam.

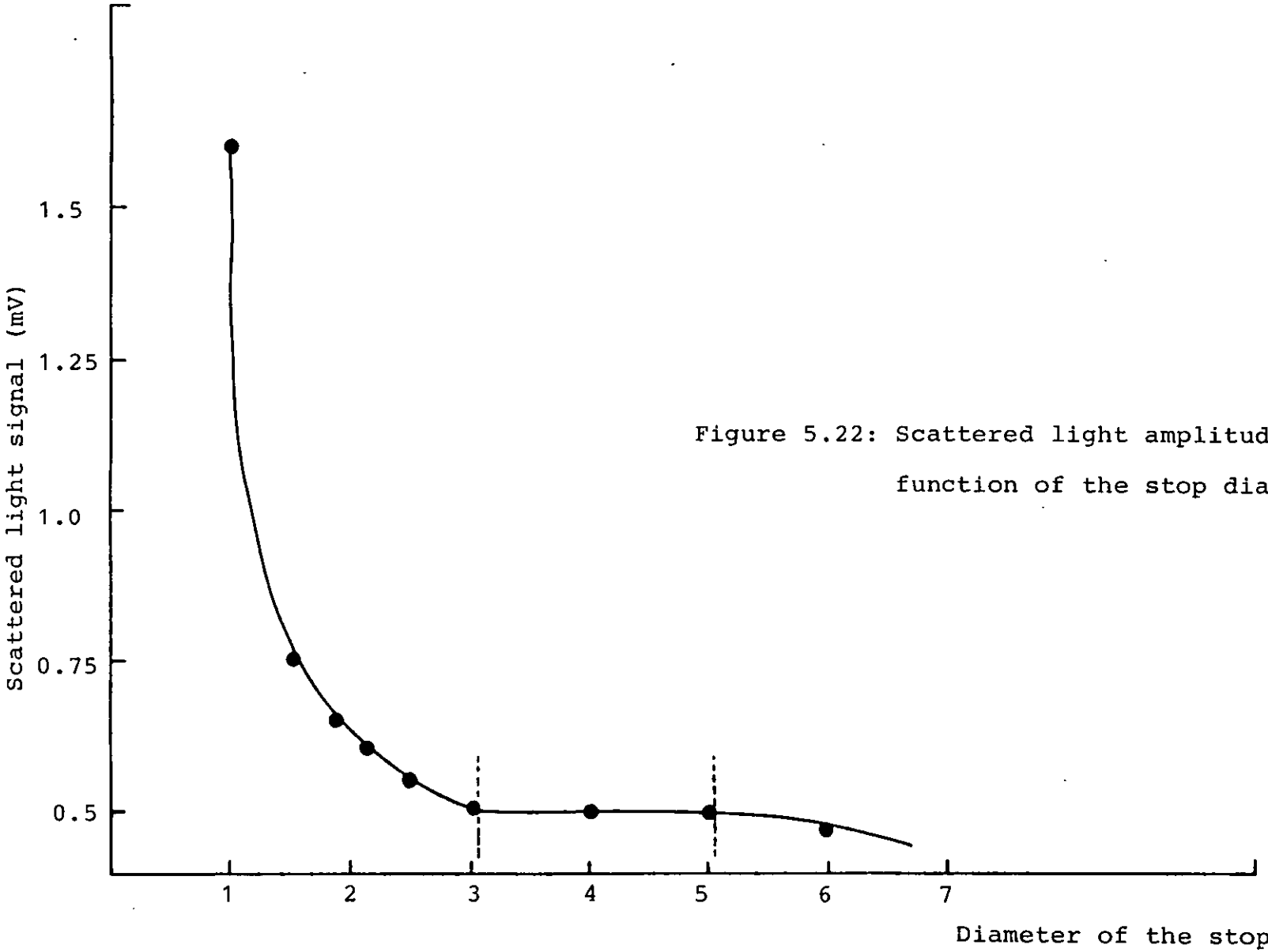

Figure 5.22: Scattered light amplitude as a function of the stop diameter.

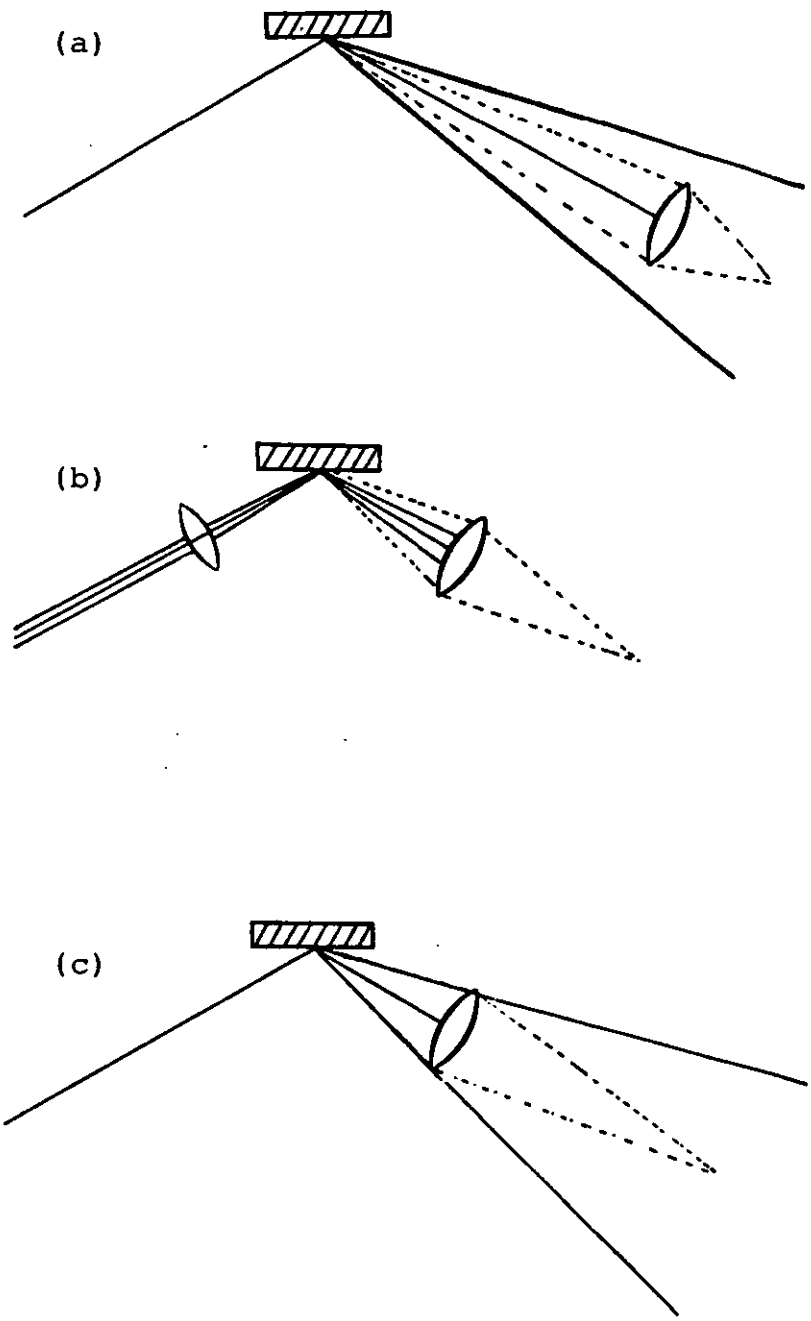

Figure 5.23: (a) Collecting lens far from the sample.

(b) Probe beam focussed.

(c) Collecting lens neat the sample.

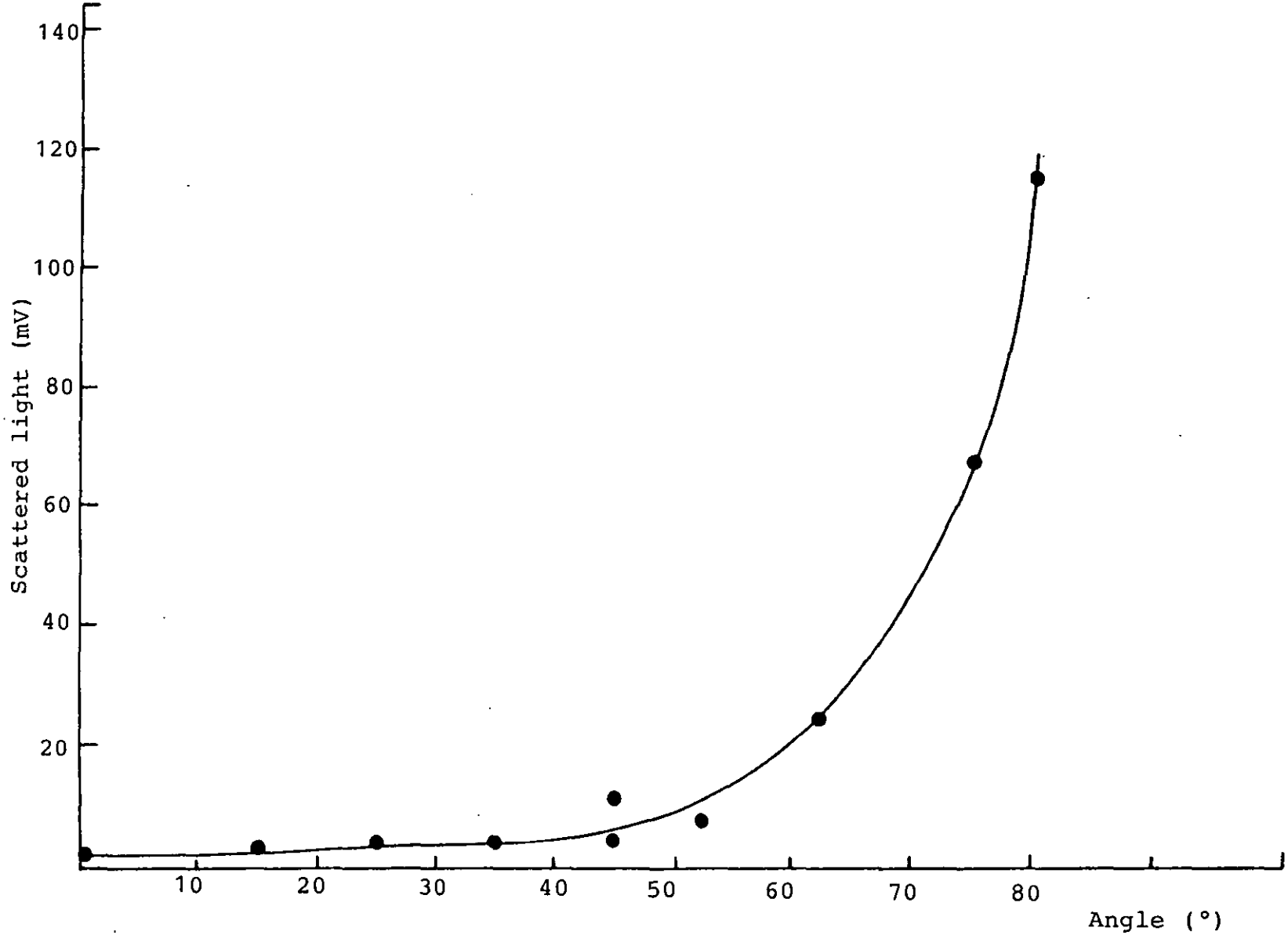

Figure 5.24: Scattered light signal dependence on the angle between the normal to the sample surface and position of the detector.

CHAPTER SIX

Conclusions and Suggestions for Further Work

Over the last twenty years, the subject of laser damage in optical materials has moved steadily from primarily a reporting of empirical observation to one of genuine scientific study. The major phenomena of laser damage have been catalogued and understood to varying degrees. Scaling laws of increasing sophistication provided the system designer with convenient and generally reliable rules of thumb governing the selection and employment of materials for windows, coatings and laser media as well as pointing the way for materials development. Progress was made in reporting carefully controlled damage measurements and in identifying cases where the experimental results agree with the theoretical predictions. Improvements have been made in surface finishing techniques, such as, diamond and laser polishing. These techniques have led to a measurable increase in laser damage thresholds.

In simpler terms, some problems have been overcome primarily through the applications of obvious solutions such as high purity starting materials, high precision fabrication and the identification of damage initiators through the use of existing instrumental methods.

The fundamental mechanisms whereby optical materials fail under intense illumination, have also been subjected to thorough investigation. Although significant progress has been made in understanding laser damage, a

quantitative model which can predict the damage level as a function of pulse length, spot-size, wavelength and material to material variation is still lacking. Outstanding issues include the relative importance of multiphoton absorption versus electron-avalanche and the importance of impurities and defects in the damage process. Scaling laws for the variation of the bulk and surface damage in optical materials have been obtained empirically for several years and provide a useful comparison with the theory. Some like the $\tau^{\frac{1}{2}}$ scaling of damage threshold, has generally been validated for a wide range of experimental conditions. Others, such as, scaling with spot-size has been a subject of controversy for several years.

In general, avalanche ionization can be considered to be the operative mechanism in laser damage in transparent materials both on the surface and in the bulk. However, due to the Fresnel reflection, the exit surfaces of a transparent material exposed to high energy laser pulse will generally damage at a lower energy level than the level at which the entrance surface damages. In fact the entrance surfaces of transparent materials fail at energy levels lower than that for the bulk, either due to contamination of the surfaces or the presence of defects. But once the surfaces are cleaned and conditioned by, for example, laser polishing, the energy level at which the entrance surfaces are damaged

can approach that of the bulk.

The damage in thin film coatings can be best described in terms of an impurity model. This model began with the exact solution of the heat diffusion equations obtained thirty years ago by Goldenberg and Trantor[1]. This solution clearly reveals that damage threshold scales with the thermal properties of the host materials as $T\sqrt{\rho CK\tau}$ with an insignificant dependence on those of the impurity. However, thin films show great variation in terms of laser induced damage. More seriously, they are generally characterized by low values of damage thresholds compared to those for bare surfaces or within the bulk of many optical materials. This situation arises undoubtedly from the influence of many extrinsic variables characteristic of materials in thin film form resulting from specific coating processes.

For laser induced damage in metals, the mechanism is rather well established on a thermal basis and laser damage in this class of material is the only one which is not the subject of too much dispute.

Advances in the laser damage field have generally required corresponding advances in the area of diagnostic instrumentation technology. The use of Auger spectroscopy[2] to probe the concentration of impurities near surfaces is an example of a sophisticated research tool being brought to bear on the optical components problem with great effect.

Another technique advanced for thin films and transparent materials is attenuated total reflection (ATR) spectroscopy[2] by which it is possible to probe for the effects of surface absorption with very high sensitivity and to distinguish between near surface absorption and bulk absorption. Other techniques include, photoacoustic spectroscopy and photothermal deflection spectroscopy which are of great promise for the indentification and imaging impurities on the surfaces of optical materials beside being capable of distinguishing between surface and bulk absorption.

In parallel with these advances in the laser damage field, there have been few methods for the detection of laser induced damage in optical materials. The occurrence of laser damage has been established by one of the following observations:

1 - The microscopic examination of the surfaces or of the track in the bulk in the case of transparent materials after the sample, has been exposed to the damaging laser pulse[3]. This method although valuable, only indicates damage at a very advanced stage and gives little information except that visible damage has taken place.

2 - Plasma production at the surfaces of optical components has been taken, for a long time, as an indicator for the occurrence of laser damage, but since, in many cases, plasmas can be produced without concurrent structural

modifications, this method of laser induced damage detection is not reliable.

3 - Comparison of the incident and transmitted/reflected laser pulse waveforms[4] to exhibit the onset and type of laser damage. This method is particularly useful for transparent materials. An illustration of this method is shown in Figure 6.1. The transmitted intensity drops to a very low level for intrinsic breakdown as essentially the whole beam is intercepted. By contrast, inclusion damage may intercept only a fraction of the incident pulse. Consequently this detection method is under serious doubt since there have been cases in which microscopic examination revealed damage even where pulse modification has not occurred.

4 - The change in the reflectivity of the optical component, especially in thin film coatings, has also been used[5]. Time resolved reflectivity measurement during and after the damaging pulse is a sensitive indicator for the onset of laser damage and reflectivity changes have consistently been seen even in cases where neither plasma formation nor pulse truncation was observed. The damage was confirmed by microscopic examination.

5 - By attaching a sensitive temperature gauge to the rear surface of the sample[6]. In this detection method, laser induced damage is related to the sudden rise in the sample temperature.

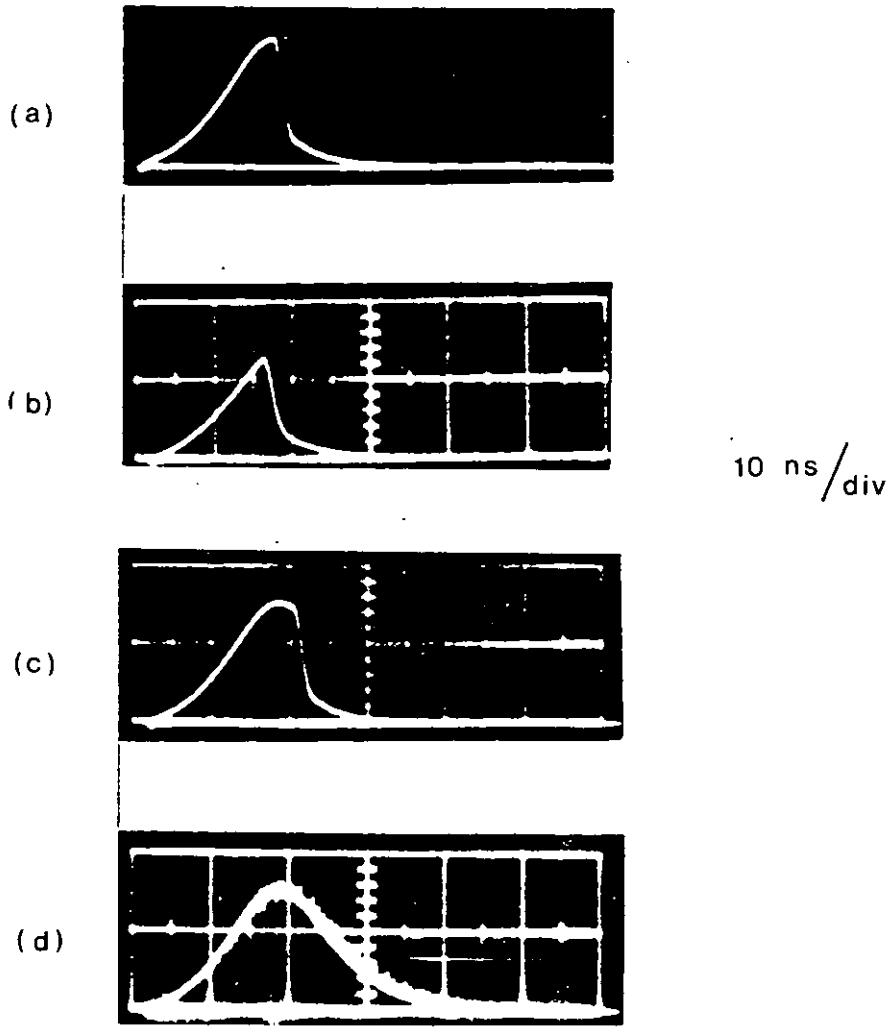

Figure 6.1: Occurrence of internal damage in NaCl due to ruby laser irradiation. The laser intensity transmitted through the sample is shown in these photos. (a) Damaged when the peak laser field was reached: $E_{damage}/E_{peak} = 1$. (b) Damaged before the peak laser field was reached $E_{damage}/E_{peak} = 0.896$. (c) Damaged after the peak laser field was reached: $E_{damage}/E_{peak} = 0.954$. (d) Three successive pulses, no damage: $E_{peak} \equiv 1$ (arbitrary units). (after ref.4).

6 - Laser induced scattering as a sensitive indicator of damage has also been investigated for some time, but, in most cases as an axillary technique incorporated with one or two of the techniques mentioned above. Again this technique has indicated damage in thin film coatings without the observation of either a visible spark or modification of the transmitted laser pulse.

All these techniques have limited quantitative capabilities with varying degrees of sensitivity.

There is a continuing search for precursors to damage which might provide a nondestructive test for damage studies as well as obtaining some quantitative data about damage mechanisms themselves. This need for a precursor or early warning is important since in addition to detecting the initial stages of laser induced damage, it might prevent catastrophic damage from occurring on subsequent shots. If this occurs beam quality may be degraded to a point which makes shutting down the laser necessary until the damaged component is replaced.

In this project we have described three new real-time damage detection techniques for monitoring the early stages of laser induced damage in optical materials. These are, the photoacoustic technique, photothermal deflection and laser scattering.

In the photoacoustic technique, damage was detected by a piezoelectric transducer attached to the

sample. In the second technique, photothermal deflection, the detection of damage was accomplished through the changes in the deflection of a He-Ne laser probing the refractive index gradient generated by the pump beam above the damage site. Two different geometries were used, parallel probing and glancing reflection. The reflection geometry is more sensitive due to the fact that the probe senses the gas immediately next to the surface together with the additional contribution to the deflection signal arising from the thermal expansion of the interaction region.

The principle of the third technique, laser scattering, is based on blocking the specular reflection of the probe beam by a small circular stop and allowing only the scattered light to be detected. Damage in this case was correlated to the increase in the scatter of the probe laser beam. The scattering technique has been used to detect damage at two important wavelengths, i.e., at 10.6 μm and in the U.V. at 248 nm. The three techniques led by the laser induced scatter method have proved to be very sensitive for the detection of the early stages of laser induced damage in optical materials. The advantage of these techniques is that they can be applied to any optical component whether it is transparent, a thin film coating or a metal. In most of the experiments reported here, although damage has been detected by using one of the three detection schemes, it was not possible

to detect damage by microscopic examination even under high magnification. In addition, the spot-size dependence of laser induced damage and the manner in which the sample is irradiated were also investigated. It was shown that the damage threshold in the case of an N - on - 1 experiment was higher than the case of 1 - on - 1 experiment due to the pre-conditioning of the surface by some sort of laser polishing. While the damage threshold scaled as $(\text{spot-size})^{-1}$ in agreement with the predictions presented in Chapter One.

An extension of this work seems possible by investigating some of the following suggestions:

1 - The total internal reflection microscopy technique (TIRM) described by Temple[7] allows structures at and near the surface of a transparent sample or in a film on a transparent substrate to be observed. This is done by illuminating the sample from within using a well-collinated polarized laser beam incident at an angle equal to or greater than the critical angle of the sample material and examining the air side of the surface using an optical microscope as shown in Figure 6.2. Since total reflection occurs at the sample surface, the only light which reaches the microscope objective is that which has been scattered by surface irregularities or defects. By replacing the microscopic objective by a light collector, this system can be used as another scattering technique for the early detection of laser

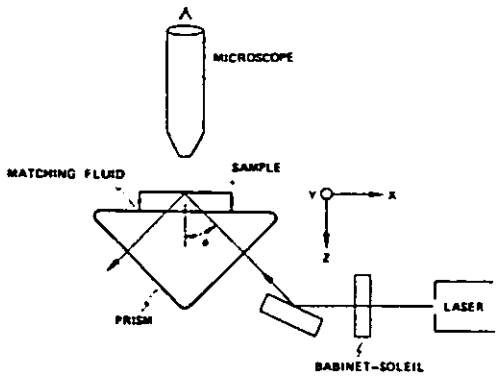

Figure 6.2: Physical setup used to illuminate transparent surfaces for microscopic examination. Not shown is a microscope slide manipulator used to grasp the sample and to slide it about on the oil-covered prism face. The Babinet-Soleil plate is used to change the plane of polarization of the illuminating laser beam. (after ref.7).

induced damage in optical transparent materials. Since during laser damage a change in the morphology of the surface is expected, this change, in turn, will result in increased scattering. This modified damage detection scheme will minimize the amount of scattered light due

to the dust particles or defects on the optical elements from reaching the detector as compared to the case of external illumination in the conventional scattering technique.

It has also been found that on very smooth surfaces, far more features are seen using TIRM than are seen under Nomarski illumination. Alternatively, TIRM can be used as a basis for high speed photography of the time evolution of the laser induced damage in transparent materials. In this case the He-Ne laser of Figure 6.2 can be replaced by a very short duration light source. If this photography is feasible, it will provide valuable information about the damage process and it will also give the exact starting time of laser damage and possibly a more accurate damage threshold value.

2 - Electron emission from laser illuminated metals, was historically the first aspect of particle production using lasers. Electron emission can be produced under conditions where little or no damage to the surfaces occurs[8,9]. It has been investigated employing both normal[8] and Q-switched lasers[10]. Although the very rapid response of the electron emission was reminiscent of a photoelectric response, it was soon recognized that the most likely process for producing electron emission was thermoionic emission [8].

Experiments in which the work function of the

surface and the photon energy in the laser beam were varied, indicated that the electron emission pulses were not critically dependent on the ratio of the work function to the photon energy as would be the case of a mechanism such as a two-photon photoelectric effect were operative. It may be possible to use the electron emission as a sensitive indicator for the early stages of laser induced damage in metals. In this case, below the threshold for surface damage, the electron emission will be proportional to the incident laser energy density and the damage threshold can be correlated with a critical photocurrent density at the surface. This experiment which must be done in a low pressure ambient gas has an important advantage, it may also be possible to calculate the surface temperature profile using Richardson's equation which has the form:

$$j = AT^2 \exp\left(-\frac{\phi}{B_k T}\right) \qquad (6.1)$$

where j is the current density, ϕ is the work function of the surface, T is the temperature and B_k is Boltzman's constant.

It would seem that this experiment would be difficult to carry out and the interpretation of the results would not be straightforward. For example, the integrated electron current would lead to the average $(\text{temperature})^2$, but it may lead to a technique for

determining the maximum temperature reached during the laser pulse and possibly give the temperature decay process after irradiation. However, if one is only interested in a precursor for the occurrence of laser induced damage, this technique may be rewarding.

3 - A simple piezoelectric transducer was found to be an excellent detector of the change in the absorption of laser energy in transparent and reflecting optical components and was able to indicate irreversible damage before any other technique. It may be that this method can be extended by using broadband transducers in which case signal processing might allow plasma production and material microcracking to be distinguished. The development of piezoelectric polymer films may offer another approach where the small size of the transducers made from these materials may overcome some of the problems associated with direct optical scattering and excitation of the acoustic transducer.

4 - Parallel photothermal deflection in which the probing of the gradient of the index of refraction is accomplished in the thin layer adjacent to the sample, is a technique most suited for opaque samples. For transparent samples which have a small absorption coefficient at the pump beam, it is better to use the collinear geometry as shown in Figure 4.1b, page 178. In this case the gradient of the index of refraction is both created and probed within the sample. The

advantage of using collinear geometry is that there would be no problem of minimum offset as discussed in Chapter Four, the probe beam can be brought into coincidence with the pump beam.

The sensitivity of these probe techniques may also be improved by using position sensors which are being developed. These sensors are potentially capable of measuring deflections of the order of 10^{-9} - 10^{-11} rad[11].

REFERENCES

CHAPTER ONE.

1 - P.D. Marker, R.W. Terhune and C.M. Savage, in Proc. 3rd Int. Conf. Quantum Electronics, Edited by: P. Grivet and N. Bloembergen, Paris, Dunuel, (1964) 1559.

2 - J.J. O'Dwyer, "The theory of dielectric breakdown in solids", Oxford, 1964.

3 - F. Seitz, Phys. Rev., 54 (1938) 54.

4 - S.R. Gunn, Rev. Sci. Instrum., 45 (1974) 936.

5 - J.G. Edwards, H.R. Gallantree and R.M. Quilliam, J. Phys., E, Sci. Instrum., 10 (1977) 699.

6 - M. Sparks, Laser Induced Damage in Optical Material, NBS. Spec. Pub., 435 (1975) 331.

7 - N. Bloembergen, IEEE. J. Quantum Electronics, QE-10, (1974) 345.

8 - A. Vaidyanthan, T.W. Walker and A.H. Guenther, Laser Induced Damage in Optical Materials, NBS. Spec. Pub., 568 (1979) 547.

9 - C. Kittel, "Introduction to solid state physics", 4th ed., Wiley, N.Y. 1971.

10 - M. Sparks, D.L. Mills, R. Warren, T. Helstein, A.A. Maradudin, L-J. Sham, L. Loh and D.F. King, Phys. Rev., B24 (1981) 3519.

11 - B.G. Gorshkov, Yu.K. Danileiko, A.F. Epifarov, V.A. Labachev and A.V. Sidorin, Soviet Phys. JETP., 45 (1977) 612.

12 - Y. Yosojima, Y. Ohmori, N. Okumura and Y. Inuishi, Jap. J. Appl. Phys., 14 (1975) 815.

13 - J.P. Anthens and M. Bass, Appl. Phys. Lett., 31 (1977) 412.

14 - R. Bullough and J.J. Gilman, J. Appl. Phys., 37 (1966) 2283.

15 - V.A. Pashkov and G.M. Zverev, Soviet Phys. JETP., 24 (1967) 516.

16 - A. Wasserman, Appl. Phys. Lett., 10 (1967) 132.

17 - C.R. Giuliano, Appl. Phys. Lett., 21 (1972) 39.

18 - N. Bloembergen, Appl. Opt., 12 (1973) 661.

19 - T.W. Walker, A.H. Guenther and P. Nilson, IEEE. J. Quantum Electronics, QE-17 (1981) 2053.

20 - M.D. Crisp, N.L. Boling and G. Dube, Appl. Phys. Lett., 21 (1972) 364.

21 - A.J. Glass and A.H. Guenther, Appl. Opt., 12 (1973) 637.

22 - M. Born and E. Wolf, "Principles of optics", Pergamon Press, 1964.

23 - W.W. Duley, "CO_2 Lasers; Effects and applications", Academic Press, 1976.

24 - M. Sparks and E. Loh, Jr., J. Opt. Soc. Am., 69 (1979) 847.

25 - B.E. Newman and D.H. Gill, Laser Induced Damage in Optical Materials, NBS, Spec. Pub., 541 (1978) 190.

26 - R.W. Hopper and D.R. Uhlman, J. Appl. Phys., 41 (1970) 4023.

27 - T.W. Humphreys, R.L. Lust and K.C. Jungling, Laser Induced Damage in Optical Materials, NBS Spec. Pub., 368 (1979)368.

28 - H. Goldenberg and M.A. Tranter, Brit. J. Appl. Phys., 2 (1952) 226.

29 - H.C. Van de Hulst, "Light scttering by small particles", Wiley, N.Y., 1975.

30 - M.R. Lange and J.K. McLever, Laser Induced Damage in Optical Materials, NBS Spec. Pub., 669 (1982) 380.

31 - D. Milam, Laser Induced Damage in Optical Materials, NBS Spec. Pub., 541 (1978) 164.

32 - D. Milam and R.A. Bradhung, Appl. Phys. Lett., 23 (1973) 654.

33 - D.W. Fradin and M. Blembergen, Appl. Phys. Lett., 22 (1973) 635.

34 - N. Alyassini and J.H. Parks, Laser Induced Damage in Optical Materials, NBS Spec. Pub., 435 (1975) 356.

35 - W. Smith, Opt. Eng., 17 (1978) 489.

36 - J.R. Bettis, R.A. House II and A.H. Guenther, Laser Induced Damage in Optical Materials, NBS Spec. Pub., 435 (1975) 338.

37 - L.A. Nesterov, A.A. Poplavskii, I.A. Fersman and L.D. Khazov, Sov. Phys. Tech. Phys., 15 (1970) 505.

38 - A.I. Rubinshtien and V.M. Fain, Sov. Phys. Solid State., 15 (1973) 332.

39 - S.I. Zakharov, A.A. Manenkov and A.M. Prokhorov, Sov. Phys. JETP., 41 (1975) 1056.

40 - A.R. Hassen, Nuovg Cimento., LxxB (1970) 21.

41 - J.O. Porteus, D.L. Decker, W.N. Faith, D.J. Grandjen, S.C. Seitel and M.J. Soileau, IEEE. J. Quantum Electronics, QE-17 (1981) 2078 .

42 - L.G. DeShazer, B.E. Newman and K.M. Leung, Laser Induced Damage in Optical Materials, NBS Spec. Pub., 387 (1973) 114.

43 - C.C. Tang, K.M. Leung and M. Bass, Laser Induced Damage in Optical Materials, NBS Spec. Pub., 462 (1976) 346.

44 - M.J. Soileau, M. Bass and E.W. Stryland, Laser Induced Damage in Optical Materials, NBS Spec. Pub., 541 (1978) 541.

45 - S.R. Foltyn, Laser Induced Damage in Optical Materials, NBS Spec. Pub., 669 (1982) 368.

46 - D.W. Fradin and M. Bass, Appl. Phys. Lett., 22 (1973) 206.

47 - L.V. Keldysh, Sov. Phys. JETP., 20 (1965) 20.

48 - M. Bass and K.M. Leung, IEEE, J. Quantum Electronics, QE-12 (1976) 82.

49 - V.I. Kovalev and F.S. Faizullov, Laser Induced Damage in Optical Materials, NBS Spec. Pub., 541 (1978) 318.

50 - V.I. Kovalev and F.S. Faizullov, Sov. Phys. Quantum Electronics., N3 (1977) 7.

51 - J. Kardch, A.F. Stewart and A.H. Guenther, Laser Induced Damage in Optical Materials, NBS Spec. Pub., 669 (1982) 164.

52 - P. Bräunlich, G. Brost and A. Schmid, Laser Induced Damage in Optical Materials, NBS Spec. Pub., 620 (1980) 406.

53 - D.L. Decker and J.O. Porteus, Laser Induced Damage in Optical Materials, NBS Spec. Pub., 638 (1981) 239.

54 - D.L. Decker, J.B. Frank, W.N. Faith and J.O. Porteus, Laser Induced Damage in Optical Materials, NBS Spec. Pub., 669 (1982) 178.

55 - R.A. House, J.R. Bettis and A.H. Guenther, Laser Induced Damage in Optical Materials, NBS Spec. Pub., 462 (1976) 310.

56 - D. Milam, Appl. Opt., 16 (1977) 1204.

57 - J.R. Bettis, A.H. Guenther and R.A. House, Opt. Lett., 4 (1979) 256.

58 - S.D. Allen, Laser Induced Damage in Optical Materials, NBS Spec. Pub., 414 (1974) 66.

59 - R.A. Hoffman, W.J. Lange and W.J. Choyke, Laser Induced Damage in Optical Materials, NBS Spec. Pub., 435 (1975) 14.

60 - T.T. Saito, Laser Induced Damage in Optical Materials, NBS Spec. Pub., 414 (1974) 227.

61 - M.J. Soileau, J.M. Bennett, J.O. Porteus, W. Faith and J. Jeringan, Laser Induced Damage in Optical Materials, NBS Spec. Pub., 462 (1976) 149.

62 - S.V. Bilibin, V.N. Egrov, A.A. Katsnelson, V.I. Kovalev, N.S. Kolesova, Yu. S. Sildrov, N.L. Tkachenka and F.S. Faizullov, Laser Induced Damage in Optical Materials, NBS Spec. Pub., 638 (1981) 258.

63 - W.E.K. Gibbs and A.D. McLachlan, Laser Induced Damage in Optical Materials, NBS Spec. Pub., 435 (1975) 90.

64 - S.A. Akhumanov, R.V. Khokhlov and A.P. Sukhorukov, Laser Handbook, Vol.2, edited by F.T. Arecchi and E.O. Schultz-BuBois, North Holland 1972.

65 - J.M. Dawson, Phys. Fluid., 7 (1964) 981.

66 - C.R. Giuliano, IEEE. J. Quantum Electronics, QE-8 (1972) 719.

67 - I.A. Fersman and L.D. Khazove, Sov. Phys. Tech. Phys., 5 (1970) 834.

68 - D.C. Emmony, R.P. Howson and L.J. Willis, Appl. Phys. Lett., 23 (1973) 598.

69 - P.A. Temple and M.J. Soileau, IEEE J. Quantum Electronics, QE-17 (1981) 2067.

70 - M.J. Soileau, J.M. Bennett, J.O. Porteus, W. Faith, J. Jeringan and T.T. Saito, NBS, Boulder, CO, Rep. 462 pp.149 (1976).

71 - M.J. Soileau, J.O. Porteus and D.L. Decker, Appl. Opt., 19 (1980) 3043.

72 - M.J. Soileau and E.W. Stryland, J. Opt. Soc. Am., 72 (1982) 1756.

73 - M. Siegrist, G. Kaech and F.K. Kneübuhl, Appl. Phys. Lett., 12 (1973) 45.

74 - M. Birnbaum, J. Appl. Phys., 36 (1965) 3688.

75 - Q.N. Maracus, G.L. Harris, C.A. Lo and R.A. McFarlane, Appl. Phys. Lett., 33 (1978) 453.

76 - M.A. Cutter, P.Y. Key and V.I. Little, Appl. Opt., 13 (1974) 1399.

77 - S.R.J. Brueck and D.J. Ehrlich, Phys. Rev. Lett., 48 (1982) 1678.

78 - J.O. Porteus, J.L. Jeringan and W. Faith, Laser Induced Damage in Optical Materials, NBS Spec. Pub., 509 (1977) 507.

79 - Z. Guosheng, P.M. Fouchet and A.E. Siegman, Phys. Rev., 26 (1982) 2144.

80 - J.F. Figueira and S.J. Thomas, Int. Con. on surface studies with lasers, Mauterndorf, Austria, 1983.

81 - M.J. Soileau, IEEE. J. Quantum Electronics, QE-20 (1984) 464.

82 - J.A. Ringlien, N.L. Boling and G. Dube, Appl. Phys. Lett., 25 (1974) 598.

83 - P.A. Temple, W.H. Lowdermilk and D. Milam, Appl. Opt., 21 (1982) 3249.

84 - J.E. Swain, H.W. Lowdermilk and D. Milam, Laser Induced Damage in Optical Materials, NBS Spec. Pub., 669 (1982) 292.

85 - A.F. Stewart and A.H. Guenther, Appl. Opt., 23 (1984) 3774.

86 - R. Hack and N. Neuroth, Appl. Opt., 21 (1982) 3239.

87 - W.H. Reichelt and E.E. Stark Jr., Laser Induced Damage in Optical Materials, NBS Spec. Pub., 387 (1973) 175.

88 - M. Bass and H.H. Barrett, IEEE. J. Quantum Electronics., QE-8 (1972) 338.

89 - J.O. Porteus and S.C. Seitel, Appl. Opt., 23 (1984) 3796.

CHAPTER TWO.

1 - C.A. Calder and W.W. Wilcox, Mat. Eval., 38 (1980) 86. Also Rev. Sci. Instrum., 45 (1974) 1557.

2 - A. Rosencwaig, Science., 218 (1982) 218.

3 - A.C. Boccara and D. Founier, Opt. Lett., 9 (1980) 377.

4 - R.J. Dewhurst, D.A. Hutchins and S.B. Palmer, J. Appl. Phys., 53 (1982) 4064.

5 - K.P. Herman, "Instrument transducers", Clarendon Press, Oxford, 1975.

6 - L. Bui, H.J. Shaw and L.T. Zitell, Elec. Lett., 12 (1976) 393.

7 - S.T. Liu and W.B. Harrison, Ferroelectronics., 27 (1980) 27.

8 - M.G. Silk, "Ultrasonic transducers for non-destructive testing", Adam Hilger Ltd., Bristol, 1984.

9 - M.G. Silk, J. Phys. E: Sci. Instrum., 16 (1983) 879.

10 - R.A. Kline and R. Green, J. Acoust. Soc. Am., 64 (1978) 1633.

11 - C.B. Scruby and H.N.G. Wadley, J. Phys. D: Appl. Phys., 11 (1978) 1487.

12 - L.E. Kinsler and A.R. Freg, "Fundamentals of acoustics", 2nd ed., Wiley, 1962.

13 - F.M. Boler, H.A. Spetzler and I.C. Getting, Rev. Sci. Instrum., 55 (1984) 1293.

14 - T.M. Procter, J. Acoust. Soc. Am., 75 (1982) 1163.

15 - J. Niewisch and P. Krämmer, Sensors and Actuators., 3 (1982/83) 187.

16 - C.H. Palmer and R.E. Green, Appl. Opt., 16 (1977) 2333.

17 - W.C. Leschek, Mat. Eval., 33 (1975) 41.

18 - S.L. McBride and T.S. Hutchins, Cand. J. Appl. Phys., 54 (1972) 84.

19 - L.J. Graham, in "Non-destructive testing handbook", edited by R.C. McMaster, Am. Soc. for non-destructive testing, 1959.

20 - F.R. Breckenridge, C.E. Tschiegg and M. Greenspan, J. Acoust. Soc. Am., 57 (1975) 626.

21 - N. Hsu, Acoustic emission stimulate, U.S. Patent 4018084, 1976.

22 - A. Nielsen, The Danish Welding Institute, 1980.

23 - H.N.G. Wadley and J.A. Simmons, Review of progress in quantitative non-destructive testing, Santa Cruz 1983, edited by D.O. Thompson and D.E. Chiment, Plenum Press, N.Y.,1983.

CHAPTER THREE.

1 - A.G. Bell, Phil. Mag., 11 (1981) 510.

2 - R.M. White, J. Appl. Phys., 34 (1963) 3559.

3 - J.F. Ready, "Effects of high-power laser radiation", Academic Press, London, 1971.

4 - L.S. Gournay, J. Acoust. Soc. Am., 40 (1966) 1322.

5 - G.A. Askaryan, A.M. Prokhorov, G.F. Chanturiya and G.P. Shipola, Soviet Phys. JETP., 17 (1963) 1403.

6 - C.E. Bell and J.A. Landt, Appl. Phys. Lett., 10 (1967) 46.

7 - D.C. Emmony, M. Siegrist and F.K. Kneübyhl, Appl. Phys. Lett., 29 (1976) 547.

8 - M. Siegrist and F.K. Kneübuhl, J. Acoust. Soc. Am., 64 (1978) 1652.

9 - P.S. Sladky, R. Danielius, V. Sirutkaitis and M. Bandys, Gzech. J. Phys., B27 (1977) 1075.

10 - C.H. Skeen and C.M. York, Appl. Phys. Lett., 12 (1968) 369.

11 - R.S. Peercy, E.D. Jones, J.C. Bushnell and G.W. Gobeli, Appl. Phys. Lett., 16 (1970) 120.

12 - E.D. Jones, Appl. Phys. Lett., 18 (1971) 33.

13 - N.C. Anderholm, Appl. Phys. Lett., 16 (1970) 113.

14 - B.P. Fairand, A.H. Caluer, R.G. Jung and B.A. Wilcox, Appl. Phys. Lett., 25 (1974) 431.

15 - J.D. O'Keefe and C.H. Skeen, Appl. Phys. Lett., 21 (1972) 464.

16 - J.A. Fox, Appl. Phys. Lett., 24 (1974) 461.

17 - H.M. Ledbetter and J.C. Moulder, J. Acoust. Soc. Am., 65 (1979) 840.

18 - K. Kubota and Y. Nakatani, Jap. J. Appl. Phys., 12 (1973) 888.

19 - R.E. Lee and R.M. White, Appl. Phys. Lett., 12 (1968) 12.

20 - C.A. Calder and W.W. Wilcox, Mat. Eval., 38 (1980) 86.

21 - R.L. Wellman, Conference on laser and electrooptics systems, San Diego, 106 (1978).

22 - A. Rosencwaig, Opt. Comm., 7 (1973) 305.

23 - R.J. von Gutfeld and R.H. Melher, Appl. Phys. Lett., 30 (1977) 257.

24 - B.I. Bleany and B. Bleany, "Electricity and magnetism", Oxford Press, 2nd ed. 1965.

25 - L.C.M. Miranda, Appl. Opt., 22 (1983) 2882.

26 - H.C. Carslaw and J.C. Jaeger, "Conduction of heat in solids", 2nd ed., Oxford Press, London, 1959.

27 - N.N. Rykalin, A.A. Voglov and M. Makarov, Soviet. Int. Con. on surface studies with lasers, Mauterndorf, 1983.

28 - C.K.N. Patel and A.C. Tam, Rev. Mod. Phy., 53 (1981) 517.

29 - A. Hardvik and H. Schlossberg, Appl. Opt., 16 (1977) 101.

30 - Y.H. Pao, "Optpacoustic spectroscopy and detection", Academic Press, 1977.

31 - C.K.N. Patel and A.C. Tam, Appl. Phys. Lett., 34 (1979) 467.

32 - A. Rosencwaig and J.B. Willis, J. Appl. Phys., 51 (1980) 4361.

33 - A.C. Tam and H. Couful, Appl. Phys. Lett., 42 (1983) 33.

34 - R.J. Dewhurst, D.A. Hutchins and S.B. Palmer, J. Appl. Phys., 53 (1982) 4064.

35 - S.I. Green, Rev. Sci. Instrum., 47 (1976) 1083.

36 - H.P. Weber, J. Appl. Phys., 39 (1968) 6041.

37 - A. Schmid, P. Horn and P. Braunlich, Appl. Phys. Lett., 42 (1983) 151.

38 - A. Rosencwaig and S. Hall, Anal. Chem., 47 (1975) 548.

39 - A. Rosencwaig, In advances in electronics and electron physics., 46 (1978) 207.

40 - A. Rosencwaig and J.B. Willis, Appl. Phys. Lett., 36 (1980) 667.

41 - D.S. Stark, P.H. Cross and H. Foster, IEEE. J. Quantum. Electronics., QE-11 (1975) 774.

42 - J.F. Figueira and S.J. Thomas, IEEE. J. Quantum. Electronics., QE-18 (1982) 1381.

43 - M. Sparks and E. Loh, Jr., J. Opt. Soc. Am., 69 (1979) 847.

44 - J.O. Porteus, M.J. Soileau and C.W. Fountain, Laser Induced Damage in Optical Materials, NBS Spec. Pub., 462 (1976) 165.

45 - T.E. Zavecz and M.A. Saifi, Appl. Phys. Lett., 26 (1975) 165.

46 - M.K. Chun and K. Rose, J. Appl. Phys., 41 (1970) 614.

47 - A.M. Prokhorov, V.A. Batanov, F.V. Bunkin and V.B. Fedorov, IEEE. J. Quantum. Electronics., QE-9, (1973) 503.

48 - J.F. Ready, IEEE. J. Quantum. Electronics., QE-12, (1976) 137.

49 - J.A. McKay, R.D. Bleach, D.J. Najel, J.T. Schriempf, R.B. Ball, C.R. Pond and S.K. Manlief, J. Appl. Phys., 50 (1979) 3231.

50 - A.N. Pirri, R.G. Wood and P.K.S. Wu, AIAA., 16 (1978) 1296.

51 - J.R. Bettis, R.A. House and A.H. Guenther, Laser Induced Damage in Optical Materials, NBS Spec. Pub., 462 (1976) 338.

CHAPTER FOUR.

1 - A.J. Bard, J. Photochem., 10 (1979) 59.

2 - W.B. Jackson, N.M. Amer, A.C. Boccara and D. Fournier, Appl. Opt., 20 (1981) 1333.

3 - J.C. Murphy and L.C. Aamdt, J. Appl. Phys., 51 (1980) 4580.

4 - D. Fournier, A.C. Boccara and J. Badoz, Appl. Opt., 21 (1982) 74.

5 - A.C. Boccara and D. Fournier, Opt. Lett., 5 (1980) 337.

6 - N. Koumuakalis, C.-S. Lee and M. Bass, Laser Induced Damage in Optical Materials, NBS Spec. Pub., 638 (1981) 160.

7 - D.L. Stierwalt, Appl. Opt., 5 (1966) 1911.

8 - A. Hordvik and H. Schlossberg, Appl. Opt., 16 (1977) 101.

9 - Y.L. Wong, R.L. Thomas and G.F. Hawkins, Appl. Phys. Lett., 32 (1978) 538.

10 - M. Luukkala and S.G. Askerov, Electron. Lett., 16 (1980) 84.

11 - R.J. Freese, Ph.D. thesis, University of Rochester, 1979,

12 - G. Busse and A. Ograboch, J. Appl. Phys., 51 (1980) 3576.

13 - Y.H. Wong, in "Scanned Image Microscopy" edited by E.A. Ash, Academic Press, London, 1980.

14 - G. Busse, Appl. Phys. Lett., 35 (1979) 1759.

15 - M. Luukkala, in "Scanned Image Microscopy" edited by E.A. Ash, Academic Press, London, 1980.

16 - P.E. Nordal and S.O. Kanstad, ibid, page 331.

17 - G. Busse, ibid, p.341.

18 - A. Rosencwaig, Science., 218 (1982) 223.

19 - G.S. Cargill, Nature., 286 (1980) 691.

20 - A. Rosencwaig, Am. Lab., 11 (1979) 39.

21 - M.A. Tamor and R.E. Hetrick, Appl. Phys. Lett., 46 (1985) 460.

22 - R. Rose, J.D. Pyrum, C. Muzny, G.J. Salama and R. Gupta, Appl. Opt., 21 (1982) 2663.

23 - A. Rosencwaig, J. Opsal and D.L. Willenberg, Appl. Phys. Lett., 43 (1983) 166.

24 - J. Opsal, A. Rosencwaig and D.L. Willenberg, Appl. Opt., 22 (1983) 3169.

25 - J.A. Abate and R. Roides, J. De. Phys., 44 (1983) 497.

26 - A. Schmidt, D. Smith, M. Guardalen and J.A. Abate, SPIE., 476 (1984) 136.

27 - H. Sontang and A.C. Tam, Appl. Phys. Lett., 46 (1985) 725.

28 - International Critical Tables, National Research Council, Vol. VIE, McGraw Hill, N.Y. 1930.

29 - Laser Focus, February (1976) 1.

30 - G.P. Davidson and D.C. Emmony, J. Phys. E: Sci. Instrum., 13 (1980) 92.

31 - L.C. Aamodt and J.C. Morphy, J. Appl. Phys., 54 (1983) 581.

CHAPTER FIVE.

1 - H.E. Bennett, Opt. Eng., 17 (1978) 480.

2 - J. Stratton, "Electromagnetic theory", McGraw Hill, N.Y. 1940.

3 - M. Kerker, "The scattering of light and other electromagnetic radiation", Academic Press, 1969.

4 - P. Beckman, "Scattering of electromagnetic waves from rough surfaces", Pergamon Press, 1963.

5 - J.F. Ready, "Effects of high-power laser radiation", Academic Press, 1971.

6 - M. Born and E. Wolf, "Principles of Optics", Pergamon Press, 1964.

CHAPTER SIX.

1 - H. Goldenberg and M.A. Tranter, Brit. J. Appl. Phys., No.2, (1952) 296.

2 - A.J. Glass and A.H. Guenther, Laser Induced Damage in Optical Materials, 8th ASIM symposium, Appl. Opt., 16 (1977) 1214.

3 - E. Yablonovitch, Appl. Phys. Lett., 19 (1971) 495.

4 - D.W. Fradin, E. Yablonovitch and M. Bass, Appl. Opt., 12 (1973) 700.

5 - N. Alyassini and J.H. Parks, Laser Induced Damage in Optical Materials, NBS Spec. Pub., 435 (1975) 356.

6 - N. Koumvakalis, C.S. Lee and M. Bass, Opt. Eng., 22 (1983) 419.

7 - P.A. Temple, Appl. Opt., 20 (1981) 2656.

8 - D. Lichtman and J.F. Ready, Phys. Rev. Lett., 10 (1963) 342.

9 - J.F. Ready and A.H. Guenther, Appl. Opt., 12 (1973) 637.

10 - J.F. Ready, Phy. Rev., 137 (1965) A620.

11 - W.B. Jackson, N.M. Amer, A.C. Boccara and D. Fournier, Appl. Opt., 20 (1981) 1333.